

FOR FURTHER TRAN *AE 21* REPORT ONR-CR215-226-4F

13
SC

ADA 054349



AD No.

DDC FILE COPY

6 A PRELIMINARY METHOD FOR CALCULATING THE
AERODYNAMIC CHARACTERISTICS OF CRUCIFORM MISSILES
TO HIGH ANGLES OF ATTACK INCLUDING EFFECTS OF
ROLL ANGLE AND CONTROL DEFLECTIONS.

10 JACK N. NIELSEN, MICHAEL J. HEMSCH
AND CHARLES A. SMITH

DDC DRAFTING
MAY 30 1978
RECEIVED
A

14 NEAR-TR-152 NIELSEN ENGINEERING & RESEARCH, INC.
MOUNTAIN VIEW, CALIFORNIA 94043

15 CONTRACT NO 00014-74-C-0050

18 ONR CR215-226-4F ONR TASK 215-226

12 335 P.

9 11 1 ANNUAL TECHNICAL REPORT PERIOD 1 OCT 76 - 30 SEPT 77

19 APPROVED FOR PUBLIC RELEASE; DISTRIBUTION UNLIMITED

16 RR01411

17 RR0141184

PREPARED FOR THE



OFFICE OF NAVAL RESEARCH • 800 N. QUINCY ST. • ARLINGTON • VA • 22217

389 783

NOTICES

Change of address

Organizations receiving reports on the initial distribution list should confirm correct address. This list is located at the end of the report. Any change of address or distribution should be conveyed to the Office of Naval Research, Code 211, Arlington, VA 22217.

Disposition

When this report is no longer needed, it may be transmitted to other organizations. Do not return it to the originator or the monitoring office.

Disclaimer

The findings and conclusions contained in this report are not to be construed as an official Department of Defense or Military Department position unless so designated by other official documents.

Reproduction

Reproduction in whole or in part is permitted for any purpose of the United States Government.

PREFACE

This technical report covers the work performed under Contract N00014-74-C-0050 from 1 October 1976 to 30 September 1977, and is the fourth report published under the program. The program is sponsored by the Office of Naval Research with significant assistance provided by NASA/Ames Research Center and the Air Force Flight Dynamics Laboratory.

Mr. David Siegel, Office of Naval Research, is the Navy Scientific Officer. Dr. Gary T. Chapman and Mr. Gerald N. Malcolm are the NASA advisors. Mr. Calvin L. Dyer is the advisor for the Air Force Flight Dynamics Laboratory.

UNCLASSIFIED

SECURITY CLASSIFICATION OF THIS PAGE (When Data Entered)

REPORT DOCUMENTATION PAGE		READ INSTRUCTIONS BEFORE COMPLETING FORM
1. REPORT NUMBER ONR-CR215-226-4F✓	2. GOVT ACCESSION NO.	3. RECIPIENT'S CATALOG NUMBER
4. TITLE (and Subtitle) A PRELIMINARY METHOD FOR CALCULATING THE AERODYNAMIC CHARACTERISTICS OF CRUCIFORM MISSILES TO HIGH ANGLES OF ATTACK INCLUDING EFFECTS OF ROLL ANGLE AND CONTROL DEFLECTIONS		5. TYPE OF REPORT & PERIOD COVERED TECHNICAL REPORT 10-01-76 to 9-30-77
7. AUTHOR(s) Jack N. Nielsen Michael J. Hemsch Charles A. Smith		6. PERFORMING ORG. REPORT NUMBER NEAR TR 152✓ 8. CONTRACT OR GRANT NUMBER(s) N00014-74-C-0050✓
9. PERFORMING ORGANIZATION NAME AND ADDRESS Nielsen Engineering & Research, Inc.✓ 510 Clyde Avenue Mountain View, California 94043		10. PROGRAM ELEMENT, PROJECT, TASK AREA & WORK UNIT NUMBERS 61153N-14 RR014-11-84, 1-12 ONR TASK NR215-226
11. CONTROLLING OFFICE NAME AND ADDRESS Office of Naval Research (Code 211) 800 N. Quincy Street Arlington, VA 22217		12. REPORT DATE 1 November 1977
14. MONITORING AGENCY NAME & ADDRESS (if different from Controlling Office)		13. NUMBER OF PAGES 333 15. SECURITY CLASS. (of this report) Unclassified 15e. DECLASSIFICATION/DOWNGRADING SCHEDULE N/A
16. DISTRIBUTION STATEMENT (of this Report) Approved for public release; distribution unlimited.		
17. DISTRIBUTION STATEMENT (of the abstract entered in Block 20, if different from Report)		
18. SUPPLEMENTARY NOTES		
19. KEY WORDS (Continue on reverse side if necessary and identify by block number) Missile Aerodynamics; Guided Missiles; Aerodynamic Characteristics; Aerodynamic Canard Control; Aerodynamic Empirical Techniques; Aerodynamic Flow Patterns; Aerodynamic Vortices; Missile Aerodynamic Loads		
20. ABSTRACT (Continue on reverse side if necessary and identify by block number) A method is presented together with a computer program for calculating the forces and moments on the components of a cruciform missile: nose, canard section, afterbody, and tail section. The program utilizes a skeleton data base for the fin normal forces and center-of-pressure positions. These quantities were derived from a set of fins of varying aspect ratio and taper ratio tested on a body having a diameter equal to half the tail span.		

UNCLASSIFIED

SECURITY CLASSIFICATION OF THIS PAGE(When Data Entered)

at *any*

< or =

Block No. 20 (Concluded)

The data base, covering a range $0.8 \leq M_{\infty} \leq 3.0$, is extended to arbitrary cruciform body-tail configurations or body-wing-tail configurations using analytical and empirical methods. Pitch, yaw, and roll control are included in the method as well as the effects of missile roll angle. Comparisons are made between the predictions of the computer program and experiment for fin forces and configuration forces and moments for body-tail and wing-body-tail combinations up to angles of attack of 45° . On the whole acceptable agreement between prediction and experiment is obtained.

deg

DISSEMINATOR REC	
RTD	DATA Section <input checked="" type="checkbox"/>
RRG	BUTT Section <input type="checkbox"/>
DIAMINDED	
JUSTIFICATION	
BY	
DISTRIBUTION/AVAILABILITY CODES	
REQ.	AVAIL. SEC/N SPECIAL
A	

UNCLASSIFIED

SECURITY CLASSIFICATION OF THIS PAGE(When Data Entered)

TABLE OF CONTENTS

<u>Section</u>	<u>Page</u>
1. INTRODUCTION	13
2. OVERVIEW OF ENGINEERING METHOD AND ITS EXTENSION TO HIGH ANGLES OF ATTACK	16
2.1 Range of Parameters	17
2.2 Aerodynamic Model of Missile; Symbols and Conventions	18
2.3 High Angle-of-Attack Body Vortex Model	21
2.3.1 Some high angle-of-attack vortex behavior	21
2.3.2 Fin normal forces in an asymmetric vortex field	28
2.3.3 Decomposition into symmetric and asymmetric vortex effects	30
2.4 Equivalent Angle of Attack Concept	30
2.4.1 K_w contribution	31
2.4.2 K_ϕ contribution	34
2.4.3 Vortex contributions	35
2.4.4 Fin deflection	36
2.5 Description of Data Base	38
2.5.1 Fins of the data base	38
2.5.2 "Vortex-free" data base	42
2.6 Program Limitations	44
3. CONSTRUCTION OF THE DATA BASE	45
3.1 Introductory Remarks	45
3.2 Wing-Alone Normal-Force Curve	46
3.2.1 Fins of aspect ratio 0.5	47
3.2.2 Fins of aspect ratio 1.0 and 2.0	54
3.2.3 Fins of aspect ratio 3.53	54
3.2.4 Tables	55

TABLE OF CONTENTS (Continued)

<u>Section</u>	<u>Page</u>
3.3 Fin Lateral Center of Pressure	55
3.3.1 Fins of aspect ratio 0.5, 1.0 and 2.0	56
3.3.2 Fins of aspect ratio 3.53	59
3.4 Fin Normal-Force Data Including Body Vortex Effects; $AR \leq 2$	59
3.4.1 Manipulation of the data	61
3.4.2 Tabulated results	62
3.5 Fin Normal-Force Data Including Body Vortex Effects; $AR = 3.53, \lambda = .06$	63
3.5.1 Manipulation of the data	63
3.5.2 Tabulated results	65
3.6 Fin Normal-Force Results Without Vortex Effects	65
3.6.1 Illustration of vortex interference effects	65
3.6.2 Tabulated results	67
4. DESCRIPTION AND USE OF DATA BASE	68
4.1 Nonlinearities in the Data Base	68
4.1.1 Characteristics of the data base	68
4.1.2 Nonlinear wing-body interference	70
4.2 Interpolation and Extrapolation in the Data Base	74
4.2.1 Aspect ratio and taper ratio interpolation and extrapolation	77
4.2.2 Mach number interpolation or extrapolation	79
4.3 Use of the Equivalent Angle of Attack Concept	79
4.3.1 Scaling for a/s_m	79
4.3.2 Scaling for vortex effects	83
4.3.3 Effects of control deflection	84

TABLE OF CONTENTS (Continued)

<u>Section</u>	<u>Page</u>
4.3.3.1 Pitch effectiveness at high Mach numbers	85
4.3.3.2 Control effectiveness at $M_{\infty} = 0.8$ and 1.3	88
4.3.3.3 Rules of determination of k_w	95
5. EXTENSION OF BODY VORTEX MODEL TO 50° ANGLE OF ATTACK	97
5.1 Previous Work	97
5.2 Preliminary Remarks	97
5.3 Shed Vortex Strength	101
5.4 Location of Point of Separation	104
5.5 Height of the Recirculation Zone	104
5.6 Computed Correlations for Body Vortex Strengths and Positions for $M_{\infty} = 0.8, 1.2, 2.0$, and 3.0	108
5.6.1 Correlations for $M_{\infty} = 0.8$	108
5.6.2 Correlations for $M_{\infty} = 1.2$	109
5.6.3 Correlations for $M_{\infty} = 2.0$	110
5.6.4 Correlations for $M_{\infty} = 3.0$	110
6. ADDITIONAL MODIFICATIONS TO THE ENGINEERING METHOD	111
6.1 Modifications to the Engineering Method for the Afterbody Section	111
6.2 Modifications to the Engineering Method for the Finned Sections	113
7. COMPARISON BETWEEN EXPERIMENT AND PREDICTIONS OF COMPUTER PROGRAM	120
7.1 Preliminary Remarks	120
7.2 Body-Tail Comparisons	120
7.2.1 Fin normal-force coefficient	120
7.2.2 Configuration induced rolling-moment coefficient	126

TABLE OF CONTENTS (Concluded)

<u>Section</u>	<u>Page</u>
7.3 Wing-Body-Tail Combination; No Control	130
7.3.1 Preliminary remarks	130
7.3.2 Tail fin normal-force coefficients	130
7.3.3 Wing-body-tail forces and moments	134
7.4 Wing-Body-Tail Combination With Canard Control	134
7.4.1 Preliminary remarks	134
7.4.2 Yaw control at zero roll angle	136
7.4.3 Yaw control at $\phi = 30^\circ$	136
7.5 Improved Afterbody Model	140
7.6 AIM-9L Missile With Yaw Control at Zero Roll Angle	144
8. CONCLUDING REMARKS AND RECOMMENDATIONS	147
8.1 Summarizing Conclusions	147
8.2 Recommendations for Further Work	150
REFERENCES	152
APPENDIX A - SPAN LOAD DISTRIBUTIONS DUE TO DEFLECTING OR TWISTING ONE FIN OF A CRUCIFORM WING-BODY COMBINATION	156
APPENDIX B - NORMAL FORCE AND LATERAL POSITION OF CENTER OF PRESSURE ON FIN OF CRUCIFORM WING-BODY COMBINATION DUE TO EXTERNAL VORTEX	166
APPENDIX C - MATHEMATICAL DERIVATION OF EQUIVALENT ANGLE OF ATTACK FORMULA FOR LARGE ANGLES OF ATTACK	180
APPENDIX D - REGION OF INFLUENCE OF ONE FIN ON ANOTHER	190
APPENDIX E - MISSILE, A COMPUTER PROGRAM FOR CALCULATING THE COMPONENT FORCES AND MOMENTS OF ARBITRARILY BANKED CRUCIFORM MISSILES WITH CONTROL DEFLECTIONS	204
LIST OF SYMBOLS	327

LIST OF ILLUSTRATIONS

<u>Figure</u>	<u>Page</u>
1 Banked canard-cruciform missile at angle of attack showing typical vortex field.	19
2 Symbols and conventions.	22-24
3 Inviscid flow in crossflow plane of body of revolution with supersonic crossflow Mach number.	27
4 Effect of roll angle and Mach number on fin normal-force coefficient of fin T14 on B_1 body.	29
5 Effect of angle of attack and free-stream Mach number on interference of body on wing.	33
6 Fins and body of systematic data base.	39
7 Body-canard-tail test configuration.	41
8 Dimensions of canard and tail fins.	43
9 Comparison of splitter-plate data and sting data for normal-force curve of fin T36 at $M_\infty = 3.0$.	48
10 Comparisons of Hill data and Falunin data for fin T36 at $M_\infty = 3.0$.	49
11 Wing-alone normal-force curves as determined on splitter plate for T36, T31, T32.	51
12 Increment in normal-force coefficient as measured on splitter plate at $M_\infty = 3.0$.	52
13 Constructed normal-force curves for wings T36, T31, and T32.	53
14 Lateral position of center of pressure of fin T14 mounted on body B_1 .	57-58

LIST OF ILLUSTRATIONS (Continued)

<u>Figure</u>		<u>Page</u>
15	Lateral position of center of pressure of fin C6 ($AR = 3.53$) mounted on body BN ₃ (ref. 7).	60
16	Effect of roll angle on normal-force coefficient for fin C6 mounted on body BN ₃ (ref. 7).	64
17	Normal-force coefficient of fin T14 on body B ₁ with and without vortex effects; $M_{\infty} = 2.0$.	64
18	Equivalent angle of attack for fin T14 on body B ₁ at $M_{\infty} = 2.0$ and $\alpha_C = 25^\circ$.	66
19	Normal-force coefficients of fin T14 on body B ₁ at $M_{\infty} = 3.0$.	69
20	Nonlinear behavior exhibited by fin T23 at $M_{\infty} = 0.8$.	69
21	Effects of aspect ratio and taper ratio on K_W at $M_{\infty} = 3.0$.	72,73
22	Effects of taper ratio and aspect ratio on K_W at $M_{\infty} = 0.8$.	75,76
23	Effect of radius-semispan ratio on wing interference factor K_W at $M_{\infty} = 3.36$.	81
24	Effect of angle of attack and control deflection on interference factor for control deflection.	86,87
25	Effect of angle of attack and control deflection on pitch control effectiveness of canard fins at $\phi = 0$.	89,90
26	Effect of angle of attack on k_w for canard fin on Army generalized missile (ref. 7).	91,92
27	Effect of α_C and ϕ_4 on k_w for canard fins C6 on Army generalized missile.	94
28	Estimate of boundary between symmetrical and asymmetrical vortex shedding.	100

LIST OF ILLUSTRATIONS (Continued)

<u>Figure</u>	<u>Page</u>
29 Flow velocity at shoulder of circular cylinder.	102
30 Vortex reduction factor used with multi-vortex tracking code.	103
31 Effect of crossflow Mach number on separation points for circular cylinder.	105,106
32 Estimated height of top of recirculation region at $x/D = 10$ for tangent-ogive cylinder.	107
33 Ratio of leeside drag to total drag for circular cylinders.	114
34 Vortex clouds calculated by program of Mendenhall (ref. 21) for cylindrical body with three caliber tangent-ogive nose.	116
35 Comparison of results for $(\Delta\alpha_{eq})_v$ and \bar{y}_v for vortex cloud and for point vortex simulation of cloud; $a/s_m = 0.50$.	117
36 Comparison of results for $(\Delta\alpha_{eq})_v$ and \bar{y}_v for vortex cloud and for point vortex simulation of cloud; $a/s_m = 0.25$.	118
37 Fin normal-force coefficients for configuration BN ₃ T ₂ at $M_\infty = 0.8$; $\phi = 10^\circ$.	122
38 Fin normal-force coefficients for configuration BN ₃ T ₂ at $M_\infty = 1.22$; $\phi = 10^\circ$.	123
39 Fin normal-force coefficients for configuration BN ₃ T ₂ at $M_\infty = 0.8$; $\phi = 20^\circ$.	124
40 Fin normal-force coefficients for configuration BN ₃ T ₂ at $M_\infty = 1.22$; $\phi = 20^\circ$.	125

LIST OF ILLUSTRATIONS (Continued)

<u>Figure</u>		<u>Page</u>
41	Fin normal-force coefficients for configuration BN ₃ T ₂ at $M_{\infty} = 0.8$; $\phi = 30^\circ$.	127
42	Fin normal-force coefficients for configuration BN ₃ T ₂ at $M_{\infty} = 1.22$; $\phi = 30^\circ$.	128
43	Fin normal-force coefficients for configuration BN ₃ T ₂ at $\phi = 45^\circ$.	129
44	Rolling-moment coefficient for configuration BN ₃ T ₂ at $M_{\infty} = 0.8$.	131
45	Rolling-moment coefficient for configuration BN ₃ T ₂ at $M_{\infty} = 1.22$.	132
46	Normal-force coefficients for tail fins of configuration BN ₃ C ₆ T ₂ at $M_{\infty} = 1.3$ and $\phi = 30^\circ$; $\delta_1 = \delta_2 = \delta_3 = \delta_4 = 0^\circ$.	133
47	Force and moment coefficients for configuration BN ₃ C ₆ T ₂ at $M_{\infty} = 1.3$ and $\phi = 30^\circ$; $\delta_1 = \delta_2 = \delta_3 = \delta_4 = 0^\circ$.	135
48	Normal-force coefficients for tail fins of configuration BN ₃ C ₆ T ₂ at $M_{\infty} = 1.3$ and $\phi = 0^\circ$ with yaw control, $\delta_1 = \delta_3 = 15^\circ$, $\delta_2 = \delta_4 = 0^\circ$.	137
49	Force and moment coefficients for configuration BN ₃ C ₆ T ₂ at $M_{\infty} = 1.3$ and $\phi = 0^\circ$ with yaw control, $\delta_1 = \delta_3 = 15^\circ$, $\delta_2 = \delta_4 = 0^\circ$.	138
50	Normal-force coefficients for tail fins of configuration BN ₃ C ₆ T ₂ at $M_{\infty} = 1.3$ and $\phi = 30^\circ$ with yaw control, $\delta_1 = \delta_3 = 15^\circ$, $\delta_2 = \delta_4 = 0^\circ$.	139
51	Force and moment coefficients for configuration BN ₃ C ₆ T ₂ at $M_{\infty} = 1.3$ and $\phi = 30^\circ$ with yaw control; $\delta_1 = \delta_3 = 15^\circ$, $\delta_2 = \delta_4 = 0^\circ$.	141

LIST OF ILLUSTRATIONS (Concluded)

<u>Figures</u>		<u>Page</u>
52	Canard vortex location and afterbody vortex clouds at start of tail section for configuration BN ₃ C ₆ T ₂ calculated by Mendenhall method.	142
53	Geometric dimensions of AIM-9L missile.	145
54	Comparison between measured and predicted characteristics of AIM-9L missile at $M_{\infty} = 0.8$ and $\phi = 0^\circ$ with yaw control; $\delta_1 = \delta_3 = 20^\circ$, $\delta_2 = \delta_4 = 0^\circ$.	146
D.1	Forward boundary of region of influence of fin F ₁ in plane of F ₂ .	194
E.1	Flow of program computations.	208
E.2	Schematic description of control of MISSILE operations by NFIN.	209
E.3	Input formats for computer program MISSILE	219-221
E.4	Input for sample case; MICOM-NWC body-canard-tail configuration (BN ₃ C ₆ T ₂).	231
E.5	Output for sample case; MICOM-NWC body-canard-tail configuration (BN ₃ C ₆ T ₂).	232-240

LIST OF TABLES

<u>Table</u>		<u>Page</u>
1	Fin Equivalent Angles of Attack and Lateral Center-of-Pressure Positions for Control Deflection of Fin 4 of Cruciform Wing-Body Combination; Slender-Body Theory	242
2	Wing-Alone Normal-Force Coefficients for Fins of the Systematic Data Base	244

LIST OF TABLES (Concluded)

<u>Table</u>		<u>Page</u>
3	Wing-Alone Normal-Force Coefficients for Fin C6 of Aspect Ratio 3.53	248
4	Lateral Center-of-Pressure Positions for Fins of Systematic Data Base; No Vortex Effects	249
5	Lateral Center-of-Pressure Positions for Fin C6 of Aspect Ratio 3.53; No Vortex Effects	253
6	Normal-Force Coefficients of Fins on Body B_1 Including Vortex Effects	254
7	Normal-Force Coefficients of Canard Fin C6 of Aspect Ratio 3.53 Including Vortex Effects	278
8	Normal-Force Coefficients of Fins on Body B_1 Without Vortex Effects	280
9	Normal-Force Coefficients of Canard Fin C6 of Aspect Ratio 3.53 Without Vortex Effects	304
10	Asymmetric Components of Normal-Force Coefficients of Fins of Systematic Data Base	306
11	Experimental Values of Wing-Body Interference Factor K_W for Fins of Systematic Data Base Tested on Body B_1 ; No Body Vortex Effects	316
12	Errors in Estimating Fin Normal-Force Coefficients Using Linear Interpolation in Aspect Ratio and Taper Ratio	320
13	Experimental Values of k_w for Canard Fin C6 Tested On Army Generalized Missile	324
14	Experimental Values of Wing-Body Interference Factor K_W for Canard Fin C6 On Army Generalized Missile; No Vortex Effects	326

A PRELIMINARY METHOD FOR CALCULATING THE
AERODYNAMIC CHARACTERISTICS OF CRUCIFORM MISSILES
TO HIGH ANGLES OF ATTACK INCLUDING EFFECTS OF
ROLL ANGLE AND CONTROL DEFLECTIONS

Jack N. Nielsen, Michael J. Hemsch, and Charles A. Smith
Nielsen Engineering & Research, Inc.

1. INTRODUCTION

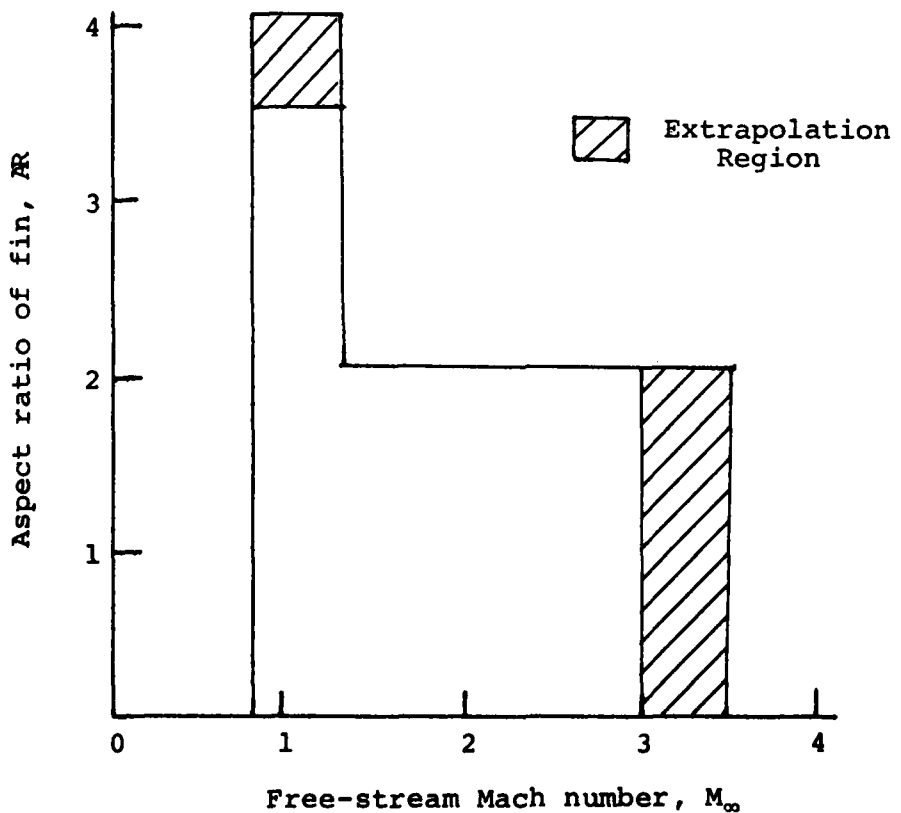
This report presents a preliminary method for calculating the aerodynamic characteristics of cruciform wing-body-tail combinations over a wide range of parameters. It utilizes a limited data base and predicts cases not in the data base on the basis of analysis and engineering assumptions. For wing-body-tail configurations close to those in the data base, the accuracy of prediction should be good. There are not many cases outside the data base for comparison with prediction. Until more such data exist, the method cannot be thoroughly checked out and should therefore be considered preliminary.

Under the sponsorship of the Office of Naval Research (ONR), Nielsen Engineering & Research, Inc. (NEAR) has been developing computer programs for the prediction of the aerodynamics of arbitrarily banked cruciform missiles at high angles of attack. The first two years of the work were devoted to the development of a computer code based on linear supersonic flow theory for the calculation of loadings on cruciform wing-body combinations. The results are reported in references 1 and 2. In 1974-1975, under the sponsorship of the Naval Weapons Center (NWC), China Lake, CA, NEAR developed an engineering method for calculating the induced rolling moments of cruciform missiles at angles of attack up to 20°. At the same time, under the joint sponsorship of NWC and NASA/Ames Research Center, NEAR obtained a systematic set of component-buildup data on a cruciform body-canard-tail missile up to 24° angle of attack at transonic and supersonic speeds. The data included individual fin loads. The engineering method is reported in reference 3. The data are presented in references 4

and 5.

Under the co-sponsorship of ONR and NASA/ARC, NEAR continued and extended the work of reference 3. The work involved two tasks: (1) development of a single comprehensive code for the engineering calculation of all missile component aerodynamic forces and moments, except minimum drag, for angles of attack up to about 20° , and (2) comprehensive comparison of predicted results with systematic data for a wide variety of configurations. This work has been reported in reference 6.

The present work is an extension of the work of reference 6 to higher angles of attack co-sponsored by the Office of Naval Research, Ames Research Center of NASA, and the Air Force Flight Dynamics Laboratory. The present method has been developed for angles of attack between 0° and 45° . The fins must be clipped delta wings lying in the range of aspect ratio and Mach number shown by the enclosed region in the following sketch.



Extrapolation into the cross-hatched regions is provided for in the method. The fin taper ratio may range from 0 to 1.0. Any missile bank angle is allowable, and arbitrary canard fin and tail fin deflections are provided for.

The computer program of reference 6 is retained in the present work as the framework of the method. A number of improvements and extensions have been made. The most important change is that a data-base approach augmented by analysis has been used to obtain fin loads without vortex effects. The vortex theory has been extended to determine body vortex effects on fin loads at high angles of attack. Improvements have been made in the treatment of the effects of afterbody vortices. The effect of body vortex asymmetry has not been included explicitly in the computer program, but tables of the asymmetric fin loads determined experimentally have been presented so that the asymmetric vortex effects can be estimated.

As an aid to the present work, tests have been made in the 11-foot wind tunnel of NASA/ARC for angles of attack up to 50° with the Army generalized missile previously used for the testing reported in references 4 and 5. This work, sponsored by NASA/ARC, has been useful for providing data-base results to higher aspect ratios in the transonic regime. It has provided independent data for comparison with the predictive method, and it has provided some understanding of the high angle of attack vortex phenomena through the use of vapor-screen photography. The results of the investigation are reported in reference 7.

An overview of the engineering method is presented in Section 2 for the information of the reader who does not require complete technical details, but who is interested in the general aspects of the method. The reader should also refer to reference 6. Section 3 describes the construction of the data base followed by a section describing its use. The Section 5 describes the construction of a high-angle-of-attack, body-alone, vortex

model to an angle of attack of 50°.

The next subject considered is miscellaneous improvements incorporated into the computer program. Comparisons between the predictions of the method and measurements are then presented for fin loads and with overall force and moment data for body-tail and body-wing-tail configuration. Because of limitations in the data base and because of special high angle of attack effects shown by the data base, recommendations are presented for further experiment and analysis.

NEAR, Inc. wishes to acknowledge the support of the following organizations and individuals: Mr. David Siegel and Cdr. R. Hite of ONR; Dr. Gary Chapman and Mr. Gerald Malcolm of NASA/ARC; and Mr. Calvin Dyer of AFFDL. Also the support of NASA/ARC with Mr. Gerald Malcolm as technical monitor in obtaining the data of reference 7 is gratefully acknowledged. NEAR, Inc. is also obliged to Mr. Ray Deep and Dr. Donald Spring of the Army Missile Research and Development Command for the loan of the Army generalized missile model for the NASA/ARC tests as well as for detailed tabulated data used in constructing the data base.

2. OVERVIEW OF ENGINEERING METHOD AND ITS EXTENSION TO HIGH ANGLES OF ATTACK

The purpose of this section of the report is to present an overview of the engineering predictive method with emphasis on the aerophysics of missiles. A brief description of the present engineering method can be given by noting that it is basically the method described in reference 6 with certain changes and additions as follows:

- (1) The equivalent angle of attack, α_{eq} , was calculated in reference 6 by a linear superposition of component angles of attack whereas a nonlinear superposition method suitable for high angles of attack is used herein.

(2) The wing-alone characteristics needed in the method are input data in reference 6 whereas they are obtained from a data base included in the program in the present case.

(3) The interference factors K_W and K_ϕ obtained from theory were used in reference 6 to obtain fin normal forces but in the new program fin normal forces are obtained with the help of a data base and experimental values of K_W .

(4) A new high-angle-of-attack body vortex theory has been included in the present computer program.

(5) Some changes have been made to improve the afterbody vortex model.

(6) An improved method of calculating panel-panel interference has been developed which permits inclusion of roll control in the current program. Arbitrary fin deflections are allowed for both sets of fins.

(7) The possibility of including two vortices per canard fin has been included in the current program.

In the following subsections we will describe the following items:

1. Range of Parameters
2. Aerodynamic Model of Missile; Symbols and Conventions
3. High Angle of Attack Body Vortex Model
4. Equivalent Angle of Attack Concept
5. Description of Data Base

The improved afterbody model is discussed in Section 5; the general treatment of control deflection is carried out in Appendix C, and the input and output formats are given in Appendix E together with a sample case.

2.1 Range of Parameters

The engineering method covers a range of angle of attack, roll angle, Mach number, ratio of body radius to missile semispan,

fin aspect ratio, fin taper ratio, fin deflection angles, axial position of the fins on the body, body-tail or body-canard tail configurations. Values of angle of attack between the missile and the free-stream velocity vector, α_c , up to 45° are covered since this is the extent of the data base used in the method. A complete range of roll angles is covered, and the Mach number range is $0.8 \leq M_\infty \leq 3.0$.

The fin parameters are specified for a pair of fins joined together. For Mach numbers 2 to 3 the aspect ratio range is 0.5 to 2.0; for Mach numbers 0.8 to 1.3 the aspect ratio range is 0.5 to 3.53. It is assumed that the fin trailing edges are unswept. These parameter ranges are dictated by the availability of data-base information.

It is assumed that the body consists of a nose followed by a circular cylinder on which cruciform fins are mounted. The radius-semispan ratio can range between 0 and 0.5, although larger values can be treated by extrapolation. Two sets of fins can be mounted at any two axial locations on the circular cylinder.

Allowance has been made for deflection of the fins as all-moveable controls. All fins can be arbitrarily deflected so that pitch control, yaw control and roll control are covered. However, a limitation on the combined effect of angle of attack and control deflection is imposed such that the equivalent angle of attack of the fin does not exceed 60° .

Both body-tail configurations with tail control or body-wing-tail configurations with canard control and/or tail control are covered.

2.2 Aerodynamic Model of Missile; Symbols and Conventions

The missile is divided into four sections for modeling purposes; the nose or forebody, the canard section, the afterbody, and the tail as shown in figure 1. The term "nose" is used when

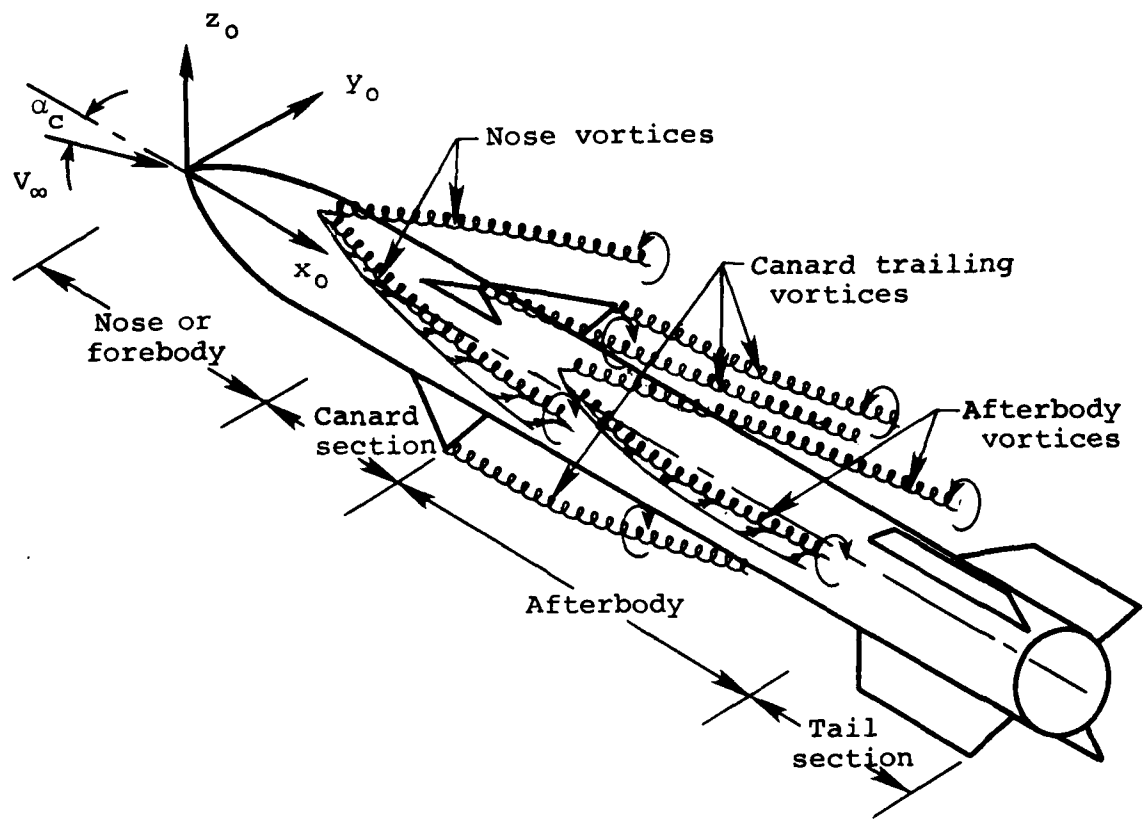


Figure 1. Banked canard-cruciform missile at angle of attack showing typical vortex field.

canard fins are present but the term "forebody" seems more appropriate for a body-tail combination. The vortex system is of particular interest. The forebody can produce a pair of nose vortices which can be symmetric or asymmetric.¹ Only two forebody vortices are allowable in the present method. The canard fins also produce trailing vortices. Figure 1 shows only one vortex per fin, but the present computer code has been extended to include the possibility of two vortices per canard fin. The afterbody in the presence of the canard vortices and body vortices can develop asymmetric vortices especially under conditions of roll or asymmetrical canard fin deflection. Finally, all the vortices can pass over the tail fins inducing nonlinear forces and moments on these fins. The computer program predicts both the strengths and paths of those vortices using experimental and analytical information.

The calculation of the missile aerodynamic characteristics proceeds from nose to base. First, the nose vortex strengths and positions are calculated at the beginning of the canard section. The forces and moments on the canard fins with no vortex effects (with or without control deflections) are determined. Then the changes in the canard-fin forces and moments due to passage of the nose vortices past the fins are determined. From the fin normal force and lateral center of pressure and the strength and position of one or two trailing vortices per fin are established.

We now have the nose and canard fin vortices passing rearward behind the trailing edges of the canard fins. These vortices, together with the free-stream flow over the afterbody, create a pressure distribution on it which is generally not symmetric left to right. An approximate method of determining the strengths and trajectories of the vortices shed from the afterbody under

¹An asymmetric vortex pair is one not having mirror symmetry right and left of the plane containing the body axis and the free-stream velocity vector.

these conditions is included in the computer program. The trajectories of all the vortices passing over the afterbody are computed.

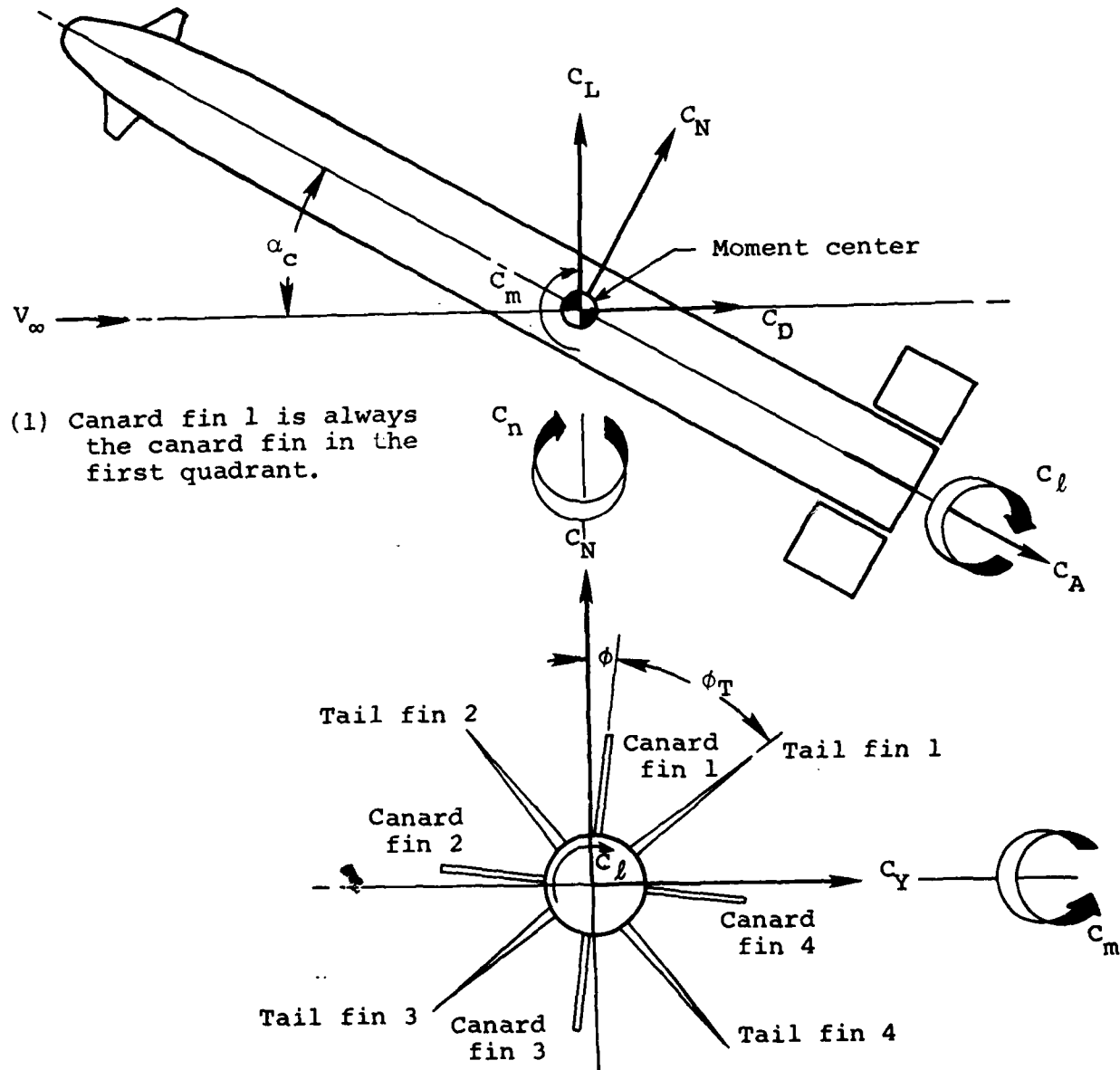
The empennage fins are treated in a manner completely analogous to that for the canard fins. The normal force and rolling moment due to these fins are determined with the help of analysis and the data base on the assumption that no vortices are present. The additional changes due to the passage of the vortices past the tail fins are then calculated and added to the vortex-free values. Implicit in this procedure for both canard and tail fins is the assumption that the nonlinear effects, due to the vortices, can be added to those without the vortices in accordance with an equivalent angle-of-attack concept.

The foregoing procedures give the forces and moments on the body nose, the afterbody, and the canard and tail fins. They do not, however, give the body forces and moments due to the pressure carryover onto the body of the canard and tail fins. These body forces and moments are determined with the help of wing-body interference quantities in a separate calculation.

Some symbols and conventions used in the analysis are given in figure 2.

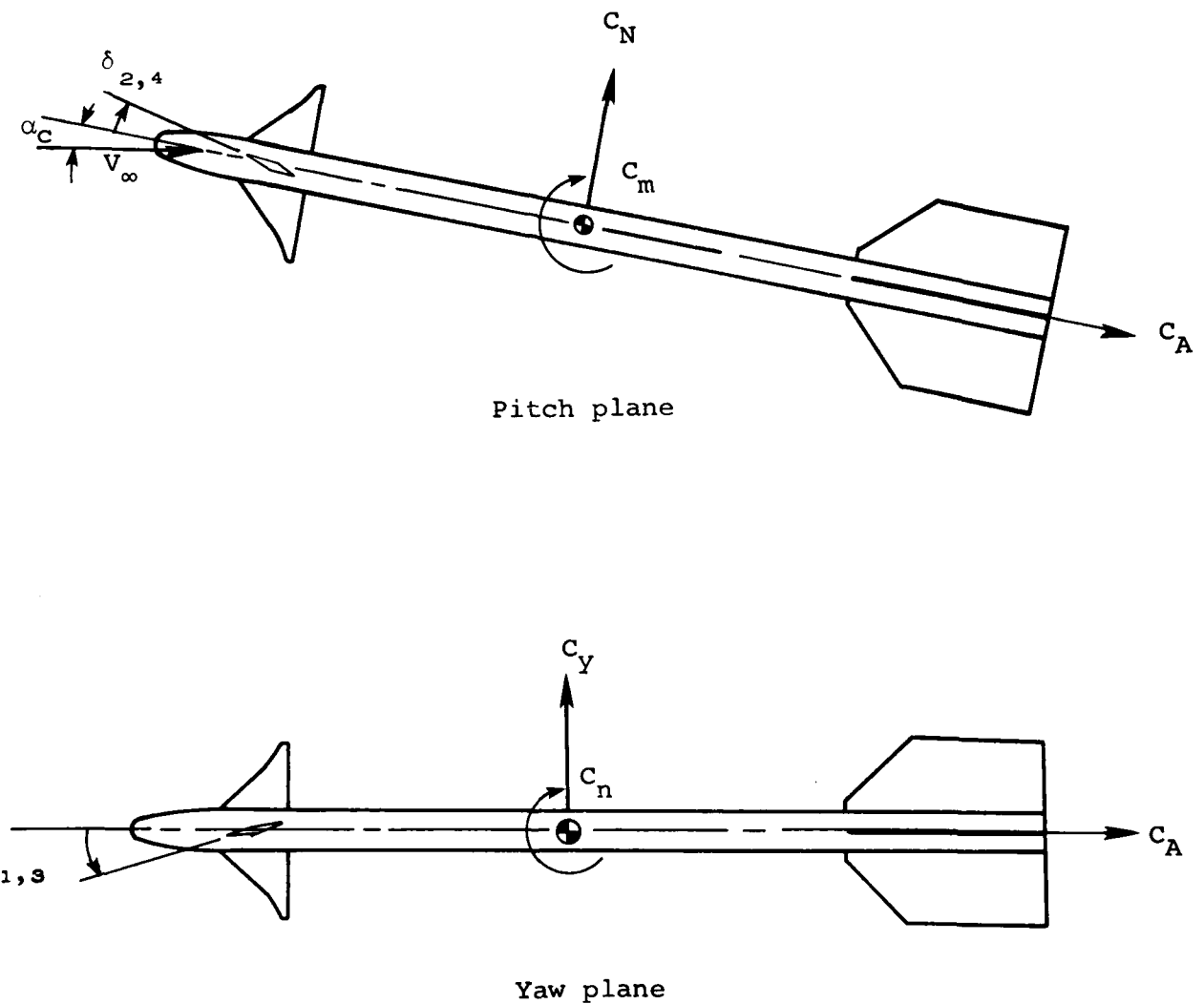
2.3 High Angle-of-Attack Body Vortex Model

2.3.1 Some high angle-of-attack vortex behavior.- The vortex model used in the method of reference 6 for angles of attack up to 20° is empirical and was developed by Seldon Spangler of NEAR, Inc. and reported in reference 8. This model is presented in the form of nondimensional curves giving the body vortex strengths and vortex core positions. It also utilizes an empirical formula for the distance behind the body apex at which vortex separation starts. The normal force and center-of-pressure position of the forebody or nose are



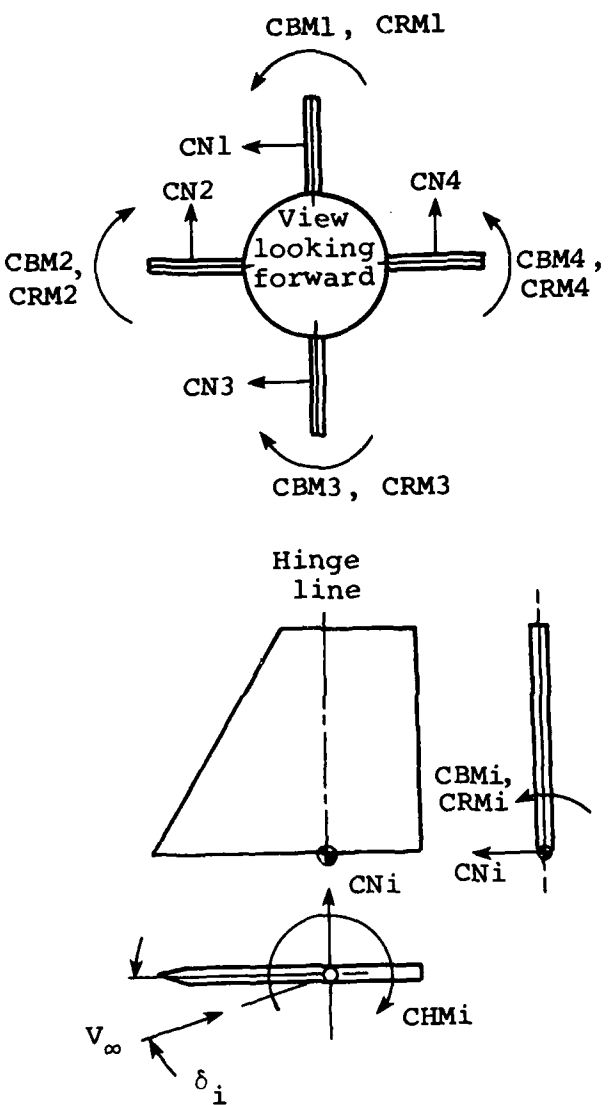
(a) Total loads and fin numbering system.

Figure 2. Symbols and conventions.



(b) Sign convention for canard deflection angles.

Figure 2. Continued.



NOTE: Normal forces are measured perpendicular to the fin planform and are considered to act at the intersection of the fin hinge line and root chord.

(c) Axis systems and positive sign convention for fins.

Figure 2. Concluded.

calculated using the viscous crossflow method of Perkins and Allen, reference 9.

The question of a body vortex model for very high angles of attack involves a number of complicating factors, the principal one being asymmetric vortex effects.

As the angle of attack increases beyond the maximum for symmetric vortex shedding, the vortex on one side is shed and a new vortex starts beneath the shed one. This process continues with increasing angles of attack, and a von Kármán vortex street is formed in a crossflow plane. A distance which can be used to measure the onset of asymmetry is the distance g_3 to the start of the third vortex. Thomson and Morrison, reference 10, have made an experimental and analytical study of vortex shedding from a cone-cylinder under these circumstances, and find that the length g_3 depends on crossflow Mach number, M_c , angle of attack, α , and Strouhal number, S , in the following way:

$$\frac{g_3}{D/2} S \tan \alpha = k(M_c)$$

where D is the body diameter and k is a constant of the order unity which depend on M_c . The Strouhal number also depends on M_c for values greater than 0.8. Using the results of reference 10, we find the following approximate results:

M_c	g_3 $\alpha = 30^\circ$	g_3 $\alpha = 45^\circ$
0.5	7.8 D	4.5 D
0.8	10.4 D	6.0 D
1.0	7.0 D	4.0 D
1.2	6.0 D	3.5 D

(It is noted that the results of reference 10 extends only to

$\alpha = 35^\circ$ so that the foregoing results for $\alpha = 45^\circ$ represent an extrapolation.) For most cruciform-canard missiles the nose lengths fall within the limits for g_3 , and they will operate in the symmetric vortex range. Many body-tail configurations will operate up to 30° angle of attack in the symmetric vortex range. We now consider some vortex behavior which has influenced our approach to modeling high angle of attack body vortices.

The question arises concerning the degree of asymmetry of body vortices for $\alpha \geq 35^\circ$, and the related question of asymmetrical fin forces. To examine the first question, we have obtained a number of pressure distributions on circular cylinders under such conditions through the courtesy of Emma Jean Landrum of NASA/Langley Research Center (LRC) together with a number of schlieren pictures from various sources. Examination of these data generally tended to suggest that there is no appreciable lateral force on the body. Also, they indicate that the vortices do not tend to become asymmetric, but rather tend to increase in vertical height with distance from the nose and to become quite elongated. As a matter of interest, an example of inviscid but rotational supersonic crossflow about a body of revolution as computed using the Euler equations is shown in figure 3. Our study indicates that symmetric vortex clouds are representative of the leeward side flow at sufficiently large crossflow Mach numbers.

With regard to the sideforce developed on a body of revolution at high crossflow Mach numbers, Chapman, Keener and Malcolm, reference 11, have correlated a large number of measurements on body sideforce and have found that negligible body sideforce exists if $M_c > 0.5$. While this result does not establish that the vortex pattern is symmetric, it does establish that any vortex asymmetries for $M_c > 0.5$ do not have significant effect on body sideforce. One is led to wonder what this means for the difference in normal forces on a fin if rotated from top center first to the right and then to the left by equal roll

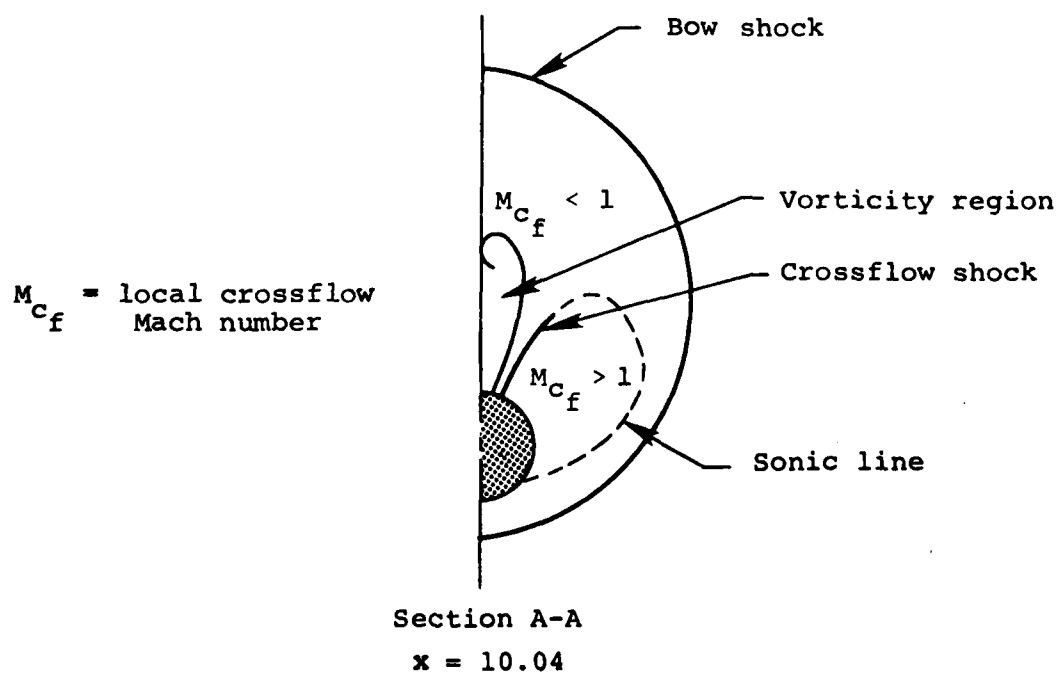
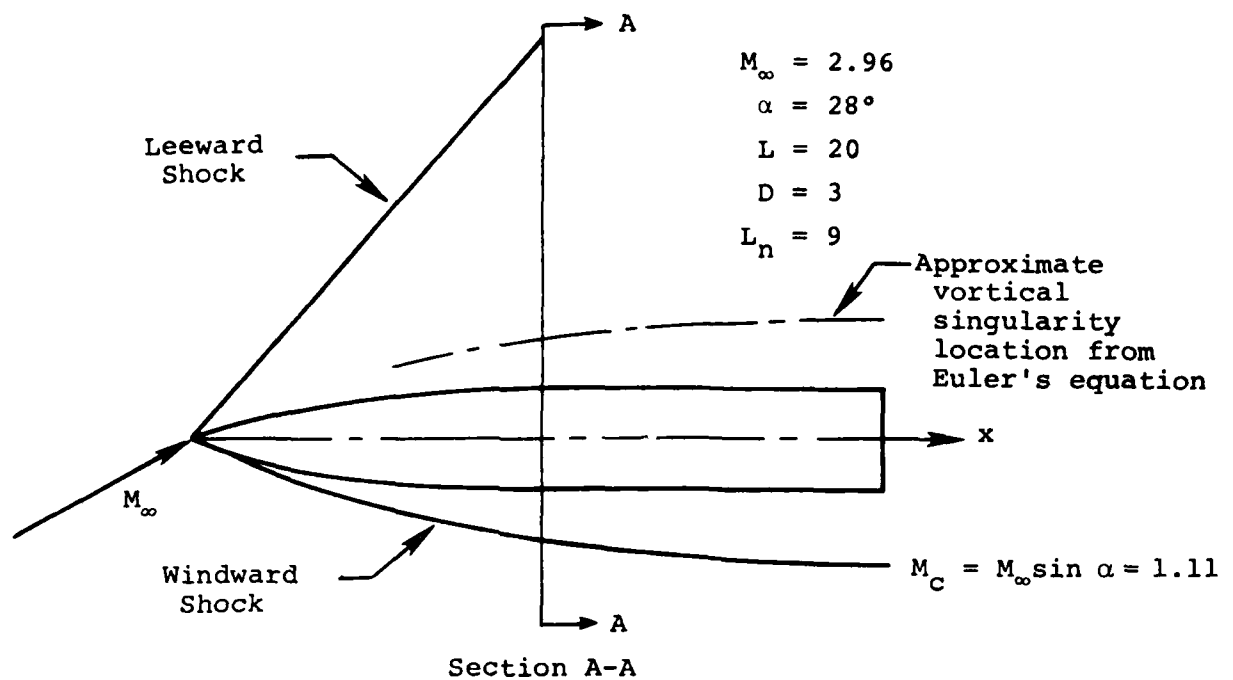


Figure 3. Inviscid flow in crossflow plane of body of revolution with supersonic crossflow Mach number.

angles. It is interesting to examine data on this subject.

2.3.2 Fin normal forces in an asymmetric vortex field.-
Figure 4 presents some results in this point taken from the data base which will be subsequently described. The results are for the following set of parameters.

Angle of attack: $\alpha_c = 30^\circ$

Fin aspect ratio: $AR = 1$

Fin taper ratio: $\lambda = 0$

Ratio of body radius
to missile semispan: $a/s_m = 0.5$

Distance from body nose
to forward point of fin: 12.46 body radii

It is noted that the distance of 12.46 body radii is larger than g_3 at 30° as given by the preceding tabulation for $M_c = 0.8$ and 1.2.

In figure 4 the fin normal-force coefficient of a cruciform body-tail combination is shown versus roll angle for a fin on the right-hand side of the missile and a fin on the left-hand side of the missile. The data are plotted against roll angle so that for any value of the roll angle the results for fins with mirror symmetry are shown as indicated by the sketches in the figure. For the windward side of the missile $0 \leq \phi \leq 90^\circ$, the fins have nearly the same normal-force coefficients for mirror symmetry for both Mach numbers. However, on the leeward side of the body, $-90^\circ < \phi \leq 0^\circ$ the normal force of the right fin is generally greater than that of the left fin indicating an asymmetric vortex condition at both Mach numbers. The solid curves in the figure are faired about half way between the upper and lower points.

The data at $M_\infty = 0.8$ and $\phi = -80^\circ$ exhibit an interesting phenomenon. The data for the left- and right-hand fins have

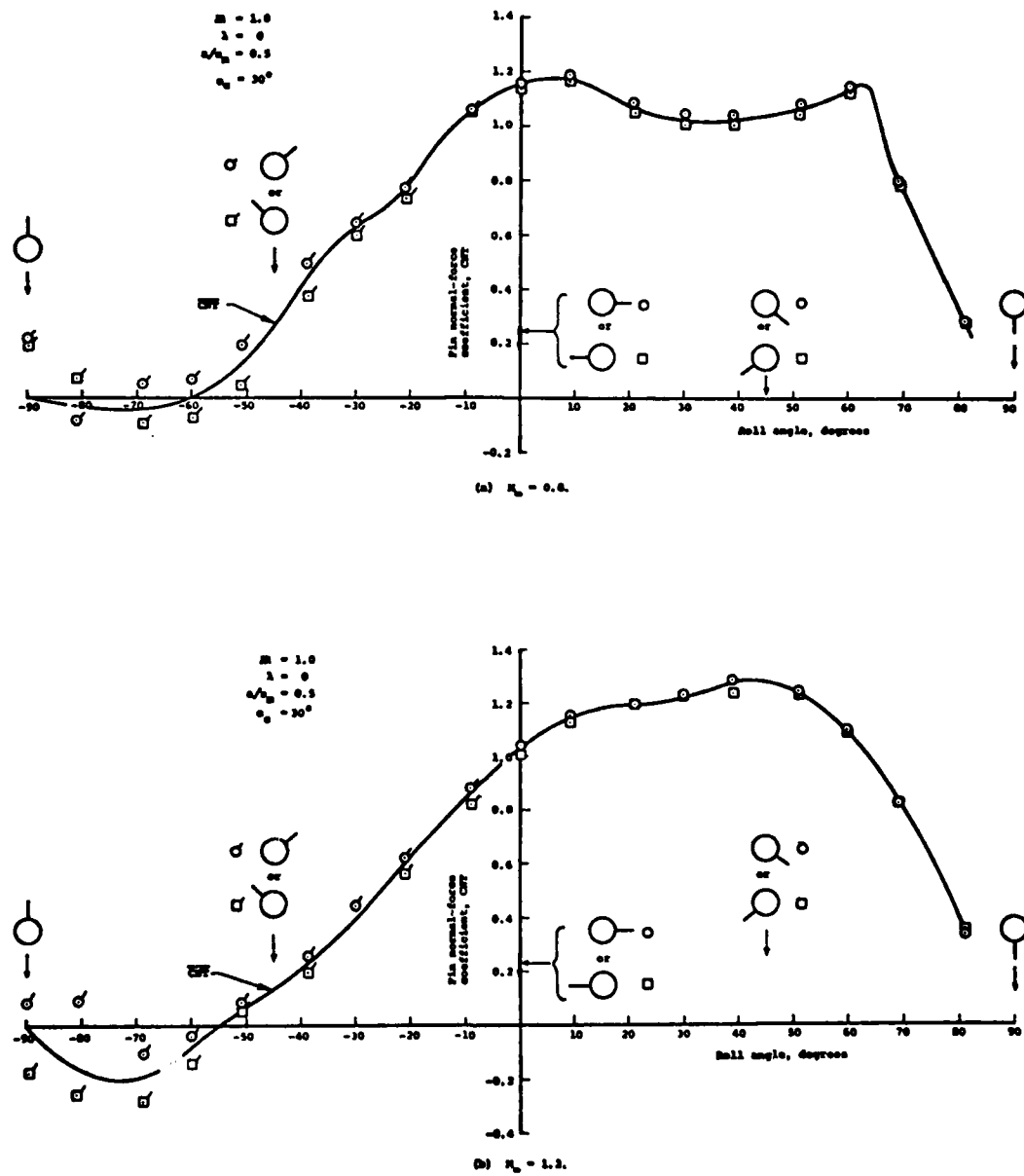


Figure 4. Effect of roll angle and Mach number on fin normal-force coefficient of fin T14 on B_1 body.

switched positions relative to the $\phi = -70^\circ$ results. At $\phi = -90^\circ$ the right-hand result has switched back again to the upper branch. This type of behavior can be explained by bistable asymmetric vortex switching.

2.3.3 Decomposition into symmetric and asymmetric vortex effects.- It is not easy to characterize asymmetric vortex effects for design purposes. A principal difficulty is that asymmetric vortex effects do not seem to be deterministic. For one thing, it is not always possible to determine the "hand" of the asymmetry. It can change from left hand to right hand or conversely through the mechanism of "vortex switching" as shown in figure 4. Also, we find experimentally that the vortex pattern can be highly unstable in certain Mach number and angle of attack ranges. It is further probable that a number of asymmetric vortex configurations occur. For engineering design purposes we will try to predict the average of the left- and right-hand results as shown in figure 4. With respect to figure 4(a), a mean $\overline{C_{NT}}$ line can be drawn between the left-hand and right-hand data, and the asymmetric effects can be considered as a $\pm \Delta C_{NT}$ variation about the mean line. The computer program has been constructed using an average symmetrical vortex model which represents most of the vortex interference and which produces $\overline{C_{NT}}$. Not incorporated into the computer program but given in a table are the values of $\pm \Delta C_{NT}$ as determined experimentally from the data base. The results for $\pm \Delta C_{NT}$ should be used only as a guide to the possible magnitude of asymmetric vortex effects. For instance, any asymmetry built into the missile, such as a conduit on the outside of the body, would change the vortex asymmetries. Until design means are found to stabilize or eliminate the asymmetric vortex effects, it will not be possible to deal with them deterministically.

2.4 Equivalent Angle of Attack Concept

We have defined the wing alone to be that surface formed by

placing two opposing fins together. We now define the equivalent angle of attack of the fin to be that angle of attack of the wing alone for which its normal force is twice that of the fin. In determining the equivalent angle of attack of a fin in a cruciform wing-body combination, we consider a number of different effects.

a. If the wing-body is pitched at zero roll, we have favorable wing-body interference at low speeds and low angles of attack usually ascribed to body upwash. At high speeds and high angles of attack this favorable result is modified as described in section 2.4.1.

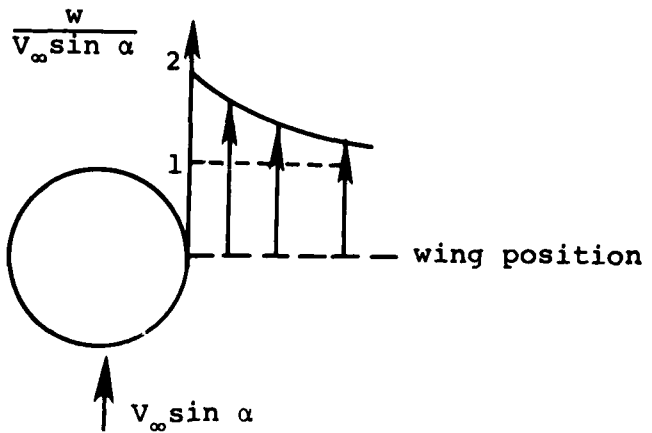
b. If a fin is mounted on a body and yawed at fixed angle of attack, its normal force will change. This $\alpha\beta$ effect changes the equivalent angle of attack as described in section 2.4.2.

c. Velocities induced normal to a fin as a result of external vortices and their internal images change the fin equivalent angle of attack as described in section 2.4.3.

d. Deflection of the fin affects its own equivalent angle of attack and those of the other fins as described in section 2.4.4.

Once the results of all these effects on the fin equivalent angle of attack have been determined and combined in a nonlinear fashion, the equivalent angle of attack of the fin is known. Its normal-force coefficient is then found from the experimental wing-alone curve. In this way the nonlinear characteristics of the wing-alone are used in the predictive method.

2.4.1 K_w contribution.- On a wing-body combination at subsonic or up to moderately supersonic speed, the effect of the body on the wing is to increase the wing lift as long as the angle of attack is small. As an example, consider the upwash in a crossflow plane normal to the fuselage. As it goes around the body, the air speeds up and produces an angle of attack equal to $2 \sin \alpha$ at the side of the body. Putting the wing panels in this field causes an increased lift over what they would develop



if the panels were part of the wing-alone at angle of attack α . The wing-body interference factor K_W is a measure of this favorable interference

$$K_W = \frac{\text{Lift of wing panel attached to fuselage (at } \alpha\text{)}}{\text{Lift of wing panel in wing alone (at } \alpha\text{)}} \quad (1)$$

According to potential flow theory, K_W runs from 1 for no body up to 2 for a small fin on a large body. The quantity $K_W\alpha$ is the equivalent angle of attack for the fin on a linearized basis.

In our current study, we have determined K_W from experimental data for a series of wings and Mach numbers up to 45° angle of attack. Figure 5 shows these experimental results for a delta fin of aspect ratio 1 mounted on a body whose diameter is one-half the total span of the wing-body. As the angle of attack is increased, the value of K_W decreases below 1, indicating adverse interference of the body on the wing. At high Mach numbers the adverse interference is substantially worse.

At high angle of attack and supersonic crossflow Mach numbers, a curved shock wave can form in front of the body (fig. 3) which can cause reduced dynamic pressures where the wing would be and which can also destroy the favorable upwash. The unfavorable

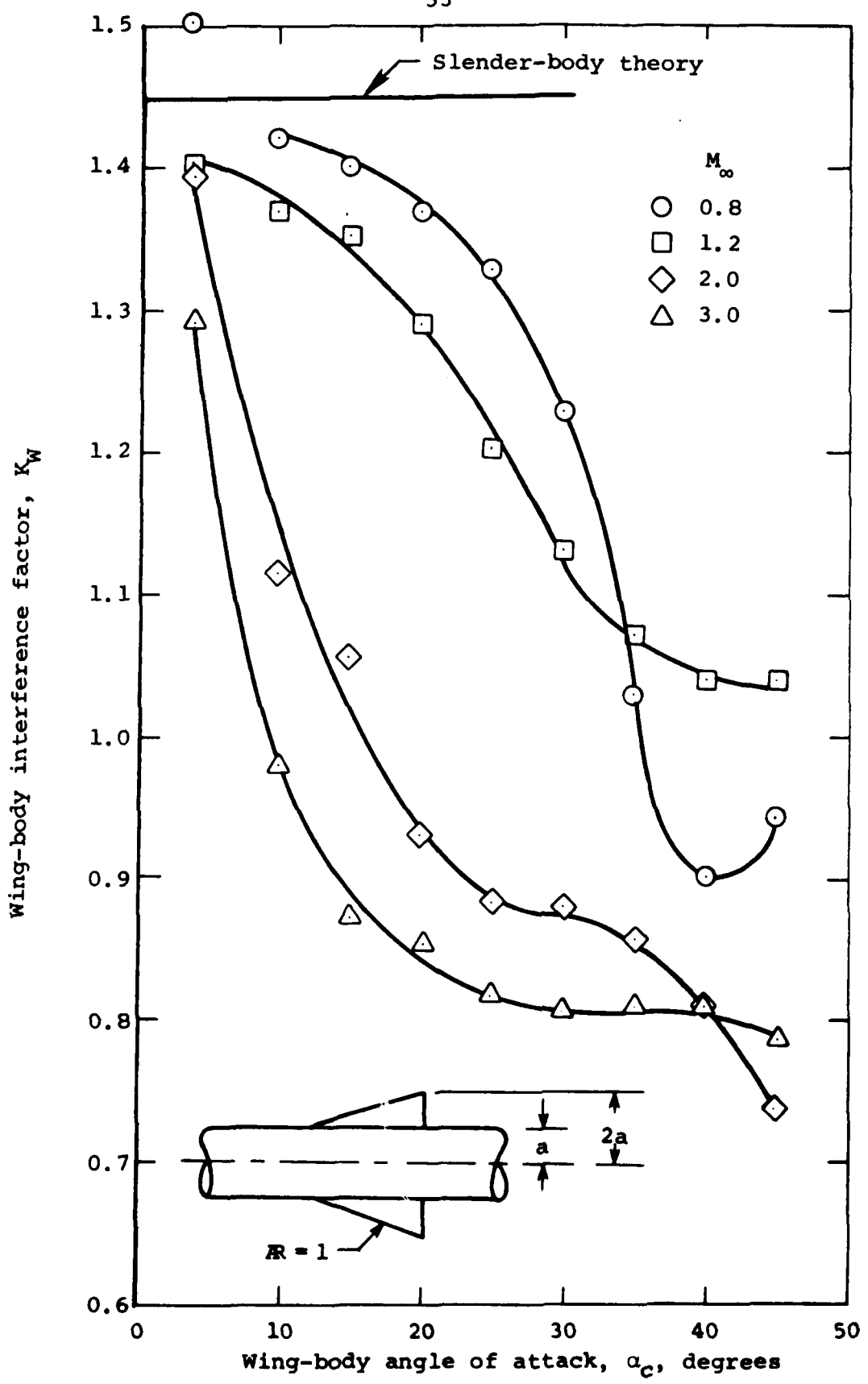


Figure 5. Effect of angle of attack and free-stream Mach number on interference of body on wing.

effect of the body on the wing is clear in this instance. However, the larger reduction in K_w for subcritical crossflow Mach numbers is not understood.

The factor K_w is an important factor in determining the equivalent angle of attack. It accounts for body upwash for the low angle of attack range but also accounts for a general loss of upwash and decrease in dynamic pressure at large angles of attack. We have described it so far in the linearized context used up to $\alpha_c = 20^\circ$ in reference 6. However, we will describe its nonlinear definition in trigonometric terms in Appendix C.

2.4.2 K_ϕ contribution.— Consider now the K_ϕ contribution. If a delta wing is pitched to angle α it develops a certain normal force dependent only on α . If it now is sideslipped by angle β so that the right-hand leading edge is yawing into the wind, slender-body theory predicts that the right half of the wing develops an additional normal-force increment proportional to the product $\alpha\beta$ and the left half of the wing loses a corresponding increment. The increment in normal force ΔC_N is given by

$$\Delta C_N = \frac{4}{AR} K_\phi \alpha\beta \quad (2)$$

in its linearized form. The factor $4/AR$ is used to make K_ϕ independent of aspect ratio (see ref. 3). Division of ΔC_N by the lift-curve slope, both determined by slender-body theory, yields the increment in equivalent angle of attack.

The factor K_ϕ is given in reference 12 on the basis of slender-body theory, for which it depends only on a/s_m . It is however, a weak function of a/s_m . We can determine K_ϕ experimentally from curves similar to those shown in figure 4, provided we remove the body vortex effects from the data. However, we do not do this. Instead, we determine the increment in equivalent angle of attack due to K_ϕ from the data and the wing-alone

normal-force curve. In applying this increment to other values of a/s_m , we assume it does not depend on a/s_m .

2.4.3 Vortex contributions.- External nose vortices can pass over canard fins or nose and canard vortices can pass over tail fins. In these processes the equivalent angle of attack of the fins is changed by flow induced normal to the fins by the external vortices and their images within the body.

The high angle-of-attack vortex model already mentioned results in a "cloud" of vortices on each side of the body. These clouds are modeled in the engineering method by potential vortices with rather large cores which are fitted to them. Thus the input for the vortex calculation is a vortex strength, a core radius, and a vortex center. The induced normal velocities across the fin depend only on spanwise distance since the external vortices are assumed to be parallel to the body. The induced normal velocities are thus determined from the Biot-Savart law with due regard for the core of the external vortex. The image vortex is assumed to have no core.

The change in equivalent angle of attack of a particular fin due to an external vortex, $\Delta(\alpha_{eq})_v$, is derived in Appendix B using reverse-flow theory. The expression for this quantity, equation (B-31), involves an integration over all four fins which is carried out within the computer program. The integrals over the fins other than the one in question represent panel-panel interference.

By a very similar application of reverse-flow theory it is possible to determine the center of pressure of the loading induced on any fin by an external vortex.

Combinations of external vortices are simply handled by linear superposition.

The integrals representing panel-panel interference are valid if all fins are within the regions of influence of each other; that is, if $M_\infty < 1$. In case $M_\infty > 1$, these integrals are

multiplied by the fractional part of the planform area of the fin for which the equivalent angle of attack is being calculated lying within the region of influence of the fin over which the integral is being taken. Expressions for this fraction for adjacent fins and opposing fins are derived in Appendix D.

2.4.4 Fin deflection.- In reference 6 both pitch control ($\delta_2 = \delta_4 \neq 0$) and yaw control ($\delta_1 = \delta_3 \neq 0$) were included in the computer program but roll control ($\delta_1 = -\delta_3$ or $\delta_2 = -\delta_4$) was not included. In the present computer program, roll control is included since each canard and tail fin can now have arbitrary deflection. This generalization of the treatment of control deflection is now described for the small angle of attack and control deflection ranges.

For a deflection of any one fin, say C4, a primary normal force occurs on the deflected fin and secondary normal forces due to panel-panel interference are induced on the other three fins which are undeflected. Let δ_4 be a positive deflection of C4 at zero angle of attack for purposes of explanation. One would expect the equivalent angle of attack of C4 due to δ_4 to be nearly equal to δ_4 . Actually it will be slightly less than δ_4 because there is a cylindrical boundary rather than a vertical wall at the fin-body juncture. The value of $\Delta(\alpha_{eq})_4 / \delta_4$ will thus be slightly less than unity and will depend on a/s_m according to slender-body theory.

The normal forces on fins C1, C2, and C3 will be in such directions as to counteract roll associated with the primary normal force on C4. It is possible to find equivalent angles of attack $\Delta(\alpha_{eq})_1$, $\Delta(\alpha_{eq})_2$, and $\Delta(\alpha_{eq})_3$ associated with the induced normal forces on fins C1, C2, and C3 using slender-body theory as well as the lateral center-of-pressure positions of the normal forces in terms of the parameter $(\bar{y}_i - a)/(s_m - a)$. This quantity and $\Delta(\alpha_{eq})_i / \delta_4$ have been calculated using the results of Appendix A for $i = 1, 2$, and 4. The cases for $i = 1$ and $i = 3$ yield

equal and opposite normal forces. These results are tabulated in Table 1, wherein, they are seen to be functions only of a/s_m . To the extent that the wing-body combination operates at low angles of attack and control deflections and the fins are generally within each others' regions of influence, these tabulated results can be used to account for direct control effects and associated panel-panel interference. In the form presented in Table 1, the results are valid well beyond the range of slender-body theory.

Table 1 has not been incorporated into the computer program, but its method of accounting for panel-panel interference has been used in the program with the necessary numerical integrations performed internally for each case. However, at supersonic speed where the fins are not generally totally within the regions of influence of one another, the expressions derived in Appendix D to account for this effect have been applied to the panel-panel interference factors. Thus the panel-panel interference decreases as the Mach number increases until at some Mach number it disappears entirely. This Mach number is higher for adjacent panels than for opposing panels.

At large angles of attack or control deflection, a linear approach is no longer used. An interference factor k_w is defined to characterize the effectiveness of the fin as a control. Let $\alpha_{eq,0}$ be the equivalent angle of attack of the fin for $\delta = 0$ and let $\alpha_{eq,\delta}$ be the value associated with a change in control deflection by δ . Then k_w is defined to be

$$k_w = \frac{\tan(\alpha_{eq,\delta}) - \tan(\alpha_{eq,0})}{\tan(\alpha_{eq,0} + \delta) - \tan(\alpha_{eq,0})} \quad (3)$$

If the fin acts in the wing-body combination in the same fashion as it does as part of the wing alone, then k_w will be unity even if the wing-alone normal-force curve is nonlinear (but monotonic

in α). In the engineering method both theoretical and experimental values of k_w are used in estimating the direct effects of control deflection.

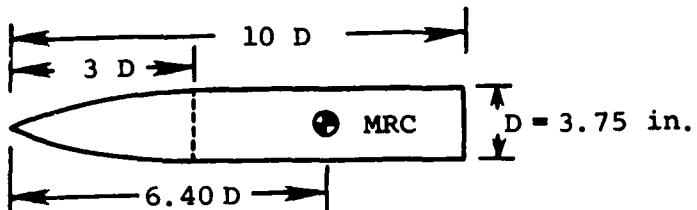
The mathematical expressions for the equivalent angle of attack of a fin subject to angle of attack, angle of sideslip, vortex effects, and control deflection are given in Appendix C.

2.5 Description of Data Base

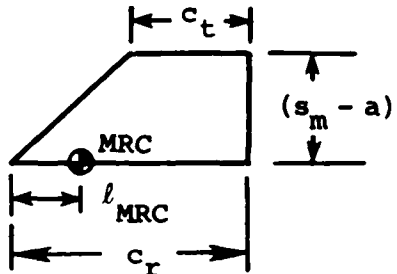
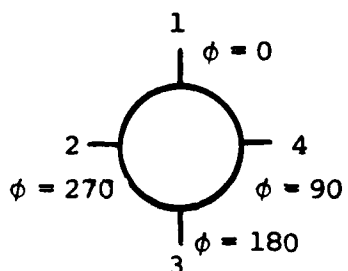
2.5.1 Fins of the data base.— The present predictive method makes use of experimental data on fin normal-force coefficients and lateral center-of-pressure positions as measured at subsonic and supersonic speed in several wind tunnels. Data were used for the systematic set of fins listed in the following sketch and tested in combination with a body and on a splitter plate.

	$\lambda = 0$	$\lambda = 0.8$	$\lambda = 1$
$AR = 2$		T23	
$AR = 1$	T14	T15	T11
$AR = 1/2$	T36	T31	T32

The fins and body of this systematic data base are shown in figure 6.

BODY GEOMETRY

MRC ~ moment reference point

FIN GEOMETRYAFT VIEW FIN POSITION NUMBERS

FIN	FIN AREA (in. ²)	ROOT CHORD (in.) c_r	SEMISPAN (in.) $(s_m - a)$	TAPER RATIO c_t/c_r	$\frac{l_{MRC}}{c_r}$
T11	7.028	3.749	1.875	1.0	0.45
T14	7.038	7.499	1.875	0.0	0.62
T15	7.024	4.996	1.875	0.5	0.55
T23	3.605	2.565	1.875	0.5	0.55
T31	14.030	9.98	1.875	0.5	0.55
T32	14.036	7.499	1.875	1.0	0.45
T36	14.056	14.998	1.875	0.0	0.55

Figure 6. Fins and body of systematic data base.

The data for these fins were generated at several facilities. The models were those constructed by the Orlando Division of Martin Marietta Corporation and described by Fidler et al. (refs. 13 and 14) and Gomillion (ref. 15). The latter reference contains information and data from the above models and from a similar set of models constructed by the Air Force. All of the fin data in the presence of the body were obtained from data tabulations supplied by Dr. Donald J. Spring of MICOM (now Army Missile Research and Development Command). The fin-alone data on the splitter plate were obtained from the tabulated data of reference 16 supplied through the courtesy of Dr. William B. Baker, Jr. of ARO, Inc. The investigation in which the data were obtained is reported in reference 17. The following tabulation summarizes the configurations and test conditions, model attitudes and test sites for the systematic data used in the present investigation.

Configuration	Mach Number	Model Attitude		Test Site
		Angle of Attack	Roll Angle	
Isolated Tail Fins	0.8 - 1.3	0° - 180°		AEDC '4T'
	1.5 - 3.0	0° - 180°		AEDC 'A'
Bodies and Bodies + Tails	0.8 - 1.2	0° - 25°	0° - 90°	McDAC 4 FT
	0.8 - 1.2	25° - 50°	0° - 90°	AEDC '16T'
	1.5 - 3.0	0° - 45°	0° - 90°	AEDC 'A'

The fins of the systematic data base had a maximum aspect ratio of 2. In order to provide some data for a higher aspect ratio at the lower Mach numbers, 0.8 and 1.3, data for a canard fin of $AR = 3.53$ and $\lambda = 0.06$ have been included in the data base.

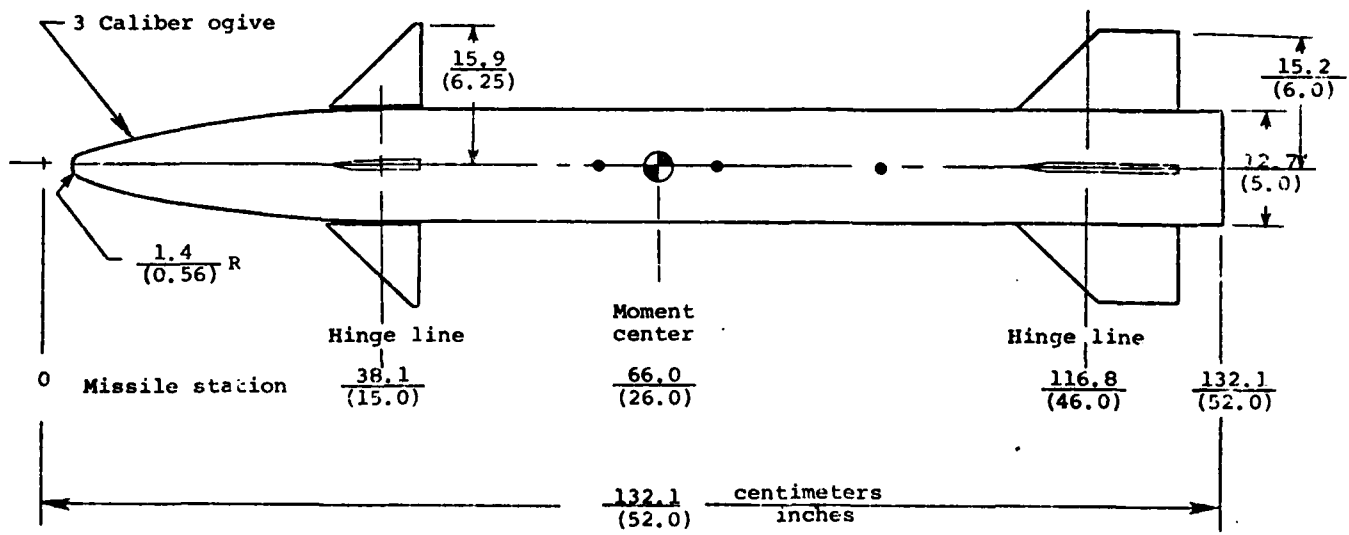


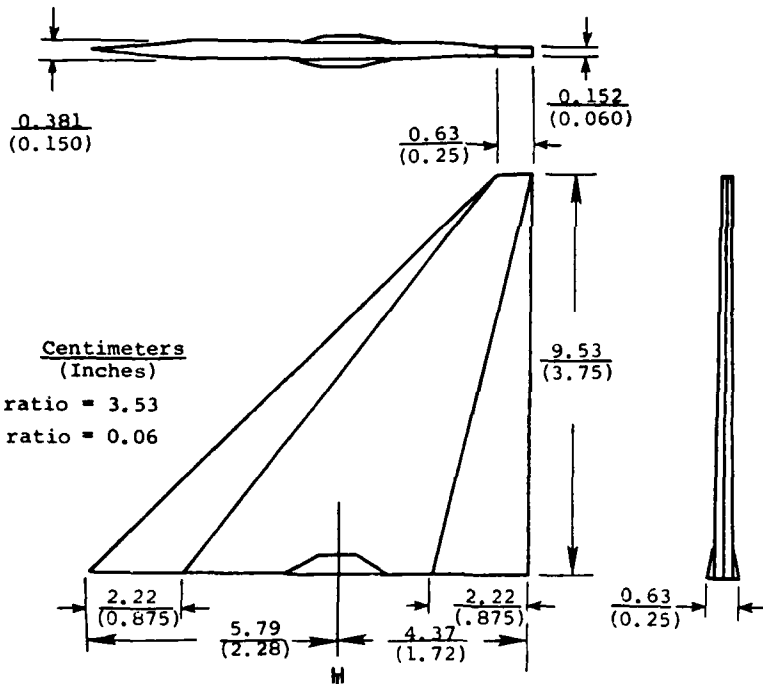
Figure 7. Body-canard-tail test configuration.

These data were obtained during the tests described in references 4 and 7. The body-canard-tail configuration shown in figure 7 is the missile tested. The canard and tail fins dimensions are shown in figure 8. Those data, taken up to about 50° angle of attack, together with the systematic data base, exhaust the supply of available high angle-of-attack cruciform missile data which includes fin loads and roll effects. The data for the missile without the canards present are not within the data base and can be used for verifying the predictive method. Also the tail-fin characteristics for the complete missile can be used for the same purpose.

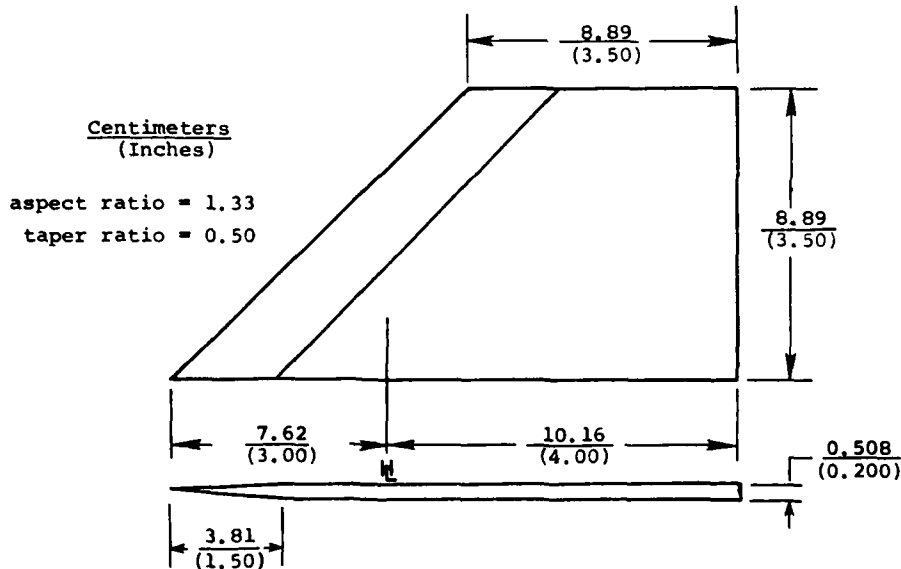
2.5.2 "Vortex-free" data base.- The systematic data base for fin loads and center-of-pressure positions is for a radius/semispan ratio of 0.5. It is not possible to extrapolate these data simply to other values of a/s_m because the normal-force component induced by body vortex effects scales differently with a/s_m than the normal-force component independent of vortex effects. Also that part influenced by the vortex depends strongly on forebody length while that part independent of the vortex is weakly dependent on forebody length. To scale properly for a/s_m , one needs data for at least three a/s_m values in order to interpolate between them. Since such data do not exist, an alternate but more difficult scheme is to decompose the measured data into parts which are vortex dependent and vortex independent and scale these parts separately by the different laws governing each. The scheme to achieve the desired decomposition has the following parts.

(1) The first step in this process is to create a body vortex model for the symmetrical (in y) part of the vortex field. Construction of this model has been one of the principal tasks of this study. It is described in detail in section 5.

(2) The next step is to utilize this body vortex model in determining the distribution of angle of attack induced by it



(a) Canard fin, C6.



(b) Tail fin, T2.

Figure 8. Dimensions of canard and tail fins.

over the four fins of the cruciform wing-body combination.

(3) The third step is to determine the average angle of attack induced on each fin by the body vortices following the results of Appendix B. At the same time the lateral center-of-pressure position of the vortex-induced load is found.

(4) The fourth and final step is to determine the vortex-induced normal-force coefficient on the fin, $(C_{NT})_v$, using the equivalent-angle-of-attack method and then subtracting it from the measured value to produce $(C_{NT})_p$ which is free of body vortex effects.

The precise details of how the four preceding steps are carried out are described later. Also described are the means of scaling the two components of the normal-force coefficient and adding them together to synthesize the aerodynamic characteristics of a configuration having different geometric parameters from those in the data base.

2.6 Program Limitations

1. The fins in each finned section must be identical, uncambered, and untwisted.
2. The leading edges of the fins must not be swept forward and the trailing edges must be unswept.
3. The included angle of attack, α_c , cannot exceed 45° .
4. The free-stream Mach number must lie between 0.8 and 3.0.
5. The fin aspect ratio must lie within the region shown on the sketch on page 14.
6. The fin equivalent angle of attack cannot exceed 60° .

3. CONSTRUCTION OF THE DATA BASE

3.1 Introductory Remarks

In the data base the primary matrix of fins consists of an aspect-ratio series of taper ratio 0.5 and a taper-ratio series of aspect ratio 1.0. The two series are formed of five fins; T11, T14, T15, T23, and T31. The two series permit linear interpolation with respect to aspect ratio and taper ratio. Data are included in the data base for four primary Mach numbers; 0.8, 1.2, 2.0, and 3.0.

The general approach of the present method consists of utilizing the fin normal-force coefficient and center-of-pressure locations of the data base and of interpolating or extrapolating the data base to other conditions not covered in the data base. The basic parameters of the data base are included angle of attack α_c , roll angle ϕ , Mach number M_∞ , fin aspect ratio AR , and fin taper ratio λ . Most of the data base is for $a/s_m = 0.5$ and a small fraction is for $a/s_m = 0.4$.

Any fin data for a cruciform wing-body combination will include the effects of body vortices. The strength of the body vortices depends on a/s_m , α_c , M_∞ , and the length of the body in front of the fin. To scale the part of the fin loads due to the vortices one must use a complicated nonlinear vortex model. If one can remove the vortex part of the fin loads, one has a set of fin loads which scale with a/s_m , α_c , ϕ , and M_∞ in a different manner from the vortex components of the loads. The first step in constructing the data base is to tabulate experimental fin normal-force coefficients and lateral center-of-pressure locations for a systematic set of values of ϕ , α_c , AR , λ , and M_∞ . (Hinge moments are not considered). The next step is to estimate and remove the vortex effects from the measured values to form a "vortex-free" data base. The "vortex-free" values are scaled

to configurations not in the data base using special methods appropriate for this purpose. The final step is to calculate the vortex contribution for the parameters of the new configuration using the vortex model and add it to the "vortex-free" contribution. The alternative to an approach like this is to obtain a data base for all possible combinations of parameters, a task of very large magnitude. Practically we must proceed as best we can with the existing data base, determine its limitations, and possibly selectively obtain new data in the future.

It is noted that superposition of vortex effects and non-vortex effects is tacitly implied in the general approach. It has been possible to do such superposition successfully for many cases in the past. However, a case has arisen where such superposition is not strictly valid. This case, pointed out in reference 6, occurs when a body vortex can act to delay the stall of a fin.

We will first describe how the wing-alone normal-force curves utilized in the method were obtained. Next the method of extracting the fin aerodynamic characteristics from the wind-tunnel data is described and the data base is presented. Then the method of subtracting the vortex effect out of the data base is described and the "vortex-free" data base is presented.

3.2 Wing-Alone Normal-Force Curve

The methods are now given of determining the normal-force curves for the basic five wings T11, T14, T15, T23 and T31 at Mach numbers of 0.8, 1.2, 2.0, and 3.0 as well as the $M = 2.0$ and 3.0 normal-force curves for T32 and T36.² For canard fin C6 normal-force curves at $M_\infty = 0.8$ and 1.3 are also determined. It was not possible to obtain such curves directly from any source, and the curves are synthesized from a variety of data. It is necessary to obtain wing-alone data to $\alpha = 60^\circ$ since the equivalent angle of attack of the fins with control deflection

²Wing T36 data are used in establishing the wing-alone curve for T31.

can approach this value.

3.2.1 Fins of aspect ratio 0.5.- We first consider the wing-alone corresponding to fin T36 ($\lambda = 0$) for $M_\infty = 3.0$. This fin is used as the starting case because the availability of data is better than for T31 or T32. We will then use the T36 curve as a guide in determining the curves for T31 and T32. We will construct a normal-force curve for T36 from data obtained for three sources.

(1) Hill (ref. 18): Wing-alone data taken on a sting support; $0 \leq \alpha \leq 40^\circ$.

(2) Falunin et al. (ref. 19): Wing-alone data for $0 \leq \alpha \leq 180^\circ$; $AR = 0.706, 2.34, 4.00$, and 6.93 ; $\lambda = 0$.

(3) Baker (ref. 17): Splitter-plate data for T36.

The procedure used is now described.

The first comparison is between the data of Hill and the splitter-plate data (ref. 16) shown in figure 9. The Hill data show no indication of stall at $\alpha = 40^\circ$ whereas the splitter-plate data signal approaching stall at $\alpha = 30^\circ$. In the wing-body combination the T36 fins attain a normal-force coefficient of 1.21, so that the splitter-plate maximum normal-force coefficient of 0.8 is suspect, and Hill's data are adopted for the data base where they differ from the splitter-plate data.

In order to provide some basis for extending the normal-force curve to $\alpha = 60^\circ$, we have compared the data of Hill with the data of reference 19 extrapolated to $AR = 0.5$. The comparison is shown in figure 10. The Falunin data are in good agreement with the Hill data up to about 40° , and they provide a guide for extrapolating the Hill data above 40° to 60° as shown in figure 10.

It is not possible to establish the T31 and T32 normal-force curves in the same way as for T36 because high angle-of-attack sting data do not appear to be available. We will use the

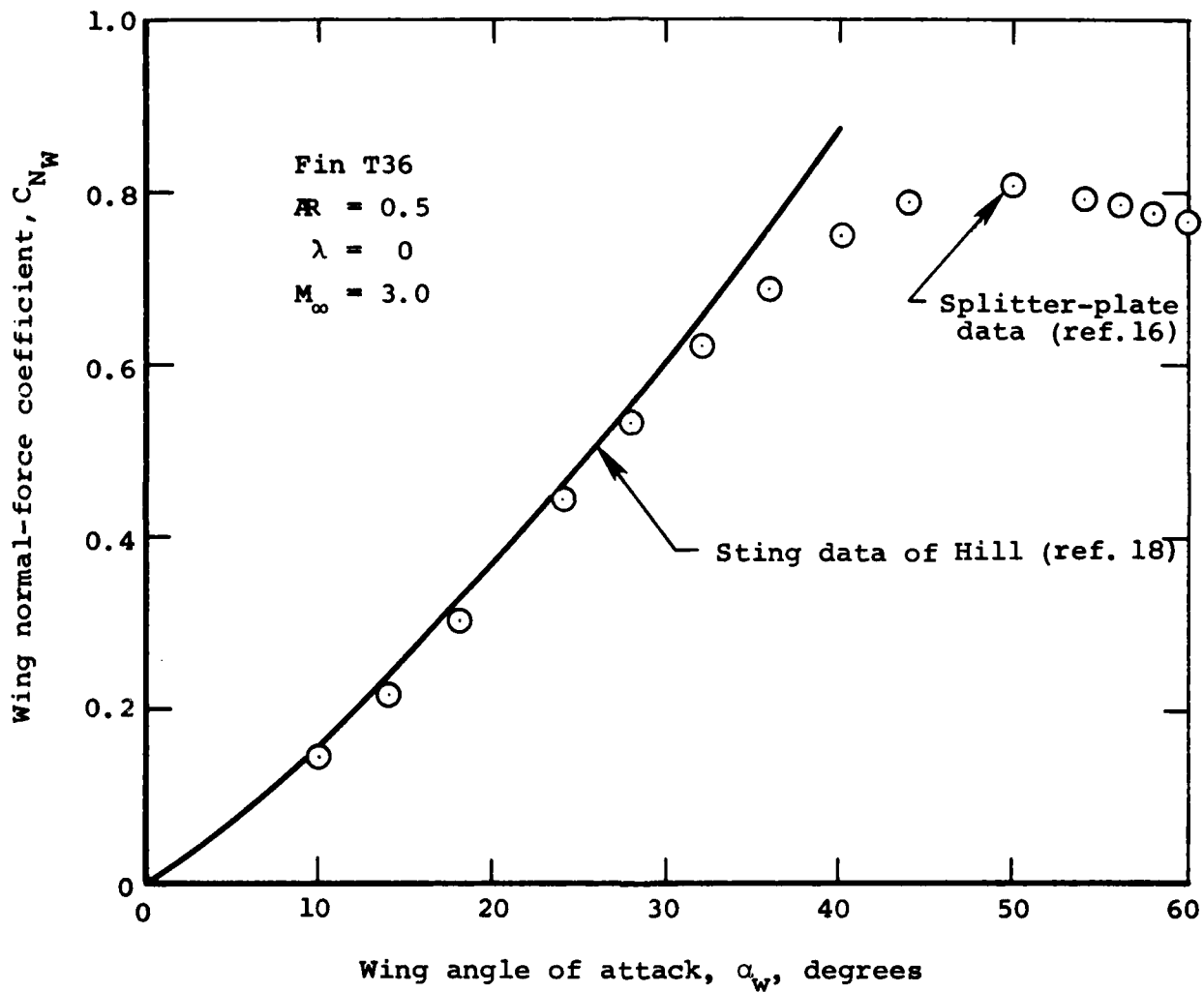


Figure 9. Comparison of splitter-plate data and sting data for normal-force curve of fin T36 at $M_\infty = 3.0$.

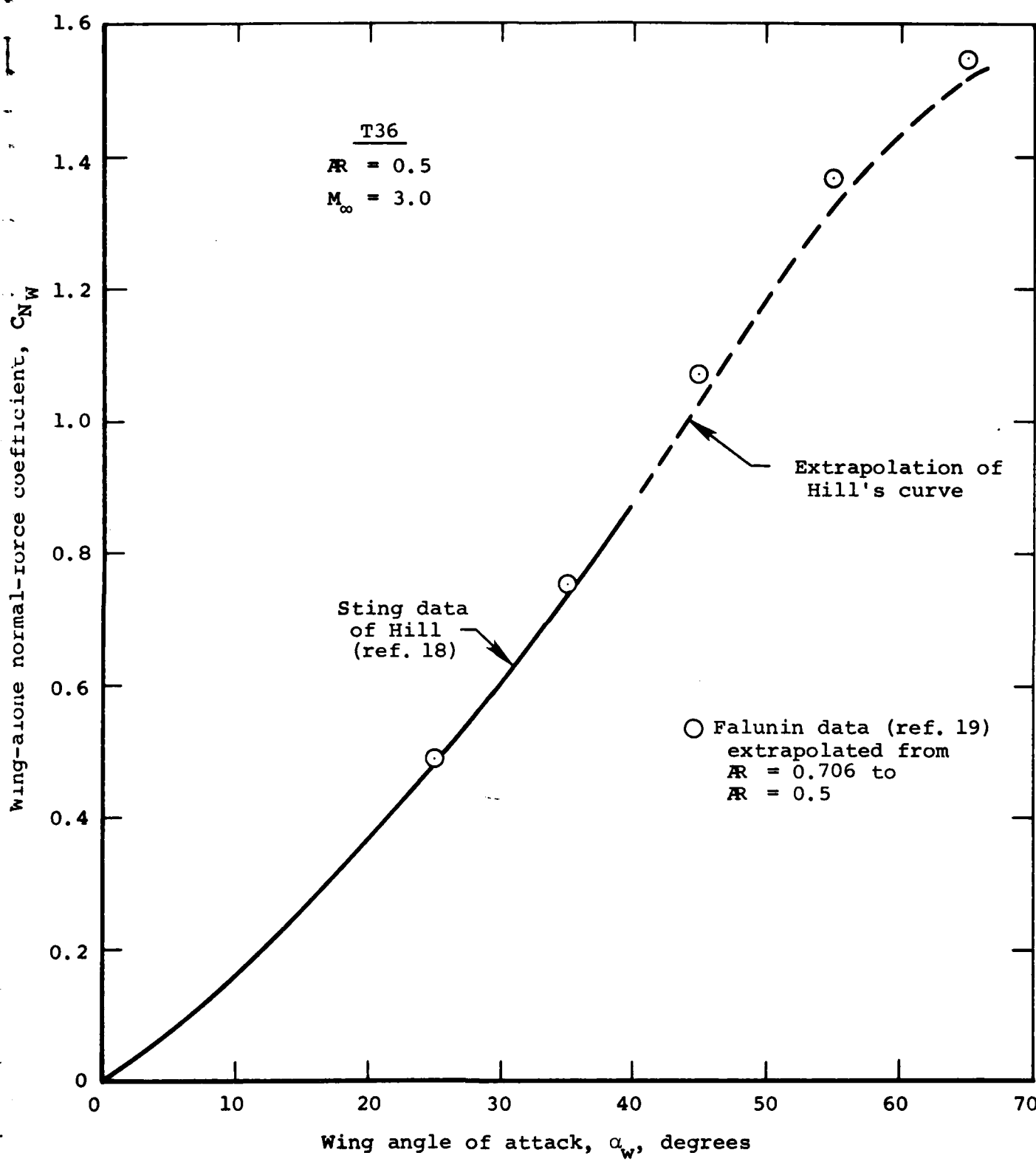


Figure 10. Comparisons of Hill data and Falunin data for fin T36 at $M_\infty = 3.0$.

splitter-plate results to obtain increments in normal-force coefficient due to changes in taper ratio up to the angle of attack for which the results appear credible. The splitter-plate data for T36, T31 and T32 are plotted in figure 11 to show the nature of the results. It appears that the data for T31 and T32 are less affected by plate boundary-layer, shock-wave interaction than T36. Also the increments in normal-force coefficient going from $\lambda = 0$ to $\lambda = 0.5$ are much greater than going from $\lambda = 0.5$ to 1.0. In figure 12 the increments in normal-force coefficients T31-T36 and T32-T31 obtained from the splitter-plate data are plotted. The T31 wing-alone curve was obtained by adding these increments (smoothed) to the T36 normal-force coefficient up to $\alpha \approx 30^\circ$. Above this angle of attack, the curve was extrapolated using the T36 curve as a guide. The T32-T31 increments shown in figure 9(b) are quite small and have been smoothed up to $\alpha = 60^\circ$. In this way the T32 normal-force curve has been established.

Figure 13 shows the family of normal-force curves for T36, T31 and T32 at $M_\infty = 3.0$. At $M_\infty = 2.0$ the same method was used to establish the wing-alone curves as at $M_\infty = 3.0$, but at $M_\infty = 1.2$ another means was used. The necessary data to apply the same method at $M_\infty = 1.2$ are lacking, but the splitter-plate data are now reliable to higher angles of attack. For instance, the T36 data at $M_\infty = 1.2$ appeared valid to about $\alpha = 40^\circ$, and T32 to about $\alpha_C = 55^\circ$. The results were extrapolated to $\alpha_C = 60^\circ$ with due regard for the maximum values of normal-force coefficient experienced by the fins in the presence of the body. In actuality data at $M_\infty = 1.15$ and 1.3 were used in establishing the $M_\infty = 1.2$ results. The same method was used at $M_\infty = 0.8$ as at $M_\infty = 1.2$, the splitter-plate being used for absolute values of normal-force coefficient at these Mach numbers up to the limits of validity rather than by differencing as at $M_\infty = 2.0$ and 3.0.

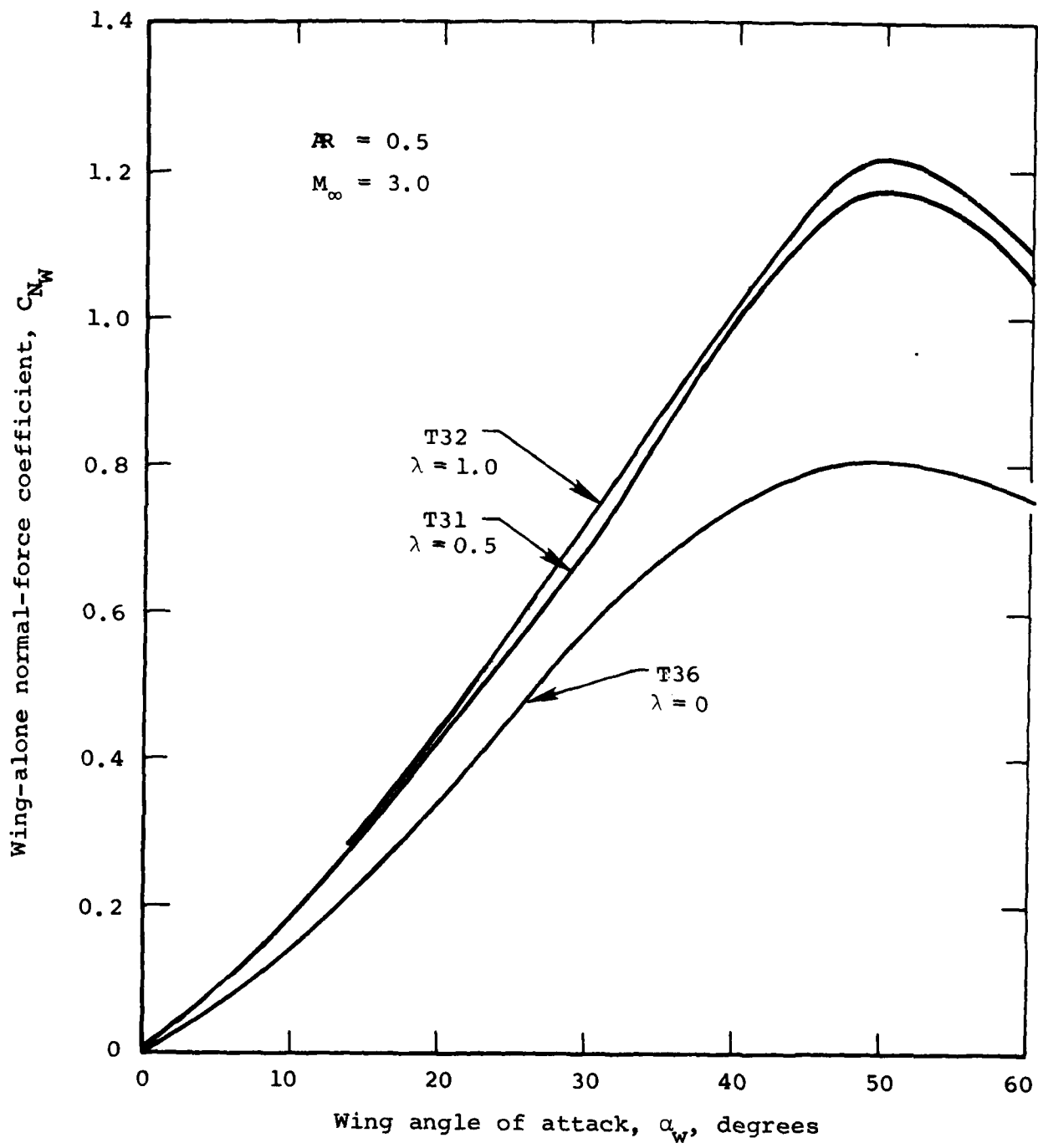


Figure 11. Wing-alone normal-force curves as determined on splitter plate for T36, T31, T32.

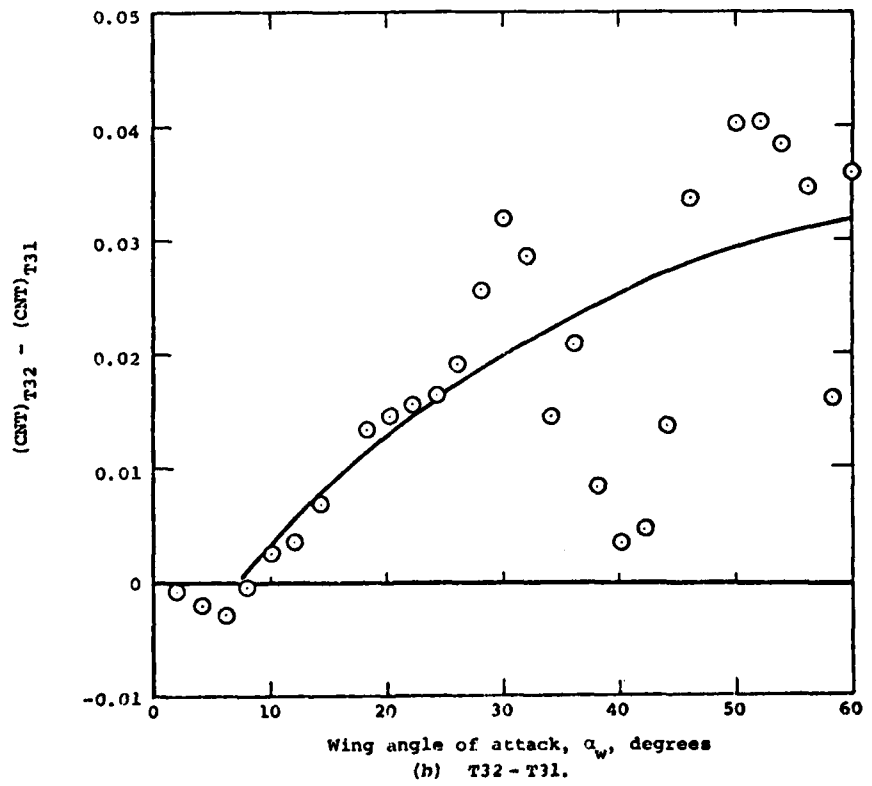
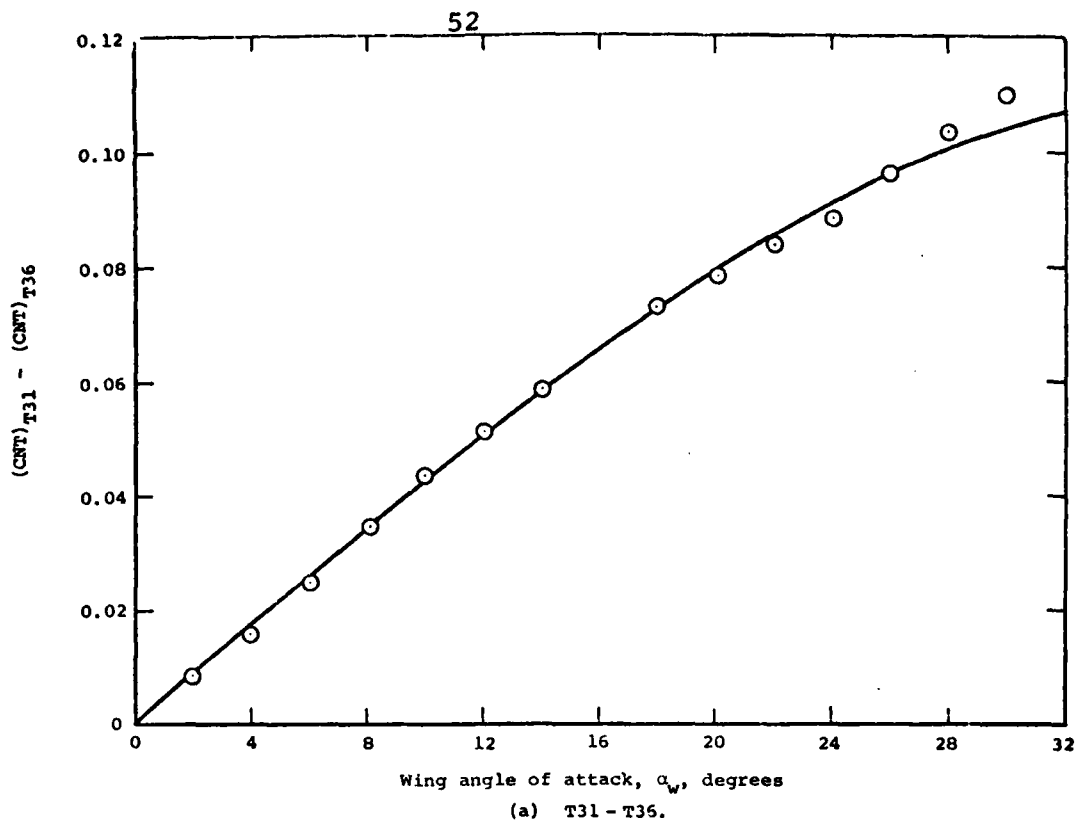


Figure 12. Increment in normal-force coefficient as measured on splitter plate at $M_\infty = 3.0$.

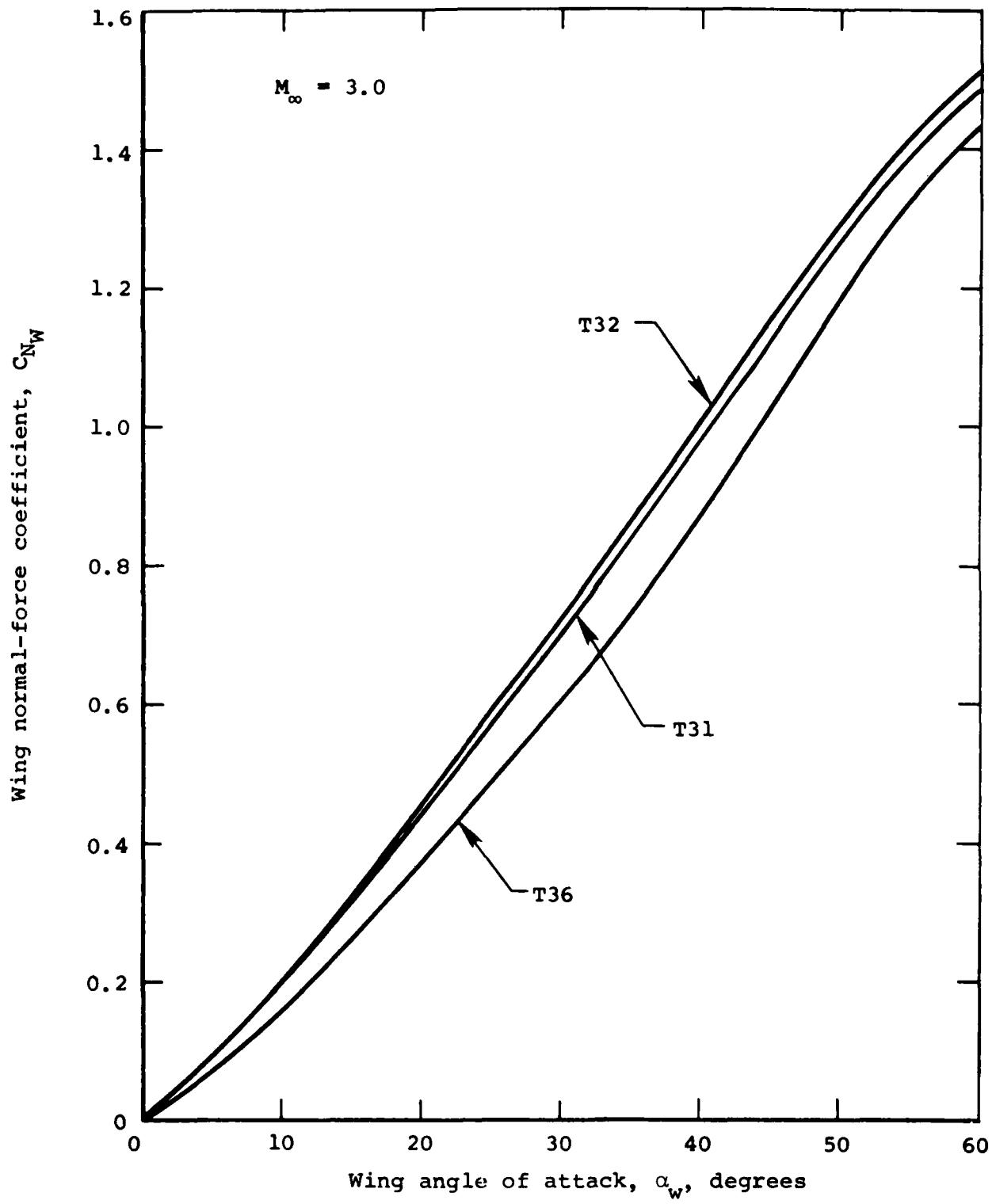


Figure 13. Constructed normal-force curves for wings T36, T31, and T32.

3.2.2 Fins of aspect ratio 1.0 and 2.0.- The wing family of unit aspect ratio, T14, T15 and T11, was treated in the same fashion as the $AR = 0.5$ family. At $M_\infty = 3.0$ data of Hill (ref. 18) for $AR = 1$ and $\lambda = 0$ were used for the T14 curve up to $\alpha = 40^\circ$, and the Falunin data (ref. 19) were used as a guide to fair the results to $\alpha = 60^\circ$. The T15 and T11 normal-force curves were established using splitter-plate differences for changes in normal-force coefficient due to taper ratio together with extrapolating beyond the range of validity of the splitter-plate results. The same method as for $M_\infty = 3.0$ was used to obtain the $M_\infty = 2.0$ wing-alone normal-force curve for the $AR = 1.0$ family. For $M_\infty = 0.8$ and 1.2 the same method was used for the $AR = 1.0$ family as was used for the $AR = 0.5$ family.

No test data for a sting-mounted wing of $AR = 2$ (T23) to high angles of attack were found for $M_\infty = 2.0$ and 3.0. Accordingly the splitter data were used to determine the differences between T23 and T15 and these were applied to T15 to estimate T23. The results were extrapolated to angles of attack beyond the validity of the splitter-plate results using the T15 results as a guide. This same procedure was used to establish the $M_\infty = 2.0$, T23 wing-alone normal-force curve. For $M_\infty = 0.8$ and 1.2 the normal-force curves were constructed in the same manner as for the $AR = 0.5$ wings.

3.2.3 Fins of aspect ratio 3.53.- The tests described in references 4 and 7 have been used to formulate the wing-alone curve for the aspect ratio 3.53 fin (C6) at Mach numbers of 0.8 and 1.3. For angles of attack up to $\alpha = 42.5^\circ$ the wing-alone curve was obtained from the equivalent angle of attack correlation given in figure 4(a) of reference 20 for $M_\infty = 0.8$. These data together with a knowledge of the maximum normal-force coefficient encountered by this fin in the wing-body tests provide a basis for constructing the curve up to $\alpha = 60^\circ$.

At $M_{\infty} = 1.30$ an equivalent angle of attack curve was available for the $AR = 3.53$ fin in figure 6(b) of reference 20. The wing-alone normal-force curve for this case was constructed with the help of this information, using the known maximum normal-force coefficient and the curves for T36 and T14 as guides at higher values of α_c .

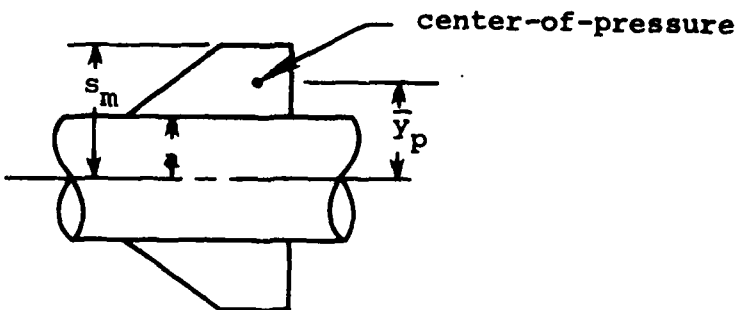
3.2.4 Tables.— The wing-alone normal-force data are presented in Table 2 for increments in angle of attack of 2° for Mach numbers of 0.8, 1.2, 2.0, and 3.0 for the fins of the systematic data base. Similar results for the $AR = 3.53$ fin (C6) at $M_{\infty} = 0.8$ and 1.3 are given in Table 3.

3.3 Fin Lateral Center of Pressure

In order to calculate rolling moments it is necessary to know the lateral position of the fin center of pressure. The loads on the fins with vortex effects removed have center-of-pressure locations which depend principally on the fin normal-force coefficient and are insensitive to roll attitude, as we will show. In addition there are loads associated with angle-of-attack distributions induced on the fin by vortices. These loadings depend in a nonlinear fashion on the position of the vortex relative to the fin. The fin loads and center-of-pressure locations associated with vortices are determined from the vortex parameters and reverse-flow theorems as discussed in Appendix B. We rely on a data-base approach for the lateral center-of-pressure location associated with nonvortex loads.

It is known that the vortex-induced load on fin T4 on the windward side of the body is quite small. Hence, the measured center-of-pressure positions in this case are almost entirely free of vortex interference. We have compiled a data base of the measured lateral center-of-pressure positions to be used together with the data-base normal-force coefficients for rolling moment calculations. The lateral position \bar{y}_p is measured from the body

centerline as shown in the following sketch:



It is convenient to specify \bar{y}_p in terms of a lateral center-of-pressure parameter, $(\bar{y}_p - a)/(s_m - a)$.

To extract the value of this parameter from the fin data, we note that the rolling-moment coefficient CRMT due to the fin should be zero when the fin normal-force coefficient CNT is zero. Assuming that both coefficients are based on reference area S_R and that the reference length is ℓ_r , we have

$$\frac{\bar{y}_p}{\ell_r} = \frac{CRMT - CRMT_0}{CNT} \quad (4)$$

where $CRMT_0$ is the value of CRMT when CNT is zero.

3.3.1 Fins of aspect ratio 0.5, 1.0, and 2.0.- The value of $(\bar{y}_p - a)/(s_m - a)$ has been determined for all the fins of the data base at $M_\infty = 0.8, 1.2, 2.0$, and 3.0 for fin T4 at roll angles of $20^\circ, 40^\circ, 60^\circ$, and 80° . Typical results are shown in figure 14 for fin T14 at all four Mach numbers. In this figure $(\bar{y}_p - a)/(s_m - r)$ is plotted versus fin normal-force coefficient, CNT4. At all Mach numbers the data from all four ϕ_4 angles correlate reasonably well (considering the expanded scales) and show a decreasing trend with increasing normal-force coefficient. At low values of CNT somewhat more scatter is evident

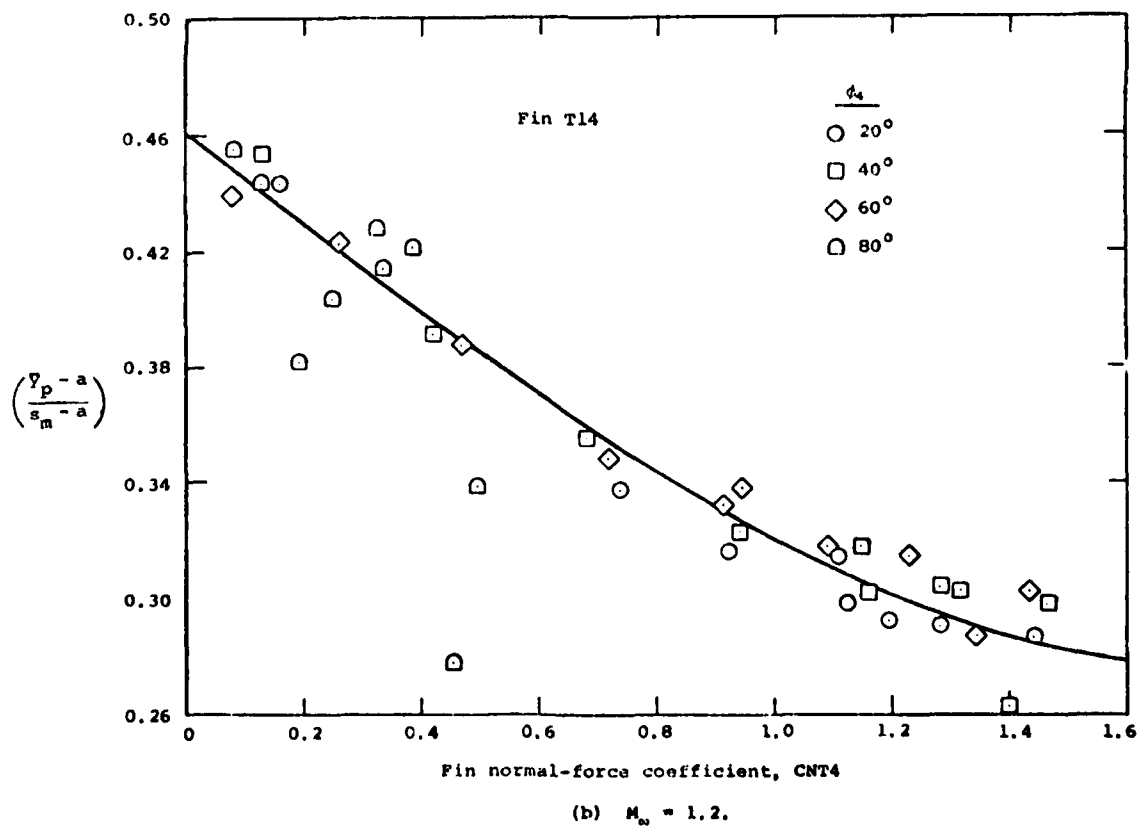
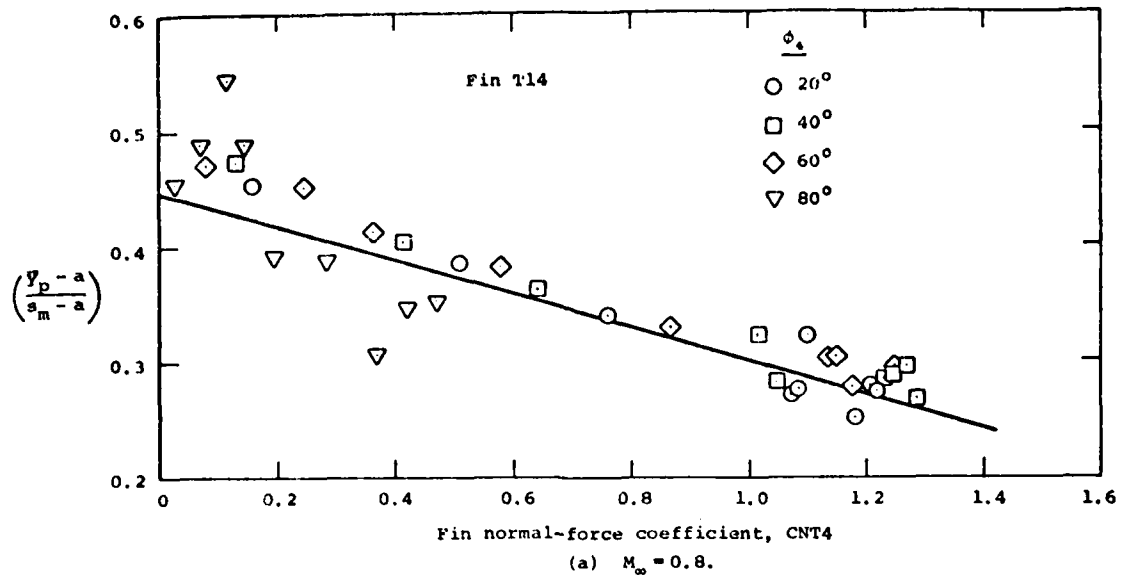


Figure 14. Lateral position of center of pressure of fin T14 mounted on body B_1 ($S_R = \text{fin planform area}$).

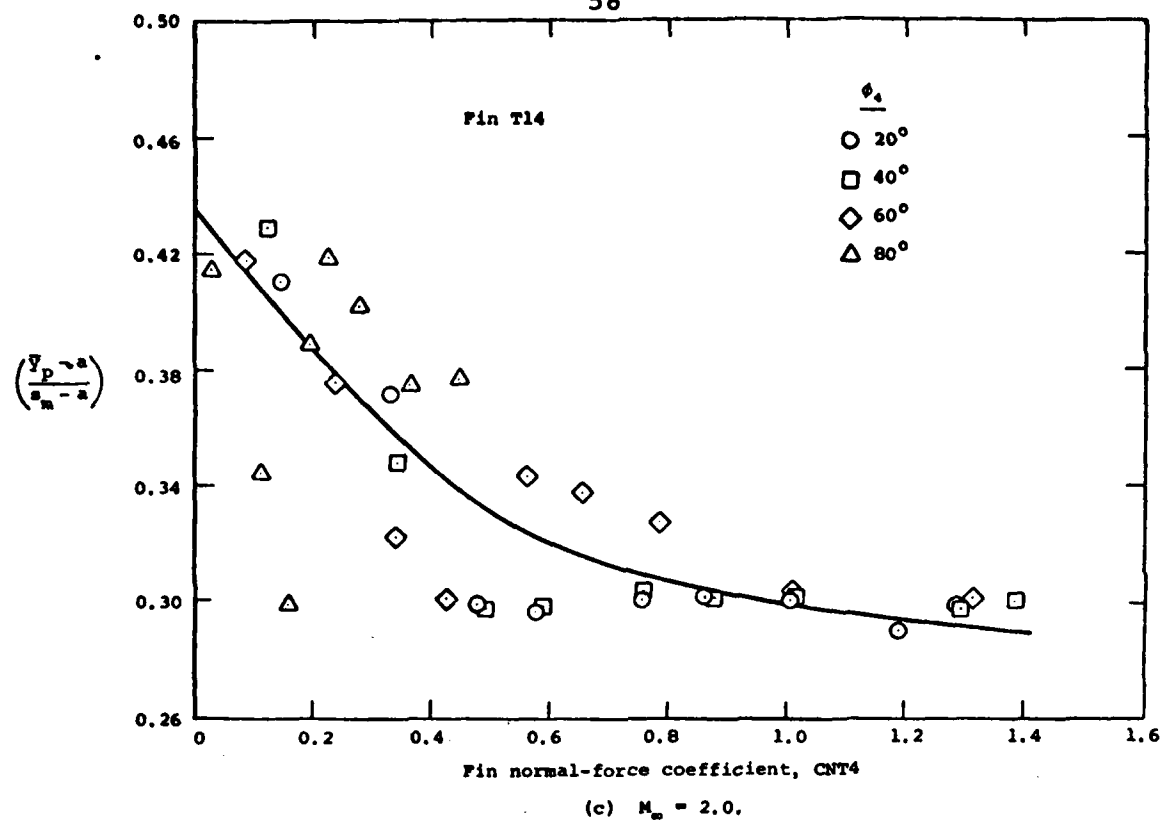
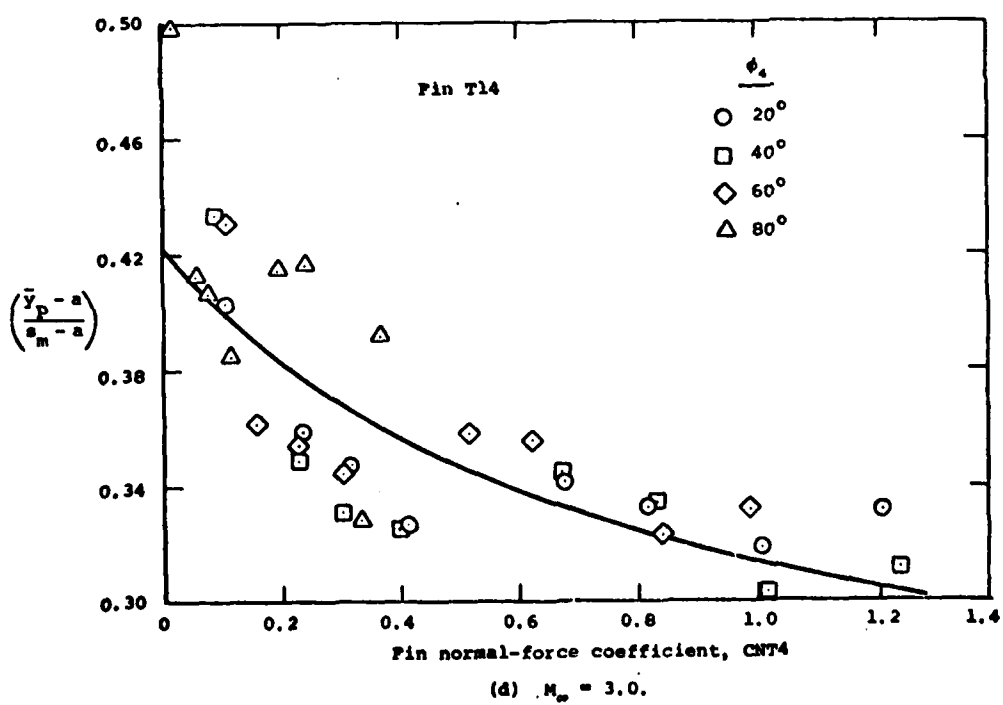
(c) $M_\infty = 2.0$.(d) $M_\infty = 3.0$.

Figure 14. Concluded.

than at large CNT. This is associated with the fact that \bar{y}_p goes to infinity unless moment and normal force experimentally go to zero simultaneously.

Correlation curves have been faired through the data points, and the curves are used in the data base for all values of ϕ . It is noted that the scatter about the curves is generally within $\pm .05$ except for a few points at low CNT4.

For an elliptical span loading the parameter $(\bar{y}_p - a)/(s_m - a)$ has a value $4/3\pi$ or .424, and for a uniform loading it has a value of 0.333 for a delta wing such as T14. Near CNT4 of zero, the experiment tends to the elliptic loading value and at large CNT it tends to the uniform-loading value.

For the purpose of the data base, the value of $(\bar{y}_p - a)/(s_m - a)$ has been tabulated for increments in CNT of 0.2. Tabulations of the results are given in Table 4.

3.3.2 Fins of aspect ratio 3.53.- The data for the canard fins of $AR = 3.53$ have also been analyzed to determine the lateral center-of-pressure parameter $(\bar{y}_p - a)/(s_m - a)$ at $M_\infty = 0.8$ and 1.3. The same method was used in this case as for the systematic fin data. In figure 15 are shown the values of $(\bar{y}_p - a)/(s_m - a)$ to an enlarged scale for $M_\infty = 0.8$ and 1.3 for the various roll angles. Mean curves have been drawn through the data, and these curves are used to generate the values in Table 5. The deviation from the mean curves is small when the total lever arm for roll, \bar{y}_p , is considered.

3.4 Fin Normal-Force Data Including Body Vortex Effects; $AR \leq 2$

In this section we will describe how the fin normal-force coefficients of the data base have been processed before their tabulation in Tables 6 and 7. While these data, which include the body vortex effects, are not used directly in the present calculative method, they are of basic value in their own right.

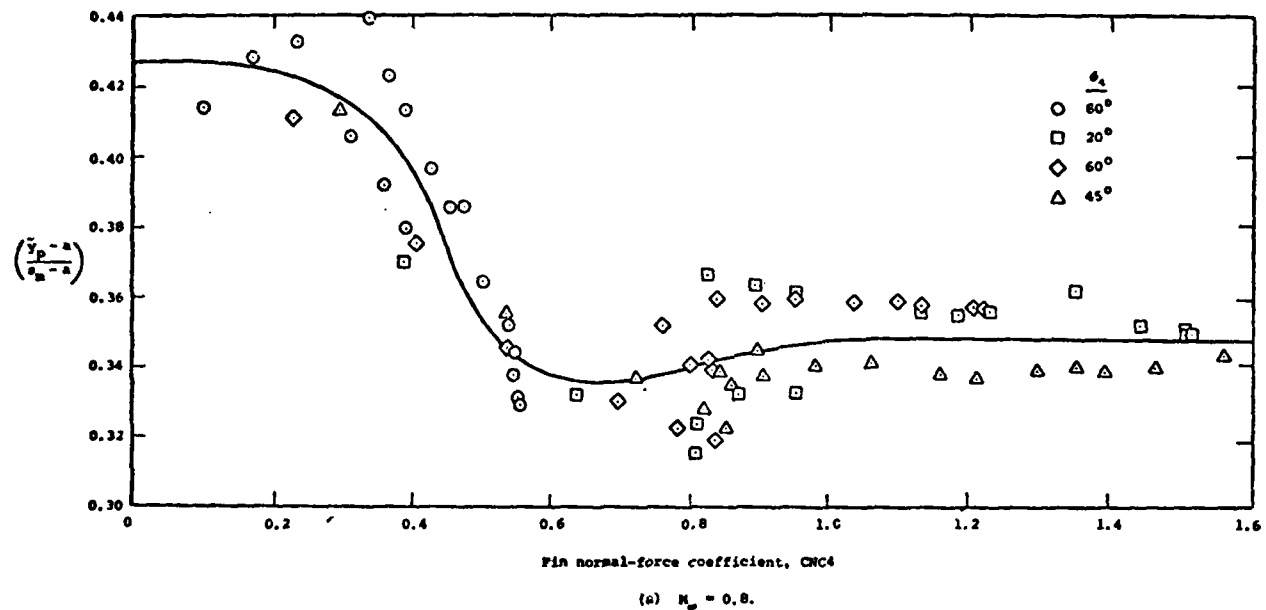
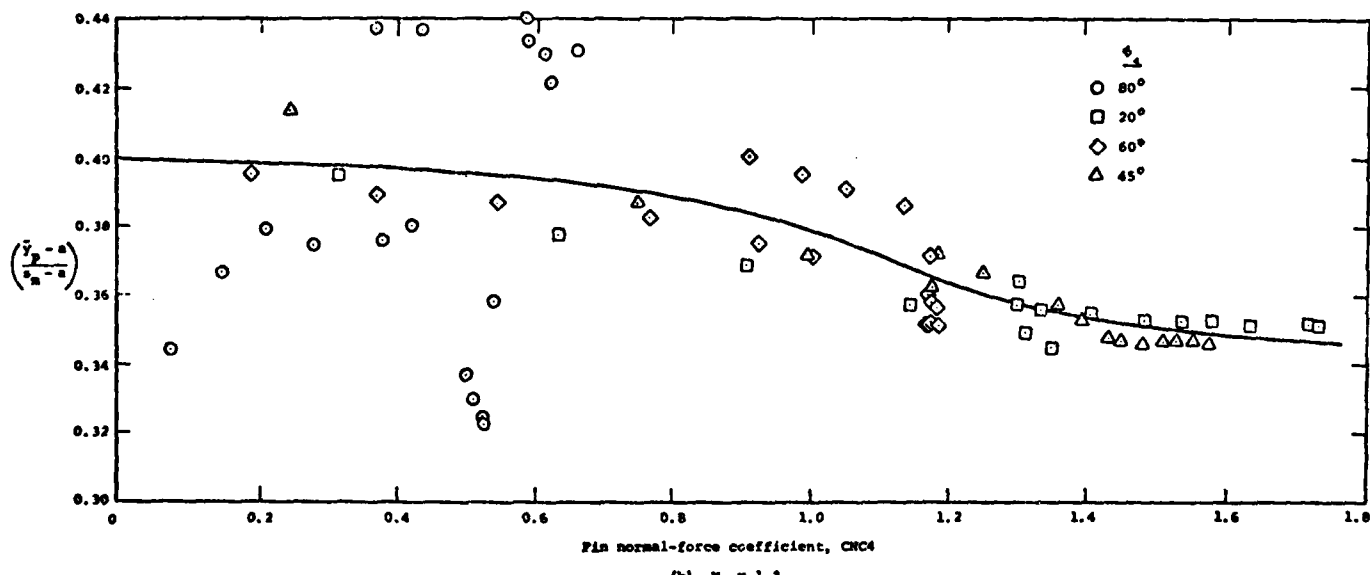
(a) $M_\infty = 0.8$.(b) $M_\infty = 1.3$.

Figure 15. Lateral position of center of pressure of fin C6 ($AR = 3.53$) mounted on body BN_3 (ref. 7) (S_R = fin planform area).

Furthermore, they will be required if better methods of subtracting the body vortex effects out of the data are developed in the future.

3.4.1 Manipulation of the data.- Before tabulation of the fin normal-force data certain operations were carried out on the measured quantities. First, at $M_\infty = 2.0$ and 3.0 it was assumed that at $\alpha_c = 0$ for all ϕ CNT1, CNT2, CNT3 and CNT4 should be zero; and the measured values at $\alpha_c = 0$ have been applied as tares to measured values of CNT1, CNT2, CNT3, and CNT4 for $\alpha_c \neq 0$.

At Mach numbers of 0.8 and 1.2 (where vortex asymmetry effects can be large) it has been assumed that the value of CNT3 at $\phi = 0$ and CNT4 at $\phi = 90^\circ$ are zero even for asymmetric vortex configurations since the effect of such asymmetry is negligible at this position. In this way the value of CNT4 at $\phi = 0$ is established. The value of CNT1 at $\phi = 90^\circ$ should coincide with that of CNT4 at $\phi = 0$. The tares for CNT1 were obtained in this fashion. At $\phi = 0$ the value of CNT2 should equal the value of CNT3 at $\phi = 90^\circ$. The tares for CNT2 were obtained in this fashion. The values of CNT2 and CNT1 at mirror positions are not necessarily the same because of vortex asymmetry. Using the above method of correcting CNT1, CNT2, CNT3 and CNT4 for tares, we have constructed curves similar to figure 4 for all fins of the data base at $M_\infty = 0.8$ and 1.2 .

Much of the available data were not taken at integral values of the α_c and ϕ . The procedure to generate data for integral values is now described. The values of CNT were plotted vs ϕ_4 for approximately constant values of α_c . Values were then read from faired curves for 10° increments in ϕ_4 . An attempt was made in this fairing to put average curves through the points at $M_\infty = 0.8$ and $M_\infty = 1.2$ as in figures 4(a) and 4(b) in order to average out the observed asymmetry. The vortex asymmetry effects

are then considered as a \pm change superimposed on the mean curve. The values of CNT for integral values of ϕ were then cross-plotted versus α_c . Values of CNT were then read from faired curves for the following values of α_c :

$0^\circ, 4^\circ, 10^\circ, 15^\circ, 20^\circ, 25^\circ, 30^\circ, 35^\circ, 40^\circ, 45^\circ$

In this way a set of CNT values for a matrix of integral values of ϕ and α_c was generated. This technique made it possible also to fill in certain small α_c ranges for which data were not taken, or if taken, contained obvious errors.

In general data up to about 25° angle of attack, at $M_\infty = 0.8$ and 1.2, were taken in the 4- by 4-Foot Wind Tunnel of McDonnell-Douglas Co. and data from about 20° - 25° and up were taken in the AEDC 16-Foot Wind Tunnel. The data at the higher angles of attack in the smaller wind tunnel were not always in good agreement with those of the larger wind tunnel in the region of overlap. This difference is believed due more to wind-tunnel wall interference than Reynolds number differences between the two wind tunnels. Accordingly the 16-Foot Wind Tunnel data were adopted in the region of overlap.

3.4.2 Tabulated results.- As a result of the foregoing manipulation of the data, Table 6 has been constructed. This table presents CNT4 values for fins T11, T14, T15, T23, and T31 at $M_\infty = 0.8, 1.2, 2.0$, and 3.0 for $-90^\circ \leq \phi_4 \leq 90^\circ$ by 10° increments up to angles of attack of 45° .

A complete set of data for T32 at $M_\infty = 3.0$ is given together with incomplete sets for T32 at $M_\infty = 2.0$ and T36 at $M_\infty = 2.0$ and 3.0. These latter data are useful for checking interpolation methods for aspect ratio and taper ratio in the data base.

The data of this table are not used directly in the engineering prediction method since they contain vortex effects which cannot be simply scaled for a/s_m or ratio of forebody length to body radius. Further manipulation is required as described in section 3.6.

3.5 Fin Normal-Force Data Including Body Vortex Effects; $AR = 3.53$,
 $\lambda = .06$

Normal-force data were taken as a function of roll angle and angle of attack on $AR = 3.53$ canard fins in connection with the 6- by 6-Foot Wind Tunnel and 11-Foot Transonic Wind Tunnel tests reported in references 4 and 7, respectively. These data are added to the systematic data base because they are the only data available for $AR > 2$.

3.5.1 Manipulation of the data.- These data have been manipulated in the same general way as the systematic data base with a few minor exceptions.

The normal-force coefficient and center-of-pressure location were measured on all four fins at $\phi = 0, 10, 20, 30$ and 45° for $M_\infty = 0.8$ and 1.3. The length-to-diameter ratio of the forebody in front of the canard fins was about 2.2, and the nose was slightly blunt. According to the correlation curve figure 3 of reference 8, the flow should be symmetric to 33° angle of attack. However, the flow appeared to be symmetric to higher angles of attack.

Curves of CNC versus ϕ_4 for $-90 \leq \phi_4 \leq 90^\circ$ were plotted from the results for CNC1, CNC2, CNC3, and CNC4 assuming mirror symmetry. An example of the results for $M_\infty = 1.3$ at $\alpha_c = 35^\circ$ is shown in figure 16. Note that for values of $\phi_4 = -45^\circ, 90^\circ$ and $+45^\circ$ two data points are available because of left-right symmetry. The differences between these data points are a net result of measurement inaccuracies together with any vortex or other flow asymmetries. There are slight differences between the points. Note that the differences at $\phi_4 = -45^\circ$, for which the fins are strongly influenced by the body vortices, are the same order of magnitude as those at $\phi = 0^\circ$ and 45° . This is also true at all angles of attack. Accordingly we have ignored any effects of asymmetry and have faired a mean curve through the data points to obtain CNC including vortex effects.

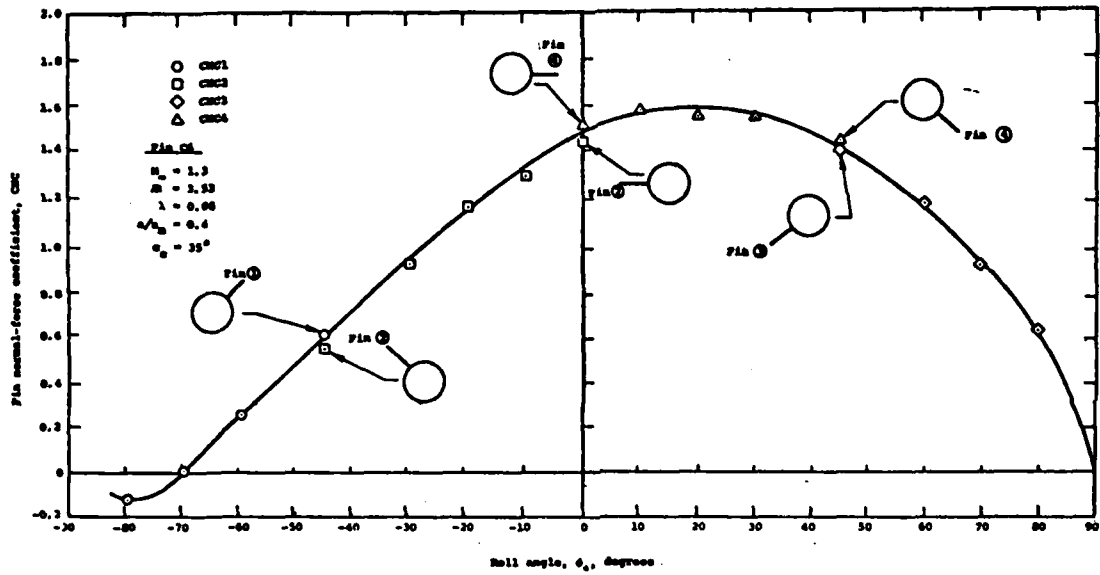


Figure 16. Effect of roll angle on normal-force coefficient for fin C6 mounted on body BN_3 (ref. 7) (S_R = fin planform area).

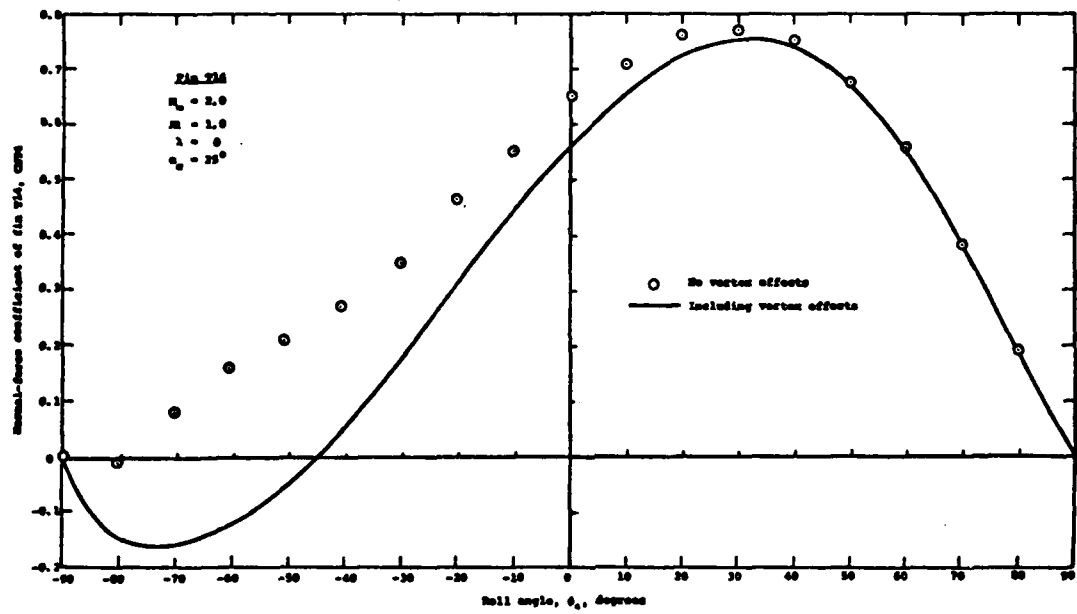


Figure 17. Normal-force coefficient of fin T14 on body B_1 with and without vortex effects; $M_\infty = 2.0$ (S_R = fin planform area).

3.5.2 Tabulated results.- The values of fin normal-force coefficient for the $AR = 3.53$ fin are presented in Table 7 for Mach numbers of 0.8 and 1.3. These results contain effects of the body nose vortices, but the effects are not so strong as those for the systematic data base which were obtained with a much longer forebody. These data represent the only results in the complete data base for $AR > 2$.

3.6 Fin Normal-Force Results Without Vortex Effects

3.6.1 Illustration of vortex interference effects.- As discussed in section 2.5.2 it is necessary to subtract the body vortex-induced effects from the measured normal-force results because the part of the normal force independent of the body vortices scales differently with the wing-body geometric parameters than the vortex-induced part of the normal force. To subtract the vortex-induced fin normal force requires a body vortex model for the range of angles of attack and Mach numbers covered in the data base as well as a means for estimating the normal-force increment induced on the fins by the body vortex. We will now provide an illustration of how the calculation is carried out.

Consider the case of fin T14 at $M_\infty = 2.0$ and $\alpha_c = 25^\circ$. The values of CNT4 as measured including vortex effects are plotted in figure 17 as the solid line taken from Table VI. The equivalent angle of attack for these values of CNT4 can be obtained from Table 2. The values of the equivalent angle of attack, designated $\alpha_{eq,0}$, are shown plotted in figure 18. The negative values of $\alpha_{eq,0}$ in the range $-90 \leq \phi_4 \leq -45^\circ$ are due to the body vortices. Using the vortex model described in Section 5 and the method described in Appendix B for computing the angle of attack induced on fin T4 by the vortices, we obtain $(\Delta\alpha_{eq})_v$ due to the vortices. This quantity is plotted in figure 18.

To correct CNT4 for vortex effects, we must find the change

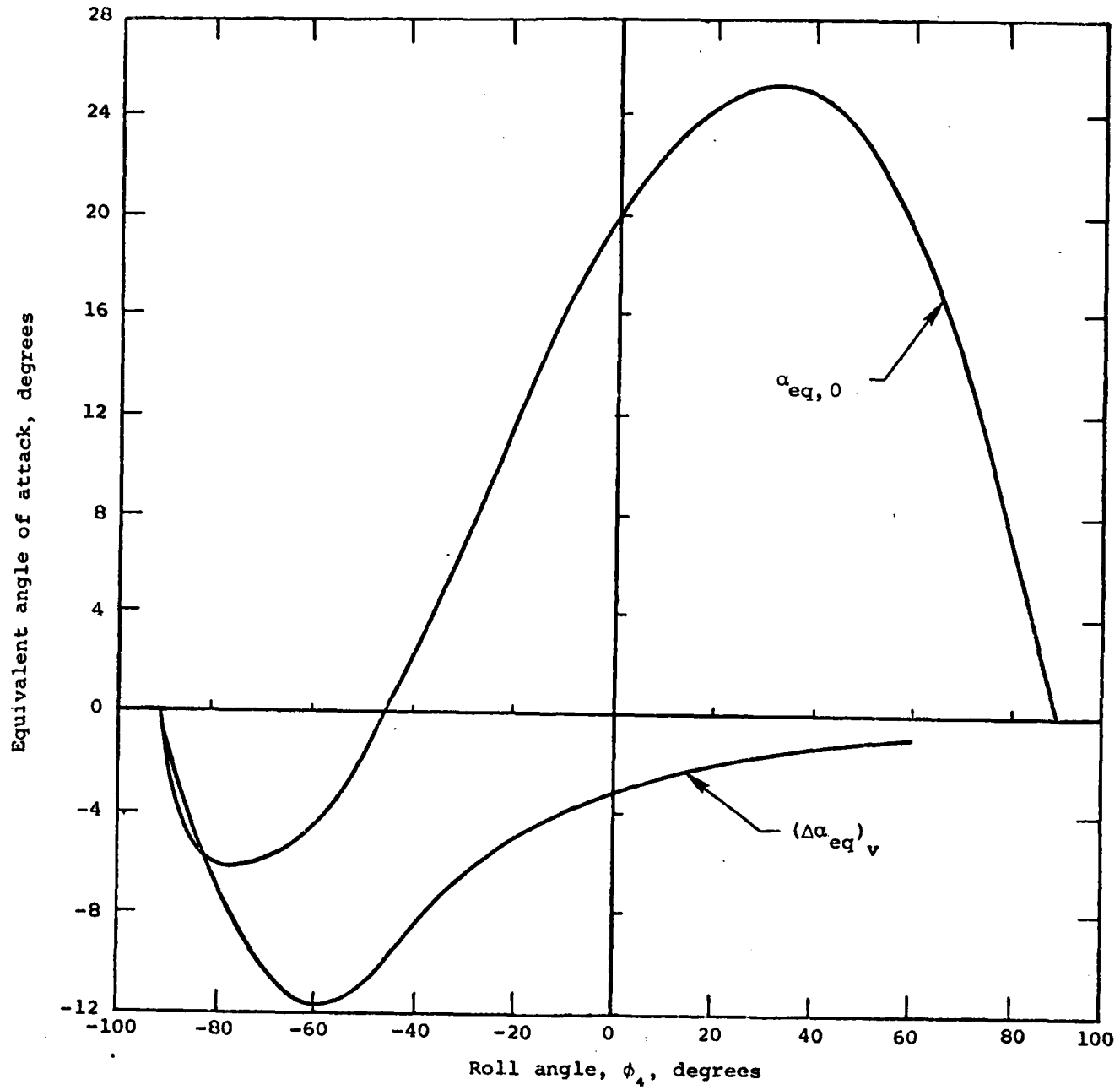


Figure 18. Equivalent angle of attack for fin T14
on body B_1 at $M_\infty = 2.0$ and $\alpha_c = 25^\circ$.

in $\alpha_{eq,0}$ due to the vortices. For this purpose we use equation (C-16) of Appendix C rewritten as follows:

$$\tan \alpha_{eq,p} = \tan \alpha_{eq,0} - \tan (\Delta\alpha_{eq})_v \quad (5)$$

Here $\alpha_{eq,p}$ is the equivalent angle of attack of the fin for no body vortices. It is noted that ordinary addition of the equivalent angle of attack has been replaced by a tangent addition theorem for high angles of attack. From the known values of $\alpha_{eq,0}$ and $(\Delta\alpha_{eq})_v$ we thus establish $\alpha_{eq,p}$. From the value of $\alpha_{eq,p}$, we go to the wing-alone normal-force curve for T14 at $M_\infty = 2.0$ and obtain $(CNT4)_p$, the value of the normal-force coefficient of fin T4 with no body vortex effect.

The values of $(CNT4)_p$ are given as points in figure 17 as a function of roll angle ϕ_4 . It is noted that the vortex effect in the fourth quadrant on fin T4 is quite small as expected. The effect is greatest near $\phi_4 = -60^\circ$. A slightly negative value of $(CNT4)_p$ is given at $\phi = -80^\circ$, whereas a small positive value is to be expected. A curve is faired through the data points to remove uncertainties in the estimates for $(\Delta\alpha_{eq})_v$. The values of $(CNT4)_p$ are read from this curve for tabulation in the data base.

3.6.2 Tabulated results.- All the data of Table 6 have been analyzed to subtract the body vortex effects from the experimental values. These vortex-free data are presented in Table 8 in a form in one-to-one correspondence with Table 6.

For fin C6 of aspect ratio 3.53 the vortex effects have been extracted from the data of Table 7, and the results are presented in Table 9. The vortex effects in this case are much less than for the other fins because of the shorter forebody.

The difference in (CNT) values between fin positions having mirror symmetry about the plane of α_c is the asymmetric component of CNT with a magnitude $2(\Delta CNT)$. This quantity is tabulated in Table 10 for $M_\infty = 0.8$ and 1.2 for the fins of the systematic data base.

4. DESCRIPTION AND USE OF DATA BASE

In this section, we will discuss some of the important effects shown by the data base. Then we will present the means for interpolating within the data base at constant a/s_m . Finally the uses of the equivalent angle of attack concept in scaling for a/s_m and for handling effects of vortices and control deflection are discussed.

4.1 Nonlinearities in the Data Base

4.1.1 Characteristics of the data base.- The CNT data base including vortex effects shows a number of phenomena which are worthwhile noting. Since the regularity of the data is best at the high Mach numbers, let us start at $M_\infty = 3.0$. In figure 19 we show curves of CNT versus ϕ for a series of angles of attack up to 35° . For $\alpha_c = 4.24^\circ$ the curve is almost symmetric in ϕ_4 , and there is negligible effect of any vortices. As the angle of attack is increased, the values of CNT tend to peak for values of ϕ_4 of about 30° . This is the result of an increased equivalent angle due to sideslip, the fin leading edge being swept forward due to roll toward the windward side.

As the angle of attack increases for negative ϕ_4 near -60° , the values of CNT become negative due to body vortex induced loads on fin T4. However, with further increases in α_c , the fin normal force again becomes positive because the body vortex moves away from the body. At high angles of attack, increases in angle of attack do not produce proportionally as much increase in CNT on the leeward side of the body as on the windward side. This effect is due in part to adverse vortex effects which increased with angle of attack. However, lower densities in the top of the body at very high angles of attack can further contribute to this effect. All fins at $M_\infty = 3.0$ show behaviors similar to that of fin T14 in figure 19. At high Mach numbers and angles of attack

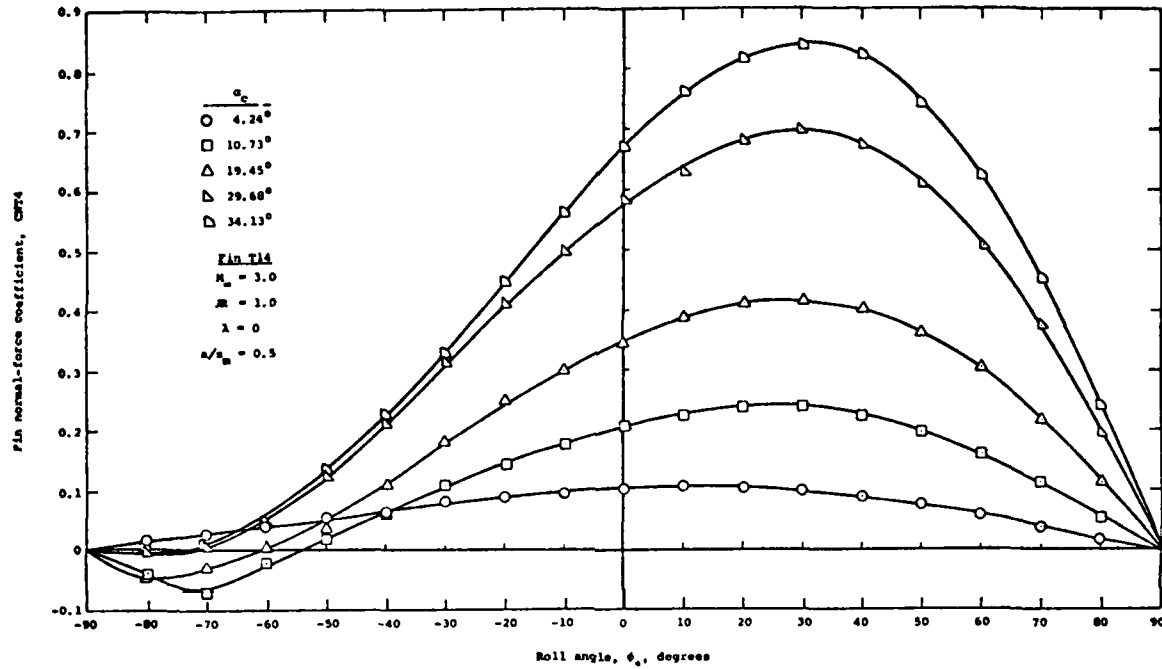


Figure 19. Normal-force coefficients of fin T14 on body B_1 at $M_\infty = 3.0$ (S_R = fin planform area).

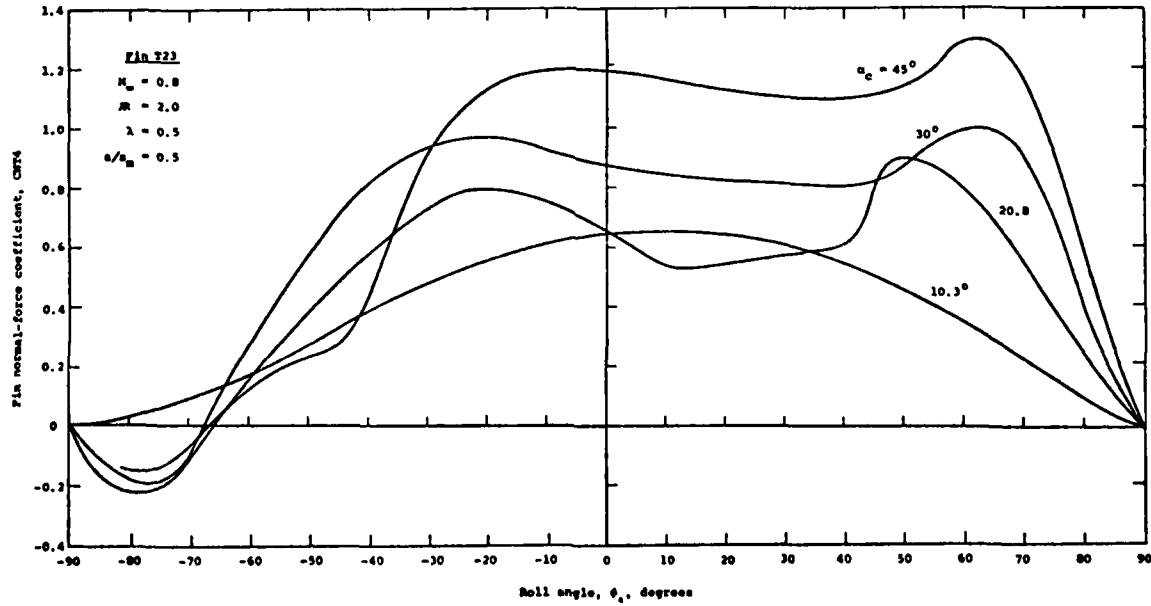


Figure 20. Nonlinear behavior exhibited by fin T23 at $M_\infty = 0.8$ (S_R = fin planform area).

there is a tendency of the flow to expand around the upper surface of a wing by means of a Prandtl-Meyer expansion and thereby to delay stall to high angles of attack.

The same general behavior as manifest for $M_\infty = 3.0$ also occurs at $M_\infty = 2.0$. At $M_\infty = 2.0$ the fins attain high values of CNT4 near $\phi_4 = 30^\circ$ as can be seen in Table 6.

Although the general behavior of the results is regular at $M_\infty = 2.0$ and 3.0 nonlinearities do exist. Adverse wing-body interference occurs at high angles of attack as was shown in section 2.4.1.

The nonlinear behavior of fin normal-force coefficient is most striking at transonic speed. One example is exhibited by data for fin T23 taken at $M_\infty = 0.8$ as shown in figure 20. The behavior of CNT4 at $\alpha_c = 10^\circ$ is quite conventional. At $\alpha_c = 20.8^\circ$ there is a general loss of fin normal force between $\phi_4 = 0$ and 50° - 60° , a region where the effect of sideslip is usually to augment the normal force. The precise reason for the nonlinear behavior is not known. No unusual shifts in lateral center-of-pressure position accompany the "stall" phenomena shown by the windward fins. The fin stall near 50° - 60° is worst for T23 ($AR = 2$) and is practically nonexistent for T31 ($AR = 0.5$). For the $AR = 1$ fins, T11, T14, and T15, there is definite fin stall in the same general range of ϕ , but the stall is not so severe as for T23. These fin stalls with roll are definitely more severe than the mild stall exhibited by the wing-alone normal-force curves for the fins. At $M_\infty = 1.2$ the stall phenomena are much milder.

4.1.2 Nonlinear wing-body interference.- One of the principal features of missile aerodynamics at high angle of attack is the tendency of the wing-body interference to change from favorable at low angles of attack to unfavorable at high angles in so far as the fin normal force is concerned. Figure 5 has

shown how the measure of wing-body interference, K_W , falls from about 1.4 at low angles of attack to about 0.75 at high angles of attack at high Mach numbers.

It is of some interest to see how K_W depends on aspect ratio and taper ratio for a given Mach number. For this reason the values of K_W have been determined approximately for all wings and all Mach numbers for no body vortex interference. These values are given in Table 11.

Let us consider the effects of aspect ratio and taper ratio on K_W first for $M_\infty = 3.0$ where the effects might be expected to be fairly regular. In figure 21(a) the effect of aspect ratio on K_W at $M_\infty = 3.0$ is shown, and in figure 21(b) the effect of taper ratio is shown. At $M_\infty = 3.0$ there appears to be no significant effect of aspect ratio on K_W up to $\alpha_C = 25^\circ$, and about a 10% effect between $AR = 0.5$ and 1.0 at $\alpha_C = 45^\circ$. Between $AR = 1$ and $AR = 2$ there is no significant effect throughout the angle of attack range $0 \leq \alpha \leq 45^\circ$.

Figure 21(b) shows a systematic effect of taper ratio on K_W , rectangular wings having larger values of K_W than delta wings. If decreases in K_W are associated with losses of dynamic pressure due to a detached shock in front of the body, then the trend of figure 21(b) can be explained. The shock losses are greatest for flow in the plane of the body axis and the free-stream velocity vector. For flow coming through the detached shock further from this plane of symmetry, less loss occurs because of shock curvature. The more outboard the flow, the less the loss of dynamic pressure. If λ is increased at constant a/s_m , more of the wing planform will be subject to outboard air. Thus K_W would be expected to increase with increases in λ .

At transonic speeds unusual nonlinearities arise. The same type of data shown in figure 21 for $M_\infty = 3.0$ is shown in figure 22 for $M_\infty = 0.8$. Figure 22(a) shows that K_W is only slightly

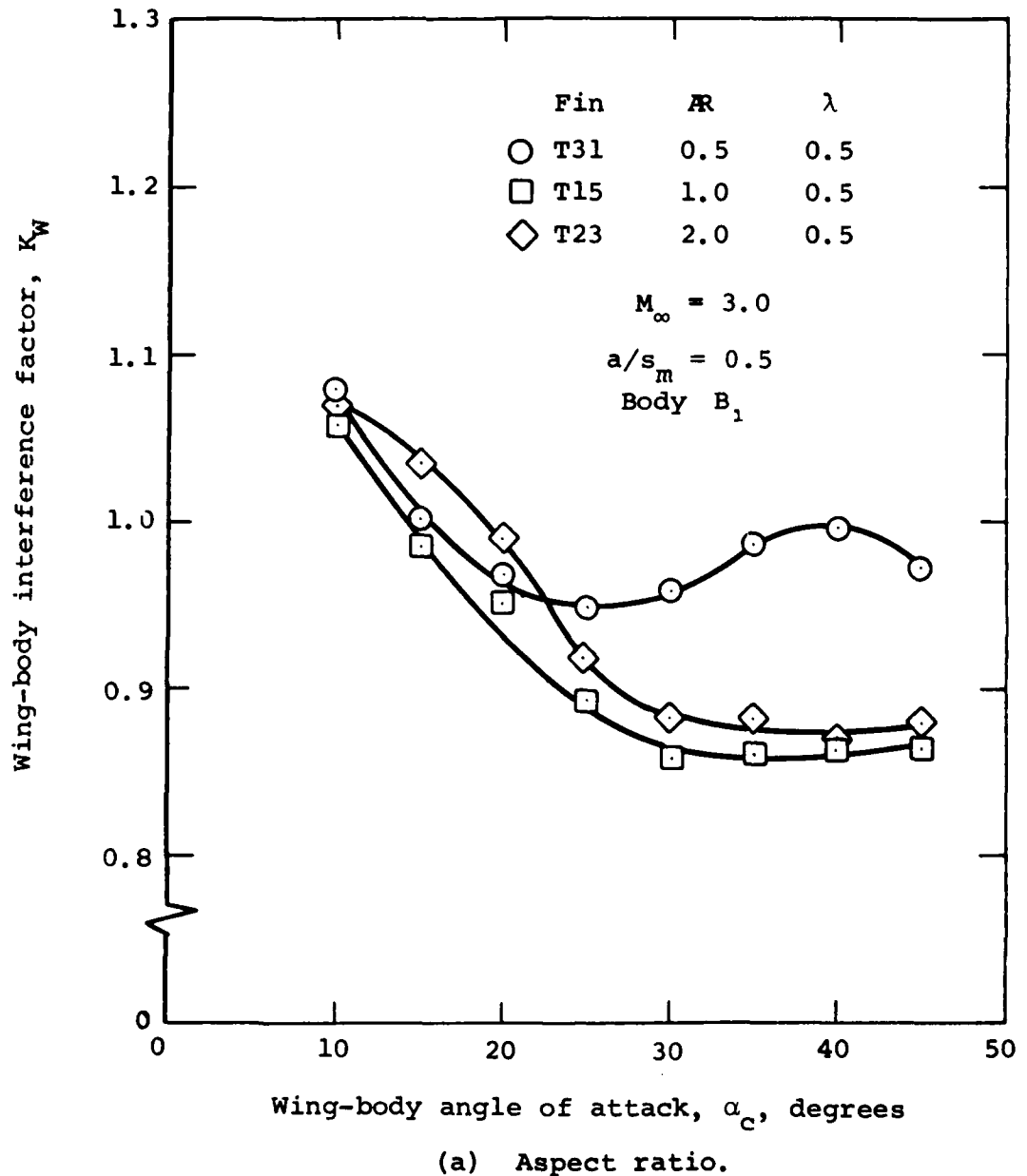


Figure 21. Effects of aspect ratio and taper ratio on K_W at $M_\infty = 3.0$.

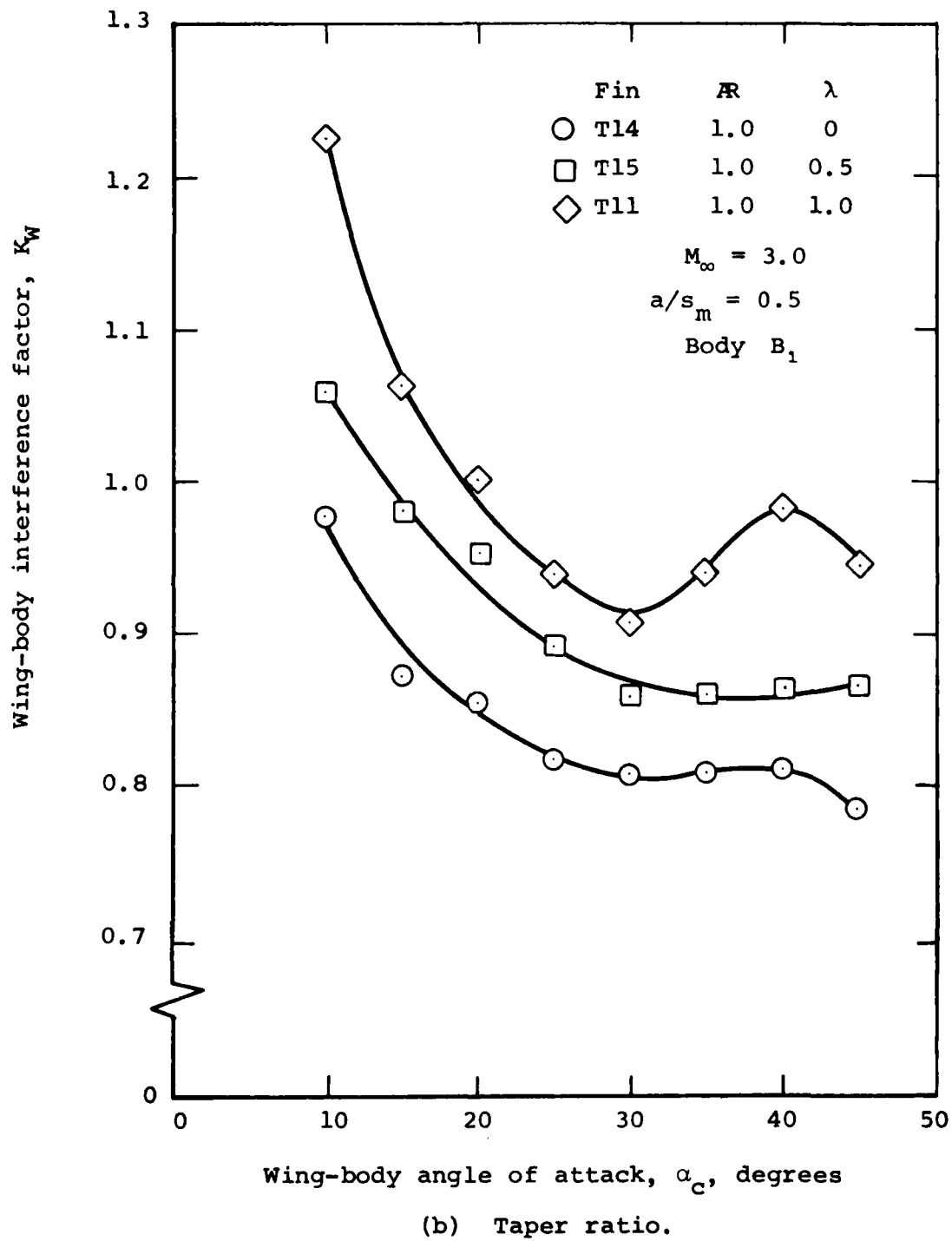


Figure 21. Concluded.

less than its slender-body theory value of 1.45 for α_c up to about 20° for all taper ratios. Thereafter large decreases in K_w occur for all taper ratios. Further increases in α_c result in slight increases in K_w for $\lambda = 0$ and $\lambda = 0.5$, and very large increases for $\lambda = 1.0$.

The same general results exhibited in figure 22(a) for the taper-ratio series of wings is also manifest by the aspect-ratio series of wings in figure 22(b). The sudden reduction in K_w above $\alpha_c = 20^\circ$, particularly for fin T23 in figure 22(b), is noteworthy. The reason for this sudden loss of K_w and its subsequent recovery at higher angles of attack is unknown.

Another interesting phenomenon exhibited by T11, T15, and T23 at $M_\infty = 0.8$ is a tendency at certain angles of attack for the maximum value of CNT for a constant α_c to occur at negative ϕ_4 rather than at positive ϕ_4 , the usual behavior. For fin T15 at $\alpha_c = 25^\circ$ and $M_\infty = 0.8$, Table 6 shows that CNT4 goes from 1.177 at $\phi_4 = -10^\circ$ to 0.763 at $\phi_4 = 10^\circ$ representing what might be called a sudden roll-induced stall. A possible explanation of this result could be an effect noted in reference 6. Here it was conjectured that body vortices passing over a fin might act like strake vortices and cause an otherwise stalled fin to maintain attached flow. We will term this behavior "strake effect." Such behavior has been documented by actual low-speed flow measurements over a wing-body combination in reference 21 by Spangler and Mendenhall. At $\phi = -10^\circ$ the fin might be close enough to the vortex for strake effect to occur, but at $\phi = +10^\circ$ the effect may be lost. Strake effect needs further attention both experimentally and theoretically since its possible effect on rolling moments is large.

4.2 Interpolation and Extrapolation in the Data Base

The values of CNT are given in the data base for specified values of α_c , ϕ , AR , λ , and M_∞ . To interpolate for CNT with respect to α_c or ϕ , a cubic spline procedure is used. The

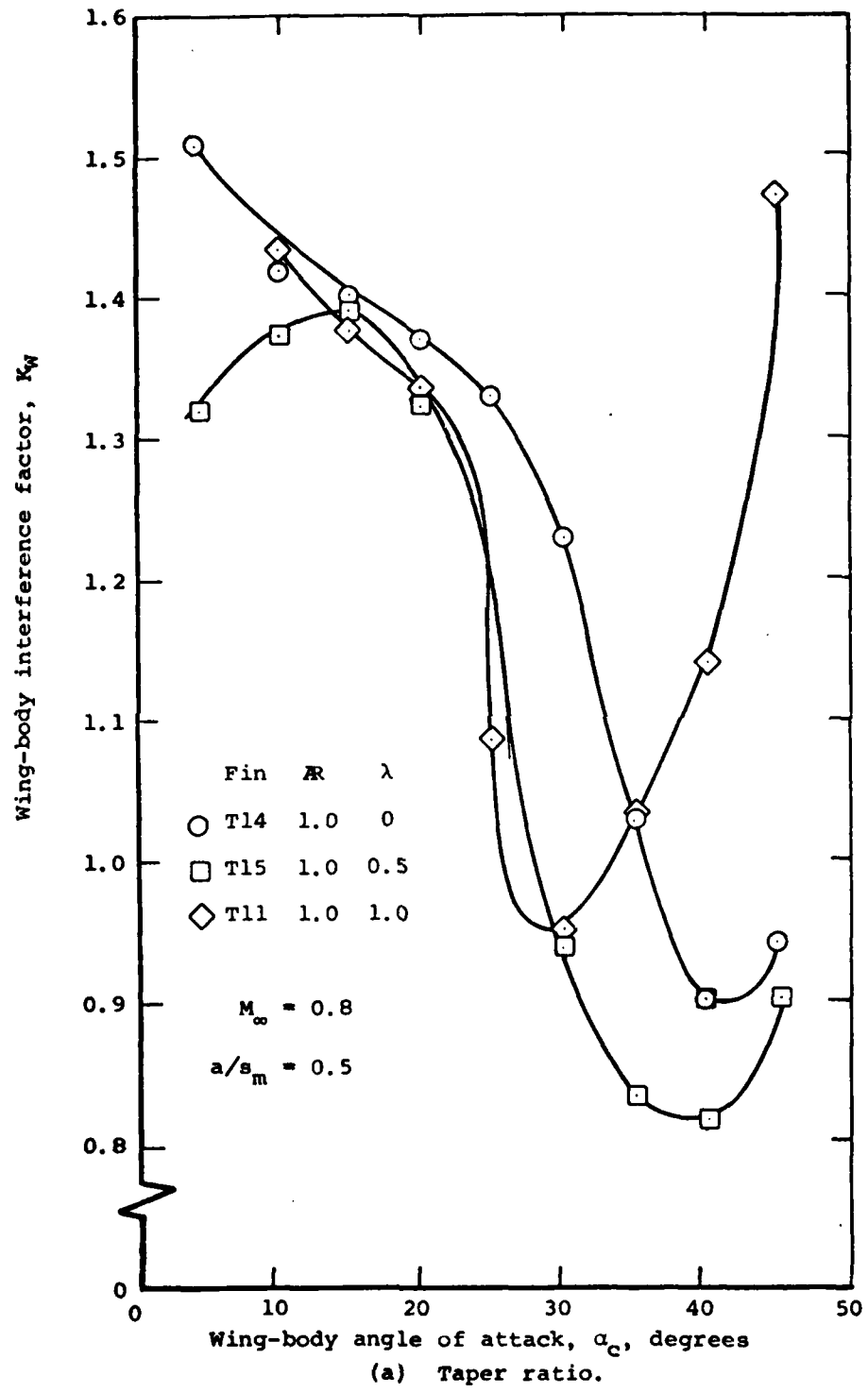
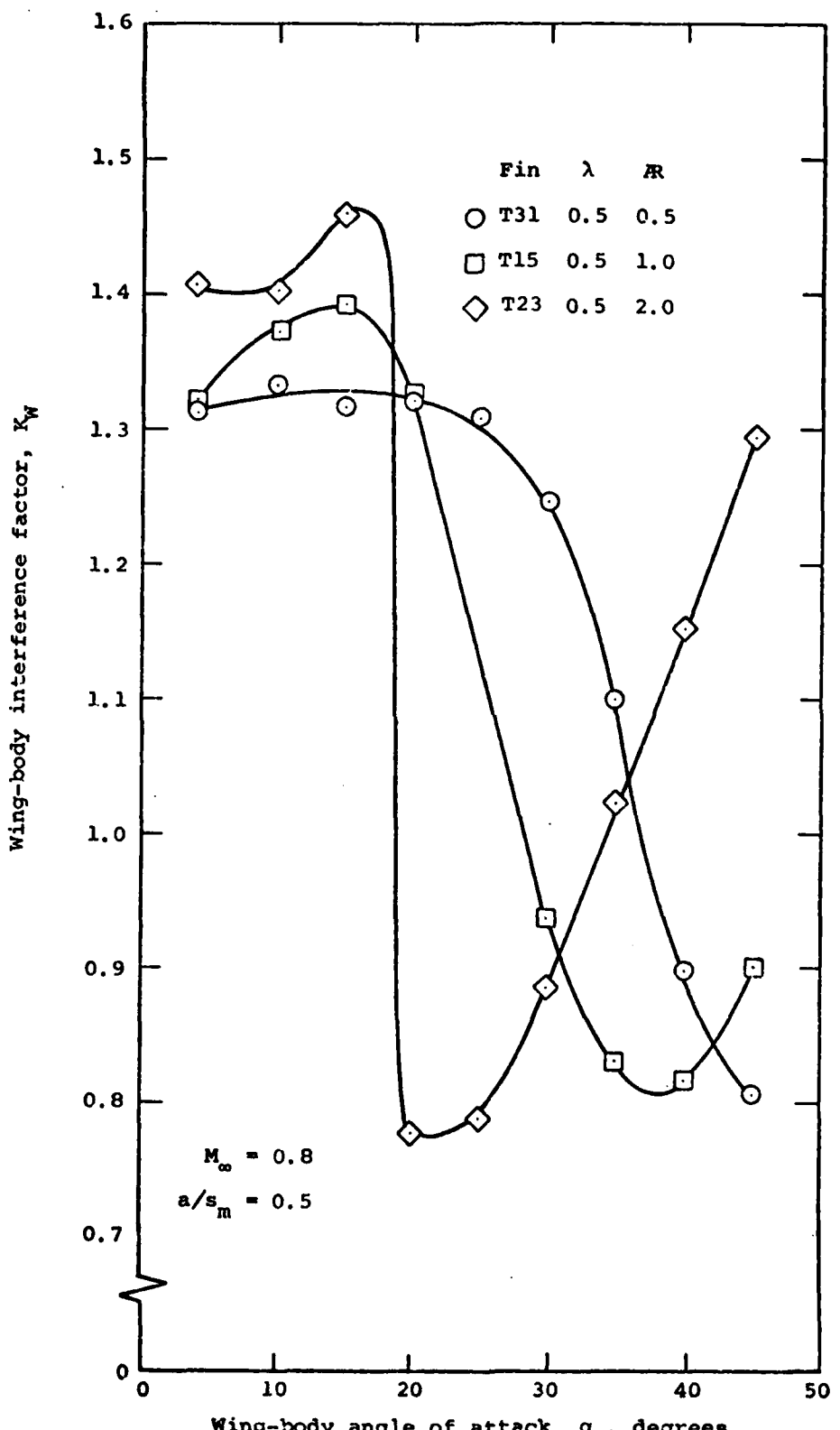


Figure 22. Effect of taper ratio and aspect ratio on K_W at $M_\infty = 0.8$.



(b) Aspect ratio.

Figure 22. Concluded.

procedures used for interpolating or extrapolating with respect to AR , λ , and M_∞ are now described.

4.2.1 Aspect ratio and taper ratio interpolation and extrapolation.- Two assumptions are made concerning aspect ratio and taper ratio.

(1) Taper-ratio effects can be obtained for any aspect ratio between 0.5 and 2.0 by linear interpolation in the data for the fins of aspect ratio 1.

(2) Aspect-ratio effects for taper ratios between 0 and 1 can be obtained by linear interpolation in the data for fins of $\lambda = 0.5$.

We now write down general formulas for the following four regions.

Region I: $0.5 \leq \lambda \leq 1.0 ; 1 \leq \text{AR} \leq 2$

If Q_I is a quantity in this region, it is given by

$$Q_I = T_{15} + 2(\lambda - 0.5)(T_{11} - T_{15}) + (\text{AR} - 1)(T_{23} - T_{15}) \quad (6)$$

Region II: $0 \leq \lambda \leq 0.5 ; 1 \leq \text{AR} \leq 2$

$$Q_{II} = T_{15} - 2(0.5 - \lambda)(T_{15} - T_{14}) + (\text{AR} - 1)(T_{23} - T_{15}) \quad (7)$$

Region III: $0 \leq \lambda \leq 0.5 ; 0.5 \leq \text{AR} \leq 1$

$$Q_{III} = T_{15} - 2(0.5 - \lambda)(T_{15} - T_{14}) - 2(\text{AR} - 0.5)(T_{15} - T_{31}) \quad (8)$$

Region IV: $0.5 \leq \lambda \leq 1.0 ; 0.5 < \text{AR} < 1.0$

$$Q_{IV} = T_{15} + 2(\lambda - 0.5)(T_{11} - T_{15}) - 2(\text{AR} - 0.5)(T_{15} - T_{31}) \quad (9)$$

These formulas are applied to fin normal-force coefficient, fin lateral center-of-pressure parameter, $(\bar{y}_p - a)/(s_m - a)$, and wing-alone normal-force coefficient.

It is clear that if $\lambda = 0.5$ or $AR = 1$, the foregoing formulas become interpolation formulas, and improved accuracy can be expected.

At $M_\infty = 2.0$ and 3.0 we have data for CNT4 for fins T32 and T36. With regard to the sketch shown in section 2.5.1, consider that T32 is found by adding to T31 an increment due to changing λ from 0.5 to 1.0. Then

$$T32 = T31 + (T11 - T15) \quad (10)$$

Likewise

$$T36 = T31 - (T15 - T14) \quad (11)$$

(The same results are obtained if an increment due to aspect ratio is added at constant taper ratio.)

Since we have actual data including vortex effects for T32 and T36, we can test the accuracy of the above formulas in predicting T32 and T36. The error will be

$$E32 = T32 - [T31 + (T11 - T15)] \quad (12)$$

$$E36 = T36 - [T31 - (T15 - T14)] \quad (13)$$

The errors E32 and E36 are given in Table 12 for those angles of attack for which data are available at $M_\infty = 2.0$ and 3.0 . Examining first T36 at $M_\infty = 2$, we find a maximum error in normal-force coefficient of about .13 while at $M_\infty = 3.0$ the error is as large as 0.16. For T32 at $M_\infty = 2.0$ the maximum error is about 0.11 while at $M_\infty = 3.0$ it is about 0.10. This example demonstrates the error magnitudes that can be expected due to extrapolation in aspect ratio or taper ratio within the region $0.5 \leq AR \leq 2.0$, $0 \leq \lambda \leq 1.0$. The closer the fin is to one of the data base, the more accurate the extrapolation. We have no data at $M_\infty = 0.8$ or 1.2 to check the accuracy of the extrapolation

for AR and λ . It is clear that filling out the data base with real data would be desirable.

4.2.2 Mach number interpolation or extrapolation.- In the systematic data base, data are available for $M_\infty = 0.8, 1.2, 2.0$ and 3.0 . Data at intermediate Mach numbers are available, but have not been put into the data base because of the scope of work involved. Since only a few Mach numbers are represented, linear interpolation is used. Thus if a quantity at Mach number M_∞ is designated Q_∞ , and if M_∞ lies between M_1 and M_2 in the data base

$$Q_\infty = Q_1 + \frac{(M_\infty - M_1)}{(M_2 - M_1)} (Q_2 - Q_1) \quad (14)$$

We do not advocate downward extrapolation in M_∞ below 0.8 , but some upward extrapolation above $M_\infty = 3.0$ is permissible as will subsequently be shown. If $M_\infty > 3$ and ΔQ is the difference in the quantity between $M_\infty = 3.0$ and $M_\infty = 2.0$, then

$$Q_M = Q_{M_\infty=3} + \Delta Q (M_\infty - 3) ; M_\infty > 3 \quad (15)$$

A special case of interpolation exists in the range $0.8 < M_\infty < 1.3$ for $2 < \text{AR} < 3.53$. In this case the systematic data base should be used to obtain the information at $\text{AR} = 2$, and the C6 fin results used for $\text{AR} = 3.53$ (neglecting λ effects). However, before performing aspect-ratio interpolation in this case, the results should preferably all be corrected to the desired a/s_m value in accordance with the method described in section 4.3. Then a linear interpolation in aspect ratio should be made. If $\text{AR} > 2$ and $M_\infty > 1.3$, extrapolation is precluded in the data base.

4.3 Use of the Equivalent Angle of Attack Concept

4.3.1 Scaling for a/s_m .- The systematic data base is all for $a/s_m = 0.5$, while the $\text{AR} = 3.53$ results are for $a/s_m = 0.4$. It is important to be able to apply these results to other values

of a/s_m . To do this we use the "vortex-free" data base, and assume that the control deflection angle is zero. Then the equivalent angle of attack is given (for fin F4) by equation (C-8) of Appendix C as

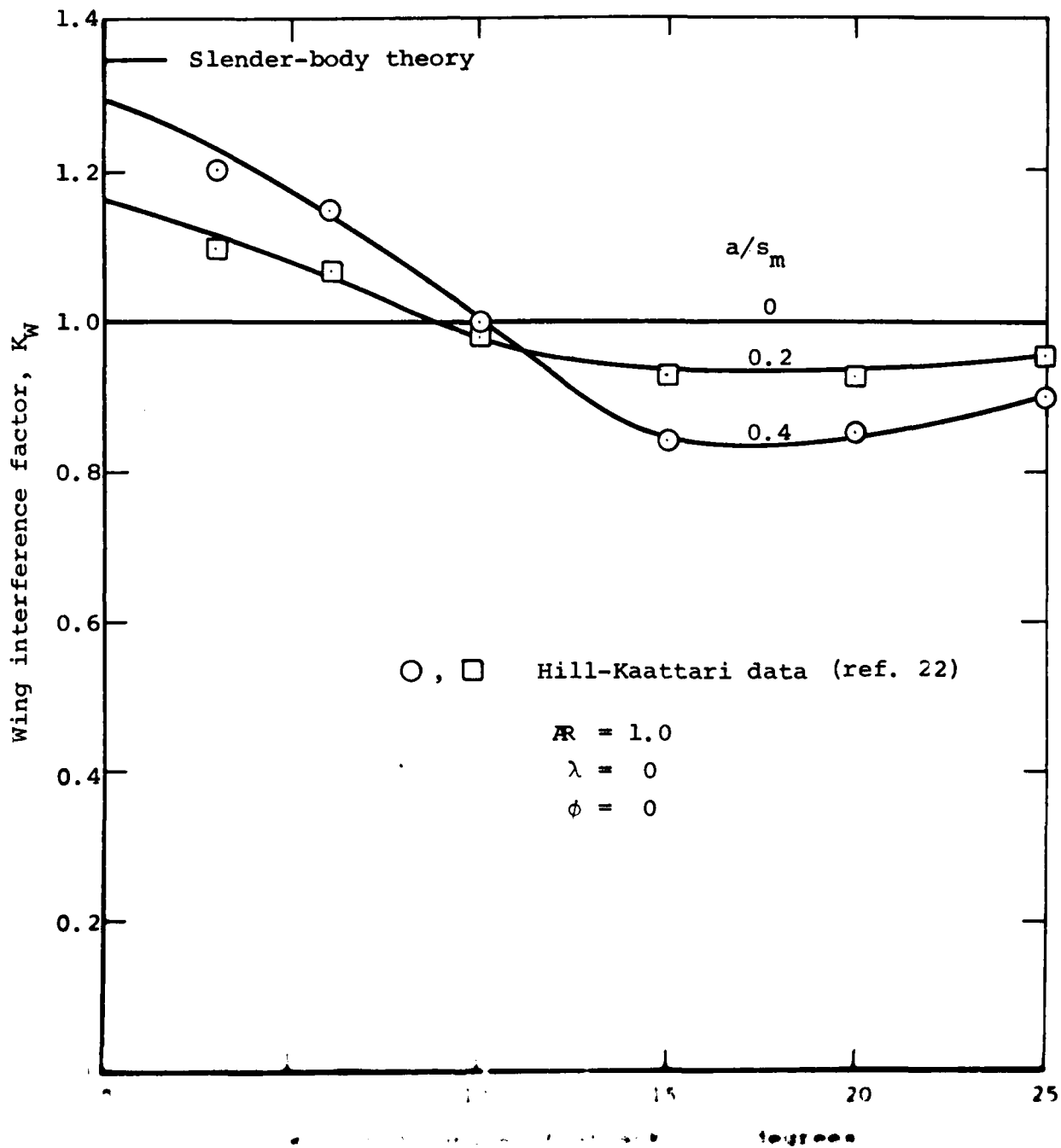
$$\tan(\alpha_{eq}) = \tan \alpha_c \cos \phi [K_w + \frac{4}{AR} K_\phi \sin \alpha_c \sin \phi] \quad (16)$$

If we change a/s_m at a fixed value of α_c and ϕ , α_{eq} can change through variations of K_w or K_ϕ with a/s_m . The dominant term in the equation is that due to K_w . The values of K_w for $a/s_m = 0.5$ are obtained as described in section 4.1.2.

By definition K_w is unity at $a/s_m = 0$. For intermediate values of a/s_m linear interpolation is used to determine K_w . Few high angle-of-attack data exist to verify this procedure since most data are for $a/s_m = 0.5$. (This case points out another gap in the data base). However, Hill and Kaattari (ref. 22) provide some data for a semispan wing-body combination mounted on a splitter plate for verification of the rule. While the data are taken at $M_\infty = 3.36$ on a splitter plate, the fin is well off the plate and is relatively free of plate boundary-layer effects. The authors show this by comparing full-span and semi-span results.

Data exists at values of $a/s_m = 0.2$ and 0.4 for a fin of $\phi = 1^\circ$ and $\alpha \approx 0$ at $M_\infty = 3.36$ in the Hill-Kaattari reference. Data for K_w for these two values of a/s_m have been obtained from figures 4 and 6 of that reference.

The data show that K_w increases



The second factor in the foregoing equation, K_ϕ , depends weakly on a/s_m according to slender-body theory, varying over the range 0.382 to 0.508 as a/s_m changes from 0 to 0.5. Remembering that the K_ϕ term is of higher order than the K_W term, we therefore neglect the change of K_ϕ with a/s_m . We have chosen not to include the slender-body dependence of K_ϕ on a/s_m in the method for several reasons. Firstly, the changes in K_ϕ are not large. Secondly, K_ϕ as determined experimentally contains all nonlinear phenomena of the data base with roll angle. It is thought best to preserve these nonlinear phenomena as measured rather than try to adjust them for the small K_ϕ dependence on a/s_m given by slender-body theory.

With the assumption that K_W is linear in a/s_m and that K_ϕ is independent of a/s_m , we can now determine the equivalent angle of attack for a value of a/s_m different from 0.5. If $(\alpha_{eq})_{0.5}$ is the value of the equivalent angle of attack at $a/s_m = 0.5$ and $(\alpha_{eq})_{a/s_m}$ is that at any value of a/s_m , the preceding equation now yields the following results:

$$\tan (\alpha_{eq})_{0.5} = \tan \alpha_c \cos \phi [K_{W0.5} + \frac{4}{AR} K_\phi \sin \alpha_c \sin \phi] \quad (17)$$

$$\begin{aligned} \tan (\alpha_{eq})_{a/s_m} = & \tan \alpha_c \cos \phi [1 + 2(a/s_m)(K_{W0.5} - 1) \\ & + \frac{4}{AR} K_\phi \sin \alpha_c \sin \phi] \end{aligned} \quad (18)$$

Thus we have

$$\tan (\alpha_{eq})_{a/s_m} = \tan (\alpha_{eq})_{0.5} - \tan \alpha_c \cos \phi (1 - 2a/s_m)(K_{W0.5} - 1) \quad (19)$$

From this equation $(\alpha_{eq})_{a/s_m}$ for the new value of a/s_m is obtained, and from this quantity the corresponding fin normal-force coefficient is obtained from the wing-alone normal-force curve.

It is assumed that the lateral center-of-pressure parameter in the form $(\bar{y}_p - a)/(s_m - a)$ does not vary with a/s_m . According to slender-body theory, this parameter varies between 0.530 and 0.567 when a/s_m varies between 0 and 0.5.

4.3.2 Scaling for vortex effects.— Consider first body vortices which influence canard fins or which influence tail fins if no canard fins are present. The strength of these vortices depends on the length of the forebody as well as its diameter. The normal-force coefficient induced on the fins depends in addition on the vortex positions with respect to the fins. The effect of these geometric parameters on the fin normal force induced by the vortices scale in a different manner than the fraction of the fin normal force which is independent of the vortex effects. The scaling for the vortex-induced effects is done in two steps. First, the body vortex strength and position are found from the vortex model described in section 5. Then using the reverse-flow methods derived in Appendix B, the average induced angle of attack on the fin due to the vortices present, $(\Delta\alpha_{eq})_v$, is calculated by equation (B-31). At the same time the lateral center-of-pressure position parameter $(\bar{y}_v - a)/(s_m - a)$ due to vortex loading is determined.

The equivalent angle of attack method now yields the fin normal-force coefficient increment due to the vortex. If the fin is operating at $(CNT)_p$ and $\alpha_{eq,p}$ without vortex effects, the value of $\alpha_{eq,0}$ including vortex effects (but no fin deflection effects) is obtained from equation (5).

$$\tan \alpha_{eq,0} = \tan \alpha_{eq,p} + \tan (\Delta\alpha_{eq})_v \quad (20)$$

We can now find the total fin normal force by looking up the fin CN in the wing-alone table, Tables 2 or 3, corresponding to $\alpha_{eq,0}$.

Since the increments in normal force $(CNT)_p$ and $(CNT)_v$ are known together with their center-of-pressure parameters, the center-of-pressure parameter for their combined effects is given by

$$\frac{(\bar{y}-a)}{s_m-a} = \frac{(C_{NT})_p \left(\frac{\bar{y}_p-a}{s_m-a} \right) + (C_{NT})_v \left(\frac{\bar{y}_v-a}{s_m-a} \right)}{(C_{NT})} \quad (21)$$

While the foregoing results have been introduced for the effects of body vortices, the discussion is general. For an empennage fin under the influence of canard and afterbody vortices, the same formulas are used and the effects are superimposed.

4.3.3 Effects of control deflection. - Effects of control deflection are also handled by use of the equivalent angle of attack concept. If at some values of α_c and ϕ , the fin operates at $\alpha_{eq,0}$ at $\delta = 0$, it would operate at $\alpha_{eq,0} + \delta$ at control deflection δ if no losses in normal force occurred as compared to the wing-alone. The factor k_w has been introduced to account for any losses in accordance with the following definition.

$$k_w = \frac{\tan (\alpha_{eq,\delta}) - \tan (\alpha_{eq,0})}{\tan (\alpha_{eq,0} + \delta) - \tan (\alpha_{eq,0})} \quad (22)$$

where

$\alpha_{eq,\delta}$ = equivalent angle of attack with fin at deflection δ .

This definition yields $k_w = 0$ if no normal force results from control deflection. It also yields $k_w = 1.0$ for a "perfect" control, one which produces the normal force it would produce as part of the wing alone. Rewriting the foregoing equation, we obtain for the equivalent angle of attack with control deflection,

$$\tan (\alpha_{eq,\delta}) = \tan (\alpha_{eq,0}) + k_w [\tan (\alpha_{eq,0} + \delta) - \tan (\alpha_{eq,0})] \quad (23)$$

In the use of this result, rules must be given for determining the values of k_w . In our previous work, reference 6, we used the slender-body values of k_w which depend on a/s_m and vary between 0.935 and 1.00. These were used to help in construction

of equivalent angle of attack curves (figure 4, ref. 20), and any inaccuracies in k_w were partially compensated for in the correlation. For angles greater than 20° , good correlation is not usually obtained unless changes in k_w with other parameters are taken into consideration. We thus need some basis for selecting the values of k_w for use in the method.

The actual data available for k_w at large angle of attack and control deflection are not extensive. Among the systematic data available for this purpose, we have the pitch-control data of Hill and Kaattari (ref. 22) at $M_\infty = 3.36$ and the control data on pitch and yaw and pitch-yaw coupling at $M_\infty = 0.8$ and 1.3 given in reference 4 and 7. We now examine values of k_w determined from these data to arrive at a set of rules for determining k_w .

4.3.3.1 Pitch effectiveness at high Mach numbers.— Data on pitch-control effectiveness (ref. 22) have been obtained on a semispan model of a wing-body combination mounted on a splitter-plate and tested at $M_\infty = 3.36$. It is of interest to examine the values of k_w resulting from those tests as presented in figure 24 for a delta wing aspect ratio 1.0. Data for angles of attack to 25° and control deflection up to 40° are shown for $a/s_m = 0.2$ and $a/s_m = 0.4$. While the values of k_w lie somewhat below the slender-body value, the use of the slender-body value is a fair approximation even at high angles of attack and control deflection. There are no large effects of control deflection on the values of k_w .

We have no data for the variation of k_w with roll angle at high angle of attack and high supersonic Mach numbers. It seems quite possible that at $\phi_4 = -90^\circ$ k_w will be less than at $\phi_4 = +90^\circ$, and that a rolling moment will develop as a result of yaw deflection at $\phi = 0$. This is an effect which should be accounted for in the predictive method when proper data or theory to evaluate this effect are available.

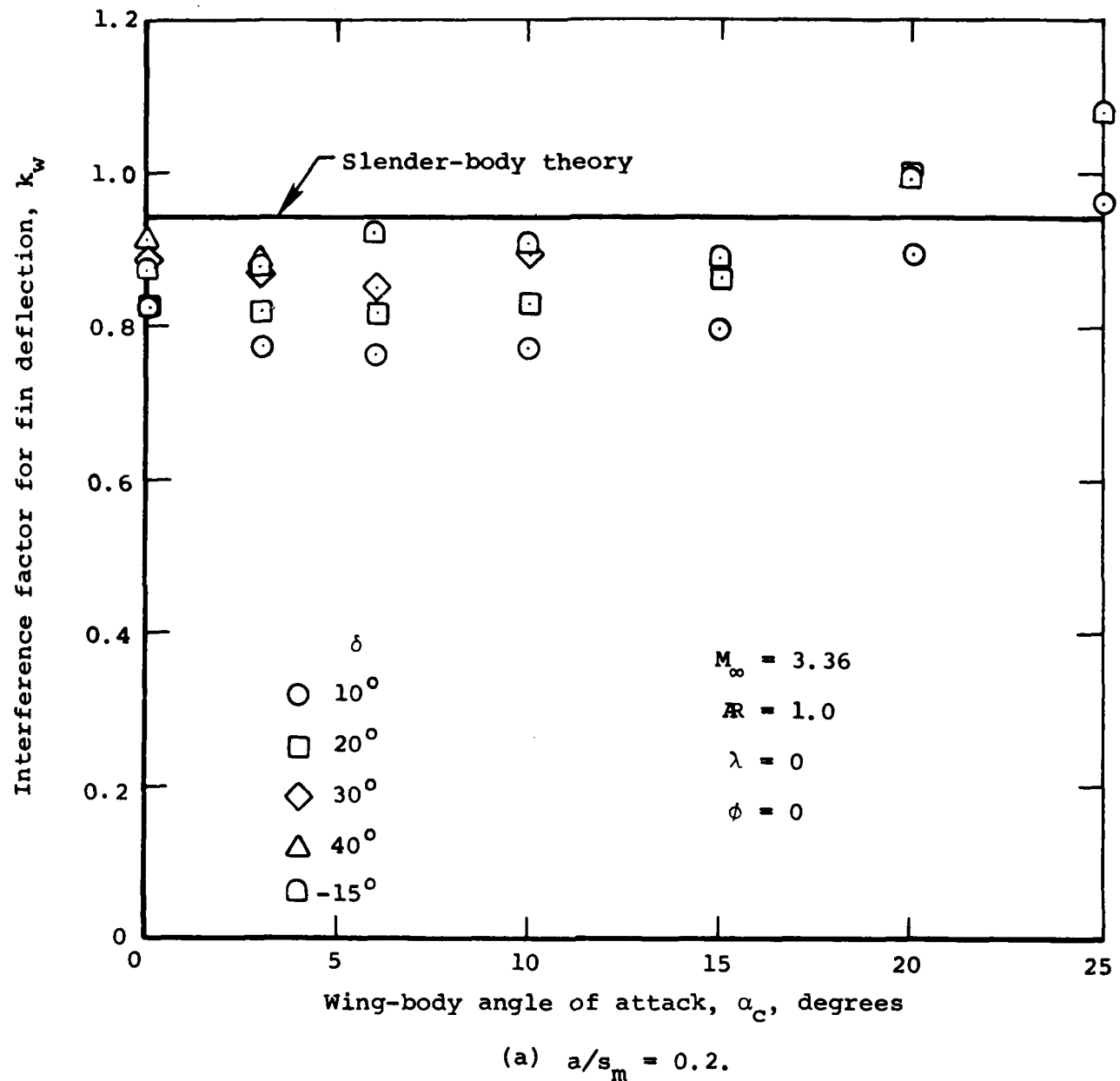


Figure 24. Effect of angle of attack and control deflection on interference factor for control deflection.

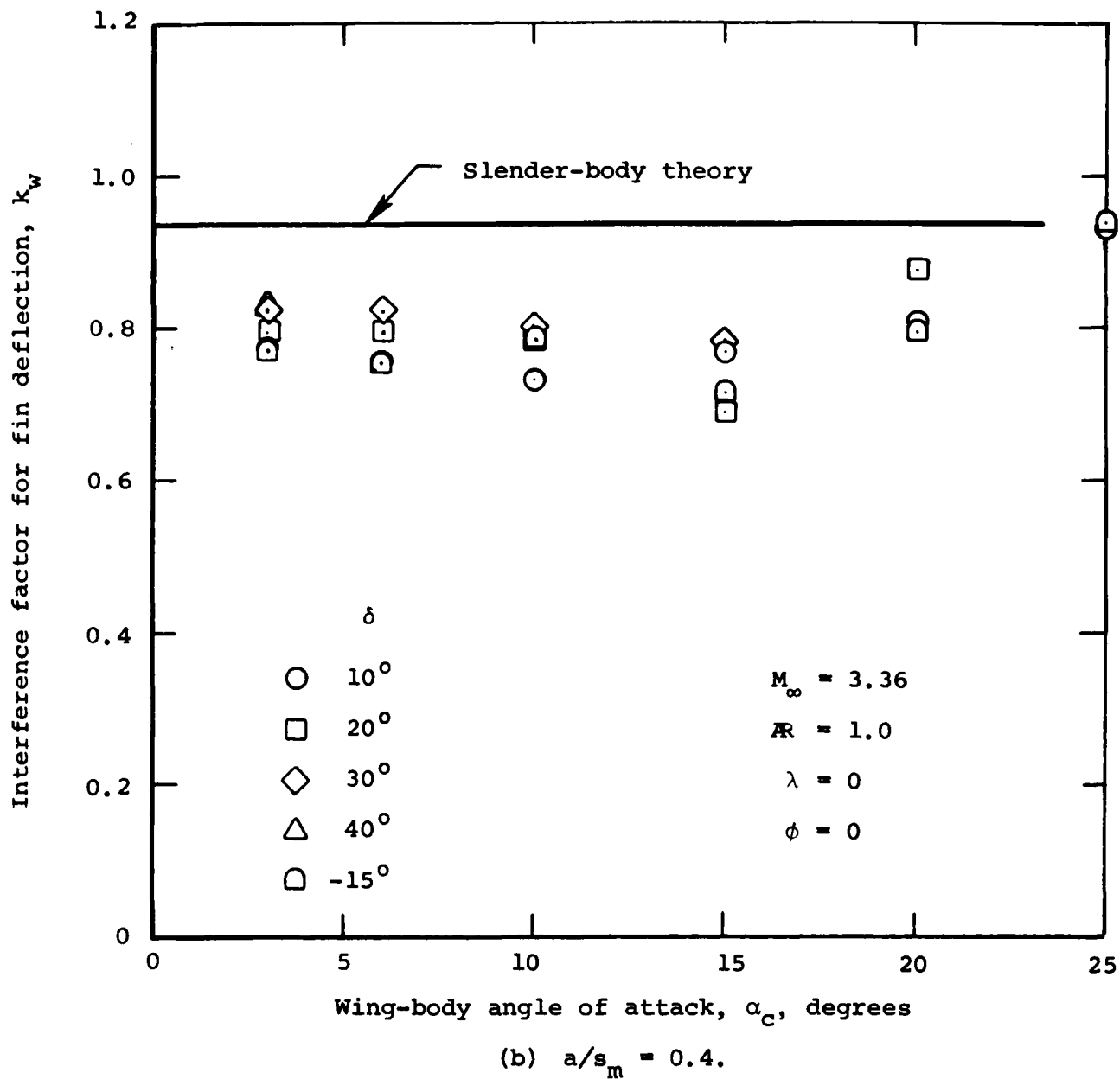


Figure 24. Concluded.

4.3.3.2 Control effectiveness at $M_\infty = 0.8$ and 1.3 . - At $M_\infty = 0.8$ and 1.3 , control effectiveness is not so good as at $M_\infty = 3.0$. Systematic control data were taken in connection with the wind-tunnel tests of the Army generalized missile in the 6- by 6-Foot Wind Tunnel (ref. 4) and the 11-Foot Transonic Wind Tunnel (ref. 7) of the Ames Research Center. These systematic data included measurements to show how k_w varies with δ at $\phi = 0$, and how k_w varies with ϕ for a fixed δ of 15° .

Figure 25 presents the values of k_w for $AR = 3.53$ C6 fins on an $a/s_m = 0.4$ body at $M_\infty = 0.8$ and 1.3 for $\delta_{2,4} = 5^\circ$, 10° , and 15° (pitch control). Examining first the $M_\infty = 0.8$ results, we see that the slender-body value of k_w is a fair approximation to results up to $\alpha_c = 20^\circ$, but thereafter k_w falls to 0 at $\alpha_c = 50^\circ$. While there is some scatter with δ , a mean curve represents the nonlinear behavior fairly well. Generally the results for $\delta_{2,4} = 15^\circ$ show the smallest values of k_w .

The behavior of the k_w results in figure 27(b) for $M_\infty = 1.3$ show a different variation with α_c than those for $M_\infty = 0.8$. The peak in the mean results near $\alpha_c = 40^\circ$ is noteworthy. We do not know the reason for the peak. Again there is some scatter due to $\delta_{2,4}$, but the mean curve gives a fair representation of the results. Near $\alpha_c = 40^\circ$, there is large effect of $\delta_{2,4}$. The values of k_w are not nearly zero at $\alpha_c = 50^\circ$ for this Mach number as they are for $M_\infty = 0.8$.

Some idea of the precision of the experimental values of k_w can be obtained since k_w was determined for different fins for the same values of ϕ_4 . For $\phi = 45^\circ$, fins T3 and T4 are mirror images as well as fins T1 and T2, and they should produce closely the same results for k_w . Figure 26 compares results for those two conditions of mirror symmetry. At $\phi_4 = 45^\circ$ figure 26(a) shows results for fins T3 and T4 which are generally within $\pm .05$ in k_w from the mean line. For $\phi_4 = -45^\circ$ fins T1 and T2 show about the

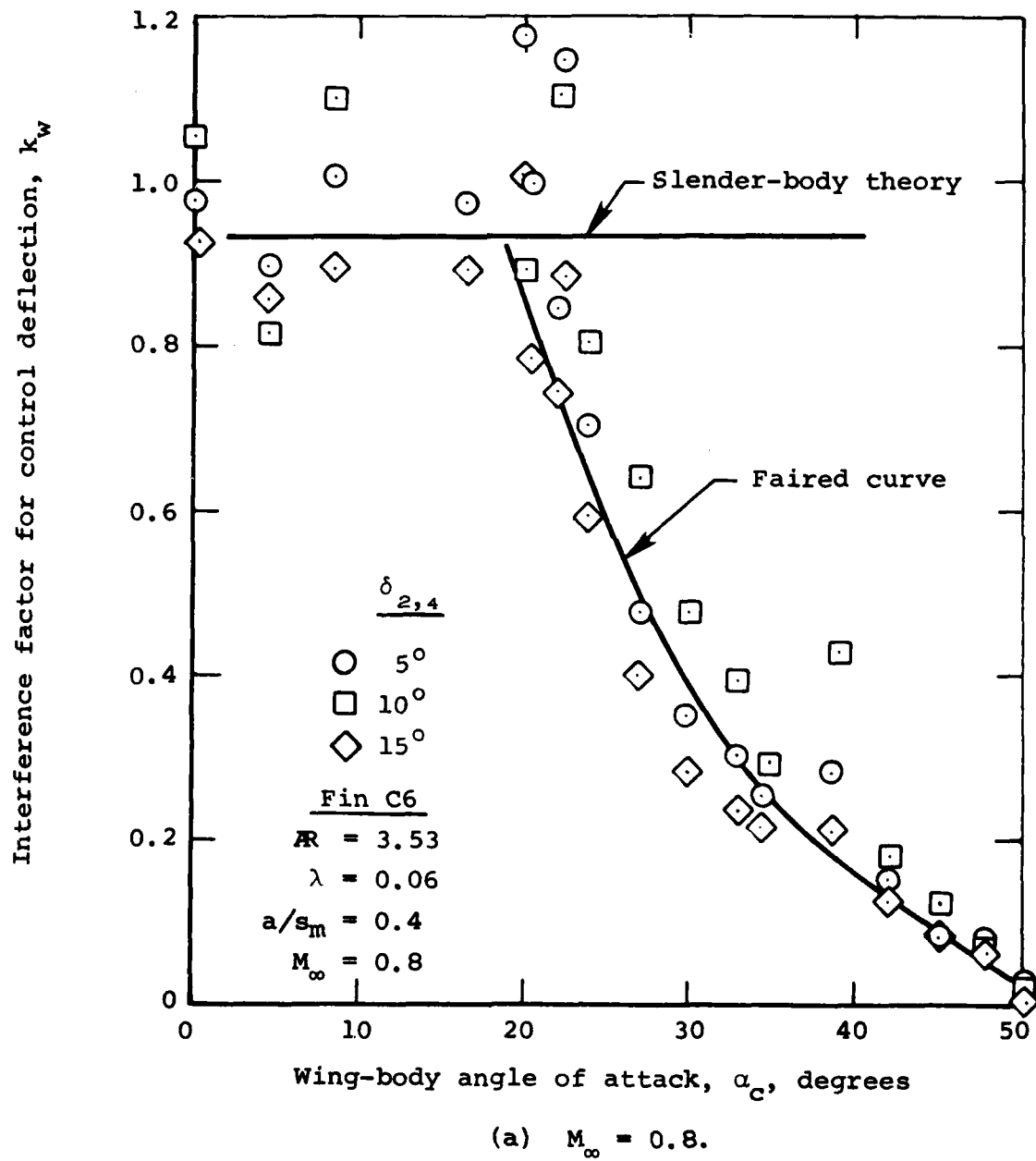


Figure 25. Effect of angle of attack and control deflection on pitch control effectiveness of canard fins at $\phi = 0$.

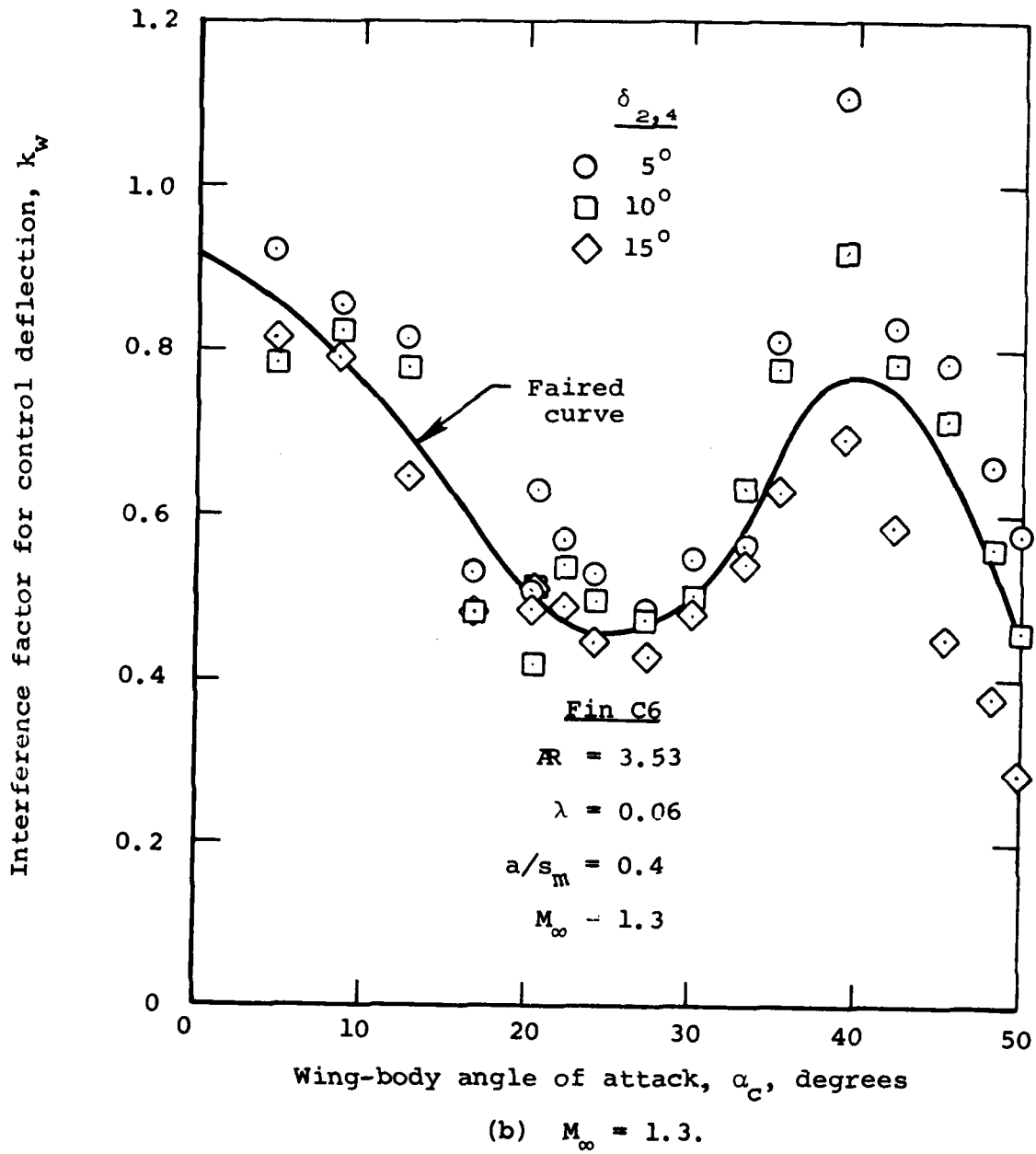


Figure 25. Concluded.

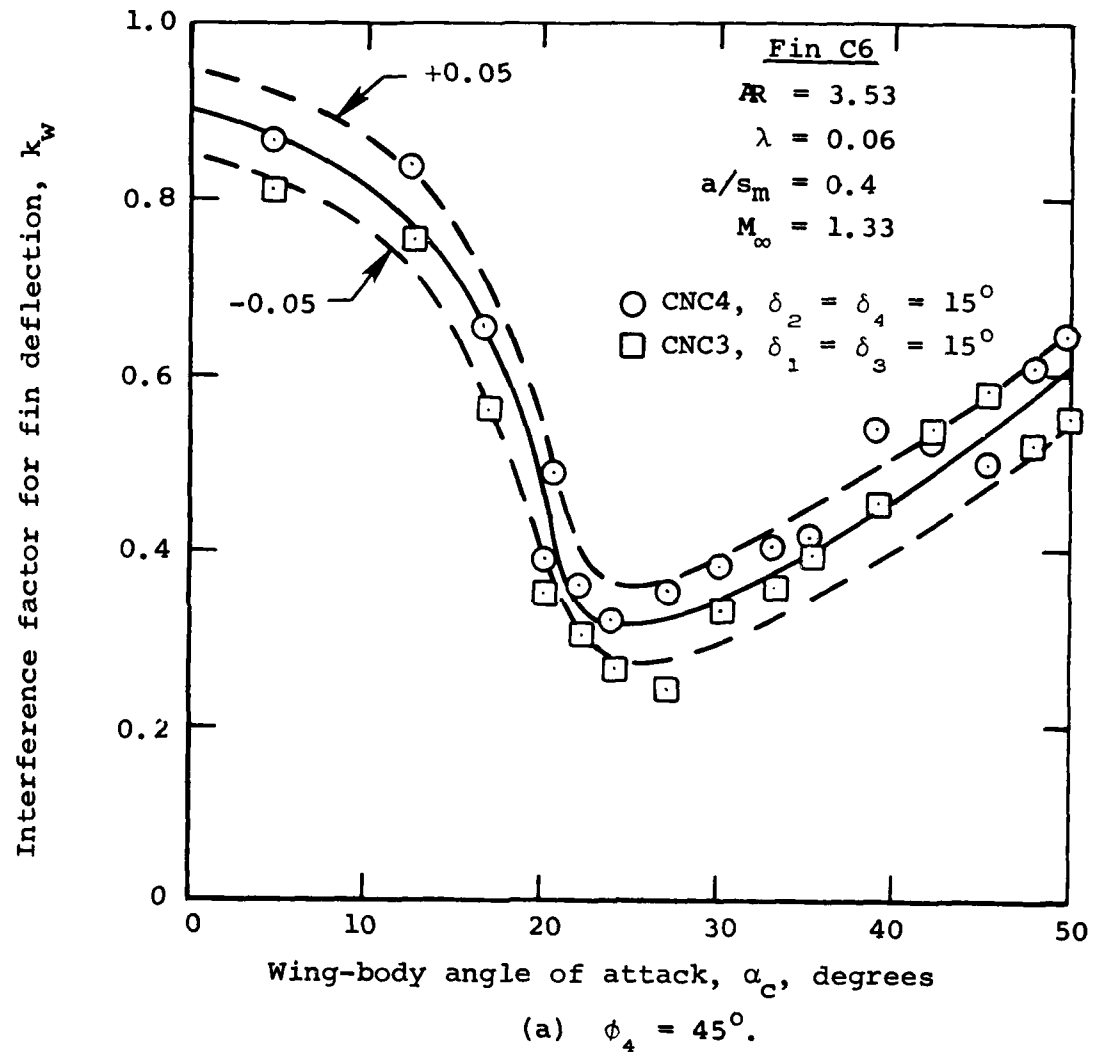


Figure 26. Effect of angle of attack on k_w for canard fin on Army generalized missile (ref. 7).

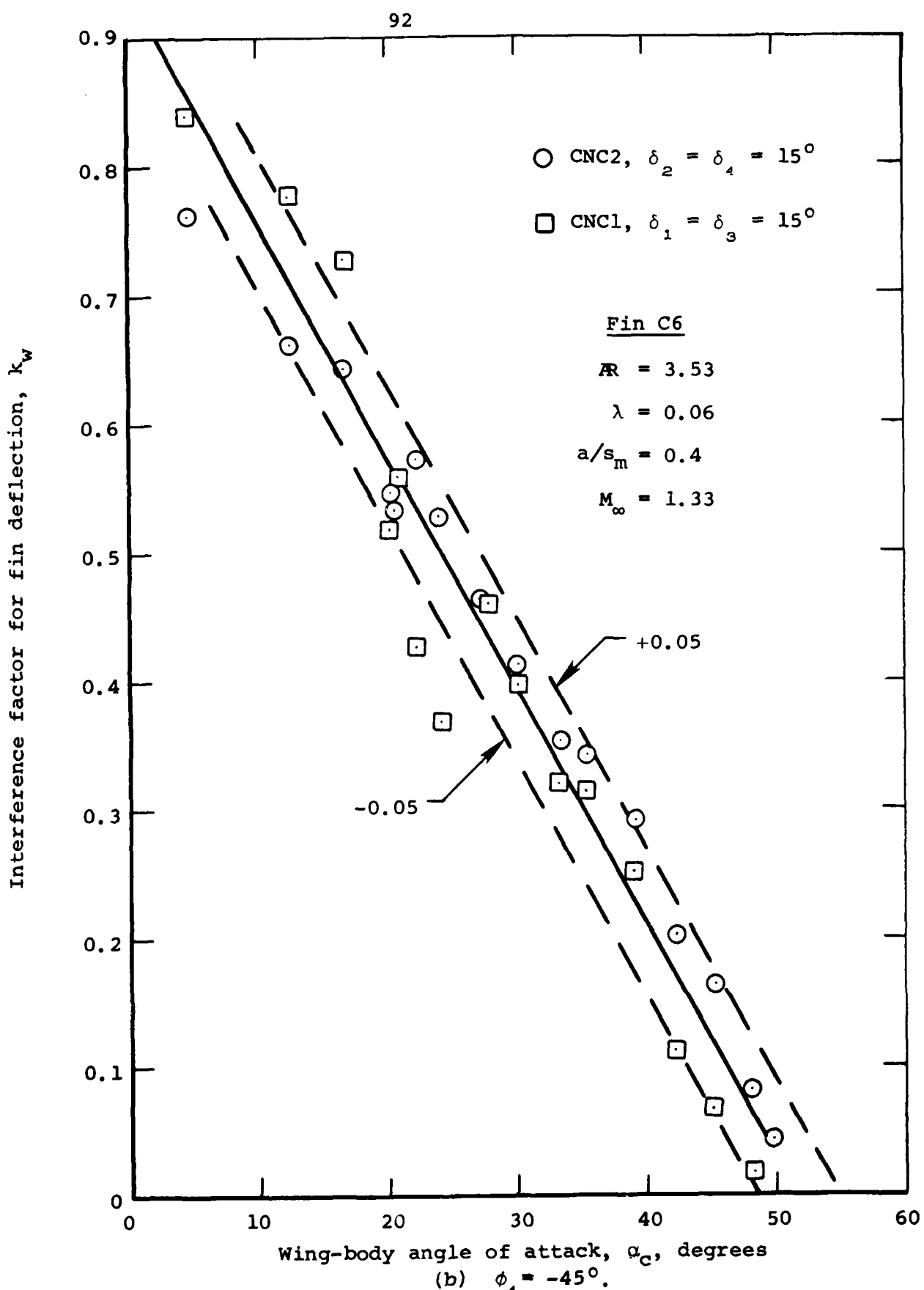


Figure 26. Concluded.

same precision. However, now the value of k_w approaches zero at $\alpha_c = 50^\circ$. We thus have an effect of ϕ_4 on k_w .

The variation of k_w with ϕ_4 demonstrates a number of nonlinearities. Figure 27(a) shows the variation of k_w with ϕ_4 at $\alpha_c = 0^\circ, 15^\circ, 25^\circ, 35^\circ$, and 45° for the fin C6 of $AR = 3.53$ at $M_\infty = 1.3$ and $\delta_{2,4} = 15^\circ$. Consider first the results for $\alpha_c = 0$. If the wind-tunnel flow were perfectly parallel and the wind-tunnel model were perfectly symmetrical about its plane of symmetry, then k_w for $\alpha_c = 0$ should be constant. The small variation in k_w with ϕ_4 at $\alpha_c = 0$ is a measure of the precision of the results as discussed above. Note that for negative ϕ_4 there is a systematic decrease in k_w as α_c increases. The reader should recall that without vortices a decrease might be expected because of increased sweep angle of the fin with decreasing ϕ_4 and possibly decreased dynamic pressure. No particular effect of the body vortices is obvious. However, some surprising nonlinear effects for positive ϕ_4 are clearly present.

For $\alpha_c = 15^\circ$, k_w increases as ϕ_4 increases from zero. This increase might be expected because of reduced sweep of the fin leading edge accompanying pitch of the wing-body combination and possible increased dynamic pressure on the impact surface. However, some phenomenon is causing k_w to peak somewhere around $\phi = 10^\circ$ for $\alpha_c = 25^\circ, 35^\circ$, and 45° . We do not know the exact reason for this behavior.

Consider now the behavior of k_w with changes in α_c and ϕ_4 for $M_\infty = 0.8$ as exhibited by figure 27(b). For $-45^\circ \leq \phi_4 \leq 45^\circ$ there is a general monotonic decrease in k_w with increases in α_c . For $\phi_4 > 45^\circ$ there is a tendency for k_w to peak at values greater than unity for values of ϕ_4 near 70° . This behavior does not signal a large increase in control normal force since the control is operating in the stalled region of the wing-alone normal-force curve in this case. A numerical example for $\alpha_c = 34.8^\circ$ and

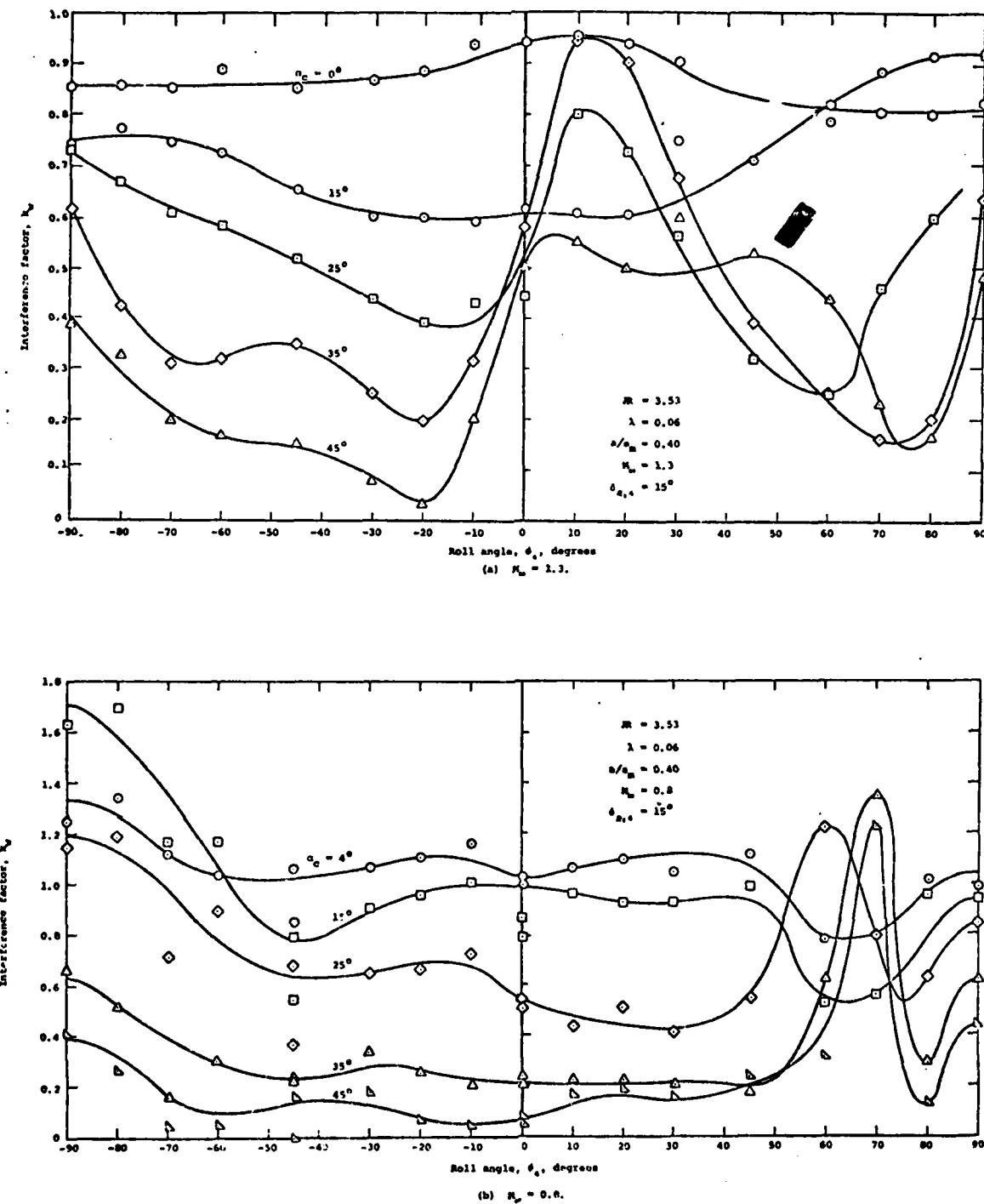


Figure 27. Effect of α_c and ϕ_4 on k_w for canard fins C6 on Army generalized missile.

$\phi_4 = 70^\circ$ shows the fin to be operating at an equivalent angle of attack of 13.4° for $\delta_4 = 0$ and at 33.6° for $\delta_4 = 15^\circ$. The change in normal-force coefficient is .066 due to control deflection. If the wing-alone went from 13.4° to 28.4° , it would achieve a change in normal-force coefficient of about .040 indicating severe stall. (At 15° angle of attack the wing-alone coefficient is about 0.315.) It is seen that the wing-alone stall is thus duplicated by the fin at $\phi_4 = 70^\circ$, although not so severely as for the wing-alone. The difference in sideslip angle between fin and wing may cause the slight difference in stall.

For $\phi_4 < -45^\circ$ there is a tendency for k_w to be greater than unity for angle of attack up to 25° . The effect is not associated with body vortices since it occurs at $\alpha_c = 4^\circ$ and 10° .

4.3.3.3 Rules of determination of k_w . On the basis of the preceding information, we will now present an approximate engineering method for predicting the effect of control deflection. Values of k_w for $M_\infty = 0.8$ and 1.3 have been determined for a matrix of values of α_c and ϕ as described above. These values are presented in Table 13. Panel-panel interference between opposing fins is small for the tabulated results. Symmetrical deflection of opposing fins was used to obtain k_w so that panel-panel interference effects of the other set of undeflected fins was minimized. The tabulated values of Table 13 can thus be considered the values of k_w for $\delta_4 = 15^\circ$, $\delta_1 = \delta_2 = \delta_3 = 0^\circ$. We also use these values for $\delta_4 < 15^\circ$ since this is conservative for the cases we have seen.

We do not have systematic data to determine k_w as a function of fin aspect ratio and taper ratio. Thus we will use these tabulated values of k_w for $M_\infty = 0.8$ and 1.3 for all the fins.

For high supersonic Mach numbers, we have seen (figure 24) that the slender-body values of k_w are reasonably good approximations to the experimental values of k_w for angles of attack

up to 25° . In the intermediate range between $M_\infty = 1.3$ and $M_\infty = 3.36$ we have no good data to determine k_w . The only guides we have are experimental values of K_W from the systematic data base. The precise factors which reduce K_W for large angles of attack are not clear, but reduced dynamic pressure appear to be an important one. Reduced dynamic pressure should also act to reduce k_w . Accordingly the following rule of thumb is used to obtain approximate values of k_w for $M_\infty > 1.3$.

$$\text{If } K_W > (k_w)_{\text{SBT}} \quad k_w = (k_w)_{\text{SBT}} \quad (24)$$

$$\text{If } K_W < (k_w)_{\text{SBT}} \quad k_w = K_W$$

This rule is believed to be conservative at $\phi = 0$. No variation of k_w with ϕ_4 is used since we do not have suitable data on the subject.

In applying k_w in the method, we obtain the change in equivalent angle of attack of the fin in question using the tangent relationship given at the beginning of section 4.3.3 which was used in extracting the experimental value of k_w . The equivalent angle of attack for the fin in question also induces changes in the equivalent angle of attack of the other fins if they are within its region of influence. For subsonic speeds these equivalent angle of attack changes are found by multiplying the equivalent angle of attack of the wing in question by the slender-body panel-panel interference factors of Table 1. For supersonic speeds, where one fin will not lie entirely in the field of influence of another fin, we must also apply the additional factors λ_{12} or λ_{24} as derived in Appendix D.

5. EXTENSION OF BODY VORTEX MODEL TO 50° ANGLE OF ATTACK

5.1 Previous Work

The body vortex model used in the earlier version of the method (ref. 6) was reported previously in references 3 and 8. It is semi-empirical and is based on data collected on various slender bodies with $\alpha_c \leq 20^\circ$ and $M_\infty \leq 2$. Various investigators have demonstrated that the body vortices for such flows are symmetrical. Although there is considerable scatter in the available data, the correlation of reference 8 has proved to be a useful tool.

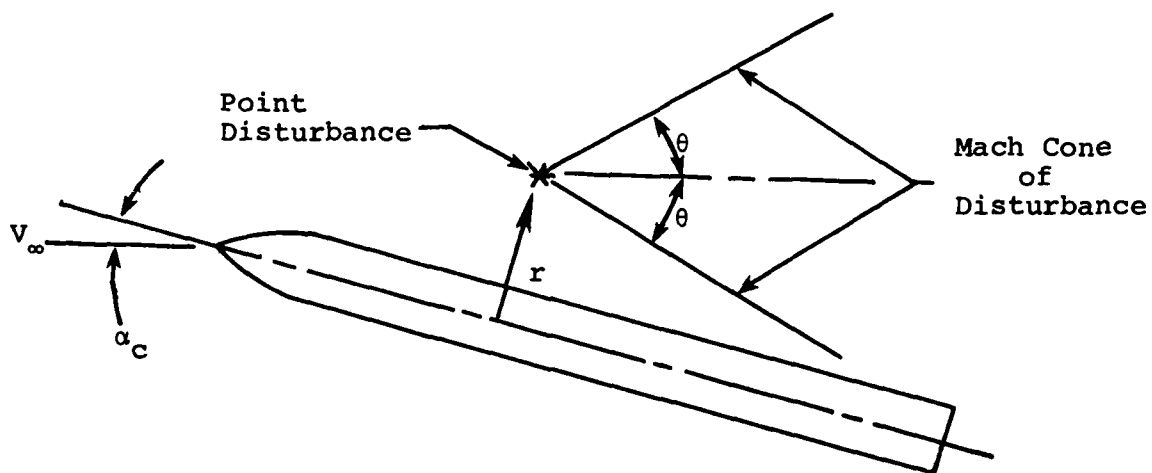
For angles of attack greater than 20°, the data on body vortices are sparse. Consequently, the authors found it necessary to develop a method based on a multi-vortex tracking code previously developed at NEAR for ONR by M. R. Mendenhall (ref. 21). Mendenhall's code is based on slender-body theory and relies on several empirical factors. Hence, the usefulness of the results depends heavily on the user's ability to estimate or bound those factors. The following subsection describes the preliminary analysis used for the required estimates. The last subsection presents the derived correlation for the Mach numbers used in the method ($M_\infty = 0.8, 1.2, 2.0, 3.0$).

5.2 Preliminary Remarks

The most surprising result of our most recent work is that, for supersonic crossflow Mach numbers, there is no essential asymmetry in the near wake of a slender body. We have been led to this conclusion by studying two-dimensional flow visualization experiments and then proceeding to the three-dimensional case. Several authors (refs. 23-25) have reported that the wakes of two-dimensional cylinders and other blunt bodies become symmetrical when M_∞ is increased to one or greater. This

phenomenon appears to be a consequence of the Law of Forbidden Signals in that any unsteadiness of the wake cannot propagate upstream if $M_{\text{wake}} > 1$. If the upstream flow is steady, only the small scale unsteadiness of the turbulence in the boundary layer can be present.

Consideration of a body at angle of attack in a supersonic flow, as shown in the sketch below, shows that the same phenomena must apply to three-dimensional flows.



The Mach cone semi-angle in the far wake (e.g., $r/D > 1$) is given approximately by

$$\sin \theta = \frac{1}{M_\infty} \quad (25)$$

However, the crossflow Mach number is defined to be

$$M_c = M_\infty \sin \alpha_c \quad (26)$$

Consideration of equations (25) and (26) shows that when $M_c \geq 1$, $\theta \leq \alpha_c$ and no signals can propagate from the far wake to the body. Recent vapor-screen work at NASA/Ames Research Center (ref. 26) and NASA/Langley Research Center (ref. 27) not only confirms this idea but suggests that, for most missiles, the minimum crossflow Mach number for symmetric wake flow may be

considerably lower than one. This idea also explains why the side force on a missile tends to zero as the free-stream Mach number increases: a symmetrical wake can't produce a side force.³

In figure 28, the boundary between the regions of symmetrical and asymmetrical vortex shedding is shown assuming that asymmetry ceases at a particular crossflow Mach number. Also shown on the graph are some vapor-screen results obtained by Jorgenson on a body with a pointed 3-caliber tangent-ogive nose and a 7-caliber cylindrical afterbody. It appears that a crossflow Mach number of 0.5 is sufficient to insure symmetrical vortex shedding for 3-D flow about slender bodies. Although this value is considerably less than the value of unity suggested by the Law of Forbidden Signals, it is not too surprising since supersonic flow begins to appear on a cylinder at a crossflow Mach number of 0.4 (ref. 28). Because of the results of the above analysis and of the meagre available data, the body vortices shed ahead of the first set of fins are assumed to be symmetrical in this report.

The multi-vortex tracking code which is used herein to estimate the vortex wake characteristics uses slender-body theory to describe the flow. As such, it assumes the flow in the cross-flow plane to be incompressible. This assumption is clearly in error for $M_c > 0.4$. Nevertheless, since little data are available on vortex strengths and positions for crossflow Mach numbers greater than 0.5, we found it necessary to use the code to generate design curves. The results are expected to be reasonable estimates since the major influences of shed vortex strength, location of separation and height of the vortex recirculation zone were accounted for empirically. Those effects are described in the next three subsections.

³

These considerations do not preclude an asymmetrical vortical wake away from the body.

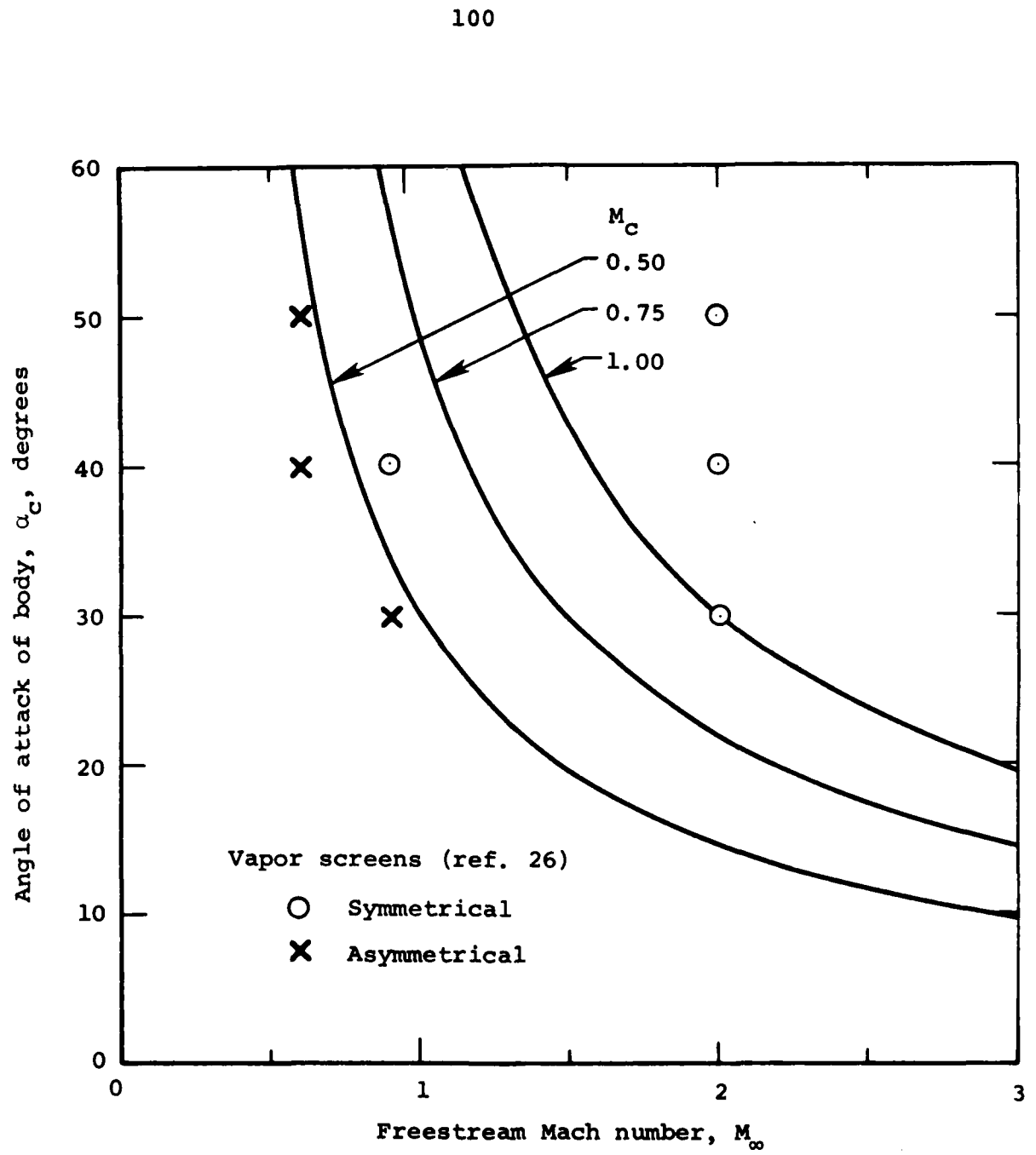


Figure 28. Estimate of boundary between symmetrical and asymmetrical vortex shedding.

5.3 Shed Vortex Strength

First, it was necessary to estimate the actual vorticity shed for $M_c > 0$ compared to the values for $M_c = 0$. The vorticity flux across the boundary layer at the separation point is given by (ref. 21)

$$\gamma = \frac{1}{2} U_e^2 \quad (27)$$

Hence, the strength of the shed vorticity is strongly dependent on the inviscid solution. An idea of the possible variation of γ with M_c can be obtained by noting that potential-flow theory gives $U_e = 2U_\infty$ at the shoulder of the cylinder for $M_c = 0$. Since Newtonian flow theory gives $U_e = U_\infty$ at the same location for infinite M_c , it is obvious that the nondimensional strength of the shed vorticity can change by a factor of approximately four at the shoulder of the cylinder.

To account for this effect, we computed U_e at the shoulder of a cylinder using the method of Van Dyke (ref. 28) for $M_c < M_{critical}$ and a finite-difference method for $M_c \geq 0.75$. The results are shown in figure 29. The results were interpolated by hand from $M_{critical}$ to $M_c = .75$. An empirical factor for reducing the strength of the shed vorticity computed by the code of reference 21 was obtained as follows:

$$\gamma_{M \neq 0} = \sigma \gamma_{M=0} \quad (28)$$

where

$$\sigma = \frac{(U_e/U_\infty)^2}_{(U_e/U_\infty)^2}_{M \neq 0} \quad (29)$$

and U_e is evaluated at the shoulder of the cylinder.

The actual σ values used are shown in figure 30. The maximum value of σ was set equal to 0.6 in accord with previous

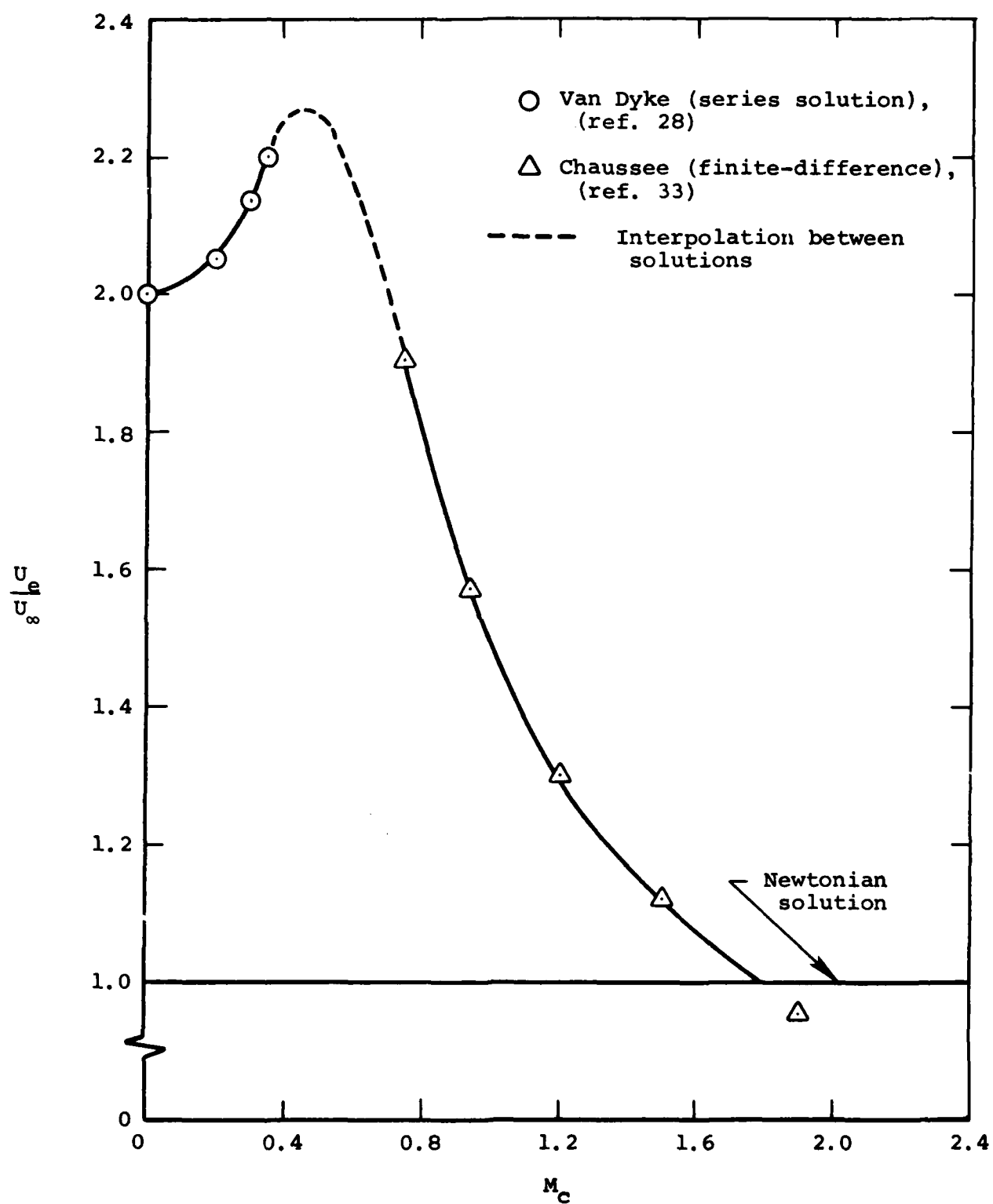


Figure 29. Flow velocity at shoulder of circular cylinder.

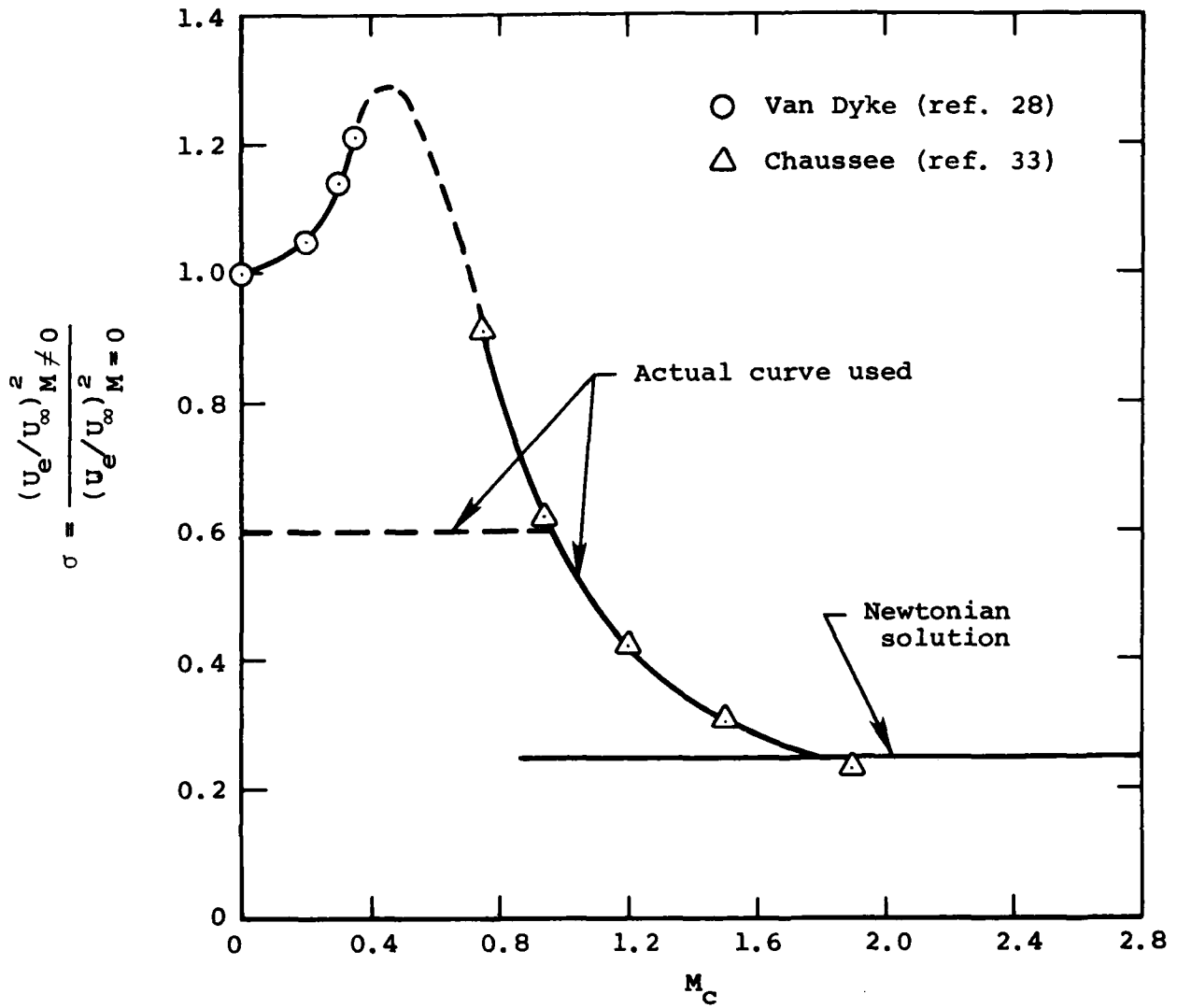


Figure 30. Vortex reduction factor used with multi-vortex tracking code.

investigators (ref. 21).

5.4 Location of Point of Separation

The angular location of the points of separation on the slender body have been estimated from pressure-distribution data obtained from NASA/Langley Research Center (ref. 29) for supersonic Mach numbers and from similar data given by Clark and Peoples (ref. 30) for $M_\infty = 0.8$. The results are shown in figure 31 together with some 3-D data obtained by Agnone, Zakkay, and Tory (ref. 31) and some 2-D crossflow data obtained by Murthy and Rose (ref. 32). Although there is considerable scatter in the data for the supersonic Mach numbers (fig. 31(a)), the vortex tracking solution is fairly insensitive to θ_s . Note that the data in figure 31 are for single locations along the axis of the test bodies. The code of Mendenhall (ref. 21) uses a modified version of Stratford's method of estimating the separation point. The correlations of figure 31 were used to obtain the coefficient in that method by trial and error. The method then was used with that coefficient to predict the point of separation all along the body.

5.5 Height of the Recirculation Zone

The multi-vortex tracking code used to develop the body vortex correlations requires that the radial location of each newly shed vortex along the body be given. This radial location has been found to have a crucial effect on the height of the calculated leeward recirculation zone. Since this factor has such a strong effect, an effort was made to determine what the height of the leeward recirculation zone actually is for various M_∞ and α_c . The results from various investigations are shown in figure 32. Few data are available for subsonic Mach numbers for $\alpha_c > 20^\circ$; as a result, the data of Jorgensen for $M_c = 0.9$

\times Agnone, Zakkay, and Tory, reference 31

\otimes Murthy and Rose, reference 32, 2-D data

M_∞

1.60

□

2.30

○

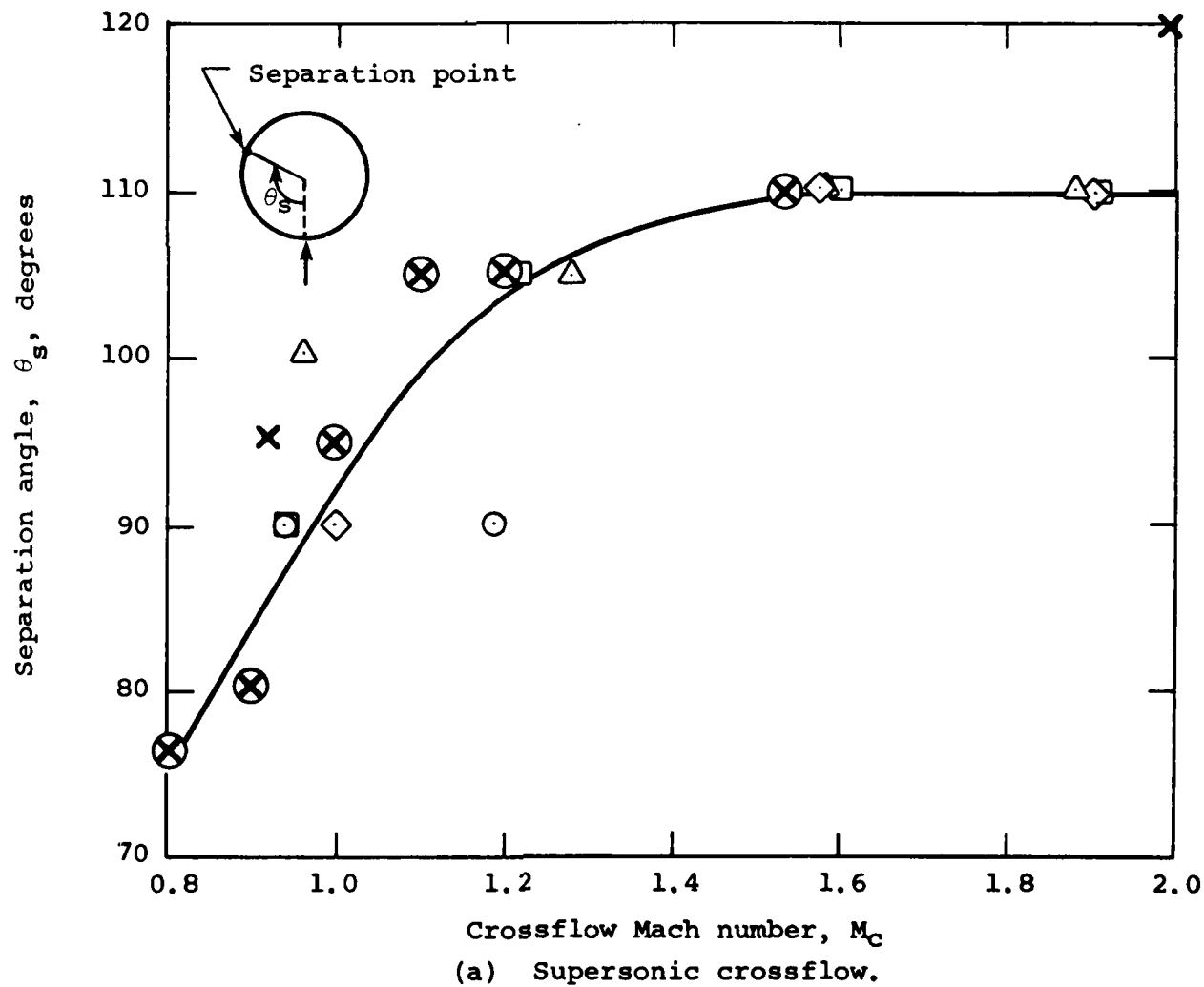
2.96

◇

4.60

△

Landrum, reference 29, $x/D = 6.2$



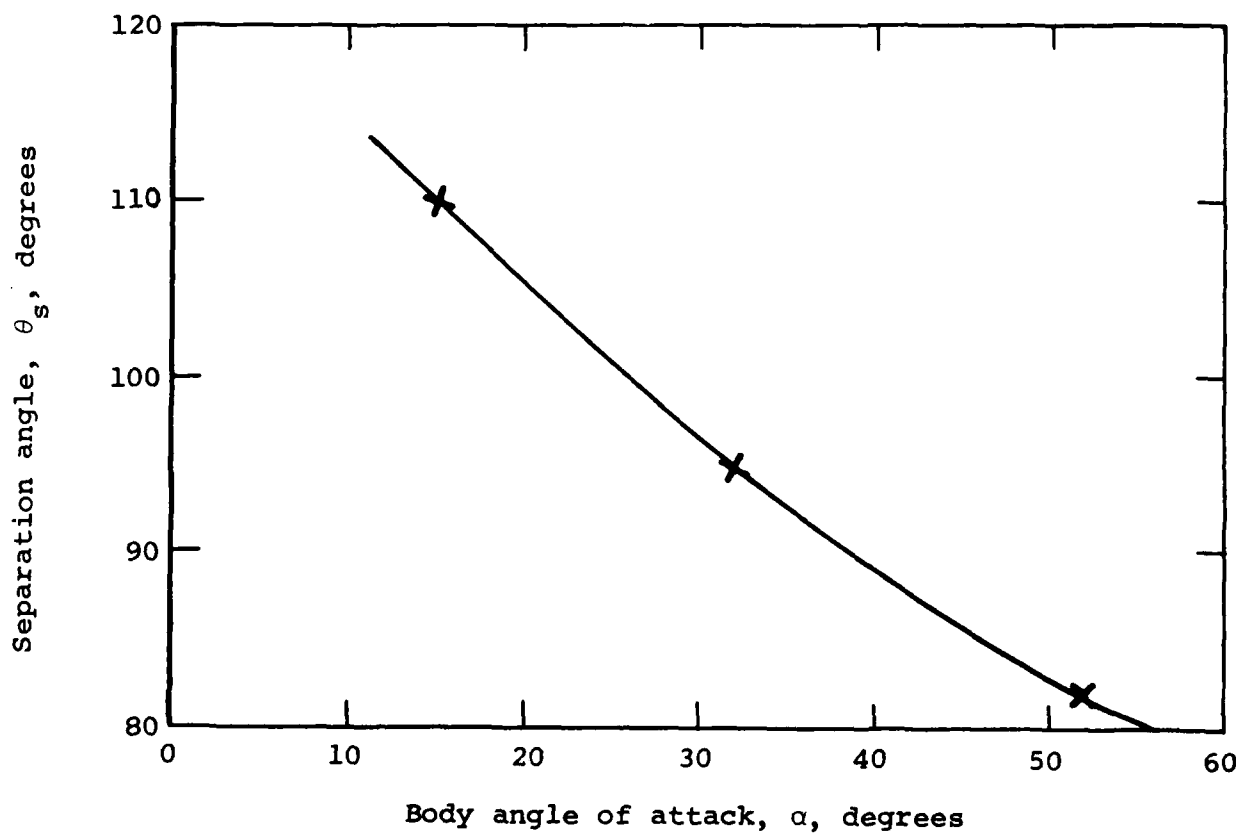
(a) Supersonic crossflow.

Figure 31. Effect of crossflow Mach number on separation points for circular cylinder.

Data of Clark and Peoples, reference 30

$$M_{\infty} = 0.8 \quad \frac{x}{a} = 2.0$$

$\frac{\alpha_c}{^{\circ}}$	$\frac{\theta_s}{^{\circ}}$	$\frac{M_c}{}$
15°	110°	0.21
32°	95°	0.42
52°	82°	0.63



(b) Subsonic crossflow.

Figure 31. Concluded.

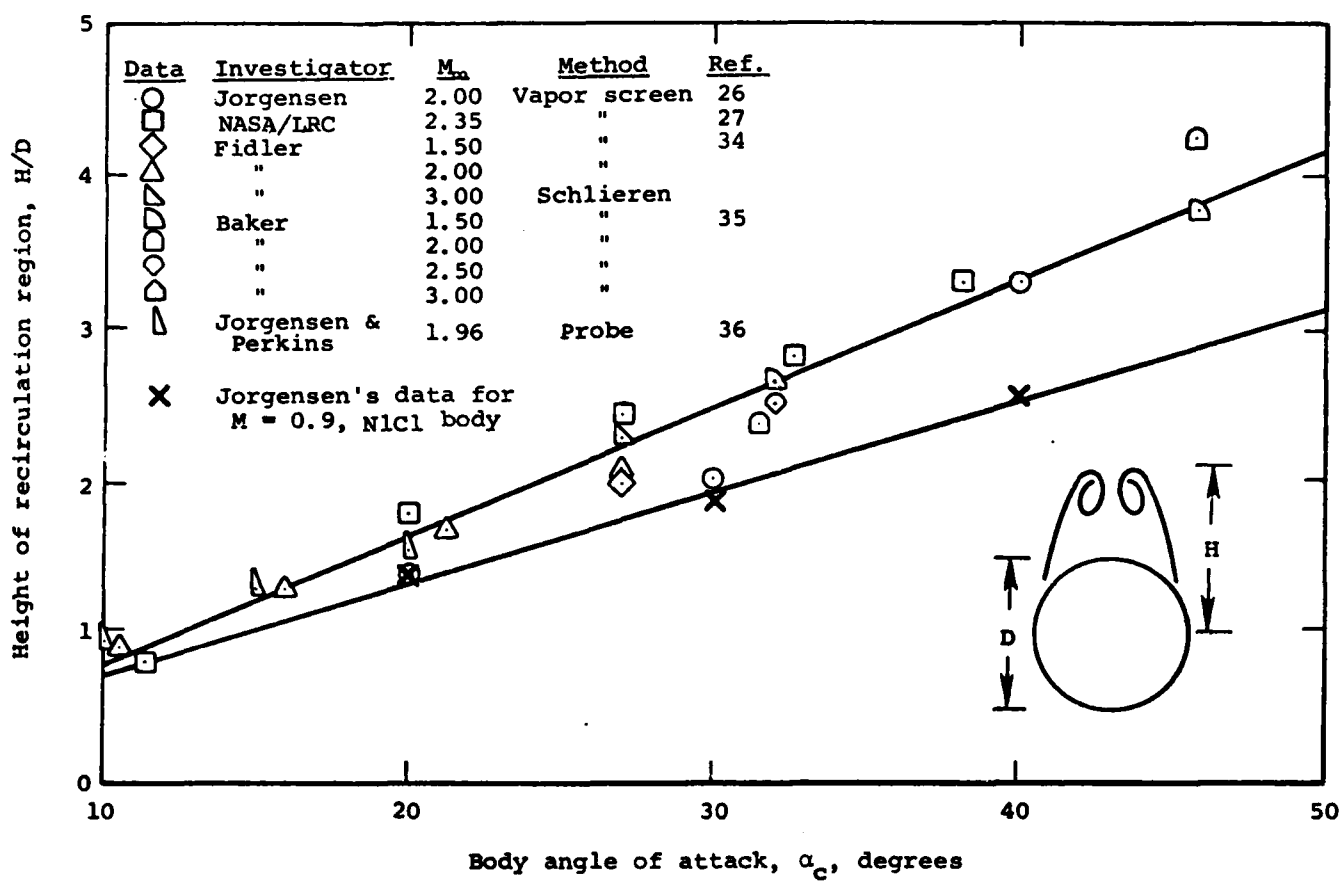


Figure 32. Estimated height of top of recirculation region at $X/D = 10$ for tangent-ogive cylinder.

were used for the case of $M_\infty = 0.8$. The value for the radial location of each newly shed vortex was adjusted by trial and error until the height of the computed recirculation zone at $x/D = 10$ matched the appropriate value given by figure 32.

5.6 Computed Correlations for Body Vortex Strengths and Positions for $M_\infty = 0.8, 1.2, 2.0$ and 3.0

The code developed by Mendenhall (ref. 21) was used to compute body vortex strengths and positions for $\alpha_c = 20^\circ, 30^\circ, 40^\circ$ and 50° at $M_\infty = 0.8, 1.2, 2.0$ and 3.0 subject to the constraints discussed in subsections 5.3-5.5. The semi-empirical method developed by Spangler, which was used in the previous method (ref. 6), has been retained for $\alpha_c \leq 10^\circ$. To bridge the gap smoothly between that method and the one reported in this section, a linear interpolation between the Spangler method for $\alpha_c = 10^\circ$ and the new method for $\alpha_c = 20^\circ$ was used for α_c between 10° and 20° . The computed results used for $\alpha_c > 20^\circ$ are presented below correlated for axial location and angle of attack. Linear interpolation is used for Mach numbers other than $0.8, 1.2, 2.0$ and 3.0 .

5.6.1 Correlation for $M_\infty = 0.8$. - The following correlation was used for vortex strength at $M_\infty = 0.8$:

$$20^\circ \leq \alpha_c \leq 30^\circ: \frac{\Gamma}{2\pi V_\infty a \sin \alpha_c} = -.06 + .136 \frac{x}{a} \sin \alpha_c \quad (25a)$$

$$30^\circ \leq \alpha_c \leq 50^\circ: \frac{\Gamma}{2\pi V_\infty a \sin \alpha_c} = -.06 + .0165 (\alpha_c - 30^\circ) + .136 \frac{x}{a} \sin \alpha_c \quad (25b)$$

The lateral position of the body vortex for $M_\infty = 0.8$ was found to be estimated adequately by the following equation:

$$20^\circ \leq \alpha_c \leq 50^\circ: \frac{y_v}{a} = .50 + .0006 (\alpha_c - 20^\circ) \frac{x}{a} \quad (26)$$

The vertical position is given by

$$20^\circ \leq \alpha_c \leq 50^\circ : \frac{z_v}{a} = .75 + .163 \frac{x}{a} \sin \alpha_c \quad (27)$$

5.6.2 Correlations for $M_\infty = 1.2$. - For $M_\infty = 1.2$ the vortex strength correlation is

$$20^\circ \leq \alpha_c \leq 50^\circ : \frac{\Gamma}{2\pi V_\infty a \sin \alpha_c} = .12 + .091 \frac{x}{a} \sin \alpha_c \quad (28)$$

The correlation for lateral position is given by the following listing for $M_\infty = 1.2$:

$\frac{x}{a}$	$\frac{y_v}{a}$
4	.665
6	.710
8	.750
10	.780
12	.800
14	.805
∞	.805

The correlation for vertical position is given by the following listing:

$\frac{x}{a} \sin \alpha_c$	$\frac{z_v}{a}$
4	1.55
6	1.85
8	2.20
10	2.58
12	3.03
14	3.50
16	3.98
18	4.45

5.6.3 Correlations for $M_\infty = 2.0$.- For $M_\infty = 2.0$, the vortex strength correlation is

$$\alpha_c = 20^\circ: \frac{\Gamma}{2\pi V_\infty a \sin \alpha_c} = .078 + .096 \frac{x}{a} \sin \alpha_c \quad (29)$$

$$30^\circ \leq \alpha_c \leq 50^\circ: \frac{\Gamma}{2\pi V_\infty a \sin \alpha_c} = .079 \frac{x}{a} \sin \alpha_c \quad (30)$$

Linear interpolation between the Γ values for $\alpha_c = 20^\circ$ and $\alpha_c = 30^\circ$ is used for α_c between 20° and 30° . The lateral position correlation is

$$20^\circ \leq \alpha_c \leq 50^\circ: \frac{y_v}{a} = 1.119 - .0169 \alpha_c \quad (31)$$

where α_c is in degrees. The vertical position correlation used for $M_\infty = 2.0$ is the same as that used for $M_\infty = 1.2$.

5.6.4 Correlations for $M_\infty = 3.0$.- The vortex strength correlations used for $M_\infty = 3.0$ are

$$\alpha_c = 20^\circ: \frac{\Gamma}{2\pi V_\infty a \sin \alpha_c} = 0.13 \frac{x}{a} \sin \alpha_c \quad (32)$$

$$30^\circ \leq \alpha_c \leq 50^\circ: \frac{\Gamma}{2\pi V_\infty a \sin \alpha_c} = 0.08 \frac{x}{a} \sin \alpha_c \quad (33)$$

Linear interpolation is used to bridge the gap between $\alpha_c = 20^\circ$ and $\alpha_c = 30^\circ$. The lateral position correlation used is

$$20^\circ \leq \alpha_c \leq 50^\circ: \frac{y_v}{a} = .19 / \sin \alpha_c \quad (34)$$

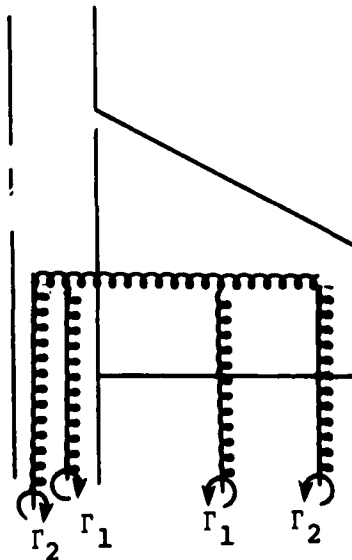
The vertical position correlation used for $M_\infty = 3.0$ is the same as that used for $M_\infty = 1.2$.

6. ADDITIONAL MODIFICATIONS TO THE ENGINEERING METHOD

A number of modifications to the method of reference 6 were made during the course of the present work in addition to those mentioned in the previous sections. These modifications fall into two categories: (1) changes to the method for the afterbody section and (2) changes to the method for the finned sections.

6.1 Modifications to the Engineering Method for the Afterbody Section

In reference 5, it was reported that the trailing vorticity sheets from the canard fins were often observed to roll up into two distinct vortices per fin rather than the one per fin assumed by the method of reference 6. The same phenomenon was observed independently by Spahr and Dickey (ref. 37). To enable the user to account for such a possibility, an option was added to the computer code for computing the strengths for given positions of two vortices shed by each canard fin. The method assumes that the vortices have independent constant-strength bound legs and trailing legs at the positions shown in the sketch below.



The normal force on the fin is related to the shed vortices by

$$N_{FIN} = \rho_\infty V_\infty \Gamma_1(t_1-a) + \rho_\infty V_\infty \Gamma_2(t_2-a) \quad (35)$$

where t is the spanwise coordinate measured from the body axis. Since the bound legs of the horseshoe vortices are assumed to be constant strength, the center of pressure for N_{FIN} must be located at

$$\bar{t} = \frac{[a+\frac{1}{2}(t_1-a)]\Gamma_1(t_1-a) + [a+\frac{1}{2}(t_2-a)]\Gamma_2(t_2-a)}{\Gamma_1(t_1-a) + \Gamma_2(t_2-a)} \quad (36)$$

For a single trailing vortex (e.g. $\Gamma_2 = 0$), equations (35) and (36) are sufficient for solving for Γ and t in terms of the computed quantities N_{FIN} and \bar{t} . However, for two trailing vortices per fin, the equations are indeterminate. The method as presently programmed requires the user to specify t_1 and t_2 . The program then computes Γ_1 and Γ_2 . The vapor-screen data of reference 5 and reference 37 suggest that $t_1 = \frac{1}{2}(s_m+a)$ and $t_2 = .95s_m$ would be useful first estimates if no other data are available.

In the original engineering method described in reference 6, the afterbody vortices, if present, were assumed to start at $\pm 50^\circ$ from the velocity vector at the body axis formed by the free-stream crossflow velocity and the velocities induced by the canard fin trailing vortices. In reference 6 it was suggested that better results could be obtained if the vortices were assumed to start at $\pm 60^\circ$ from the z_o (vertical) direction. The present version of the computer program uses the second assumption.

It was also suggested in reference 6 that better results would be obtained if canard fin trailing vortices from the windward side were combined with the afterbody vortices if the trailing vortices came too close to the body. During the course of the

present work, it was found that combining the vortices as described above did improve the results. The user may still exercise the option of not combining vortices by appropriate choices of the program run parameters. The method for combining a trailing vortex from the windward side with the appropriate afterbody vortex consists of algebraically summing the vortex strengths and placing the new vortex at the old position of the old afterbody vortex.

In addition to the above modifications, the vortex tracking procedure for the afterbody section was modified. The modification consists of assuming each vortex to have a solid-body rotation core. The image vortices are not changed.

The heuristic model for afterbody vortex strengths described in reference 6 assumes that all of the crossflow drag is due to flow separation on the leeward side of the lifting body. This is a reasonable assumption for angles of attack less than 20° and for low crossflow Mach numbers. However, as the crossflow Mach number increases, the fraction of the total crossflow drag which is due to leeward flow separation decreases. Data from several investigations illustrating this phenomenon for two-dimensional flow are shown in figure 33. The leeside drag was computed by multiplying an estimated average leeside pressure times the frontal area of the cylinder. To account for the effect shown in figure 33, the present version of the method uses only the leeside drag coefficient in computing afterbody vortex strength.

It should be noted that the crossflow drag coefficient table, which is built into the computer program, has been modified slightly to give better agreement with the three-dimensional results obtained by Jorgensen (ref. 26).

6.2 Modifications to the Engineering Method for the Finned Sections

During the course of the present work, it was recognized

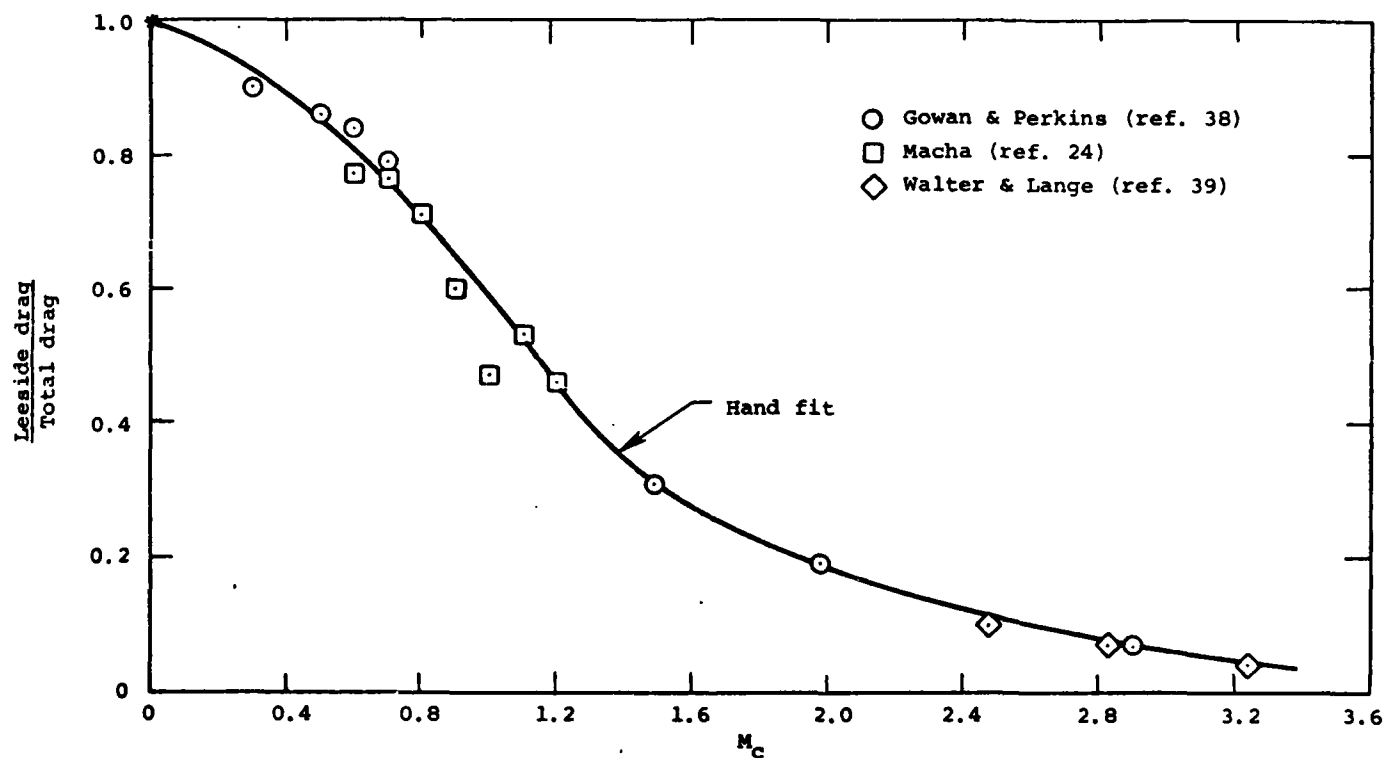


Figure 33. Ratio of leeside drag to total drag for circular cylinders.

that vortices cannot be properly tracked in the presence of a wing-body combination (finned section) unless the diffuse nature of the vortex is taken into account. Single vortex representations of vortex "clouds" give unrealistic vortex paths, yet the tracking of large numbers of vortices would require excessive running time. A compromise was reached by simply assuming that the positions of the vortices in the crossflow plane remain fixed over the fins. Available vapor-screen data seem to indicate that this assumption is reasonable.

The diffuse nature of the vortices must also be taken into account when the effects of the vortices on the fins are computed. The previous method gave the user the option of limiting the maximum velocity which could be induced on the fins or of specifying a vortex core size. With the availability of the code developed by Mendenhall for computing the strengths and positions of vortex clouds, it became possible to test the accuracy of the above options.

The example case used for the test is shown in figure 34. It represents the body vortex clouds at $M_\infty = 3.0$, $\alpha_c = 20^\circ$ and $x/a = 16.5$ for a 3-caliber tangent-ogive nose with a cylindrical afterbody. The effects of the vortices on the fins were computed for four cases: (1) the vortex clouds were used to compute the boundary conditions on the fins (2) the equivalent point vortices (two) were used with the spanwise angle of attack induced on the fins limited to 0.3 radians, (3) the equivalent point vortices were used assuming a vortex core radius equal to one-half the body radius, and (4) the equivalent point vortices were used assuming a vortex core radius equal to the body radius. The vortex-induced equivalent angle of attack and corresponding moment arm for fins with $a/s_m = 0.5$ are shown in figure 35 as a function of roll angle. Note that the agreement among the cases improves as the fin rolls away from the center of the vortex cloud. Similar results for $a/s_m = 0.25$ are shown in figure 36. On the basis of the results shown in figure 35 and 36, we chose to model the

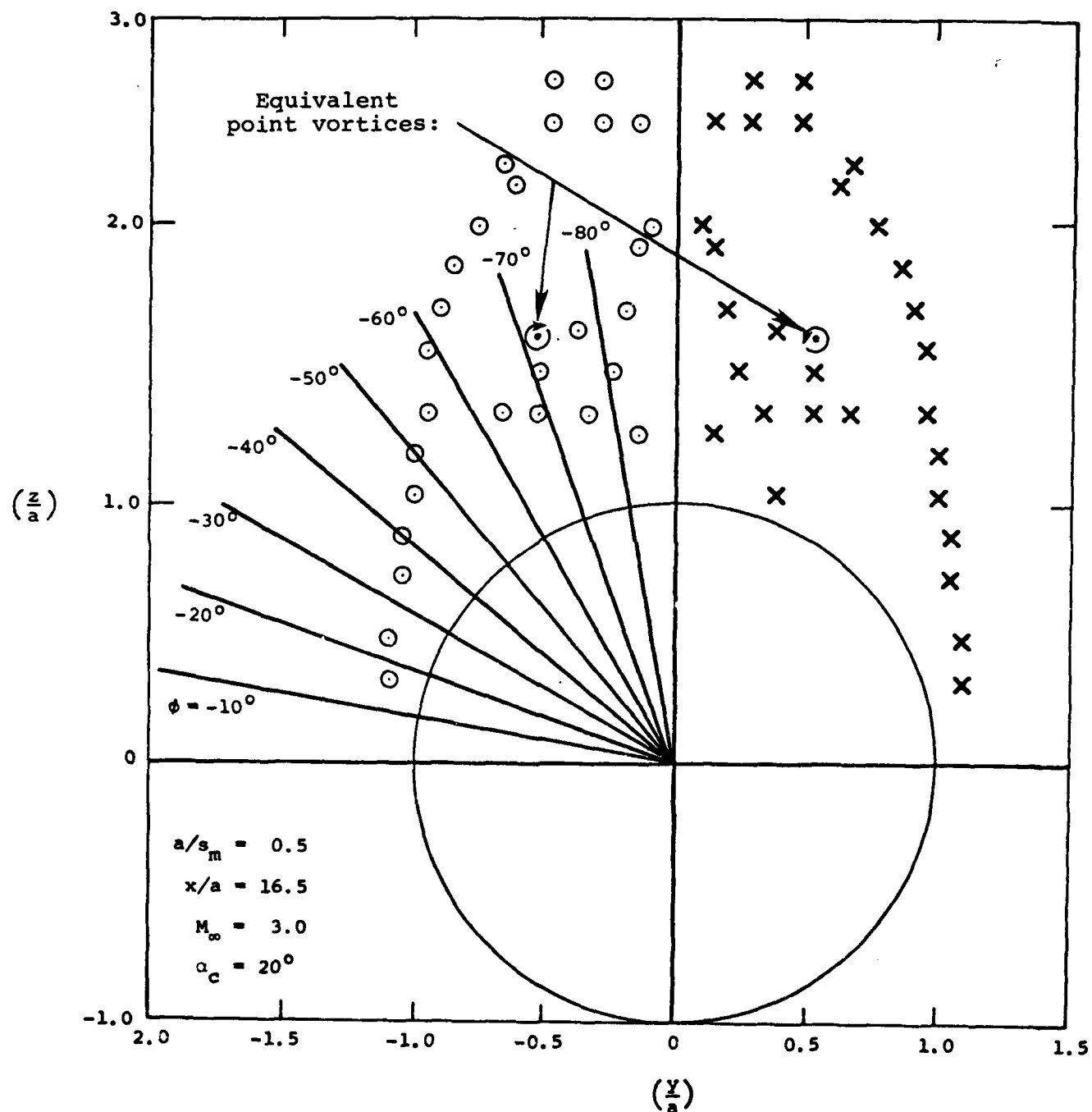


Figure 34. Vortex clouds calculated by program of Mendenhall (ref. 21) for cylindrical body with three caliber tangent-ogive nose.

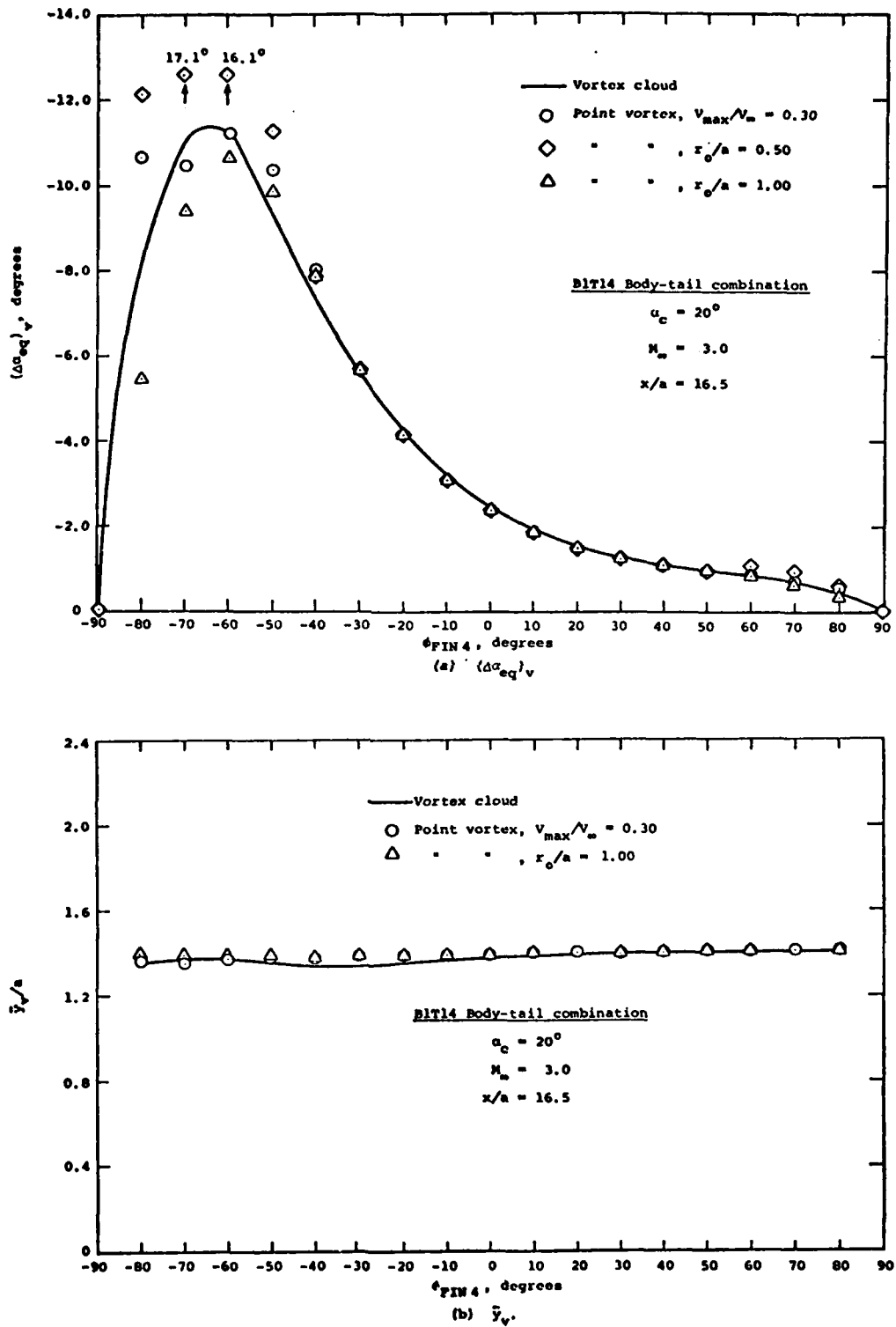


Figure 35. Comparison of results for $(\Delta\alpha_{eq})_v$ and \bar{y}_v for vortex cloud and for point vortex simulation of cloud; $a/s_m = 0.50$.

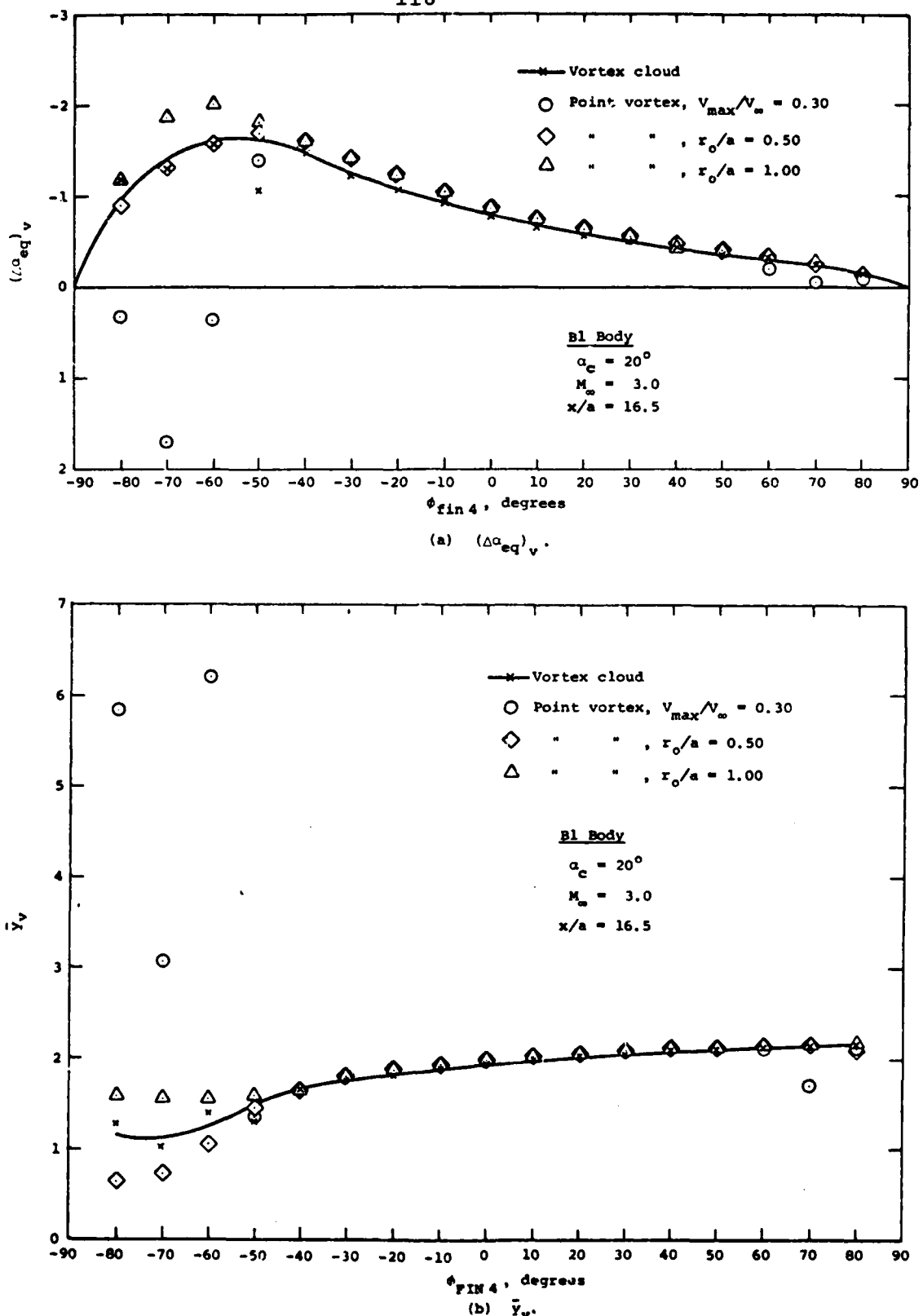


Figure 36. Comparison of results for $(\Delta\alpha_{eq})_v$ and \bar{y}_v for vortex cloud and for point vortex simulation of cloud; $a/s_m = 0.25$.

vortex clouds with point vortices which have large cores. The vortex core diameter is assumed to vary linearly from the missile nose such that it would be equal to the body diameter 10 calibers downstream of the nose tip. The same formula for core size was used for vortex tracking over the afterbody.

The previous method assumed that the only contribution to the body load in a finned section is the lift carryover from the fins. This assumption is adequate for low crossflow Mach numbers for which most of the body lift is due to leeside flow separation. For high crossflow Mach numbers, it seems appropriate to include the windward fraction of the crossflow drag when computing the body loads in the finned section. Although this model was adopted for the present version of the computer program, the authors are unaware of any data which could be used to verify directly the above conjecture.

It was mentioned previously in section 2 that the reverse-flow method used to compute the effect of vortices on the fins has been revised. The previous method (ref. 6) was approximate and based on theory available at that time. The present reverse-flow method is exact under the assumptions of slender-body theory. The theoretical development is described in Appendix B. Mach number effects are also accounted for in the present version. The theoretical development for those effects is present in Appendix D.

7. COMPARISON BETWEEN EXPERIMENT AND PREDICTIONS OF COMPUTER PROGRAM

7.1 Preliminary Remarks

The quantity of data available on body-tail or wing-body-tail configuration to high angles of attack (i.e. 45°) and which also includes fin forces and moments and the effects of roll angle is not large. Most of the available data has gone into constructing the data base which is part of the predictive method. The investigations of references 4 and 7 do provide data to high angles for checking the predictive method for a particular version of the Army generalized missile, figures 7 and 8. However, the canard fins C6 from these investigations were used to provide high-aspect-ratio fin data in the data base for the Mach number range 0.8 to 1.3. We can, however, use the body-tail data for an independent check of the predictive method. Also the tail fin forces and moments and the complete configuration forces and moments will serve the same purpose for the wing-body-tail configuration. These data are available in the Mach number range 0.8 to 1.3. Thus, we have no independent data suitable for checking the predictive method to high angles of attack at Mach numbers above 1.3.

7.2 Body-Tail Comparisons

7.2.1 Fin normal-force coefficient.- A systematic series of comparisons between data and prediction of the computer program for fin normal-force coefficient is given in figures 37-43 in accordance with the following listing.

Figure	M_∞	ϕ
37	0.8	10°
38	1.22	10°
39	0.8	20°
40	1.22	20°
41	0.8	30°
42	1.22	30°
43	0.8 and 1.22	45°

The body-tail configuration has a value of tail fin aspect ratio (1.33) not in the data base, and its a/s_m ratio is .417 whereas that of the data base is 0.5.

Inspection of figure 37 for $M_\infty = 0.8$ and $\phi = 10^\circ$ shows certain general features which reoccur. Data from two wind tunnels are shown, and in the region of overlap, $\alpha_c = 20^\circ-25^\circ$, the agreement is generally good. The accuracy of the data near $\alpha_c = 50^\circ$ is thought to be good, but no verification of this belief is available. Fin 1 is definitely influenced by the body vortices at high angles of attack, and the prediction is only fair for $\alpha_c = 30^\circ-45^\circ$.

Fins 2, 3, and 4 are not influenced greatly by body vortices, and the predictive and experimental results are in fair agreement. The stall of fin 4 approaching $\alpha_c = 20^\circ$ is not so severe as predicted.

Figure 38 shows results for $M_\infty = 1.22$ directly comparable with those for $M_\infty = 0.8$ in figure 37. For fin 1 the normal-force coefficient for $\alpha_c > 35^\circ$ is not well predicted by the method. However, fin 4 no longer exhibits a transonic stall. On balance better agreement is obtained between data and prediction at this Mach number than at $M_\infty = 0.8$.

Figure 39 for $M_\infty = 0.8$ and $\phi = 20^\circ$ exhibits almost the same features as figure 37 for $\phi = 10^\circ$. Also figures 38 and 40

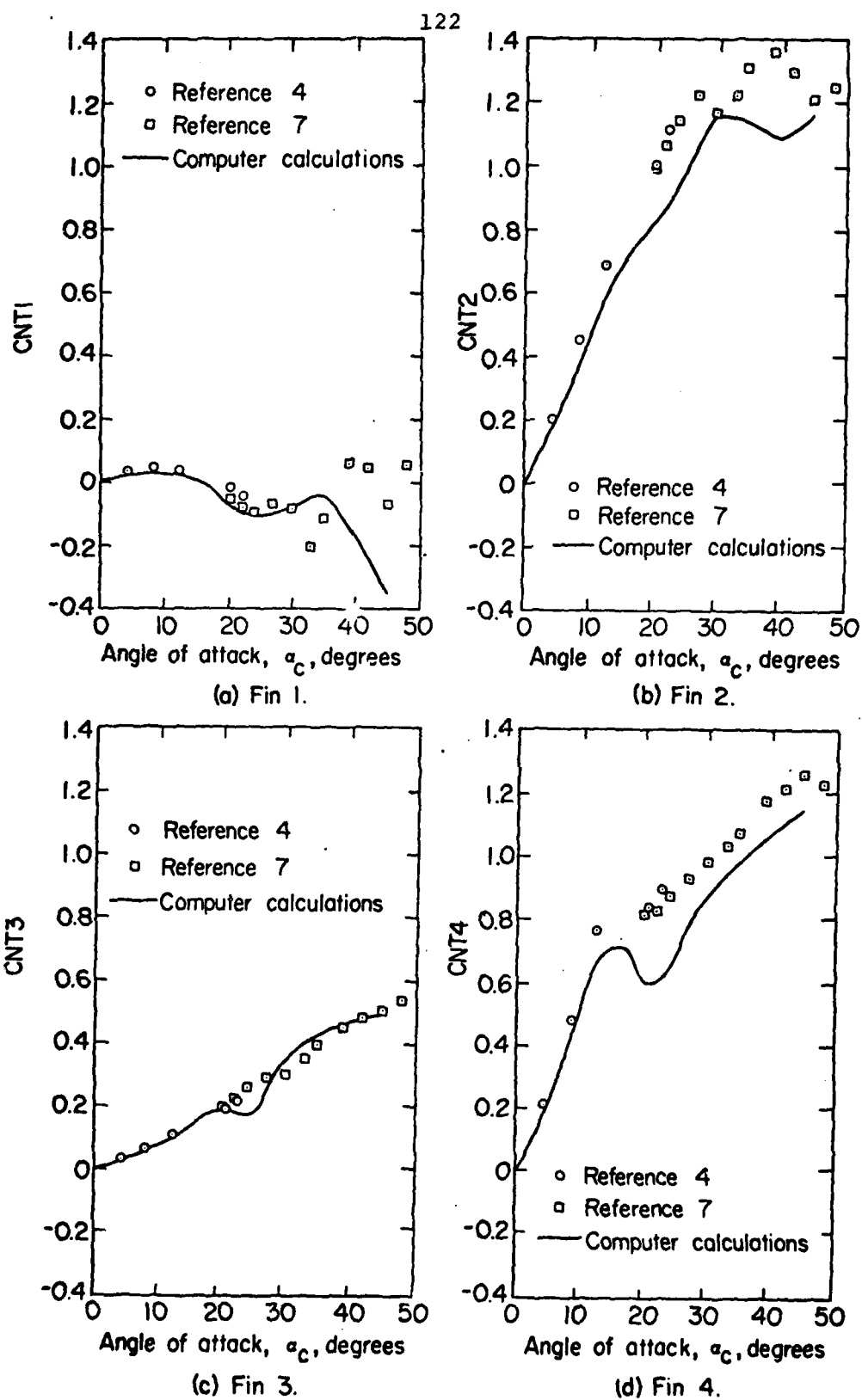


Figure 37. Fin normal-force coefficients for configuration BN₃T₂ at $M_\infty = 0.8$; $\phi = 10^\circ$.

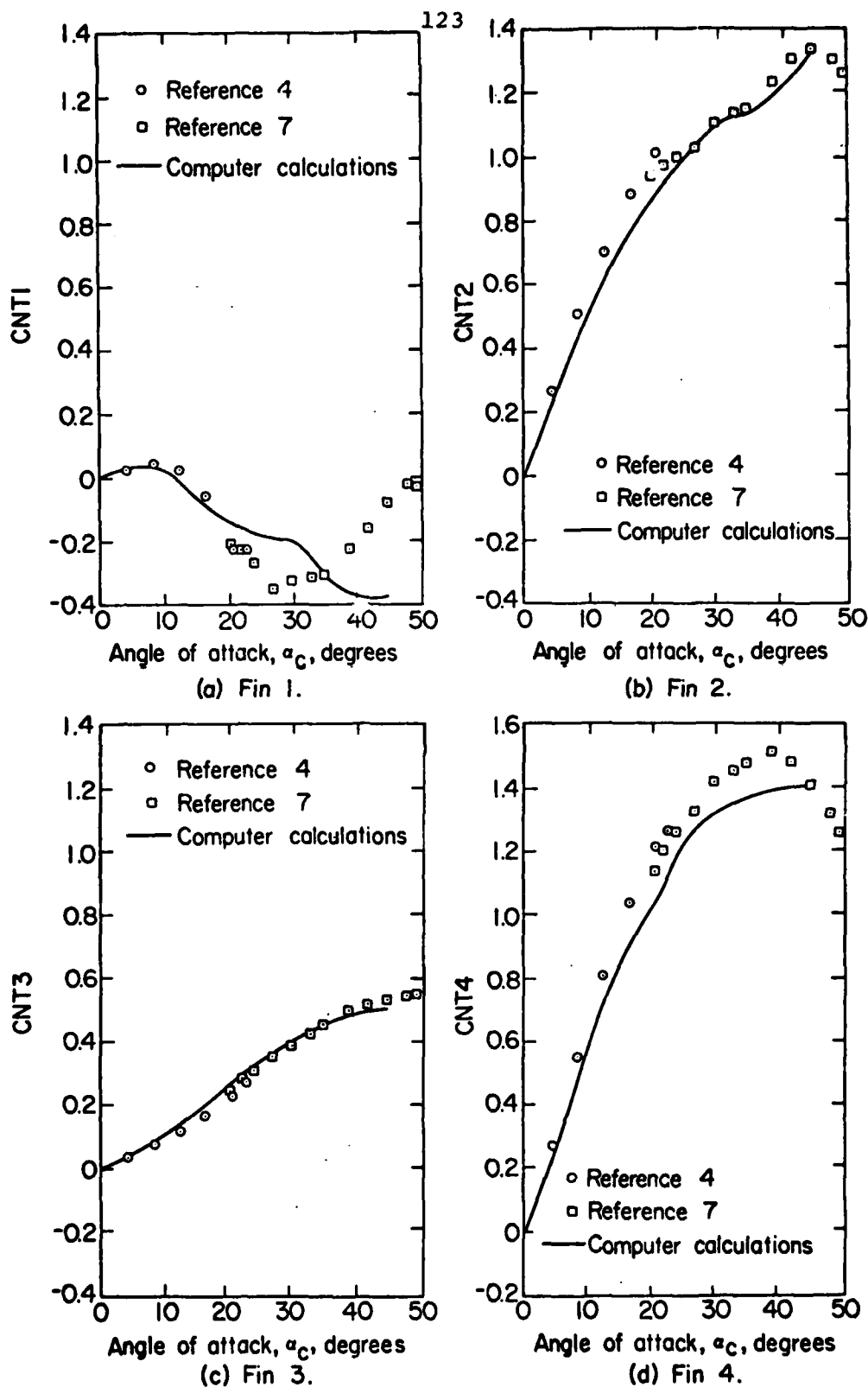
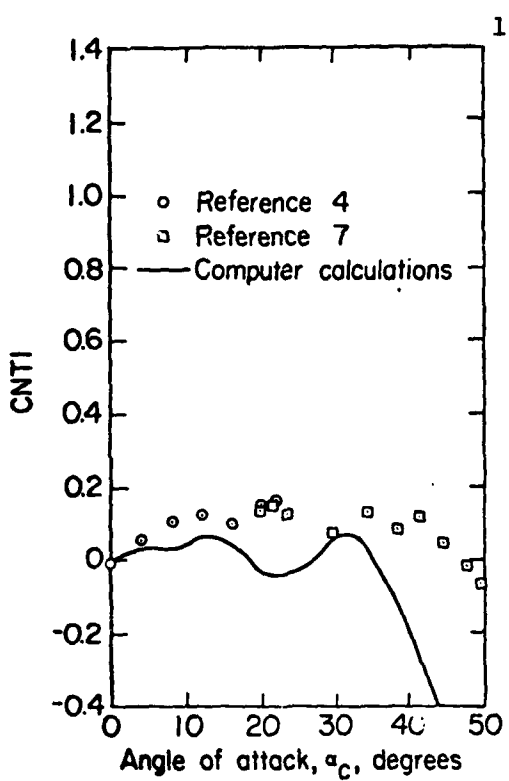
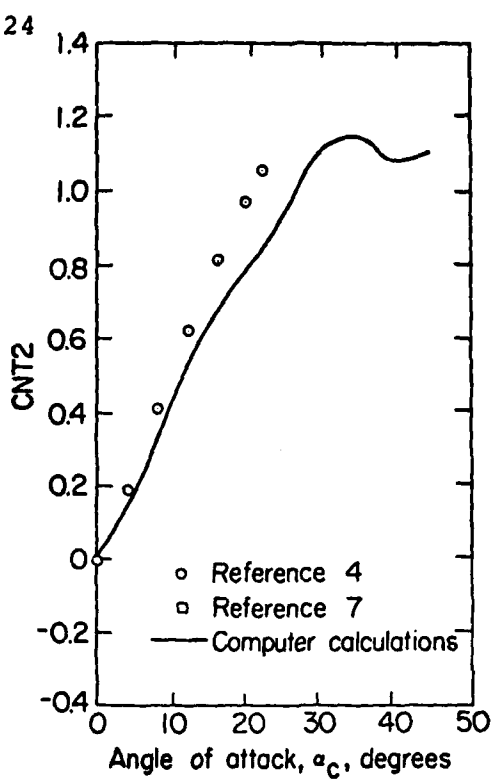


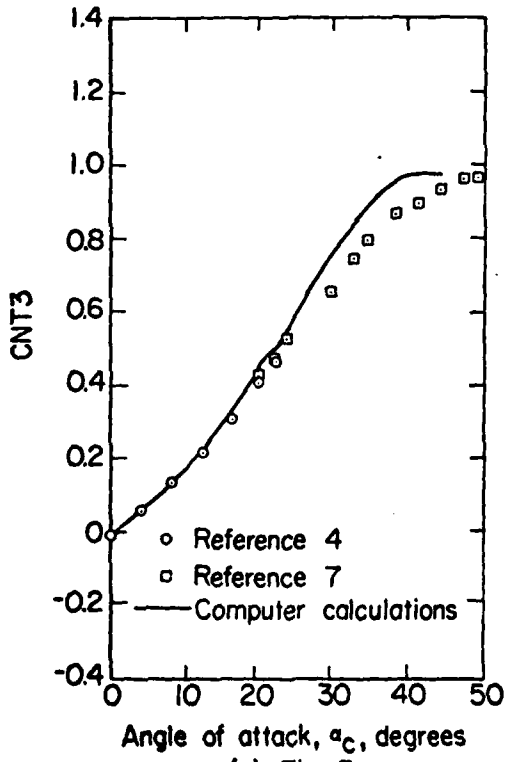
Figure 38. Fin normal-force coefficients for configuration BN₃T₂ at $M_\infty = 1.22$; $\phi = 10^\circ$.



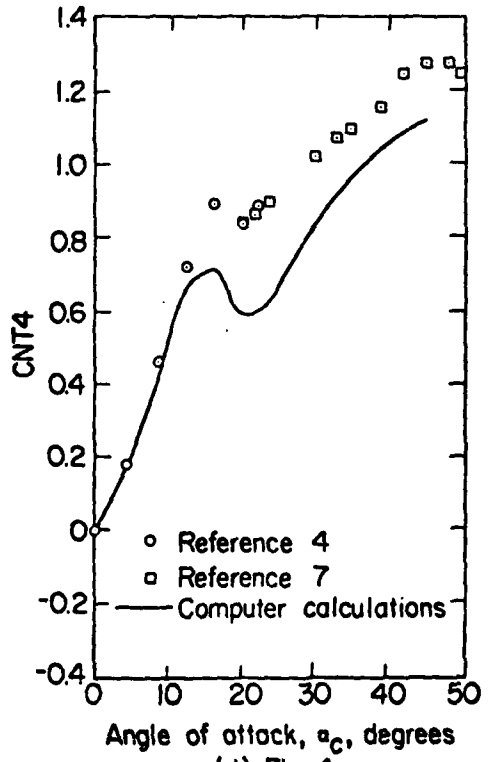
(a) Fin 1.



(b) Fin 2.



(c) Fin 3.



(d) Fin 4.

Figure 39. Fin normal-force coefficients for configuration BN₃T₂ at M_∞ = 0.8; $\phi = 20^\circ$.

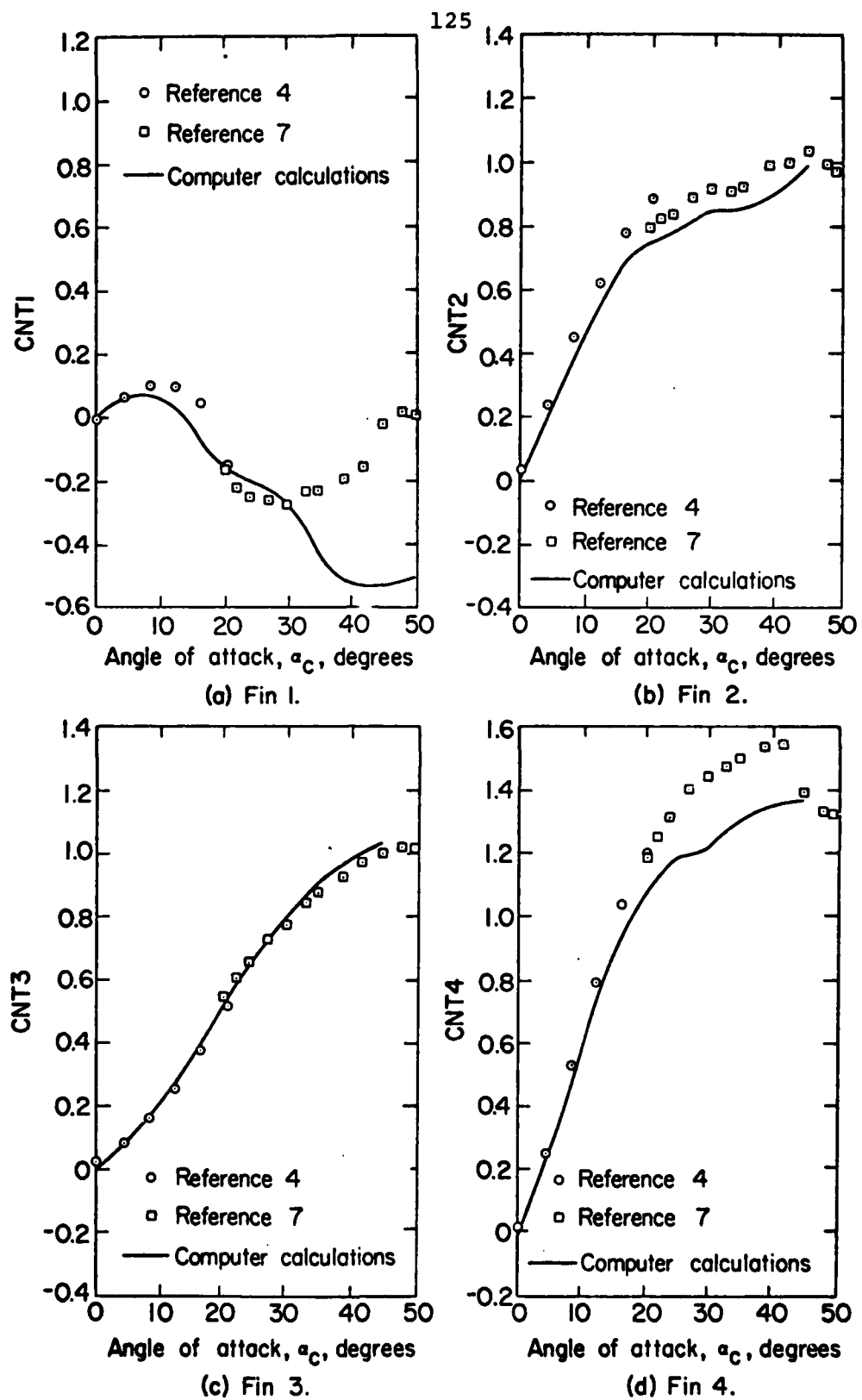


Figure 40. Fin normal-force coefficients for configuration BN₃T₂ at M_∞ = 1.22; $\phi = 20^\circ$.

for $M_{\infty} = 1.22$ exhibit similar results.

Figure 41 for $\phi = 30^\circ$ and $M_{\infty} = 0.8$ now shows a change in the behavior of the CNT1 force for $\alpha_c > 30^\circ$. The computer program predicts a large loss of normal force in this range and the data exhibited a loss which is not so large. The fin is generally more influenced by body vortices at the higher ϕ angle since the body vortices are the cause of the negative normal force. It will be recalled that the body vortices are actually vortex clouds in high-angle-of-attack vortex model and that these are approximated by concentrated vortices with large cores for predictive purposes. This approximation causes some loss of predictive accuracy when the fin is near the vortex.

Figure 42 shows no effects not exhibited by figure 40.

Figure 43 for $\phi = 45^\circ$ is of special interest since it yields information concerning the asymmetric effects associated with vortices (or other unknown causes). Considering first fins 1 and 2, which have mirror symmetry, at $M_{\infty} = 0.8$ they exhibit closely the same results for $\alpha_c < 20^\circ$, and establish the general level of precision of the data. For $\alpha_c > 30^\circ$, there are differences in CNT1 and CNT2 as large as 0.2 probably as a result of vortex asymmetry. It is noted that the difference between CNT1 and CNT2 is of variable sign, probably as a result of vortex switching. The same phenomenon is exhibited by fins 3 and 4 at $M_{\infty} = 0.8$, but the magnitude of the difference is generally less.

At $M_{\infty} = 1.22$ CNT1 and CNT2 in figures 43(c) and 43(d) exhibit much less asymmetry than the corresponding results at $M_{\infty} = 0.8$. The crossflow Mach number exceeds 0.5 at $M_{\infty} = 1.22$ at $\alpha = 23^\circ$, which is below the angle of attack for the onset of asymmetric vortex shedding. It appears, therefore, that asymmetric vortex effects on CNT are small in the present instance.

7.2.2 Configuration induced rolling-moment coefficient.- One

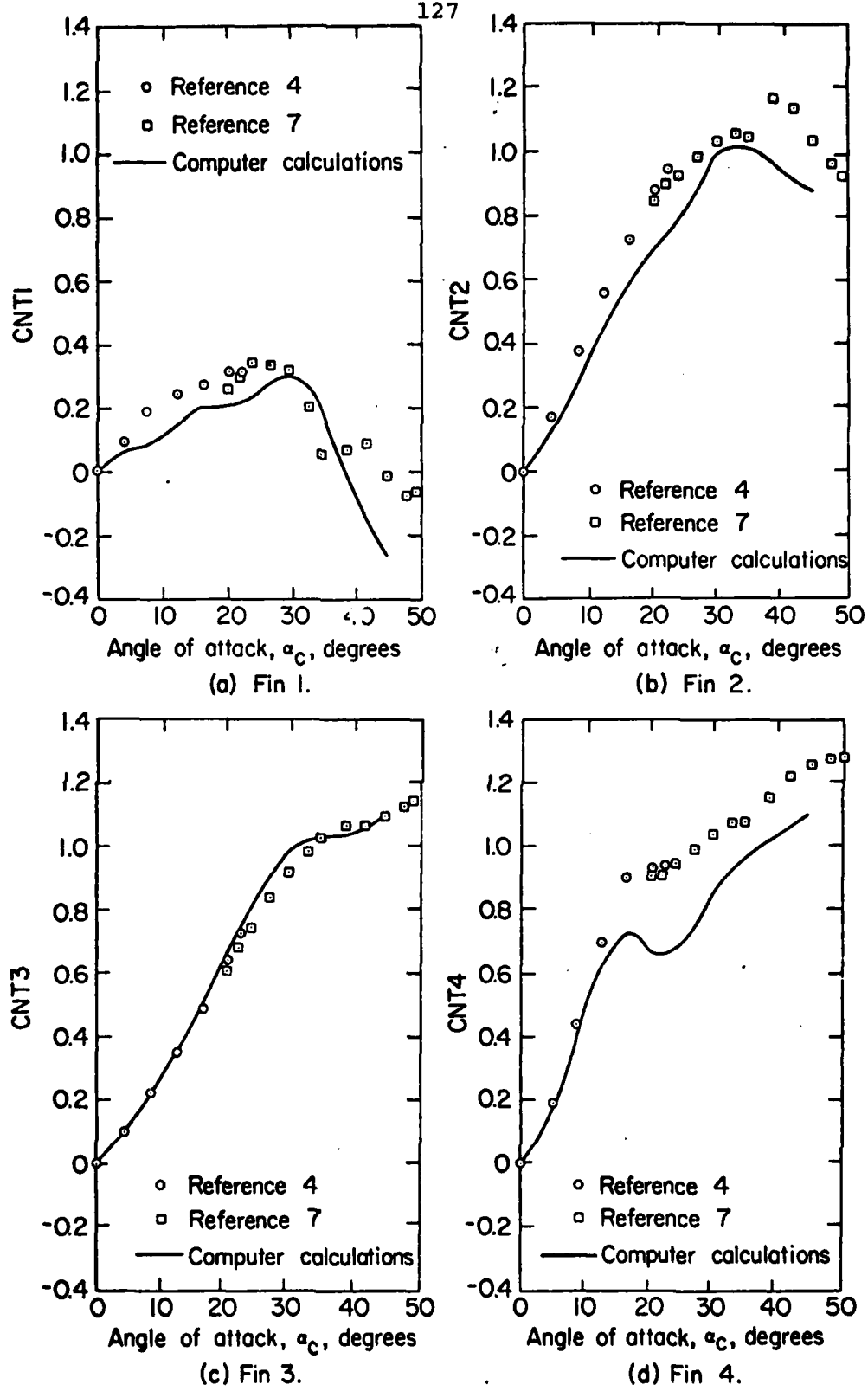


Figure 41. Fin normal-force coefficients for configuration BN₃T₂ at $M_\infty = 0.8$; $\phi = 30^\circ$.

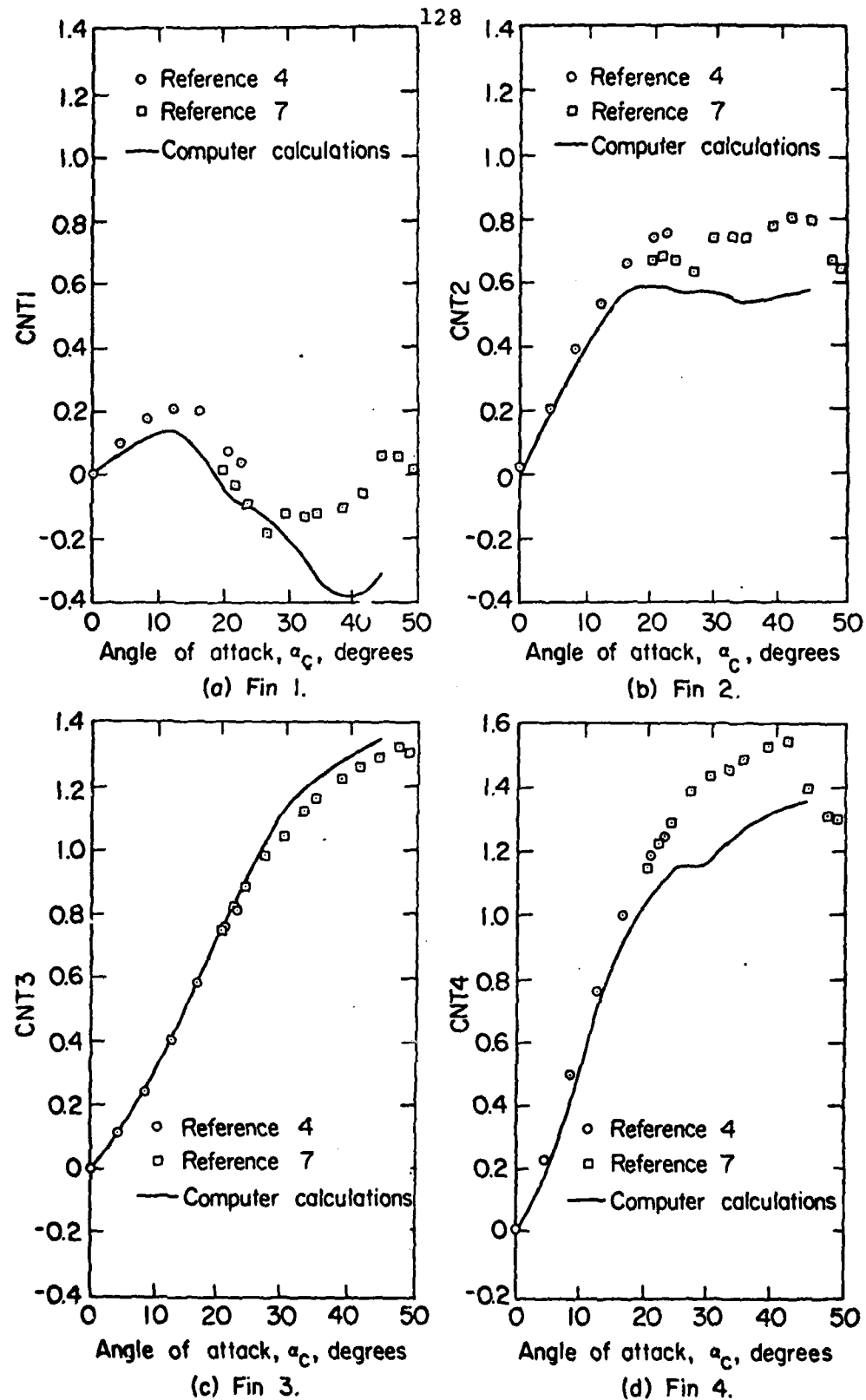


Figure 42. Fin normal-force coefficients for configuration BN₃T₂ at $M_\infty = 1.22$; $\phi = 30^\circ$.

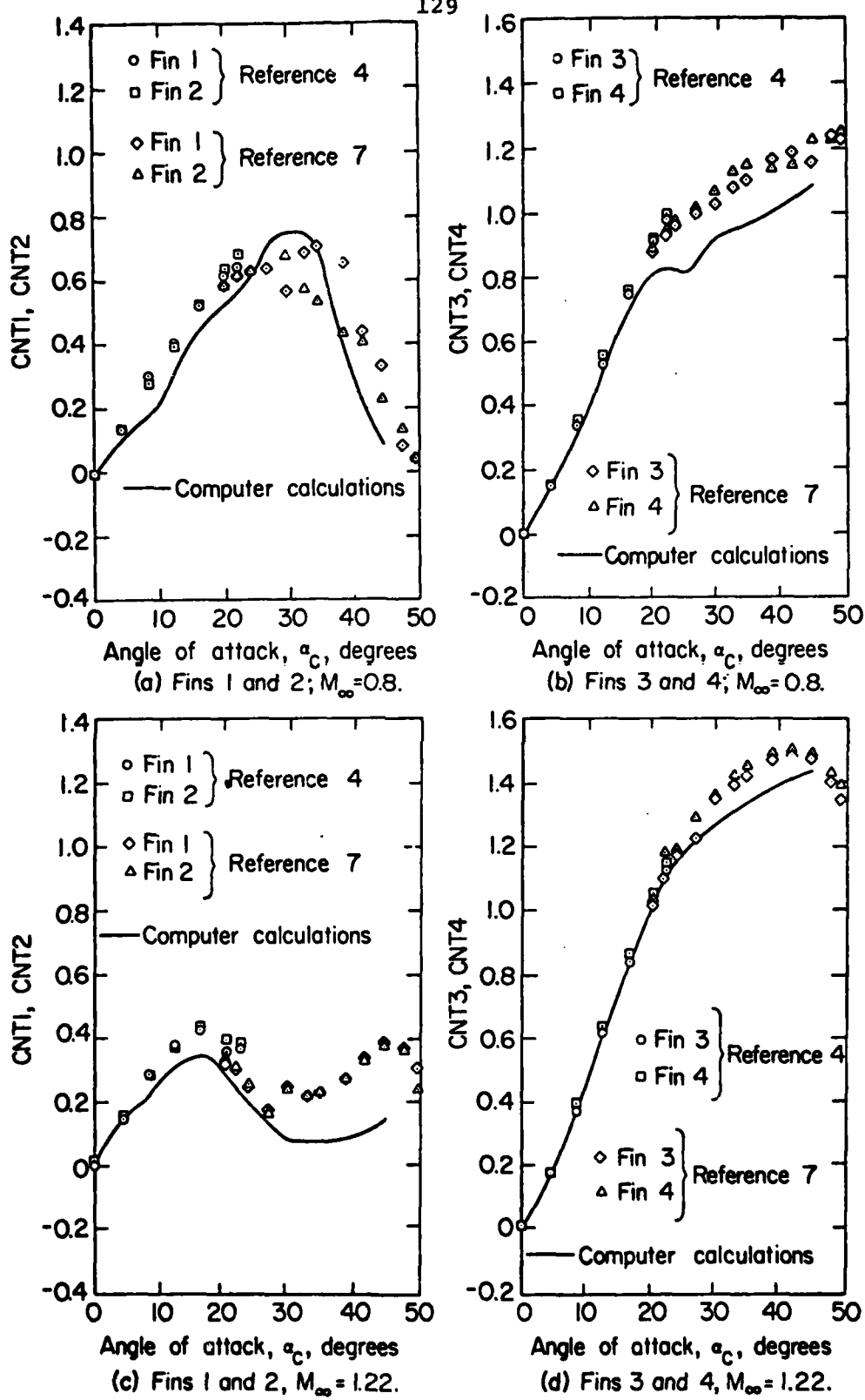


Figure 43. Fin normal-force coefficients for configuration BN, T_2 at $\phi = 45^\circ$.

of the quantities of interest at high angle of attack is the rolling moment induced on a missile with no control deflection. The rolling-moment coefficients for the body-tail configuration are shown in figure 44 for $M_\infty = 0.8$ and $\phi = 10^\circ, 20^\circ$, and 30° . The overall agreement between prediction and experiment is good to about $\alpha_c = 40^\circ$, and the prediction is somewhat high thereafter. The data for $\phi = 10^\circ$ show several oscillations in the range $\alpha_c = 25^\circ$ to $\alpha_c = 40^\circ$. The oscillations could be associated with vortex switching.

The induced rolling-moment coefficients for $M_\infty = 1.22$ are presented in figure 45. The predictions are generally good, except that they are too high at the upper end of the angle of attack range. No probable effects of vortex switching are evident.

7.3 Wing-Body-Tail Combination; No Control

7.3.1 Preliminary remarks.- The wing-body-tail configuration for which suitable data are available for evaluating the predictive method is BN₃C₆T₂ described in figures 7 and 8. The aspect of the predictive method being evaluated is not its ability to predict the canard fin normal-force coefficients and lateral center-of-pressure coefficients, but rather its ability to track the trailing vortex system behind the canard fins, to predict the afterbody vortex strengths and positions, and to predict the tail fin characteristics when subject to this vortex system. For this purpose we will compare prediction and theory for both tail fin normal forces and complete configuration forces and moments in accordance with the following listing.

Figure	M_∞	ϕ	δ_1, δ_3	δ_2, δ_4	Quantities
46	1.3	30°	0	0	C_{NTi} ; $i = 1, 2, 3, 4$
47	1.3	30°	0	0	C_N, C_m, C_n, C_l

7.3.2 Tail fin normal-force coefficients.- Figure 46 shows

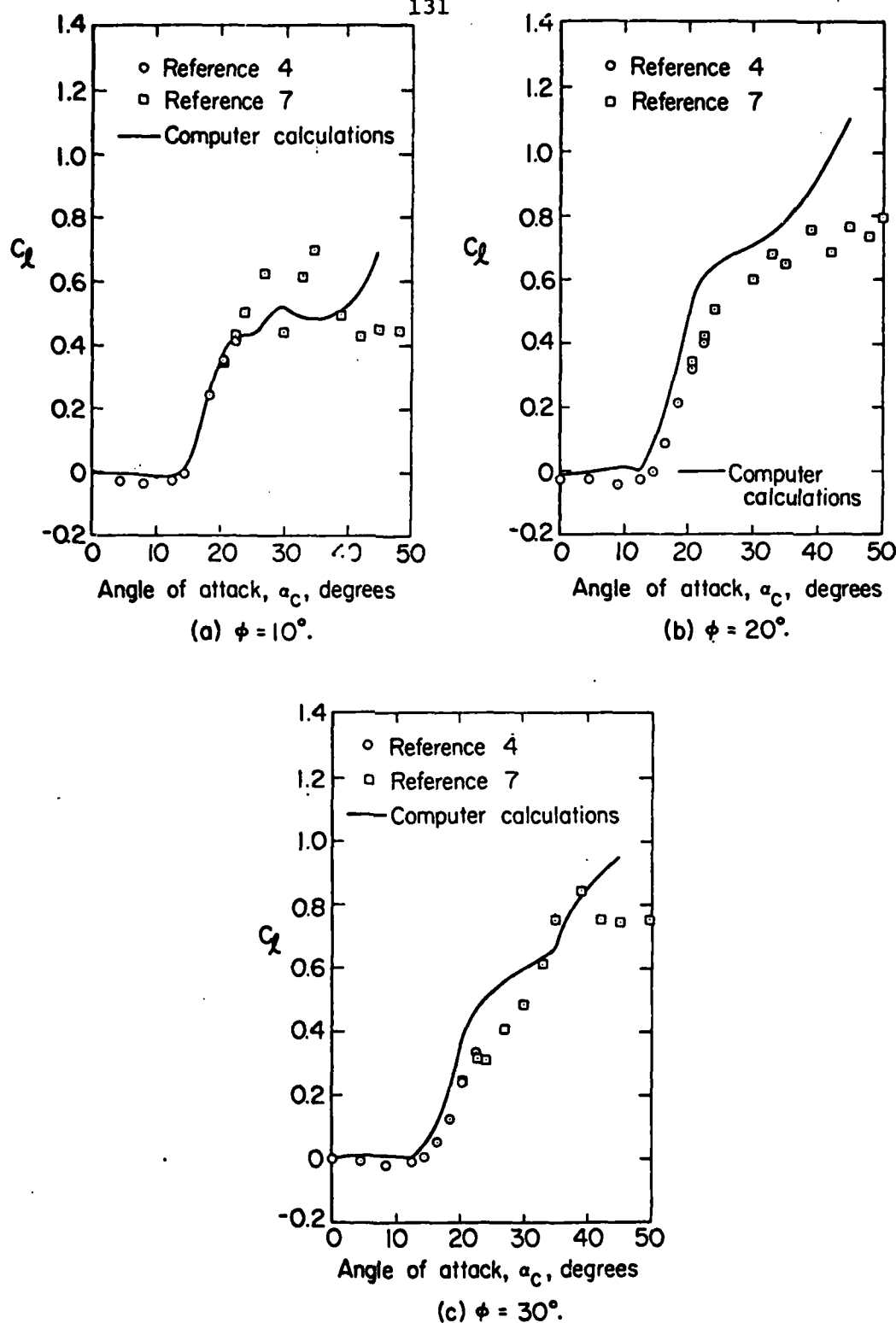


Figure 44. Rolling-moment coefficients for configuration BN₃T₂ at M_∞ = 0.8.

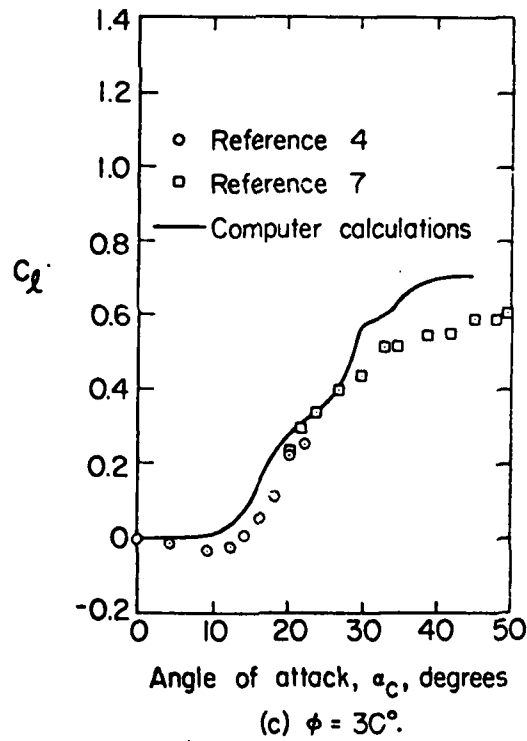
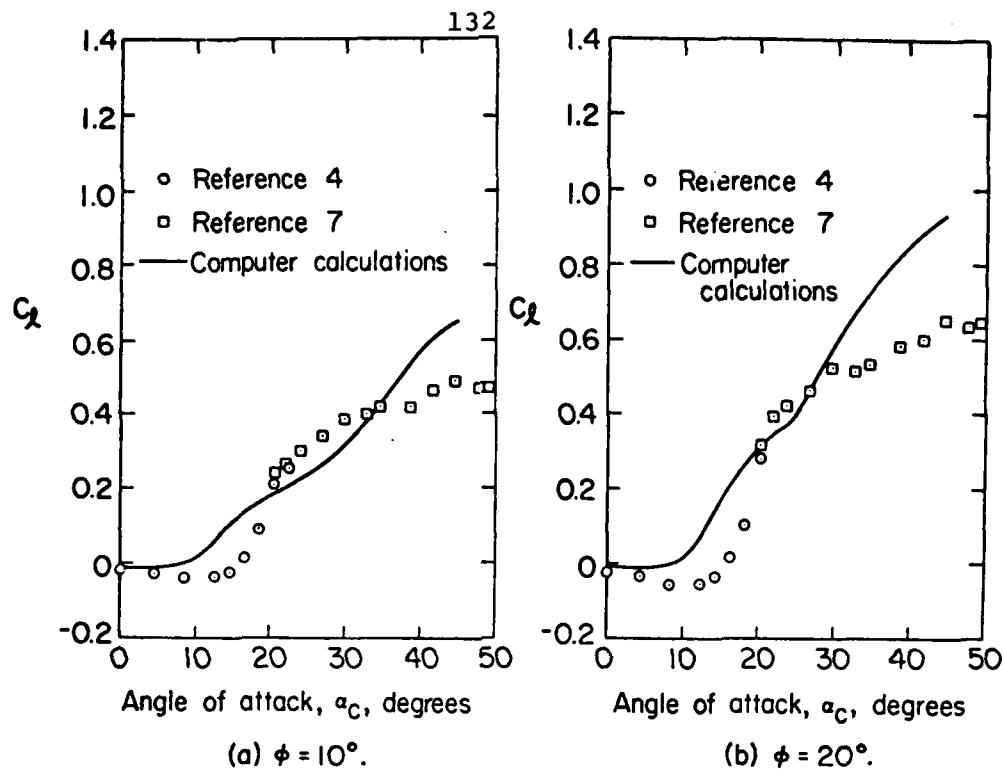


Figure 45. Rolling-moment coefficients for configuration BN₃T₂ at $M_\infty = 1.22$.

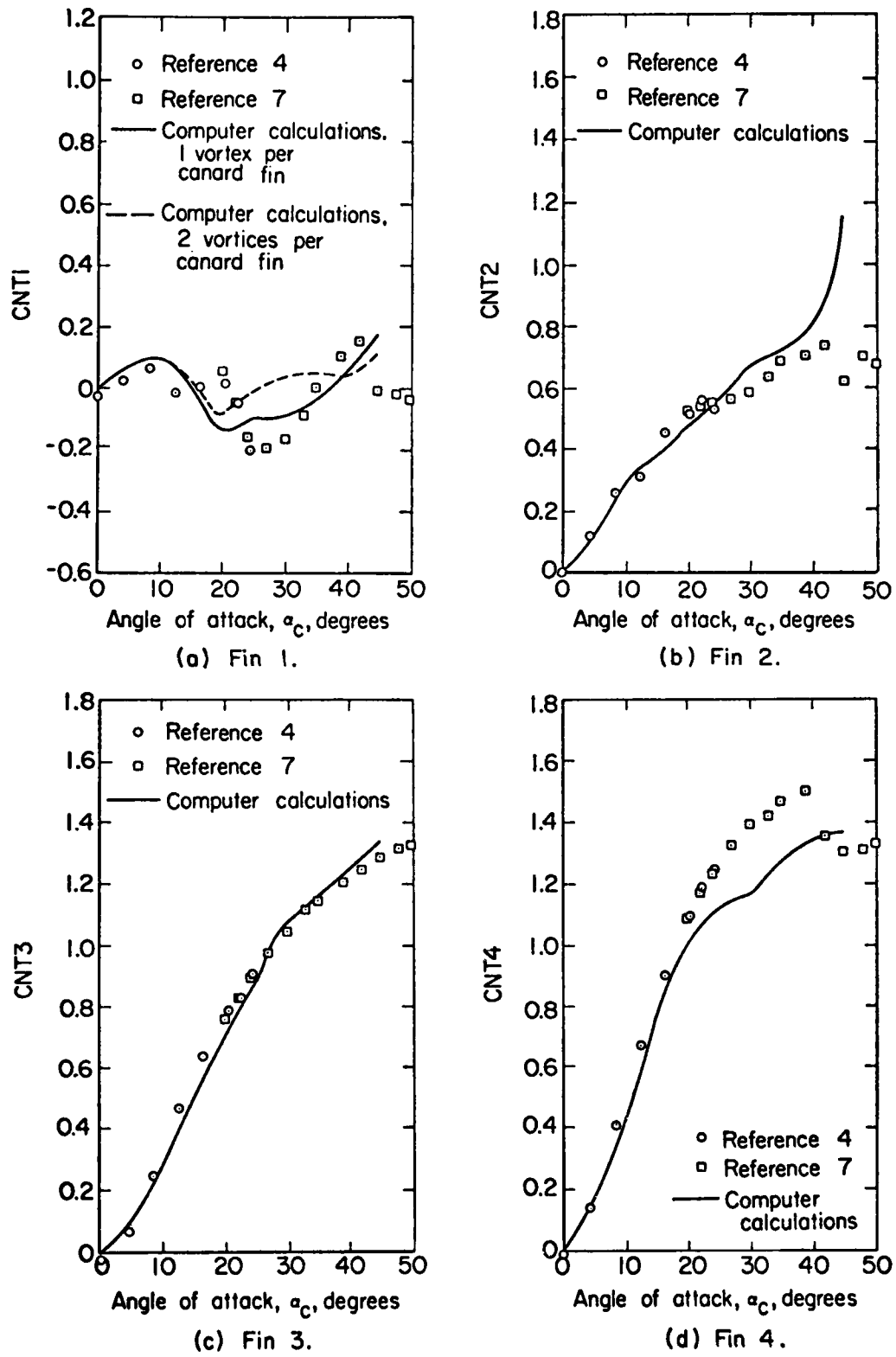


Figure 46. Normal-force coefficients for tail fins of configuration $BN_3C_6T_2$ at $M_\infty = 1.3$ and $\phi = 30^\circ$;
 $\delta_1 = \delta_2 = \delta_3 = \delta_4 = 0^\circ$.

the normal-force coefficients at $M_\infty = 1.3$ and $\phi = 30^\circ$ for fins 1, 2, 3, and 4 with no control. In this figure two theoretical curves are shown for fin T1, one using one vortex per canard fin and one using two vortices per canard fin. There is nothing to choose between the two since the agreement up to about $\alpha_c = 42.5^\circ$ is good. For fin T2 agreement is good to about $\alpha_c = 40^\circ$, for fin T3 to 45° . For fin T4 the data are under predicted for $20^\circ < \alpha_c < 40^\circ$. The predicted stall does not develop.

7.3.3 Wing-body-tail forces and moments.- In figure 47 the normal-force, pitching-moment, yawing-moment, and rolling-moment coefficients for the complete wing-body-tail configuration are given for the same condition as figure 46. For all these coefficients comparison was made between data and prediction calculations based on one vortex per panel and two vortices per panel. The predictions based on two vortices per panel are better for normal-force coefficient, but otherwise not much difference is to be noted. The only serious deviation from theory is the yawing moment which is valid to about $\alpha_c = 35^\circ$

7.4 Wing-Body-Tail Combination With Canard Control

7.4.1 Preliminary remarks.- The ability of the method to predict the effects of canard control on the tail fin normal forces and the complete configuration forces and moments is demonstrated by several sets of calculations. First a set of calculations have been made at $\phi = 0$ using yaw control, and secondly a set of calculations has been made at $\phi = 30^\circ$ with yaw control. The figures showing these effects are as follows.

Figure	M_∞	ϕ	δ_1, δ_3	δ_2, δ_4	Quantities
48	1.3	0	15°	0	C_{NTi} ; $i = 1, 2, 3, 4$
49	1.3	0	15°	0	C_N, C_m, C_n, C_l
50	1.3	30°	15°	0	C_{NTi} ; $i = 1, 2, 3, 4$
51	1.3	30°	15°	0	C_N, C_m, C_n, C_l

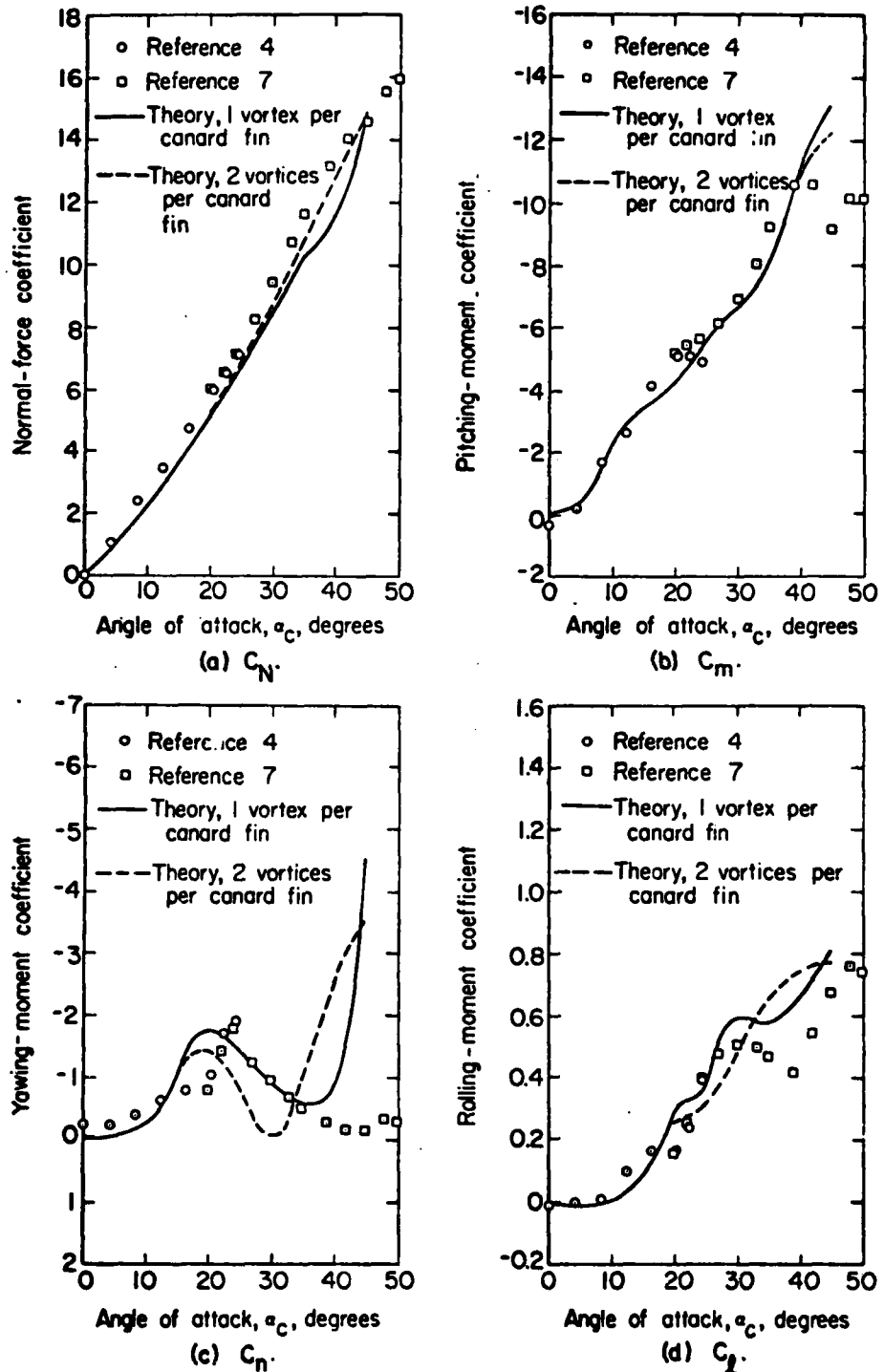


Figure 47. Force and moment coefficients for configuration $BN_3C_6T_2$ at $M_\infty = 1.3$ and $\phi = 30^\circ$; $\delta = \delta_2 = \delta_3 = \delta_4 = 0^\circ$.

It is to be remembered that the normal-force coefficients for the canard fins (C6) were used in the data base, and that the values of k_w used to determine the additional normal force due to control deflection were also derived from C5 canard control deflection data. Accordingly, no comparisons are shown for canard fin quantities.

7.4.2 Yaw control at zero roll angle.- In figure 48 the tail fin normal-force coefficients are shown for 15° of yaw control at zero roll angle. For fin T1 and T4 predictions are shown for two vortices for canard fin. Adding the second vortices is not warranted. Fin 2 exhibits higher experimental values of CNT2 than predicted in the range $15^\circ < \alpha_c < 35^\circ$. This is believed to be strake effect of the vortex from canard fin C3 acting on T2.

The complete wing-body-tail characteristics corresponding to the conditions of figure 48 are given in figure 49. Predictions are shown using 1 and 2 vortices per canard fin. In the cases of yawing-moment and rolling-moment coefficient significant differences between the two predictions exist, but in each case there is no justification to go to the added complication of two vortices per canard fin. For all coefficients but yawing-moment, the predictions are in fair agreement with experiment up to about 40° angle of attack.

The results of figures 46 and 47 for the effect of roll with no control and the results of figures 48 and 49 for the effects of yaw control with no roll show generally the same degree of comparison between prediction and experiment. The next pair of figures examines the case of the combined effects of roll and control.

7.4.3 Yaw control at $\phi = 30^\circ$.- Figure 50 shows the tail fin normal-force coefficients for 15° of canard fin yaw control at a roll angle of 30°. Fin T1 is strongly influenced by the vortices in this case, but the predicted normal-force curve for this

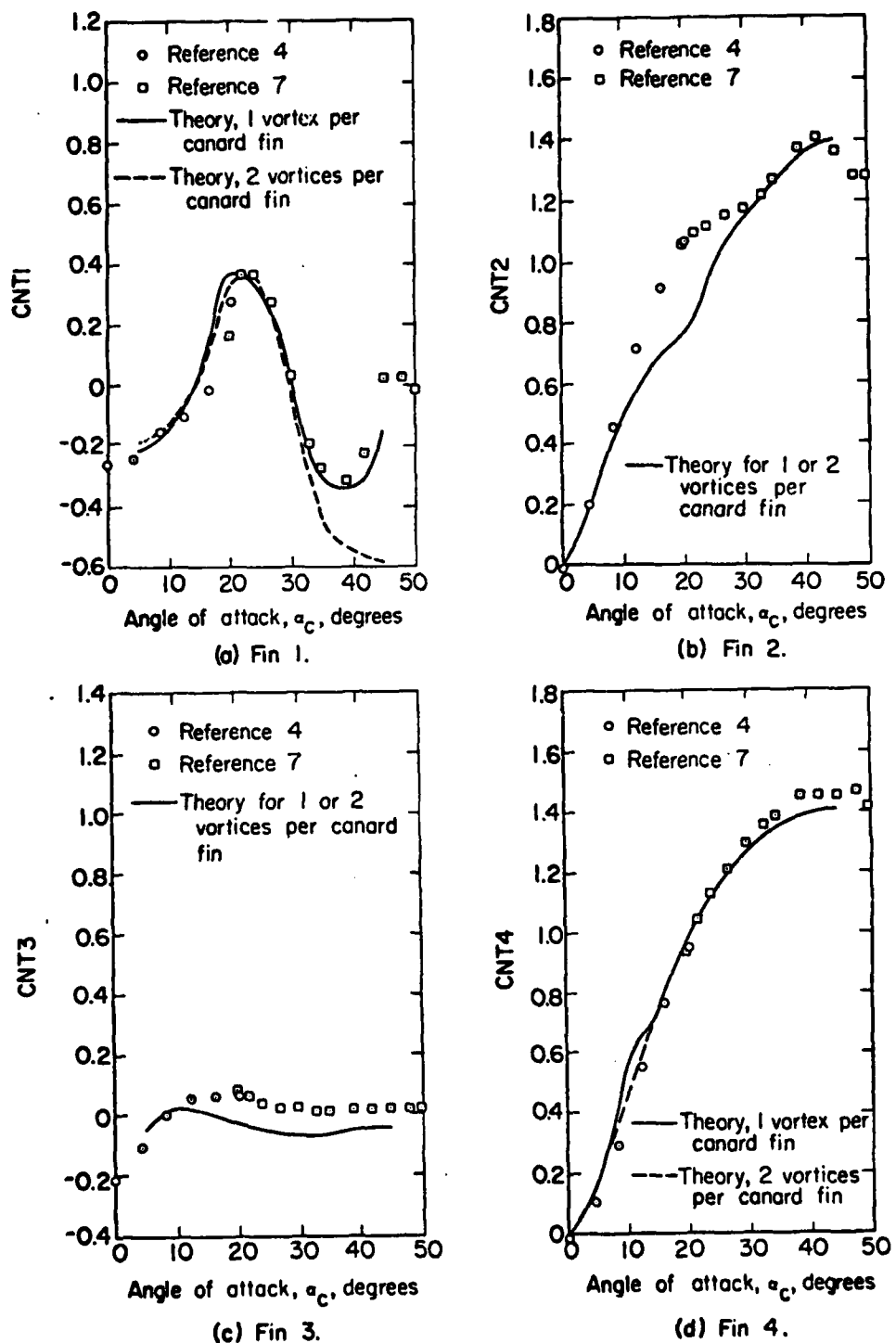


Figure 48. Normal-force coefficients for tail fins of configuration $BN_3C_6T_2$ at $M_\infty = 1.3$ and $\phi = 0^\circ$ with yaw control, $\delta_1 = \delta_3 = 15^\circ$; $\delta_2 = \delta_4 = 0^\circ$.

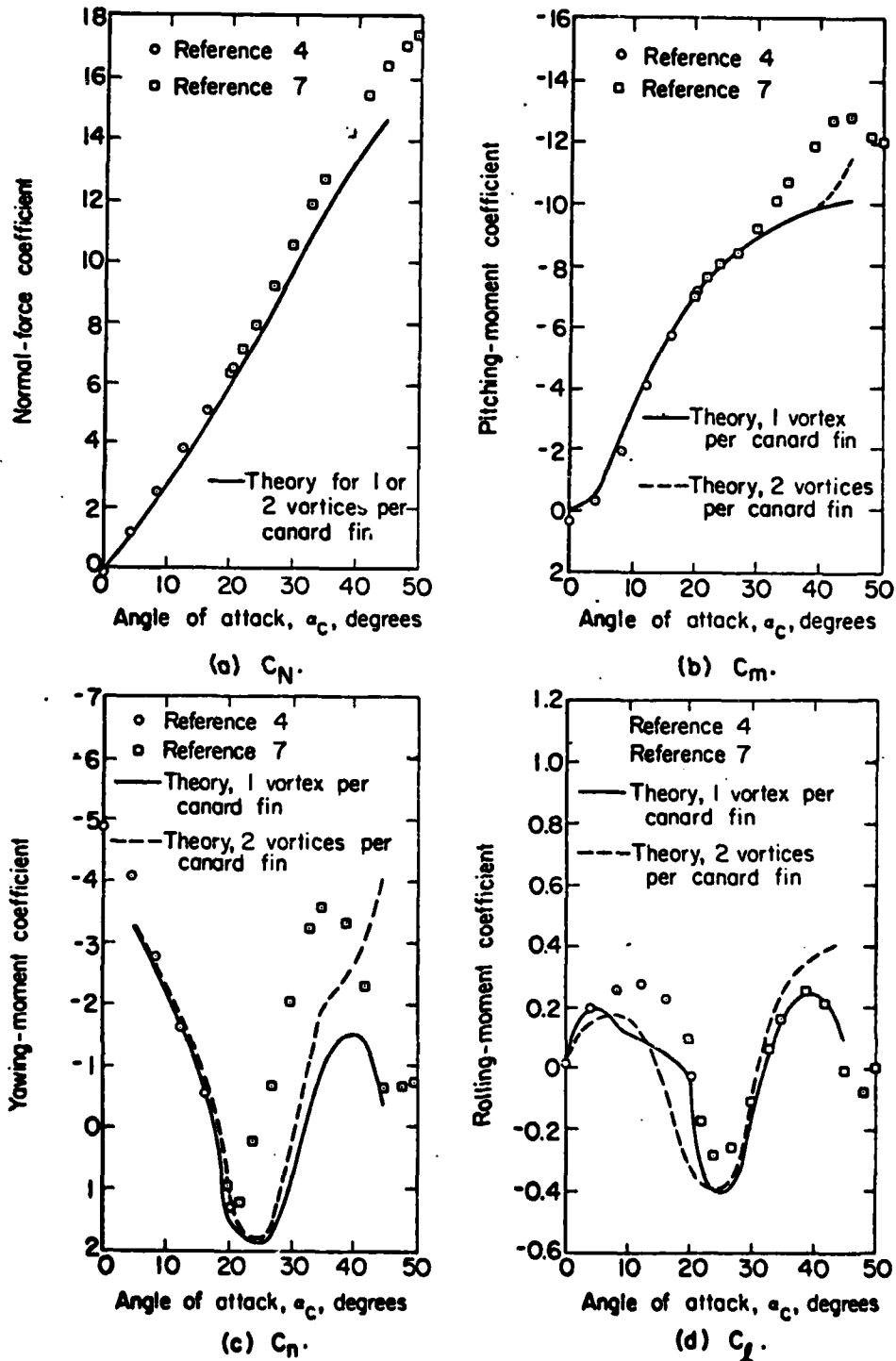


Figure 49. Force and moment coefficients for configuration $BN_3C_6T_2$ at $M_\infty = 1.3$ and $\phi = 0^\circ$ with yaw control,
 $\delta_1 = \delta_3 = 15^\circ$; $\delta_2 = \delta_4 = 0^\circ$.

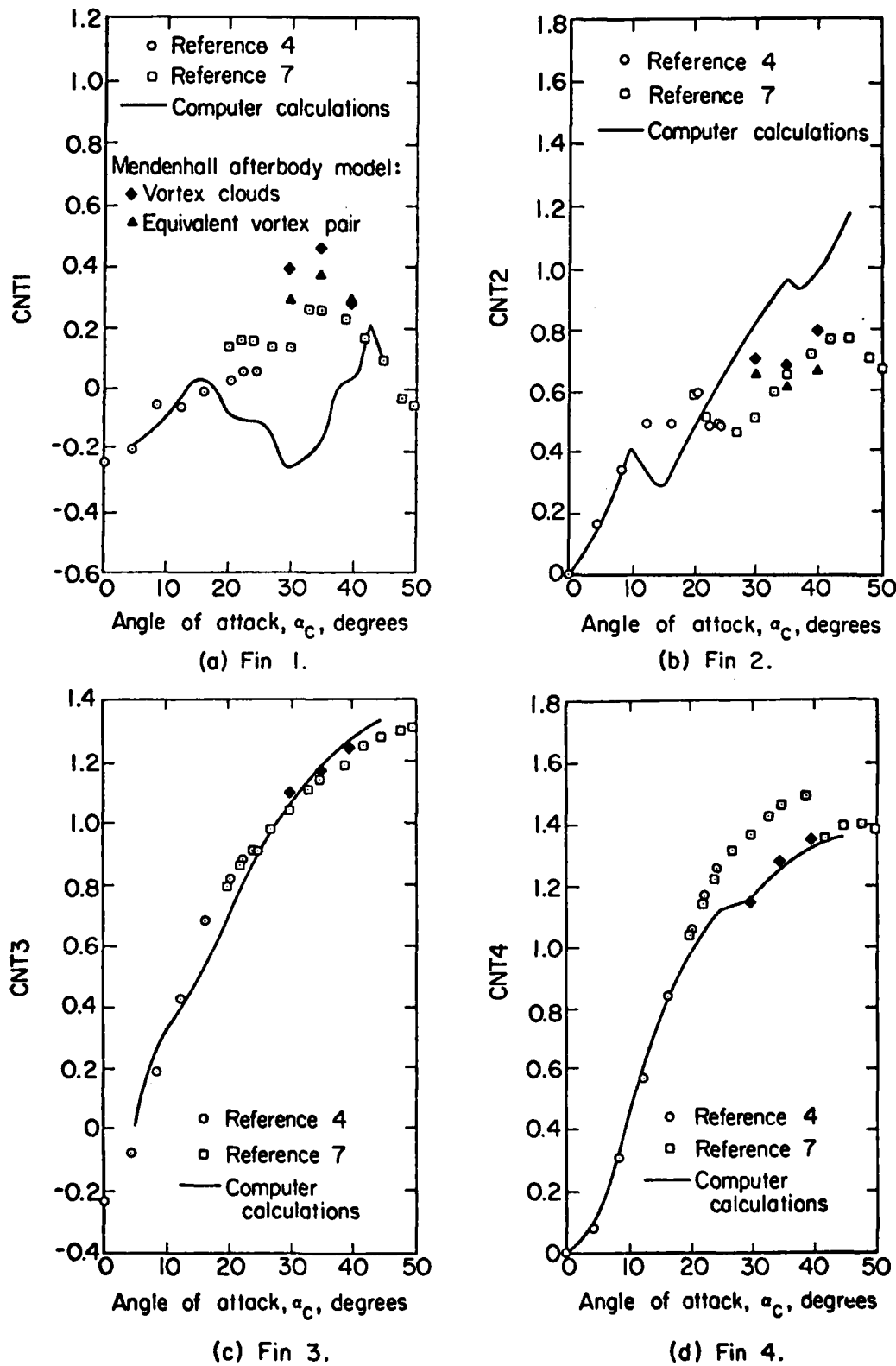


Figure 50. Normal-force coefficients for tail fins of configuration BN₃C₆T₂ at $M = 1.3$ and $\phi = 30^\circ$ with yaw control, $\delta_1 = \delta_3 = 15^\circ$; $\delta_2 = \delta_4 = 0^\circ$.

fin is not good above $\alpha_c = 20^\circ$. The same statement can be made for fin T2 which is also influenced by the vortices.

The complete wing-body-tail coefficients shown in figure 51 exhibit fair agreement between experiment and prediction for C_N and C_m , but poor agreement for C_n and C_λ . It is suspected that the afterbody model presently incorporated in the complete model is simply inadequate for cases of combined roll angle and control deflection. A vortex cloud approach to the afterbody model rather than the approach of several discrete afterbody vortices seems a way out of this difficulty as the next section will describe.

7.5 Improved Afterbody Model

In connection with reference 21 Mendenhall has developed a computer program for calculating the vortex wake on the leeward side of a body of revolution at high angles of attack on the basis of incompressible flow. This program uses the boundary-layer separation criteria of Stratford as modified by Mendenhall for calculating the boundary-layer separation points in the crossflow plane. It does not use the heuristic boundary-layer separation criterion of the present computer program. The program was modified to allow for canard vortices in the crossflow plane at the trailing edge of the canard fins where the calculation is started. The vortex wake of the afterbody between the canard fins and the tail fins has been calculated for the conditions of figures 50 and 51 for $\alpha_c = 35^\circ$, 40° , and 45° . The calculative results at the start of the tail fins are shown in figure 52 for $\alpha_c = 35^\circ$. This figure shows the position of the canard fin vortices as well as the individual vortices making up the vortex clouds shed by the afterbody.

It is noted that the vortices from fins C1, C2 and C4 pass sufficiently far above the tail fins that their influence on them

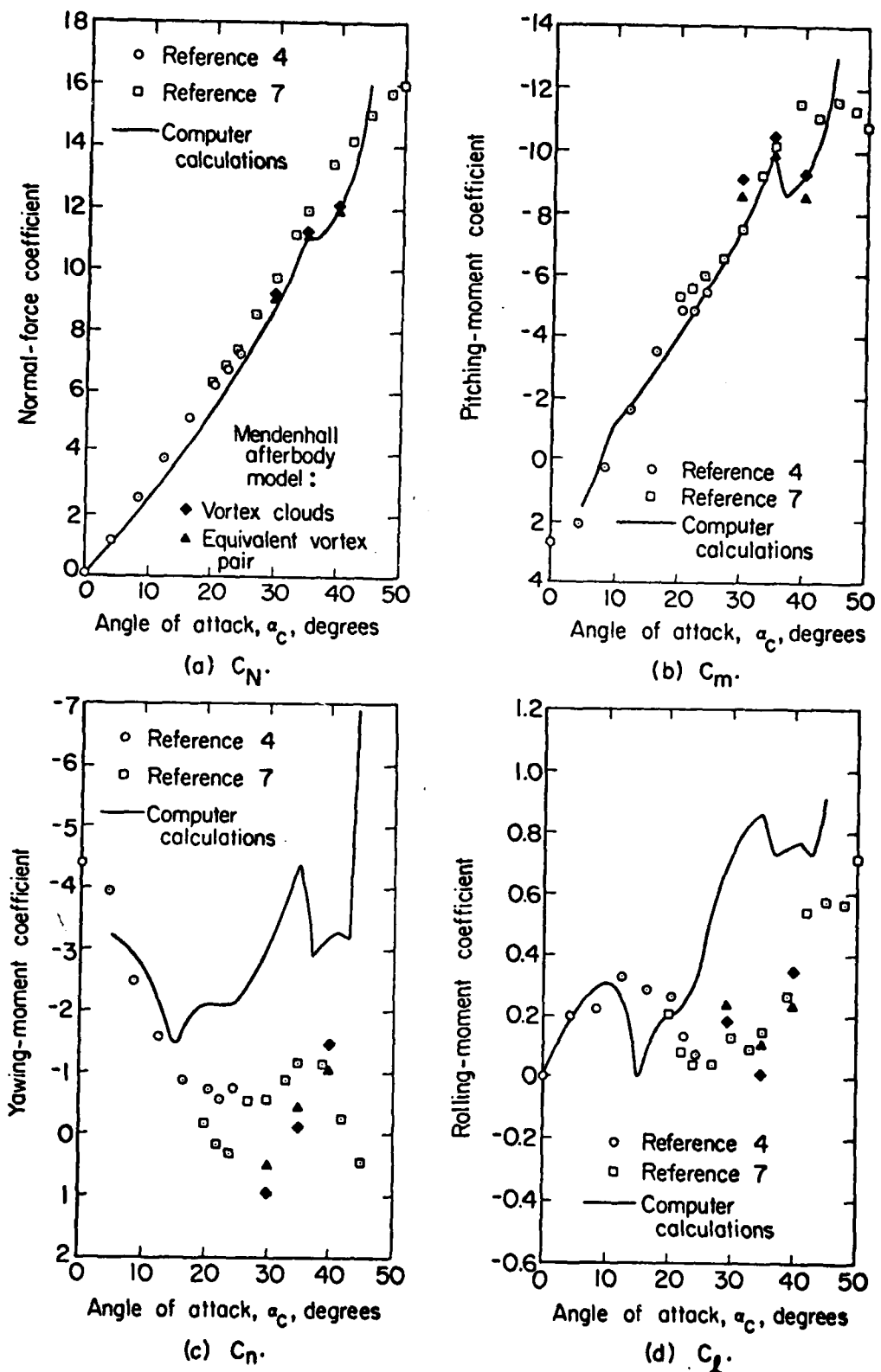


Figure 51. Force and moment coefficients for configuration BN₃C₆T₂ at $M_{\infty} = 1.3$ and $\phi = 30^\circ$ with yaw control; $\delta_1 = \delta_3 = 15^\circ$; $\delta_2 = \delta_4 = 0^\circ$.

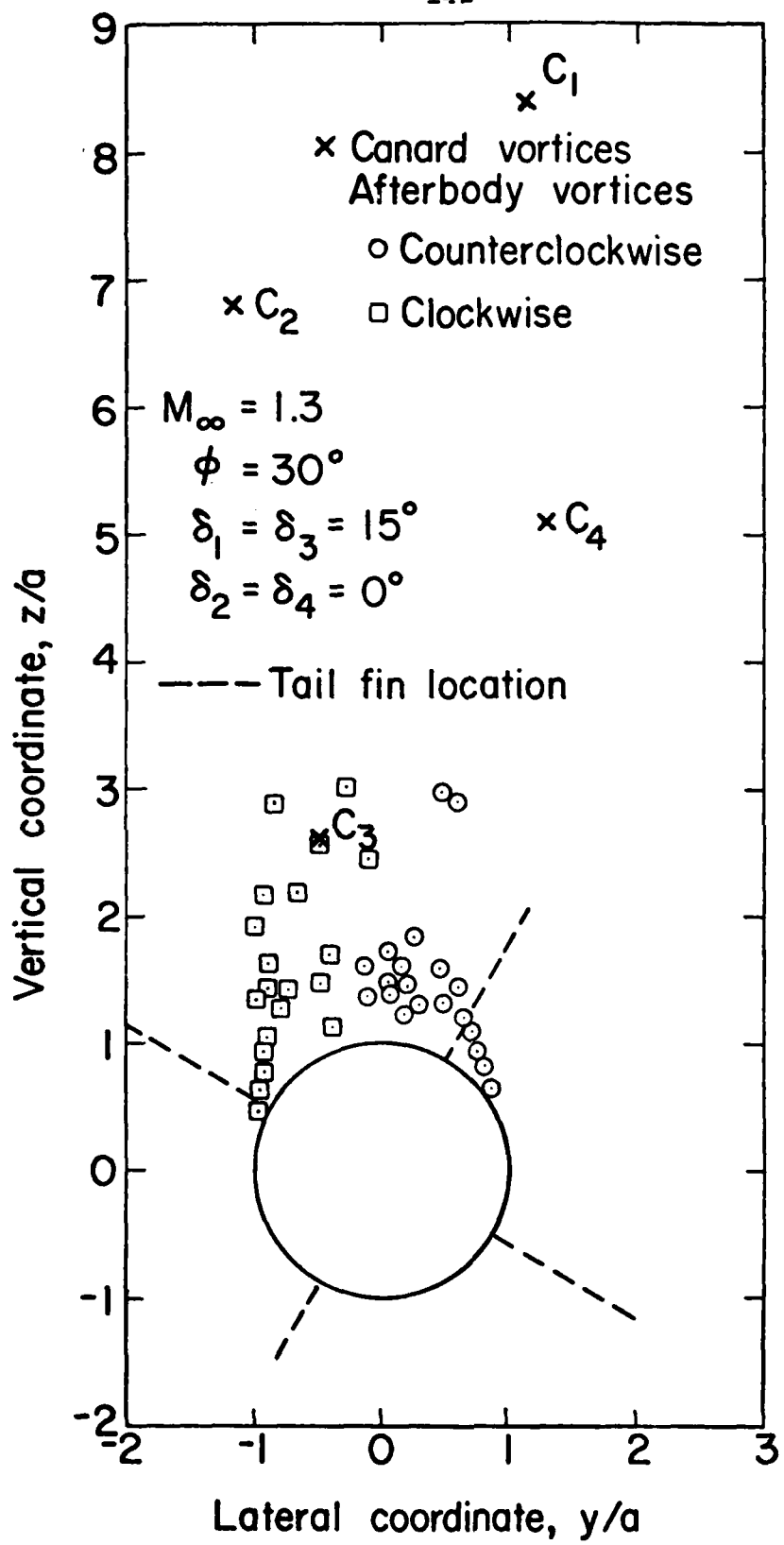


Figure 52. Canard vortex location and afterbody vortex clouds at start of tail section for configuration BN₃C₆T₂ calculated by Mendenhall method.

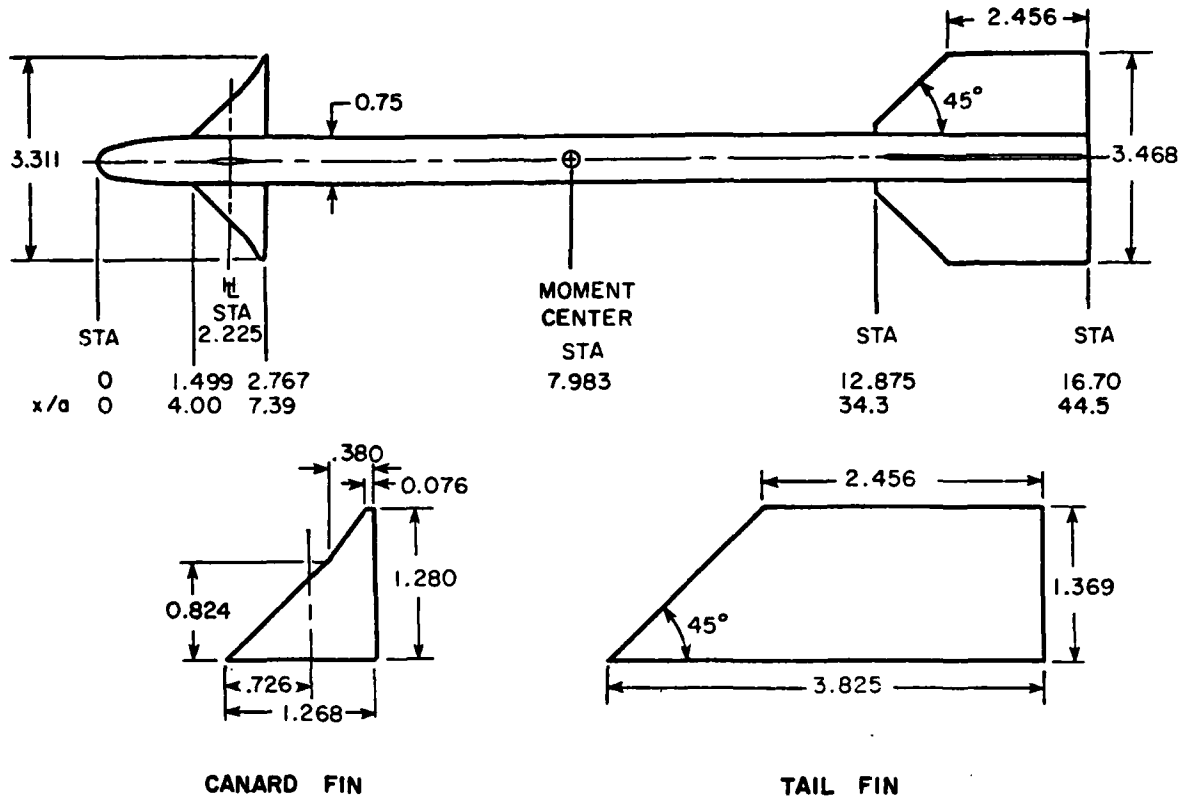
is very small. The principal influences on the tail fins are clearly due to canard vortex C3 and the afterbody vortex clouds. Because canard fin C3 is deflected for yaw control, it sheds a strong vortex. This vortex moves up close to the left side of the afterbody and has a strong influence on the boundary-layer separation from the left side of the body. In fact, as seen in figure 52, vortex C3 is within the left afterbody vortex cloud. It is the strong nonlinear coupling between canard vortex C3 and the development of the left afterbody vortex cloud that is not well modelled by the afterbody vortex model in the computer program. It is also of significance that the afterbody vortex clouds have values of $\Gamma/2\pi aV_\infty$ of about ± 0.25 compared to that for the C3 vortex of -0.16. It is thus quite clear that the afterbody vorticity dominates the nonlinear tail behavior at $\alpha_c = 35^\circ$.

Using the vortex strengths and positions given by the Mendenhall method for $\alpha_c = 30^\circ$, 35° , and 40° , the quantities given in figures 50 and 51 have been recomputed using the computer program. These calculations have been performed in two manners; first using all the individual vortices in each cloud and then using average vortices. Examination of figure 50 shows that the predictions of CNT1 and CNT2 for the leeward fins are now much improved. Only small changes occurs for the windward fins as must be expected. With respect to the complete configuration quantities given in figure 51, the good predictions for C_N and C_m are generally unchanged but those for yawing-moment coefficient and rolling-moment coefficient are now very much improved.

Considerable improvement in computational accuracy can be obtained by incorporating the Mendenhall afterbody model into the computer program for those cases when canard fin vorticities pass close to the body. This step has not been taken in the present work.

7.6 AIM-9L Missile With Yaw Control at Zero Roll Angle

There are very few, if any, data known to the authors to α_c of 40° to 50° to verify the predictive method which have not been used so far. Some data to lower maximum angles of attack exist for the AIM-9L missile. The overall dimensions of the AIM-9L missile used for calculations by the predictive method are shown in figure 53. Predictions have been made of overall force and moment coefficients for this missile for $M_\infty = 0.8$, $\phi = 0^\circ$, and $\delta_1 = \delta_3 = 20^\circ$ with $\delta_2 = \delta_4 = 0$. A comparison is made in figure 54 between the predicted and measured values of normal-force coefficient, pitching-moment coefficient, yawing-moment coefficient, and rolling-moment coefficient. Fair agreement is obtained overall. However, the rolling-moment coefficient is underpredicted by about 35% although the shape of the nonlinearity is correct. The vorticity due to canard fin C3 passes close to a tail fin at $\alpha_c = 8^\circ$. If this vorticity were represented by a cloud rather than a concentrated vortex, perhaps improved predictions would be obtained.



All dimensions in inches

Figure 53. Geometric dimensions of AIM9L missile.

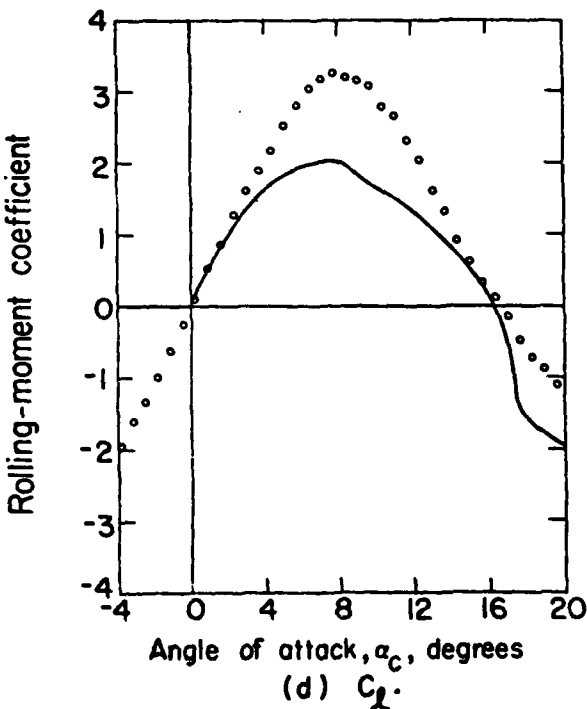
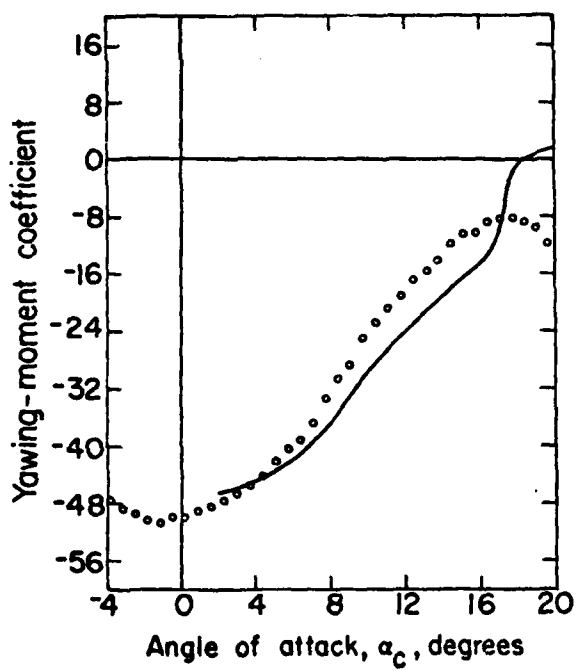
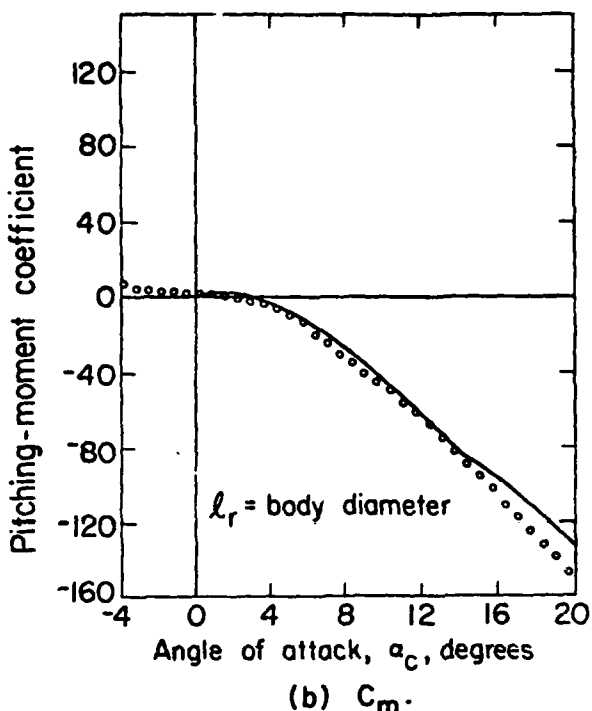
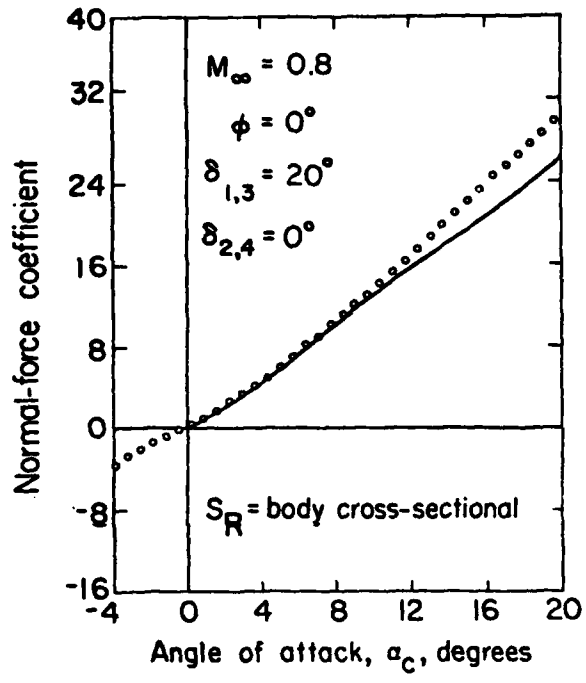


Figure 54. Comparison between measured and predicted characteristics of AIM9L missile at $M_\infty = 0.8$ and $\phi = 0^\circ$ with yaw control;
 $\delta_1 = \delta_3 = 20^\circ$; $\delta_2 = \delta_4 = 0^\circ$.

8. CONCLUDING REMARKS AND RECOMMENDATIONS

8.1 Summarizing Conclusions

(1) The present paper describes a preliminary method together with an associated computer program for estimating the force and moments acting on the various components of a cruciform wing-body-tail combination up to angles of attack of 45° between Mach numbers of 0.8 and 3.0. The data base used in the present method is incomplete. Suitable data for checking the method for $M_\infty > 1.3$ are not available to the best knowledge of the authors. The afterbody model used in the computer program is not accurate for wing-body-tail combinations when canard vortices pass too close to the afterbody. Sufficient data are not available on control effectiveness for use in the method. For these reasons the method should be considered preliminary.

(2) The method utilizes a data base with a limited number of fin planforms, four Mach numbers, and essentially one a/s_m ratio. It utilizes theory to interpolate and extrapolate in the data base with respect to fin aspect ratio, fin taper ratio, a/s_m ratio, and body geometric characteristics. The method also covers arbitrary roll angle, arbitrary fin deflection angles, and two sets of cruciform fins with interference between the forward and rear sets.

(3) The present method can be considered as an extension of the method of reference 6 designed to be valid up to angles of about 45° . The principal extensions to the earlier method include the following:

(a) The equivalent angle of attack concept used in reference 6 with a linear addition theorem has now been generalized to use a nonlinear addition theorem.

(b) The wing-alone normal-force coefficient and

lateral center-of-pressure position used in the method are now obtained from a data base within the program instead of being input data.

(c) The fin normal-force coefficient and lateral center-of-pressure position as a function of angle of attack and angle of roll without vortex interference are now obtained from a data base within the program.

(d) A special high-angle-of-attack body vortex theory has been developed for the predictive method.

(e) Some changes have been introduced into the afterbody model in an attempt to improve its accuracy.

(f) A more general method of handling panel-panel interference has been developed which permits inclusion of roll control in the current program.

(4) Comparison between high-angle-of-attack data for a body-tail configuration up to $\alpha_C = 45^\circ$ have been made for $\phi = 10^\circ, 20^\circ, 30^\circ$, and 45° .

(a) At $M_\infty = 0.8$ the fin normal forces were generally predicted fairly well with two exceptions. The coefficient CNT1 was not well predicted for $\alpha_C > 35^\circ$ at $\phi = 10^\circ$ and $\phi = 20^\circ$. Also the stall measured on fin T4 is milder than that predicted.

(b) At $M_\infty = 1.22$ the results exhibit generally the same behavior as at $M_\infty = 0.8$.

(c) For $\phi = 45^\circ$ the coefficients CNT1 and CNT2 were very nearly equal at $M_\infty = 1.22$ at all angles of attack, whereas differences as large as 0.2 occurred between these quantities at $M_\infty = 0.8$ for the same angle of attack. Furthermore the sign of the difference was neither consistant nor regular, a fact suggesting that bistable vortex flow existed during the test conditions. These results are consistant with the view of Chapman et al. (ref. 11) that the crossflow is basically symmetric

if the crossflow Mach number exceeds 0.5.

(d) The rolling-moment coefficients of the body-tail combination were well predicted up to about $\alpha_c = 40^\circ$ at $M_\infty = 0.8$, and to a somewhat lesser angle at $M_\infty = 1.22$. The predictions tended to be high at very high angles of attack.

(5) Comparison has been made between prediction and data for the tail fin normal-force coefficients of a wing-body-tail combination at $M_\infty = 1.3$ and $\phi = 30^\circ$ with $\delta_1 = \delta_2 = \delta_3 = \delta_4 = 0$. Also the complete configuration normal-force coefficient, pitching-moment coefficient, yawing-moment coefficient, and rolling-moment coefficient prediction are compared with experiment. Good results are obtained for the fin normal-force coefficients and for the configuration coefficients up to $\alpha_c = 45^\circ$ in most cases.

(6) As a test of the ability of the program to predict control effects, the same quantities as above were determined for the same configuration at $M_\infty = 1.3$ with $\delta_1 = \delta_3 = 15^\circ$ and $\delta_2 = \delta_4 = 0$. Generally fairly good results are obtained, better results being obtained using one vortex per canard panel than using two vortices per canard panel. A stall predicted for fin T2 did not develop, and the second peak of the yawing-moment curve was underpredicted.

(7) The combined effects of roll angle and control deflection on the tail fin normal-force coefficients and the complete configuration characteristics were predicted. The following quantities were fairly well predicted: CNT3, C_N , C_m . The following quantities were poorly predicted: CNT1, CNT2, C_n and C_ρ . It is suspected that the heuristic afterbody model used in the method is too approximate for this case. Accordingly, a vortex-cloud calculation was made of the flow over the afterbody in the presence of the canard vortices using the computer program of Mendenhall. Using the vortex cloud afterbody model in the computer program greatly improved the agreement between experiment and theory. This improvement has not been incorporated into

the computer program.

(8) The computer program predicts the normal-force coefficient and moment coefficient of the AIM-9L missile with yaw control at $\phi = 0$ fairly well up to $\alpha_c = 20^\circ$, the limit of the data.

8.2 Recommendations for Further Work

During the present work, a number of gaps in the high-angle-of-attack technology base came to light. Some of them are now listed.

(1) In section 3.2 a rather elaborate procedure was described for "constructing" the wing-alone curves corresponding to the fins of the data base. An interference-free set of wing-alone force and moment data to high angle of attack is needed through the Mach number range since none now exists. Systematic variations in aspect ratio and taper ratio are required.

(2) No suitable data on cruciform missile forces and moments together with fin forces and moments are available for $M_\infty > 1.3$ for checking the present method since the only ones now available have been incorporated into the data base of the predictive method.

(3) Nearly all the data used in the data base are for $a/s_m = 0.5$. Data for other values of a/s_m are needed to verify the present method of treating other values of a/s_m .

(4) In the Mach number range $1.3 < M_\infty < 3.0$, the maximum aspect ratio associated with the fins of the systematic data base is 2. Data for higher aspect ratios are needed.

(5) The high-angle-of-attack body vortex model used in the predictive method is an empirical adaptation of an incompressible model. Clearly a compressible model is desirable. Also vortex clouds were replaced by single vortices with large cores in the method. Some of the difficulty in getting accurate results for fins near

or inside body vortices at high angle of attack may be associated with these points which require further work.

(6) It is clear that the present afterbody model is not of sufficient accuracy under all conditions; notable one of combined roll and fin deflection for wing-body-tail combination. This difficulty can be alleviated in part by the use of "vortex cloud" methods, but further experimental and analytical work is desirable to model the afterbody properly for high angle of attack.

(7) There are not sufficient systematic control data on cruciform canard missiles for $M_\infty > 1.3$ to provide good data on the dependence of the control interference parameter k_w on α_c and ϕ .

REFERENCES

1. Dillenius, M. F. E. and Nielsen, J. N.: Supersonic Lifting-Surface Computer Program for Cruciform Wing-Body Combinations in Combined Pitch and Sideslip. NEAR TR 74, December 1974.
2. Dillenius, M. F. E. and Nielsen, J. N.: Prediction of Aerodynamics of Missiles at High Angles of Attack in Supersonic Flow. NEAR TR 99, October 1975.
3. Hemsch, M. J., Nielsen, J. N., and Dillenius, M. F. E.: Method for Calculating Induced Rolling Moments for Cruciform Canard Missiles at Angles of Attack up to 20 Deg. NWC TP 5761, May 1975.
4. Hemsch, M. J. and Nielsen, J. N.: Test Report for Canard Missile Tests in Ames 6- by 6-Foot Supersonic Wind Tunnel. NEAR TR 72, August 1974.
5. Hemsch, M. J.: Reduced Vapor Screen Data from Canard Missile Tests in Ames 6- by 6-Foot Supersonic Wind Tunnel. NEAR TR 81, February 1975.
6. Hemsch, M. J., Smith, C. A., Nielsen, J. N. and Perkins, S. C., Jr.: Calculation of Component Forces and Moments of Arbitrarily Banked Cruciform Missiles with Control Deflection. Report ONR-CR215-226-3, November 1976.
7. Schwind, R. G.: High Angle Missile Test in the Ames 11-Foot Transonic Wind Tunnel, NEAR TR 134, August 1977.
8. Mendenhall, M. R. and Nielsen, J. N.: Effect of Symmetrical Vortex Shedding on the Longitudinal Aerodynamic Characteristics of Wing-Body-Tail Combinations. NEAR TR 69, NASA-CR-2473, January 1975.
9. Allen, H. J. and Perkins, E. W.: A study of Effects of Viscosity on Flow Over Slender Inclined Bodies of Revolution. NACA TR 1048, 1951.
10. Thomson, K. D. and Morrison, D. E.: The Spacing, Position, and Strength of Vortices in the Wake of Slender Cylindrical Bodies at Large Incidence. J. Fluid Mech, 1971, Vol. 50, part 4, pp. 751-783.
11. Chapman, G. T., Keener, E. R., and Malcolm G. N.: Asymmetric Aerodynamic Forces on Aircraft Forebodies at High Angles of Attack - Some Design Guides. Paper published in Agard Conference Proceedings No.199 on Stall-Spin Problems of Military Aircraft, November 1976.

12. Nielsen, J. N.: "Missile Aerodynamics", McGraw-Hill Book Company, Inc., 1960, pp. 125-129.
13. Fidler, J. E.: A Systematic Experimental Approach to Upgrading Missile Aerodynamic Technology. Paper presented at the 9th Navy Symposium on Aeroballistics, John Hopkins/APL, May 1972.
14. Fidler, J. E. and Bateman, M. C.: Aerodynamic Methods for High Incidence Missile Design. Jour. Space and Rockets, Vol. 12, No. 13, March 1975, pp. 162-168.
15. Gomillion, G. R.: A Compilation of Static Stability and Fin Loads Data for Slender Body Missile Models With and Without Tail Fins and Wings. AEDC-TR-75-125, Vol. I-V, March 1976.
16. No author listed: High Alpha Aerodynamics in Fin Alone (Data reported in AEDC-TR-75-124). Vols. 1 and 2, Propulsion Wind Tunnel Facility, ARO Inc., July 1974.
17. Baker, W. B., Jr.: Static Aerodynamic Characteristics of a Series of Generalized Slender Bodies With and Without Fins at Mach Numbers from 0.6 to 3.0 and Angles of Attack from 0 to 180 Degs., AEDC-TR-65-124, Vol. II, May 1976.
18. Hill, William A., Jr.: Experimental Lift of Low-Aspect-Ratio Triangular Wings at Large Angles of Attack and Supersonic Speeds. NACA RMA57I17, November, 1957.
19. Falunin, M. P., Ul'yanou, G. S.; Makshin, A. A., and Mosin, A. F.: Supersonic Aerodynamic Characteristics of Delta Wings at High Angles of Attack from Izv. AN.SSSR Mekhanika Zhidkosti i Gaza, Vol. 3, No. 5, pp. 105-108, 1968.
20. Nielsen, J. N., Hemsch, M. J., and Dillenius, M. F. E.: The Induced Rolling Moments of Cruciform Wing-Body Combinations as Influenced by Panel-Panel Interference. NEAR TR 75, November 1974.
21. Spangler, S. B. and Mendenhall, M. R.: Further Studies of Aerodynamic Loads at Spin Entry. NEAR TR 141, July 1977.
22. Hill, W. A., Jr. and Kaattari, G. E.: Force and Pressure-Distribution Investigation to High Angles of Attack on All-Movable Triangular and Rectangular Wings in Combination with a Body at Supersonic Speeds. NACA RM A56C12, July 1956.

23. Thomann, H.: Measurement of the Recovery Temperature in the Wake of a Cylinder and of a Wedge at Mach Numbers Between 0.5 and 3. The Aeronautical Research Institute of Sweden (FFA), FFA Report 84, June 1959.
24. Macha, J. M.: A Wind Tunnel Investigation of Circular and Straked Cylinder in Transonic Crossflow. Texas A & M Research Foundation, TAMU Report 3318-76-01, November 1976.
25. Dewey, C. F., Jr.: Near Wake of a Blunt Body at Hypersonic Speeds. AIAA J., Vol. 3, No. pp. 1001-1010, 1965.
26. Jorgensen, L. H.: Prediction of Static Aerodynamic Characteristics for Slender Bodies Alone and with Lifting Surfaces to Very High Angles of Attack. NASA TM X-73,123, July 1976.
27. Sawyer, W. C.: Private Communication (NASA/Langley Research Center).
28. Van Dyke, M.: Perturbation Methods in Fluid Mechanics, 2nd Ed., The Parabolic Press, 1975.
29. Landrum, Emma Jean: Private Communication (NASA/Langley Research Center).
30. Clark, W. H. and Peoples, J. R.: Occurrence and Inhibition of Large Yawing Moments during High Incidence Flight of Slender Missile Configurations. AIAA Paper No. 72-968, September 1972.
31. Agnone, A. M., Zakkay, V. and Tory, E.: Aerodynamics of Slender Finned Bodies at Large Angles of Attack. AIAA Paper No. 77-666, June 1977.
32. Murthy, V. S. and Rose, W. C.: Form Drag, Skin Friction and Vortex Shedding Frequencies for Subsonic and Transonic Cross Flows on Circular Cylinders. AIAA Paper No. 77-687, June 1977.
33. Chaussee, D. S.: Private Communication. NEAR, Inc.
34. Fidler, J. E.: Private Communication. NEAR, Inc.
35. Baker, W. B., Jr.: Static Aerodynamic Characteristics of a Series of Generalized Slender Bodies With and Without Fins at Mach Numbers from 0.6 to 3.0 and Angles of Attack from 0 to 180 Degrees. AEDC TR-75-124, Vols. I and II, May 1976.

36. Jorgensen, L. H. and Perkins, E. W.: Investigation of Some Wake Vortex Characteristics of an Inclined Ogive-Cylinder Body at Mach Number 2. NACA Report 1371, 1958.
37. Spahr, J. R. and Dickey, R. R.: Wind-Tunnel Investigation of the Vortex Wake and Downstream Field Behind Triangular Wings and Wing-Body Combinations at Supersonic Speeds. NACA RM A53D10, June 1953.
38. Gowen, F. E. and Perkins, E. W.: Drag of Circular Cylinders for a Wide Range of Reynolds Numbers and Mach Numbers. NACA TN 2960, June 1953.
39. Walter, L. W. and Lange, A. H.: Surface Temperature and Pressure Distributions on a Circular Cylinder in Supersonic Cross-Flow. NAVORD Report 2854, June 1953 (Aeroballistic Research Report 180).

APPENDIX A

SPAN LOAD DISTRIBUTIONS DUE TO DEFLECTING OR TWISTING
ONE FIN OF A CRUCIFORM WING-BODY COMBINATION

APPENDIX A

SPAN LOAD DISTRIBUTIONS DUE TO DEFLECTING OR TWISTING
ONE FIN OF A CRUCIFORM WING-BODY COMBINATION

A.1 INTRODUCTION

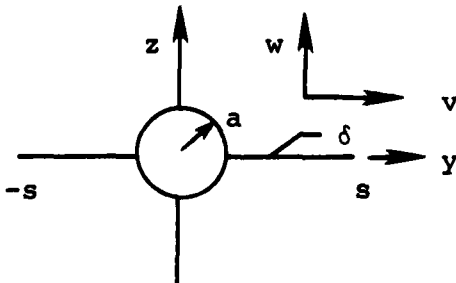
If one fin of a cruciform wing-body combination is deflected, it will induce loadings on the other three fins. These loadings act to counter the rolling moment generated by the deflected fin. The span loadings on the fins in this situation are important influence coefficients which are used to determine the forces induced on the fins of a cruciform wing-body combination by a system of linear external vortices. The purpose of this appendix is to derive formulas for the fin span loadings. The span loadings will be derived on the basis of slender-body theory. However, the manner in which they will be used to determine vortex induced fin loads will permit their use beyond the bounds of slender-body theory.

To obtain the fin normal force induced by a vortex requires the span loadings due to unit deflection of a single fin in reverse flow. To obtain the fin rolling moment induced by a vortex requires the span loadings due to a single fin with a linear twist proportional to distance from the body axis.

A.2 BOUNDARY VALUE PROBLEM

Consider the cross section of a cruciform wing-body combination at zero roll angle and zero angle of attack but with the right fin deflected by angle, δ , positive trailing edge down.

$$\tau = y + iz$$



(A-1)

The crossflow plane is designated by the complex variable. The body radius is "a" and the fin semispan is "s". The vector velocity in the crossflow plane is $v + iw$, and the axial component of velocity is "u". Let the right panel be deflected by the angle δ so that free-stream velocity V_∞ induces an uniform upwash $V_\infty \sin \delta$ through the fin. We must find a potential ϕ which produces equal and opposite downwash on the right fin and at the same time causes no flow normal to the other fins or the body. We are to find the span loadings cc_ℓ along the span of all four fins. The quantity "s" can be a function of x .

A.3 CONFORMAL RELATIONSHIPS

The method of solution is to find the complex potential W which produces unit velocity at a given point on the deflected wing in the range $a \leq y \leq s$ and zero at all other points on the contour. Then the effect of all such fundamental solutions over the range is summed by integration. The fundamental solution is that given by Adams and Dugan in reference A-1. The span loadings are found by evaluating the potential function at the trailing edges.

In obtaining the solution, we will use the theory of conformal transformation. Let the cross-section of the cruciform wing-body combination in the τ plane be transformed into a circle of radius R in the σ plane with

$$\sigma = \xi + i\eta \quad (A-2)$$

The appropriate transformation is (following ref. A-1)

$$\tau^2 + \frac{a^4}{\tau^2} = \sigma^2 + \frac{R^4}{\sigma^2} \quad (A-3)$$

with

$$2R^2 = s^2 + \frac{a^4}{s^2} \quad (A-4)$$

The reciprocal relationships between points in the τ and σ planes are

$$\left. \begin{aligned} \sigma &= \frac{1}{2} \left[\sqrt{\left(\tau^2 + \frac{a^4}{\tau^2} \right)} - 2 + \sqrt{\left(\tau^2 + \frac{a^4}{\tau^2} \right)} + 2 \right] \\ \tau &= \frac{1}{2} \left[\sqrt{\left(\sigma^2 + \frac{1}{\sigma^2} \right)} - 2a^2 + \sqrt{\left(\sigma^2 + \frac{1}{\sigma^2} \right)} + 2a^2 \right] \end{aligned} \right\} \quad (A-5)$$

In these relationships we have set $R = 1$ for convenience and confined attention to the upper half plane.¹ In equation (A-3) we have put the fields at ∞ into the identity relationship

$$\sigma \rightarrow \tau \text{ as } \tau \rightarrow \infty \quad (A-6)$$

unlike the transformation in reference A-1 where a scaling is involved.

Letting $R = 1$, a point on the unit circle $e^{i\theta_0}$ corresponds to y_0 in the physical plane. From equation (A-3)

$$e^{2i\theta_0} + e^{-2i\theta_0} = y_0^2 + \frac{a^2}{y_0^2} \quad (A-7)$$

so that

$$y_0^2 = \cos 2\theta_0 + \sqrt{(\cos 2\theta_0 - a^2)(\cos 2\theta_0 + a^2)} \quad (A-8)$$

and

¹The final formulas for nondimensional quantities are generalized to any R by substituting " a/R " for "a" in the formula and similarly for any other distances.

$$y_0 = \frac{1}{\sqrt{2}} [\sqrt{\cos 2\theta_0 - a^2} + \sqrt{\cos 2\theta_0 + a^2}] \quad (A-9)$$

If $y_0 = s$, then from equations (A-7) and (A-4) with $R = 1$

$$s^2 + \frac{a^4}{s^2} = 2 \cos 2\theta_0 = 2$$

or

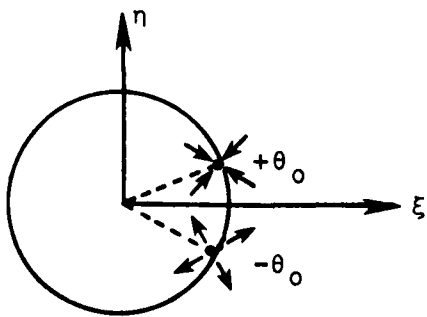
$$\theta_0 = 0 ; y = s \quad (A-10)$$

Let the point $e^{i\gamma}$ correspond in the σ plane to $y = a$ in the τ plane. Then from equation (A-7)

$$\cos 2\gamma = a^2 \quad (A-11)$$

A.4 COMPLEX POTENTIAL FOR DEFLECTION OF RIGHT HORIZONTAL FIN

The potential at the trailing edge of the deflected fin is needed. This is accomplished with a minimum of algebra by first finding the complex potential following the method of Adams and Dugan. Consider points on the upper and lower surfaces of the wing at $y = y_0$ and consider a sink of strength dm at $e^{i\theta_0}$ and a source at point $e^{-i\theta_0}$ in the σ plane.



The complex potential for the sink is (assuming dm is positive)

$$dW_1 = -\frac{dm}{2\pi} \ln(\sigma - e^{i\theta_0})$$

and for the pair, we have

$$dW = \frac{-dm}{2\pi} \ln \left(\frac{\sigma - e^{i\theta_0}}{\sigma - e^{-i\theta_0}} \right) \quad (A-12)$$

It can be shown that the circle

$$\sigma = e^{i\theta}$$

is a streamline of the complex potential given by equation (A-12). However, circle points $e^{i\theta_0}$ and $e^{-i\theta_0}$ are singular points since many streamline converge at these points, with a net mass flow through the circle at these points. Since ϕ and ψ are equal at corresponding points in the τ and σ planes in the conformal transformation of the flow, we can evaluate ψ on the wing panel in the τ plane. Let the velocity components in the τ plane be v and w . Then on the wing panel

$$\frac{d\psi_0}{dy_0} = -w = +\delta V_\infty ; \quad a \leq y_0 \leq s \quad (A-13)$$

Now since only half the source or sink flow passes through the fin, we have

$$\frac{dm}{2} = \delta V_\infty dy \quad (A-14)$$

and

$$dm = 2d\psi_0 = 2\delta V_\infty dy_0 \quad (A-15)$$

Now summing all sources and sinks along both sides of the right panel between $a \leq y_0 \leq s$, we have

$$w = -\frac{1}{\pi} \int_{\psi(a)}^{\psi(s)} \ln \left(\frac{\sigma - e^{i\theta_0}}{\sigma - e^{-i\theta_0}} \right) d\psi_0 \quad (A-16)$$

Integrating by parts, yields

$$\begin{aligned} -W(\sigma) &= \frac{\psi(\gamma)}{\pi} \ln \left(\frac{\sigma - e^{i\gamma}}{\sigma - e^{-i\gamma}} \right) - \frac{i}{\pi} \int_0^\gamma \psi(\theta_0) \frac{d}{d\theta_0} \left[\ln \left(\frac{\sigma - e^{+i\theta_0}}{\sigma - e^{-i\theta_0}} \right) \right] d\theta_0 \\ -W(\sigma) &= \frac{\psi(\gamma)}{\pi} \ln \left(\frac{\sigma - e^{+i\gamma}}{\sigma - e^{-i\gamma}} \right) - \frac{i}{\pi} \int_0^\gamma \frac{(1 - \sigma^2)\psi(\theta_0)d\theta_0}{\sigma^2 - 2\sigma \cos \theta_0 + 1} \\ &\quad - \frac{i}{\pi} \int_0^\gamma \psi(\theta_0)d\theta_0 \end{aligned} \quad (A-17)$$

The third integral is an additive constant.

We now evaluate ψ_0 by integrating equation (A-13)

$$\psi_0 = \delta V_\infty y_0 + k \quad (A-18)$$

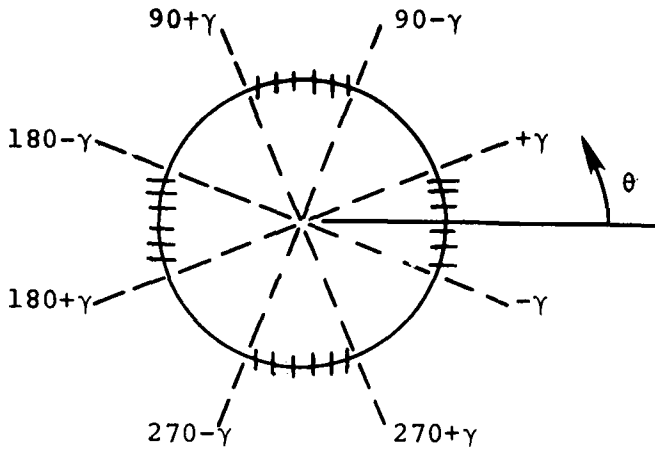
where k is an arbitrary constant which we will set equal to zero. Including the third integral in equation (A-17), we find

$$\begin{aligned} -W(\gamma) &= \frac{\delta V_\infty a}{\pi} \ln \left(\frac{\sigma - e^{i\gamma}}{\sigma - e^{-i\gamma}} \right) \\ &\quad + \frac{i\delta V_\infty \sqrt{2}}{\pi} \int_0^\gamma \frac{(\sigma \cos \theta_0 - 1)[\sqrt{\cos 2\theta_0 - a^2} + \sqrt{\cos 2\theta_0 + a^2}]}{(\sigma^2 - 2\sigma \cos \theta_0 + 1)} d\theta_0 \end{aligned} \quad (A-19)$$

A.5 FIN SPAN LOADINGS DUE TO DEFLECTION OF RIGHT HORIZONTAL FIN

In the transformation of the missile cross-section at the fin trailing edges into the unit circle in the σ plane, the

four fins are mapped onto four arcs on the circle as shown below.



If we evaluate $W(\sigma)$ on the unit circle, its real part will be ϕ_t , the trailing-edge potential function, and its imaginary part will be a constant.

$$\phi_t = \text{R.P. } W(\sigma) \Big|_{\sigma} = e^{i\theta} \quad (\text{A-20})$$

On the unit circle, we can easily show that

$$\text{I.P.} \left[\frac{(\sigma \cos \theta_0 - 1)}{\sigma^2 - 2 \sigma \cos \theta_0 + 1} \right] = \frac{i \sin \theta}{2(\cos \theta - \cos \theta_0)} \quad (\text{A-21})$$

$$\text{R.P. } \ln \left[\frac{\sigma - e^{i\gamma}}{\sigma - e^{-i\gamma}} \right] = \frac{1}{2} \ln \left[\frac{1 - \cos(\theta - \gamma)}{1 - \cos(\theta + \gamma)} \right] \quad (\text{A-22})$$

Utilizing these results in equation (A-19) yields

$$-\phi_t(\theta) = \frac{\delta V_\infty a}{\pi} \ln \left[\frac{1 - \cos(\theta - \gamma)}{1 - \cos(\theta + \gamma)} \right]$$

$$\frac{-\delta V_\infty}{\sqrt{2\pi}} \sin \theta \int_0^\gamma \frac{\sqrt{\cos 2\theta_0 - a^2} + \sqrt{\cos 2\theta_0 + a^2}}{(\cos \theta - \cos \theta_0)} d\theta_0 \quad (\text{A-23})$$

If the point at which the potential is required lies in the interval $-\gamma \leq \theta \leq \gamma$, the integral is defined to be the Cauchy principal value integral. For all fins but the right horizontal fin the integral is regular. The potential ϕ_t is determined by numerical integration of equation (A-23). The span loading is then obtained for the right horizontal fin from the following result:

$$\begin{aligned} cc_1 &= \int_{l.e.}^{t.e.} (P_l - P_u) dx = \frac{-2}{V_\infty} \int_{l.e.}^{t.e.} (u_l - u_u) dx \\ &= \frac{-2}{V_\infty} [\phi_{t_l} - \phi_{t_u}] \end{aligned} \quad (A-24)$$

Similar results hold for the other fins, the signs depending on which direction is taken for positive loading.

A.6 FIN SPAN LOADINGS FOR TWISTED HORIZONTAL RIGHT FIN

To obtain the rolling moments on the fins due to a uniformly deflected right fin, we must find the span loading of a linear twisted right fin. Consider equation (A-17) rewritten as

$$-w(\gamma) = \frac{\psi(\gamma)}{\pi} \ln \left(\frac{\sigma - e^{i\gamma}}{\sigma - e^{-i\gamma}} \right) + \frac{2i}{\pi} \int_0^\gamma \frac{(\sigma \cos \theta_0 - 1)\psi(\theta_0) d\theta_0}{\sigma^2 - 2\sigma \cos \theta_0 + 1} \quad (A-25)$$

We consider a linearly twisted wing such that on the wing surface

$$w = -y_0 V_\infty \quad a \leq y_0 \leq s \quad (A-26)$$

From equation (A-13)

$$\frac{\partial \psi}{\partial y_0} = -w = y_0 V_\infty \quad (A-27)$$

$$\psi = \frac{y_0^2}{2} V_\infty \quad (A-28)$$

where y_0^2 is given in terms of θ_0 and γ by equations (A-8) and (A-11).

Equation (A-25) now becomes

$$-w(\sigma) = \frac{a^2 V_\infty}{2\pi} \ln \left(\frac{\sigma - e^{i\gamma}}{\sigma - e^{-i\gamma}} \right) + \frac{iV_\infty}{\pi} \int_0^\gamma \frac{(\sigma \cos \theta_0 - 1)y_0^2 d\theta_0}{\sigma^2 - 2\sigma \cos \theta_0 + 1} \quad (A-29)$$

Using the results of equations (A-21) and (A-22), we can write for the trailing-edge potential function

$$-\phi_t = \frac{a^2 V_\infty}{4\pi} \ln \left[\frac{1 - \cos(\theta - \gamma)}{1 - \cos(\theta + \gamma)} \right] - \frac{V_\infty \sin \theta}{2\pi} \int_0^\gamma \frac{y_0^2 d\theta_0}{(\cos \theta - \cos \theta_0)} \quad (A-30)$$

This integral is obtained numerically in the same manner as the previous result, equation (A-23).

A.7 REFERENCE

- A-1. Adams, Gaynor J. and Dugan, Duane W.: Theoretical Damping in Roll and Rolling Moment Due to Differential Wing Incidence For Slender Cruciform Wings and Wing-Body Combinations. NACA TR 1088, 1952.

APPENDIX B

NORMAL-FORCE COEFFICIENT AND LATERAL POSITION
OF CENTER OF PRESSURE ON FIN OF CRUCIFORM
WING-BODY COMBINATION DUE TO EXTERNAL VORTEX

APPENDIX B

NORMAL-FORCE COEFFICIENT AND LATERAL POSITION
OF CENTER OF PRESSURE ON FIN OF CRUCIFORM
WING-BODY COMBINATION DUE TO EXTERNAL VORTEX

B.1 INTRODUCTION

Vortices originating upstream of a set of fins on a cruciform wing-body combination can induce large normal forces on the fins. A means is required for estimating such normal forces with due regard for the complicating influences of panel-panel interference. In this appendix we will derive a method based on a reverse-flow theorem for determining both the normal-force coefficient and its lateral center-of-pressure position. Since the results of this derivation are to be used with the equivalent angle of attack concept to determine fin induced loads, we will determine the change in equivalent angle of attack of the fin rather than its change in normal force. Consider that the fin normal force is changed by an amount¹ $(CNF)_v$ as the result of angle-of-attack changes on the fin induced by an external vortex and its image. Let $(dC_N/d\alpha)_F$ be the normal-force-curve slope of the wing formed by joining two fins together. The change in normal-force coefficient $(CNF)_v$ is then equivalent to a change in the wing angle of attack, $(\Delta\alpha_{eq})_v$, given by

$$(\Delta\alpha_{eq})_v = \frac{(CNF)_v}{(dC_N/d\alpha)_F} \quad (B-1)$$

It is noted that the quantity $(\Delta\alpha_{eq})_v$ is the ratio of two normal force quantities. We will calculate both quantities using slender-body theory. The resulting ratio has much greater range of validity than either quantity alone which is subject to the limitations of slender-body theory. This is an example of the same technique which has been used to determine interference factor K_w and

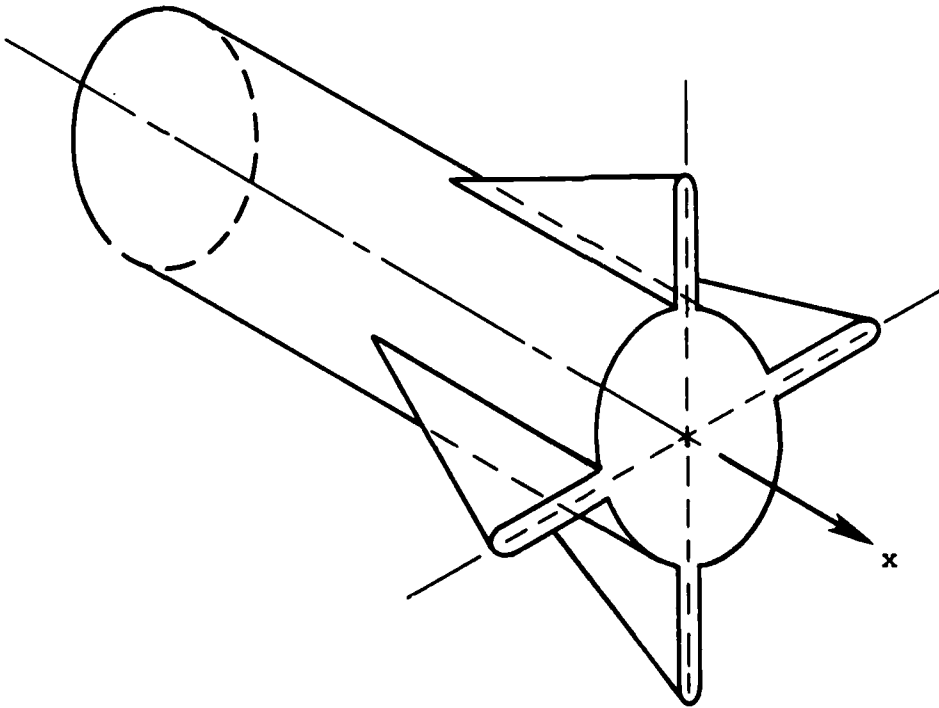
¹We base the coefficient on the fin planform area

K_B (ref. B-1), which are well-known to be accurate far beyond the range of slender-body theory.

In what follows we will first establish a reverse-flow theorem which is applicable to a nonplanar configuration such as a cruciform wing-body combination. Then we will show how specific applications of the reverse-flow theorem will yield both the normal force and rolling moment induced by an external vortex on a fin.

B.2 REVERSE-FLOW THEOREM

We derive the reverse-flow theorem to be used in the present work following the method of reference B-2. Consider first a cruciform wing-body combination at zero angle of attack as sketched below.



Let S be the surface enclosing the wing-body combination and let \vec{n} be the unit outward normal to the surface S at any point on fins or body.

Consider the two perturbation potentials² ψ and ψ' which are solution to Laplace's equation in the region external to S and satisfy different boundary conditions on S . Let the unprimed quantities refer to direct flow and the primed quantities to reverse flow. Then from reference B-2, equation (6), the following reciprocal relationship exists.

$$\iint_S \psi \frac{\partial \psi'}{\partial n} dS = \iint_S \psi' \frac{\partial \psi}{\partial n} dS \quad (B-2)$$

We now choose ψ and ψ' to be certain functions as follows:

$$\left. \begin{aligned} \psi &= \phi(x, y, z) & \psi' &= u'(x, y, z) \\ \frac{\partial \phi}{\partial x} &= u(x, y, z) & \psi' &= \frac{\partial \phi'}{\partial x} \\ \frac{\partial \phi}{\partial n} &= v_n(x, y, z) & v'_n &= \frac{\partial \phi'}{\partial n} \end{aligned} \right\} \quad (B-3)$$

Applying equation (B-2) yields

$$\iint_S \phi \frac{\partial u'}{\partial n} dS = \iint_S u' v_n dS \quad (B-4)$$

The irrotational condition gives

$$\frac{\partial u'}{\partial n} = \frac{\partial v'_n}{\partial x} \quad (B-5)$$

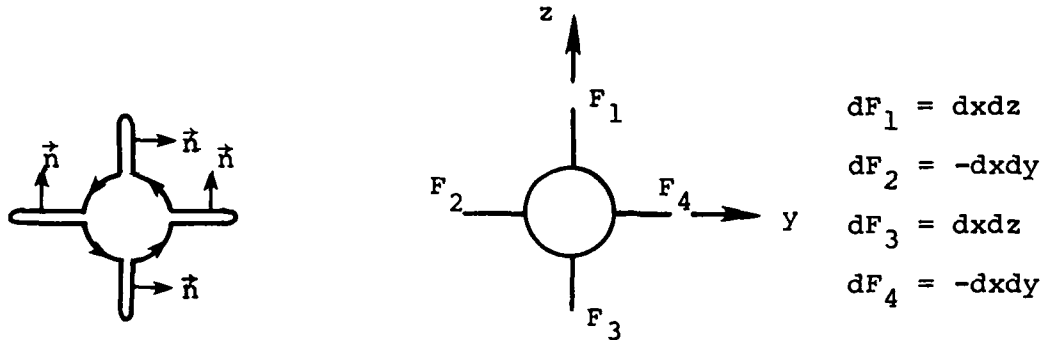
if \vec{x} goes into \vec{n} by a 90° right-hand rotation.

We thus find

$$\phi \frac{\partial u'}{\partial n} = \phi \frac{\partial (v'_n)}{\partial x} = \frac{d}{dx} (\phi v'_n) - v'_n \frac{\partial \phi}{\partial x} \quad (B-6)$$

²Special symbols defined and used only in this appendix are not included in the list of symbols.

Integrating over the fin surfaces with unit normals \vec{n} as shown



and designating these parts of S as S_1 , we have

$$\iint_{S_1} \phi \frac{\partial u'}{\partial n} dS_1 = \iint_{-\infty}^{+\infty} \frac{d(\phi v'_n)}{dx} dx dy - \iint_{S_1} v'_n \frac{\partial \phi}{\partial x} dS_1 \quad (B-7)$$

At $x = +\infty$ we find $\phi = 0$, and at $x = -\infty$ we have that v'_n is zero. Hence

$$\iint_{S_1} \phi \frac{\partial u'}{\partial n} dS_1 = - \iint_{S_1} v'_n u dS_1 \quad (B-8)$$

Considering now the opposite fin surface, we have

$$\frac{\partial u'}{\partial n} = \frac{-\partial v'_n}{\partial x} \quad (B-9)$$

and designating the surfaces of the fins as S_2 , we have similar to equation (B-8)

$$\iint_{S_2} \phi \frac{\partial u'}{\partial n} dS_2 = - \iint_{S_2} v'_n u dS_2 \quad (B-10)$$

Recognizing that the direction of integration is counterclockwise we have

$$dS = dS_1 = -dS_2 \quad (B-11)$$

and since we will deal only with solutions for which v'_n or

v'_n will be zero on the body, we can write

$$\iint_S \phi \frac{\partial u'}{\partial n} dS = \iint_{\sum F_i} v'_n u dS \quad (B-12)$$

Utilizing equation (B-4), we now have

$$- \iint_{\sum F_i} v'_n u dS = \iint_{\sum F_i} u' v_n dS \quad (B-13)$$

At this point we make use of the linear pressure coefficient relationship

$$P = \frac{-2u}{V_\infty} \quad (B-14)$$

to write equation (B-13) in the form we will be using

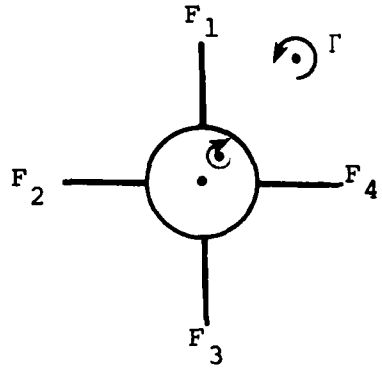
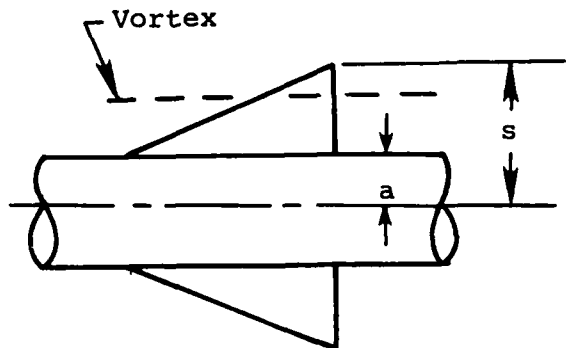
$$- \iint_{\sum F_i} \alpha'_n P dS = \iint_{\sum F_i} \alpha_n P' dS \quad (B-15)$$

where

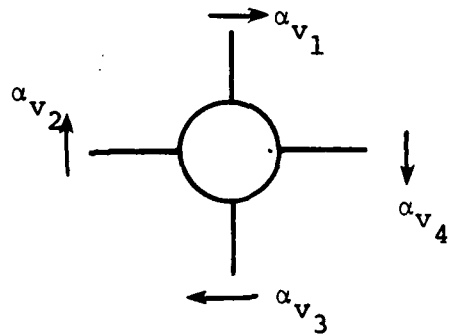
$$\alpha_n = \frac{v_n}{V_\infty} \quad \alpha'_n = \frac{v'_n}{V_\infty} \quad (B-16)$$

B.3 FIN NORMAL FORCE DUE TO EXTERNAL VORTEX

Consider now a planview and a rearview of a cruciform wing-body combination at zero angle of attack with a vortex parallel to the x axis.



As a direct-flow boundary condition, let each fin of zero thickness have local angle of attack $\alpha_v(y)$ induced by the vortex. We will define positive directions of α_v in accordance of what will be induced by a vortex in the first quadrant with counterclockwise vorticity.



The boundary conditions on the fin surfaces designated by \vec{n} in the sketch following equation (B-6) are now

$$\left. \begin{array}{l} F_1: \alpha_{n_1} = \alpha_{v_1}(y) \\ F_2: \alpha_{n_2} = \alpha_{v_2}(y) \\ F_3: \alpha_{n_3} = -\alpha_{v_3}(y) \\ F_4: \alpha_{n_4} = -\alpha_{v_4}(y) \\ \text{Body: } \alpha_n = 0 \end{array} \right\} \quad (B-17)$$

Actually we are letting the fins be twisted in accordance with the foregoing equations, but are keeping the body unchanged by the image vortex. The pressure coefficient associated with this direct flow is that due to the vortex, P_v .

Let us now set up the reverse-flow boundary conditions. We take these to be

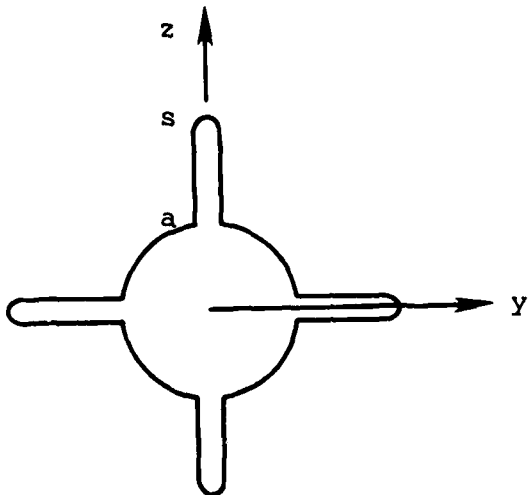
$$\alpha'_n = -1 \quad \text{on upper surface and } +1 \text{ on lower surface of } F_4 \quad (B-18)$$

$$\alpha'_n = 0 \quad \text{on } F_1, F_2, F_3 \text{ and the body}$$

We designate the associated pressure coefficient as P_δ . Equation (B-15) now gives

$$-\iint_{F_4} P_v dS = \iint_{\sum F_i} P_\delta \alpha_n dS \quad (B-19)$$

Consider the integral around fin F_1 from the right side to the left side



On fin F_1 we have for each side

Right Side	Left Side
$dS = dS_1$	$dS = -dS_2$
$dS_1 = dx dz$	$dS_2 = -dx dz$
$P_\delta = P_{\delta_R}$	$P_\delta = P_{\delta_L}$
$\alpha_n = \alpha_1(y)$	$\alpha_n = -\alpha_1(y)$

(B-20)

Considering both sides of F_1 we have

$$\iint_{F_1} P_\delta \alpha_n dS = \int_a^s \alpha_1(y) \int_{-\infty}^{+\infty} (P_{\delta_L} - P_{\delta_R}) dx dy \quad (B-21)$$

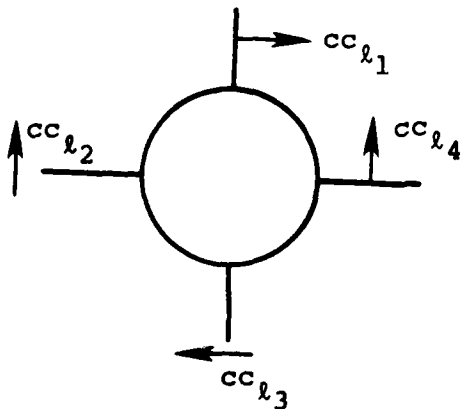
Define a span loading associated with P_δ

$$(cc_{\ell})_1 = \int_{\ell.e.}^{t.e.} (P_{\delta_L} - P_{\delta_R}) dx \quad (B-22)$$

The limits could be $\pm\infty$, but no contribution to the integral occurs for points off the wing. Accordingly

$$\iint_{F_1} P_\delta \alpha_n dS = - \int_a^s \alpha_1(y) (cc_{\ell})_1 dy \quad (B-23)$$

Let us now define positive span loading in accordance with its direction for the induced loading due to deflection of F_4 trailing edge down.



Continuing with F_2

Upper Side

$$dS = dS_1$$

$$dS_1 = -dx dy$$

$$P_\delta = P_{\delta_u}$$

$$\alpha_n = \alpha_{v_2}$$

Lower Side

$$dS = -dS_2$$

$$dS_2 = dx dy$$

$$P_\delta = P_{\delta_l}$$

$$\alpha_n = -\alpha_{v_2}$$

$$\iint_{F_2} P_\delta \alpha_n dS = \int_{-s}^{-a} \alpha_{v_2} \int_{-\infty}^{+\infty} (P_{\delta_l} - P_{\delta_u}) dx dy \quad (B-24)$$

$$\iint_{F_2} P_\delta \alpha_n dS = \int_{-s}^{-a} \alpha_{v_2} (y) (cc_l)_2 dy \quad (B-25)$$

For fin F_3

Right Side

$$dS = dS_1$$

$$dS_1 = dz dx$$

$$\alpha_n = -\alpha_{v_3}$$

$$P_\delta = P_{\delta_R}$$

Left Side

$$dS = -dS_1$$

$$dS_2 = -dz dx$$

$$\alpha_n = \alpha_{v_3}$$

$$P_\delta = P_{\delta_L}$$

$$\begin{aligned} \iint_{F_2} P_\delta \alpha_n dS &= - \int_{-s}^{-a} \alpha_{v_3} \int_{-\infty}^{+\infty} (P_{\delta_R} - P_{\delta_L}) dx dz \\ &= - \int_{-s}^{-a} \alpha_{v_3} (z) (cc_l)_3 dz \end{aligned} \quad (B-26)$$

For fin F_4

Upper Surface

$$dS = dS_1$$

$$dS_1 = -dydx$$

$$P_\delta = P_{\delta_u}$$

$$\alpha_n = +\alpha_{v_4}$$

Lower Surface

$$dS = -dS_2$$

$$dS_2 = dydx$$

$$P_\delta = P_{\delta_l}$$

$$\alpha_n = -\alpha_{v_4}$$

$$\begin{aligned} \iint_{F_4} P_\delta \alpha_n dS &= - \int_a^s \alpha_{v_4} \left[\int_{-\infty}^{+\infty} (P_{\delta_u} - P_{\delta_l}) dx dy \right] dy \\ &= \int_a^s \alpha_{v_4} (y) (cc_l)_4 dy \end{aligned} \quad (B-27)$$

Let us now evaluate the left-hand term of equation (B-19)

Upper Surface

$$dS = dS_1 = -dx dy$$

$$P_v = P_{v_{u_1}}$$

Lower Surface

$$dS = -dS_2 = -dx dy$$

$$P_v = P_{v_l}$$

$$\alpha_n = +1$$

$$\begin{aligned} \frac{N_{F_4}}{q_\infty} = & - \int_a^{s_m} \alpha_{v_1} (z) (cc_\ell)_1 dz + \int_{-s_m}^{-a} \alpha_{v_2} (y) (cc_\ell)_2 dy \\ = & - \int_{-s_m}^{-a} \alpha_{v_3} (z) (cc_\ell)_3 dz + \int_a^{s_m} \alpha_{v_4} (y) (cc_\ell)_4 dy \end{aligned} \quad (B-29)$$

The foregoing result will yield the normal-force coefficient of F_4 due to the vortex. To convert this result to equivalent angle of attack following equation (B-1), we note that for the wing alone composed of two fins the semispan is $(s_m - a)$. The lift-curve slope of this wing is 2 per radian based on the reference area $\pi(s_m - a)^2$. Based on the planform area the fin lift-curve slope is

$$\left(\frac{dC_N}{d\alpha} \right)_F = \frac{2\pi(s_m - a)^2}{S_w} = \frac{\pi(s_m - a)^2}{S_F} \quad (B-30)$$

Equation (B-29) in terms of equivalent angle of attack is thus

$$\begin{aligned} (\alpha_{eg})_4 = & - \frac{1}{\pi(s_m - a)^2} \int_a^{s_m} \alpha_{v_1} (cc_\ell)_1 dz + \frac{1}{\pi(s_m - a)^2} \int_{-s_m}^{-a} \alpha_{v_2} (cc_\ell)_2 dy \\ = & - \frac{1}{\pi(s_m - a)^2} \int_{-s_m}^{-a} \alpha_{v_3} (cc_\ell)_3 dz + \frac{1}{\pi(s_m - a)^2} \int_a^{s_m} \alpha_{v_4} (cc_\ell)_4 dy \end{aligned} \quad (B-31)$$

To carry out this calculation for the fin of a cruciform wing-body combination, the values α_{v_1} , α_{v_2} , are determined from the external vortex and its image by the Biot-Savart law. The values α_{v_3} , α_{v_4} are obtained from equations (A-23)

B.5 FIN ROLLING MOMENT DUE TO EXTERNAL VORTEX

To obtain a result for rolling-moment coefficient comparable to equation (B-30), one must take a linearly twisted F_4 fin rather than F_4 with uniform unit deflection. Consider the following reverse-flow conditions comparable to equation (B-17)

$$\begin{aligned} F_4: \quad \alpha'_n &= -y \text{ on upper surface} \\ &\qquad\qquad\qquad a \leq y \leq s \quad (B-32) \\ \alpha'_n &= y \text{ on lower surface} \end{aligned}$$

$$F_1, F_2, F_3, \text{ Body: } \alpha'_n = 0$$

Let the span loadings in F_1, F_2, F_3 , and F_4 due to this set of boundary conditions be designated $(cc_{\ell t})_1, (cc_{\ell t})_2, (cc_{\ell t})_3$ and $(cc_{\ell t})_4$ where "t" denotes twist. Let the positive convention be as before. Then by analogy with equation (B-29), the rolling moment is given by

$$\begin{aligned} R_{F_4} = - \int_a^{s_m} \alpha_{v1} (cc_{\ell t})_1 dz + \int_{s_m}^{-a} \alpha_{v2} (cc_{\ell t})_2 dy \\ - \int_{-s}^{-a} \alpha_{v3} (cc_{\ell t})_3 dz + \int_a^{s_m} \alpha_{v4} (cc_{\ell t})_4 dy \quad (B-33) \end{aligned}$$

The necessary span loadings to evaluate equation (B-33) numerically are given by equation (A-30) of Appendix A. The lateral center-of-pressure position of the force on fin F_4 is then obtained from equation (B-29) and (B-33).

$$\overline{Y_4} = \frac{R_{F_4}}{N_{F_4}} \quad (B-34)$$

This result is valid beyond the range of slender-body theory, depending as it does only on the shape and not the magnitude of the span-loading results.

B.6 REFERENCES

- B-1. Nielsen, Jack N.: "Missile Aerodynamics" McGraw-Hill Book Co., Inc., New York, 1960, pp. 118-129.
- B-2. Heaslet, Max A. and Spreiter, John, R.: Reciprocity Relations in Aerodynamics, NASA TR 1119, 1953.

APPENDIX C

MATHEMATICAL DERIVATION OF EQUIVALENT ANGLE OF ATTACK
FORMULA FOR LARGE ANGLES OF ATTACK

APPENDIX C

MATHEMATICAL DERIVATION OF EQUIVALENT ANGLE OF ATTACK
FORMULA FOR LARGE ANGLES OF ATTACK

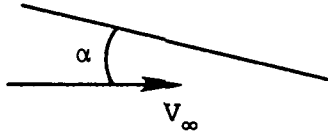
C.1 INTRODUCTION

In reference 6 a formula was given for the equivalent angle of attack of the fin of a cruciform wing-body combination based on linear superposition. Such a result is valid as long as the small angle assumption can be made; that is,

$$\sin \alpha = \alpha \quad \cos \alpha = 1 \quad (C-1)$$

However in the present work, which comtemplates large angles of attack, a nonlinear definition of equivalent angle of attack is required. There is no unique definition of the equivalent angle of attack for large angles. The only requirement imposed on the definition is that it be useful in the engineering method.

Consider a two-dimensional lifting surface at angle of attack α as shown



The component of velocity normal to the surface is $v_n = V_\infty \sin \alpha$ and that parallel to the surface is $v_p = V_\infty \cos \alpha$. The angle of attack can be then defined as

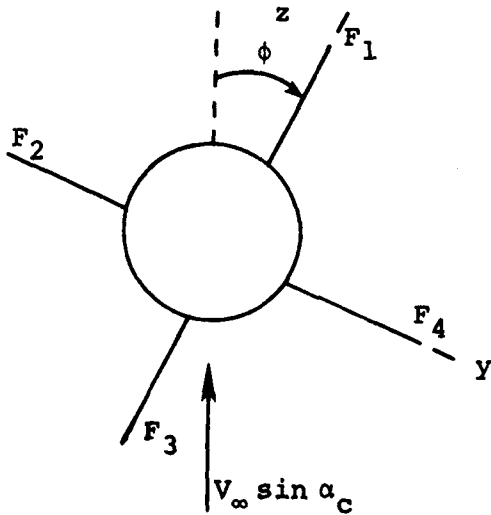
$$\tan \alpha = \frac{v_n}{v_p} \quad (C-2)$$

In the rest of this section we will develop an equation for the angle of attack of a fin on a cruciform wing-body combination which

is pitched and rolled. If the fin angle of attack given by the resulting expression is accurate, then the fin normal force will be equivalent to that acting on a wing alone composed of two opposing fins joined together at their root chords and at the same angle of attack. In this way the experimental nonlinear behavior of a wing-alone can be related to that of the fin in the wing-body combination.

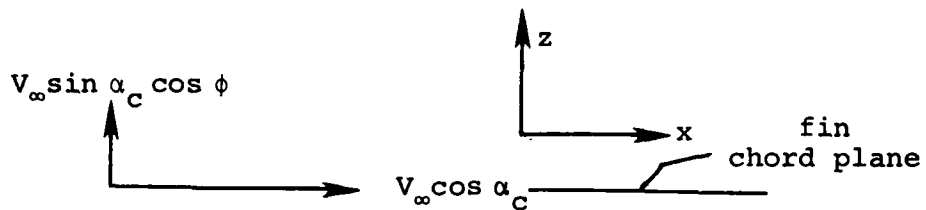
C.2 EQUIVALENT ANGLE OF ATTACK FOR NO CONTROL DEFLECTION

Consider now a cruciform wing-body combination with the x axis rearward along the body axis, the y axis lateral along the right horizontal fin, F_4 , and the z axis vertical along the upper fin F_1 . Let the combination first be pitched in a plane containing the free-stream velocity and the x axis by an angle α_c . Let it then be rolled right wing down by angle ϕ . In a plane normal to the body axis we now have the following picture.



The free-stream velocity now has components $V_\infty \cos \alpha_c$ along x , $-V_\infty \sin \alpha_c \sin \phi$ along y , and $V_\infty \sin \alpha_c \cos \phi$ along z . The velocity

component along y has no contribution to the velocity components in a plane normal to fin chord plane and parallel to the x,z plane



The component of the free-stream velocity parallel to the fin chord is

$$v_{p4} = V_\infty \cos \alpha_c \quad (C-3)$$

We now need the component of velocity normal to the fin chord. We consider an effective average value which is used together with v_{p4} from equation (C-3) to determine the angle of attack as follows:

$$\tan \alpha_{eq4} = \frac{v_{n4}}{v_{p4}} \quad (C-4)$$

We have previously discussed in section 2.4 that four factors contribute directly or indirectly to the equivalent angle of attack of a fin.

- (1) Upflow in crossflow plane due to α_c as augmented by body blockage (Beskin upwash). The factor from this effect is K_W .
- (2) Coupling between angles of attack and sideslip as evidence by changes in sweep of fin leading edge. The factor for this effect is K_ϕ .
- (3) Normal flow due to control deflection as modified by lack of a perfect reflection plane on the body, control gap effects, and panel-panel interference.

The factor for this effect is k_w . It is not considered in this section of the Appendix.

- (4) Flow induced normal to the fin with $\delta_1 = \delta_2 = \delta_3 = \delta_4 = 0$ by any vortices assumed parallel to the body axis.

Let the equivalent angle of attack due to the vortices including panel-panel interference be $(\alpha_{eq})_{4,v}$ as given by equation (B-31).

The upwash along the z axis associated with the first factor is

$$K_w V_\infty \sin \alpha_c \cos \phi \quad (C-5)$$

The upwash associated with the second factor is

$$\frac{4}{(AR)} K_\phi V_\infty \sin^2 \alpha_c \sin \phi \cos \phi \quad (C-6)$$

The factor $\frac{4}{(AR)}$ is used to keep K_ϕ insensitive to changes in fin aspect ratio.¹ The fourth component due to the vortices is along the axis of z and is equal to $V_\infty \cos \alpha_c \tan(\alpha_{eq})_{4,v}$. The total velocity normal to F_4 is

$$v_{n_4} = V_\infty [K_w \sin \alpha_c \cos \phi + \frac{4}{AR} K_\phi \sin^2 \alpha_c \sin \phi \cos \phi + \cos \alpha_c \tan(\alpha_{eq})_{4,v}] \quad (C-7)$$

Combining equations (C-3), (C-4), and (C-7) we find

$$\tan(\alpha_{eq})_4 = \frac{K_w \sin \alpha_c \cos \phi + \frac{4}{AR} K_\phi \sin^2 \alpha_c \sin \phi \cos \phi + \cos \alpha_c \tan(\alpha_{eq})_{4,v}}{\cos \alpha_c} \quad (C-8)$$

We now write similar expression for the equivalent angles of attack for fins F_1, F_2 , and F_3 . For fin F_1 we must replace ϕ by $\phi - 90^\circ$ in equation (C-8) and change the subscripts on (α_{eq}) . We

¹See "Missile Aerodynamics" pp. 125-129

then get

$$\tan(\alpha_{eq})_1 = \frac{K_W \sin \alpha_c \sin \phi - \frac{4}{AR} K_\phi \sin^2 \alpha_c \sin \phi \cos \phi + \cos \alpha_c \tan(\Delta \alpha_{eq})_{1,v}}{\cos \alpha_c} \quad (C-9)$$

For fin F_2 we must replace ϕ by $\phi-180^\circ$ in equation (C-8), reverse the sign of the vortex contribution since positive velocity is up. Finally we must reverse the sign of the resulting expression since positive α_{eq} produces positive lift. In this fashion we find

$$\tan(\alpha_{eq})_2 = \frac{K_W \sin \alpha_c \cos \phi - \frac{4}{AR} K_\phi \sin^2 \alpha_c \sin \phi \cos \phi + \cos \alpha_c \tan(\Delta \alpha_{eq})_{2,v}}{\cos \alpha_c} \quad (C-10)$$

For fin F_3 we replace ϕ by $\phi+90^\circ$, reverse the sign of the vortex contribution and then change the sign of the resulting expression

$$\tan(\alpha_{eq})_3 = \frac{K_W \sin \alpha_c \sin \phi + \frac{4}{AR} K_\phi \sin^2 \alpha_c \sin \phi \cos \phi + \cos \alpha_c \tan(\Delta \alpha_{eq})_{3,v}}{\cos \alpha_c} \quad (C-11)$$

EXTRACTION OF VALUES OF K_W AND K_ϕ FROM EXPERIMENTAL DATA

One problem we face is evaluating the constants K_W and K_ϕ from experimental data at high angles of attack. To evaluate K_W , consider F_4 at $\phi = 0$ and $\delta_4 = 0$. Equation (C-8) yields

$$\tan(\alpha_{eq})_4 = K_W \tan \alpha_c + \tan(\Delta \alpha_{eq})_{4,v} \quad (C-12)$$

or

$$K_W = \frac{\tan(\alpha_{eq})_4}{\tan\alpha_c} - \frac{\tan(\Delta\alpha_{eq})_{4,v}}{\tan\alpha_c} \quad (C-13)$$

The horizontal fin is usually not strongly influenced by body vortices, and the first term gives a fair approximation to K_W . If we have K_W for one value of a/s_m , we can estimate it for another a/s_m by assuming a linear relationship in a/s_m and knowing K_W is unity by definition for $a/s_m = 0$. The value of K_W varies with α_c and M_∞ for a given wing-body combination.

If the body crossflow Mach number exceeds unity, a normal shock will lie beneath the wing-body in the crossflow plane. A loss of dynamic pressure will occur which has the effect of decreasing K_W . In case $K_W < 1$, we apply K_W also to the vortex-induced term in equation (C-12), and equation (C-13) becomes

$$K_W = \frac{\tan(\alpha_{eq})_4}{\tan\alpha_c + \tan(\Delta\alpha_{eq})_{4,v}} \quad (C-14)$$

To obtain K_W from equations (C-13) or (C-14) we obtain $(\alpha_{eq})_4$ from the wing-alone curve. The quantity $(\Delta\alpha_{eq})_{4,v}$ is obtained from equation (B-31) of Appendix B.

To obtain K_ϕ , we write equation (C-8) :

$$\begin{aligned} \tan(\alpha_{eq})_4 = K_W \tan\alpha_c \cos\phi + \frac{4}{AR} K_\phi \sin\alpha_c \tan\alpha_c \sin\phi \cos\phi \\ + \tan(\Delta\alpha_{eq})_{4,v} \end{aligned} \quad (C-15)$$

We obtain K_ϕ from equation (C-15) by obtaining $(\alpha_{eq})_4$ and $(\Delta\alpha_{eq})_{4,v}$ as before, and assuming K_W does not vary with ϕ .

C.4 EQUIVALENT ANGLE OF ATTACK WITH ALL FINS DEFLECTED

The foregoing results give the theoretical basis for the

equivalent angle of attack without control deflection. In the general case we will have four controls all with different deflection angles. Each control will then have an effect on the equivalent angle of attack of any other control. We now consider this problem.

Consider a cruciform wing-body combination at angle of attack α_c and roll angle ϕ . As a result of these two parameters alone we obtain a fin normal-force coefficient (CNT)_p from the data base and a corresponding equivalent angle of attack $\alpha_{eq,p}$. If vortices are present, we calculate an increment in equivalent angle of attack $(\Delta\alpha_{eq})_v$ assuming $\alpha_c = 0$, and $\delta_1 = \delta_2 = \delta_3 = \delta_4 = 0$. For a general fin with no fins deflected but with vortices present, the equivalent angle of attack $\alpha_{eq,0}$ is given by

$$\tan \alpha_{eq,0} = \tan \alpha_{eq,p} + \tan (\Delta\alpha_{eq})_v \quad (C-16)$$

The term $\tan \alpha_{eq,p}$ is associated with the first two terms on the right-hand side of equation (C-15).

Consider now that fin F_4 is deflected by angle δ_4 . The tangent of the equivalent angle of attack of the fin is increased by an amount

$$k_w [\tan (\alpha_{eq,0} + \delta_4) - \tan \alpha_{eq,0}] \quad (C-17)$$

without any panel-panel interference due to deflection of other fins. This follows from the definition of k_w given by equation (22).

Consider now that fins F_2 , F_3 , and F_4 are deflected by amounts δ_2 , δ_3 , and δ_4 . In Table 1 we have presented numerical results based on slender-body theory showing how much equivalent angles of attack of fins F_1 , F_2 , F_3 and F_4 are changed by unit deflection of F_4 in terms of the following parameters.

$$\left. \begin{aligned} \Lambda_{4(1)} &= \frac{\Delta(\alpha_{eq})_1}{\delta_4} \\ \Lambda_{4(2)} &= \frac{\Delta(\alpha_{eq})_2}{\delta_4} \\ \Lambda_{4(3)} &= \frac{\Delta(\alpha_{eq})_3}{\delta_4} \\ \Lambda_{4(4)} &= \frac{\Delta(\alpha_{eq})_4}{\delta_4} \end{aligned} \right\} \quad (C-18)$$

The last fraction is k_w as given by slender-body theory.

There exists a reciprocal relationship between the values of Λ of the following form.

$$\Lambda_{4(1)} = \Lambda_{1(4)} \quad (C-19)$$

Thus the $(\Delta\alpha_{eq})$ induced on fin F_1 by unit deflection of fin F_4 is equal to the value of $(\Delta\alpha_{eq})$ induced on fin F_4 due to unit deflection of F_1 . These reciprocal relationships are based on slender-body theory in which each fin is entirely within the region of influence of each other fin. However, in case F_4 is not entirely within the region of influence of F_1 , we must use a factor λ_{12} to account for this fact. The factor λ_{12} is given in Appendix D and is the fraction of the planform of F_4 within the region of influence of F_1 . For opposing fins, a similar factor λ_{24} has been derived in Appendix D. With these factor, we obtain the following changes in (α_{eq}) on fin F_4 due to δ_1 , δ_2 and δ_3 .

$$\left. \begin{array}{l} \delta_1 : \lambda_{12} k_w \tan (\delta_1 \Lambda_{1(4)}) \\ \delta_2 : \lambda_{24} k_w \tan (\delta_2 \Lambda_{2(4)}) \\ \delta_3 : \lambda_{12} k_w \tan (\delta_3 \Lambda_{3(4)}) \end{array} \right\} \quad (C-20)$$

k_w = fin deflection interference factor for fin F_4

λ_{24} = fraction part of F_4 in region of influence of F_2
at $\alpha_c = 0$

λ_{12} = fraction part of F_4 in region of influence of F_1
at $\alpha_c = 0$

$\Lambda_{1(4)}$ = average angle of attack induced on F_4 due to unit
deflection of F_1 (Table 1)

$\Lambda_{2(4)}$ = average angle of attack induced on F_4 due to unit
deflection of F_2 (Table 1)

$\Lambda_{3(4)}$ = average angle of attack induced on F_4 due to unit
deflection of F_3 (Table 1)

The total equivalent angle of attack of fin F_4 , $\alpha_{eq,4}$, from
all factors is now

$$\begin{aligned} \tan (\alpha_{eq})_4 &= \tan \alpha_{eq,p} + \tan (\Delta \alpha_{eq})_{4,v} \\ &+ k_w [\tan (\alpha_{eq,0} + \delta_4) - \tan \alpha_{eq,0}] \\ &+ \lambda_{12} k_w \tan (\delta_1 \Lambda_{1(4)}) \\ &+ \lambda_{24} k_w \tan (\delta_2 \Lambda_{2(4)}) \\ &+ \lambda_{12} k_w \tan (\delta_3 \Lambda_{3(4)}) \end{aligned} \quad (C-21)$$

Formulas for F_1 , F_2 and F_3 can be written by analogy.

APPENDIX D

REGION OF INFLUENCE OF ONE FIN ON ANOTHER

APPENDIX D

REGION OF INFLUENCE OF ONE FIN ON ANOTHER

D.1 INTRODUCTION

Panel-panel interference effects at subsonic and transonic speeds can be well predicted for slender missiles by using interference factors based on slender-body theory. This procedure assumes fins are completely within the region of influence of one another. At supersonic speeds it is possible that a fin may lie entirely in front of the region of influence of an adjacent fin. In this case panel-panel interference will not exist. As an engineering approximation we will make the assumption that the panel-panel interference factors determined on the basis of slender-body theory can be scaled by the ratio of the area of influence on the fin to the area of the fin itself. The analysis will be based on the zero angle of attack case. We define this ratio for adjacent fins to be λ_{12} and for opposing fins to be λ_{13} or λ_{24} .

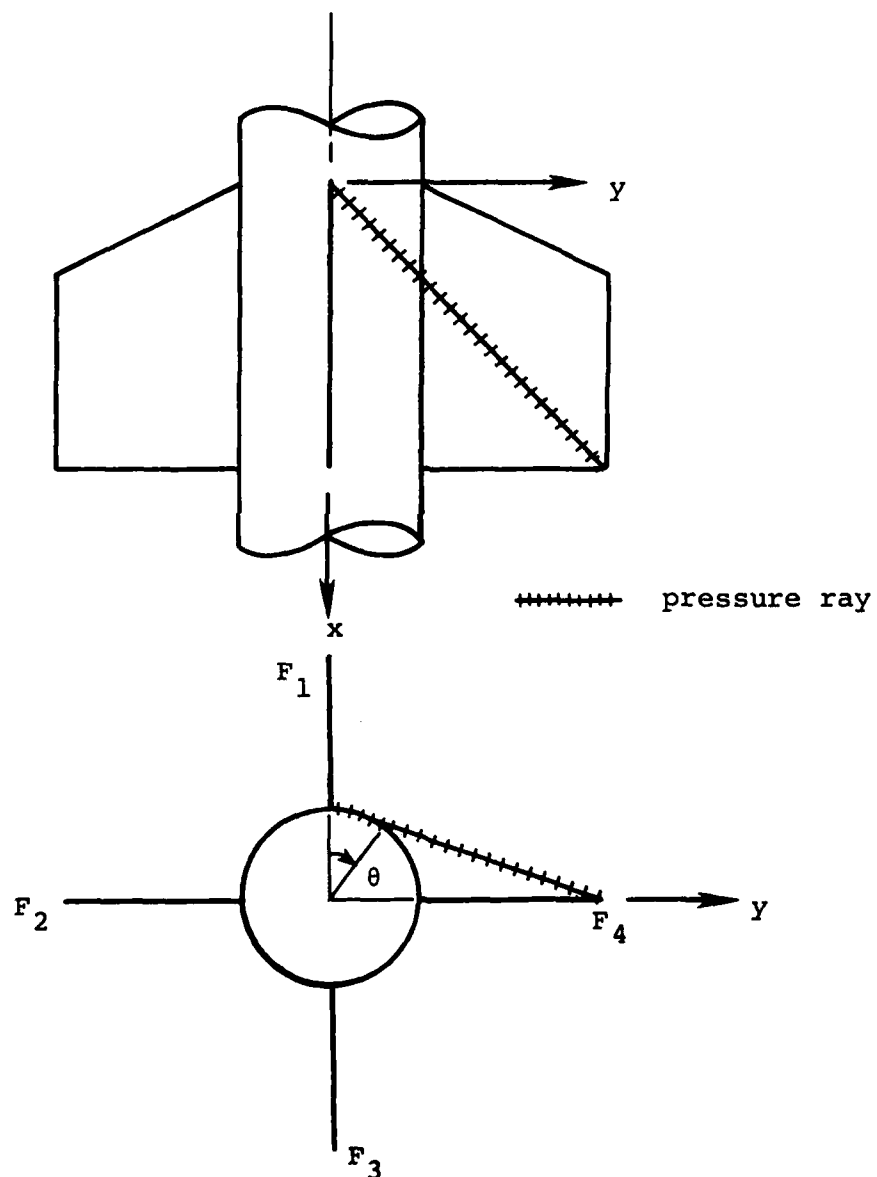
D.2 RELATIONSHIPS FOR NO INTERFERENCE BETWEEN ADJACENT FINS

Consider a disturbance emanating from the root chord of fin F_1 , moving around the body surface an angular distance θ , and then moving laterally in a plane tangent to the body. On the body the ray will travel laterally a distance $R\theta$ and in the tangent plane it will travel laterally a distance $R/\tan\theta$ before it hits F_4 . It is assumed that this is the shortest lateral path between F_1 and F_4 and is therefore the shortest downstream distance. If the Mach number is M_∞ , we know from small disturbance theory that the total downstream distance during this lateral travel is

$$x = (\theta + \frac{1}{\tan\theta}) R\sqrt{M_\infty^2 - 1} \quad (D-1)$$

The y coordinate on fin F_4 is

$$y = \frac{R}{\sin\theta} \quad (D-2)$$



These two equations yield the forward boundary of the region of

influence of F_1 on F_4 . Figure (D-1) shows an example of the forward boundary of the region of influence in the plane of F_4 for $M_\infty = \sqrt{2}$. It starts at the root chord at a distance $(\pi/2)R\sqrt{M_\infty^2-1}$ behind the leading edge of the root chord and asymptotically approaches the Mach line from a point a distance $R\sqrt{M_\infty^2-1}$ behind the leading edge of the root chord. If the root chord is shorter than $(\pi/2)R\sqrt{M_\infty^2-1}$, F_4 will lie in front of the region of influence of the F_1 . The criterion for no interference between adjacent fins is thus

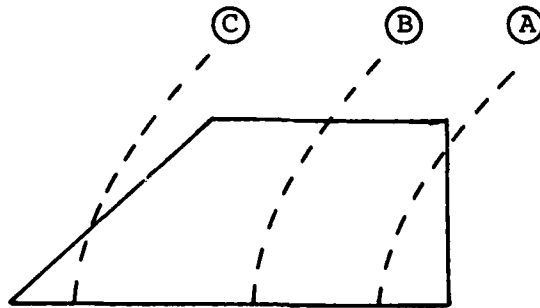
$$c_r \leq \frac{\pi}{2} R\sqrt{M_\infty^2-1} \quad (D-3)$$

D.3 REGION OF INFLUENCE BETWEEN ADJACENT FINS

Let the planform area of fin F_4 lying within the region of influence of fin F_1 be designated S_i , and let the area of fin F_4 be S_F . Then the factor λ_{12} referenced above is defined to be

$$\lambda_{12} = \frac{S_i}{S_F} \quad (D-4)$$

In case the inequality of equation (D-3) holds, λ_{12} is zero. Otherwise we distinguish the following subcases depending on where the forward boundary of the region of influence intersects the outer edge of the fin; (a) on the trailing edge, (b) on the tip, (c) on the leading edge.



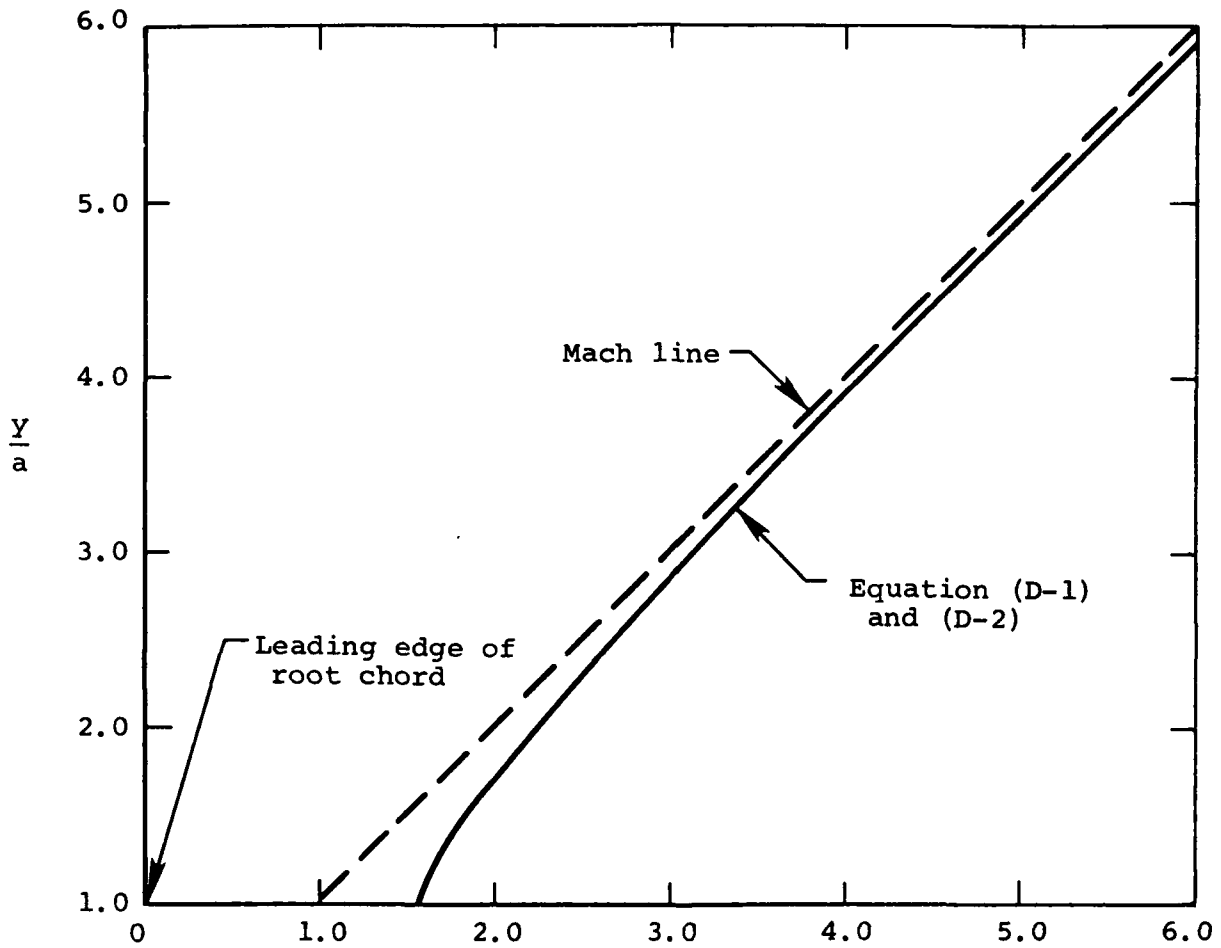


Figure D-1. Forward boundary of region of influence of fin F_1 in plane of F_2 .

$$\frac{x}{a\sqrt{M_\infty^2 - 1}}$$

The parametric form of the boundary given by equations (D-1) and (D-2) is awkward for analytical purposes. A close approximation to this boundary is given by the hyperbola

$$\left(\frac{Y}{R} - 1\right)^2 = \left(\frac{x}{R\sqrt{M_\infty^2 - 1}} - 1\right)^2 - \left(\frac{\pi}{2} - 1\right)^2 \quad (D-5)$$

A comparison between the two results is shown in the following listing:

θ (degs.)	$\frac{x}{R\sqrt{M_\infty^2 - 1}}$	$y/R,$ Equations (D-1) and (D-2)	$y/R,$ Equation (D-5)
10	5.85	5.76	5.85
12	4.91	4.81	4.87
14	4.26	4.13	4.21
16	3.77	3.63	3.71
18	3.39	3.24	3.32
20	3.10	2.92	3.02
25	2.58	2.37	2.47
30	2.26	2.00	2.12
35	2.04	1.74	1.87
40	1.89	1.56	1.68
50	1.71	1.31	1.42
60	1.62	1.15	1.24
70	1.59	1.06	1.15
80	1.573	1.02	1.03
90	1.571	1.00	1.00

The accuracy of the approximation is sufficient for present purposes.

Let x^* be the value of x given by equation (D-5) at $y = s_m$.

$$\frac{x^*}{R\sqrt{M_\infty^2-1}} = 1 + \sqrt{\left(\frac{s_m}{R} - 1\right)^2 + \left(\frac{\pi}{2} - 1\right)^2} \quad (D-6)$$

We now distinguish the following three cases for $c_r > \frac{\pi}{2} R\sqrt{M_\infty^2-1}$:

Case A Trailing-edge intersection

$$c_r < x^* \quad (D-7)$$

Case B Tip intersection

$$(1-\lambda)c_r \leq x^* \leq c_r \quad (D-8)$$

Case C Leading-edge intersection

$$0 < x^* \leq (1-\lambda)c_r \quad (D-9)$$

Note that λ is the ratio of the tip chord to the root chord.

Case A

For case A the area of the region of influence on fin F_4 can be written

$$S_i = \int_{\frac{\pi}{2} R\beta}^{c_r} (y-R) dx \quad (D-10)$$

$$= R \int_{\frac{\pi}{2} R\beta}^{c_r} \sqrt{\left(\frac{x}{R\beta} - 1\right)^2 - c^2} dx \quad (D-11)$$

where

$$c = \pi/2 - 1 ; \beta = \sqrt{M_\infty^2-1} \quad (D-12)$$

In more compact form

$$S_i = R^2 \beta \int_c^{\frac{c_r}{\beta R} - 1} \sqrt{\xi^2 - c^2} d\xi \quad (D-13)$$

$$S_i = \frac{R^2 \beta}{2} \left\{ \left(\frac{c_r}{\beta R} - 1 \right) \sqrt{\left(\frac{c_r}{\beta R} - 1 \right)^2 - c^2} - c^2 \cosh^{-1} \left[\frac{\left(\frac{c_r}{\beta R} - 1 \right)}{c} \right] \right\} \quad (D-14)$$

From equation (D-4) and the definition of the wing-alone aspect ratio

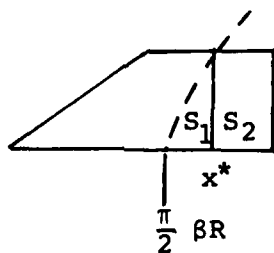
$$AR = \frac{2(s_m - R)^2}{S_F} \quad (D-15)$$

we find

$$\lambda_{12} = \frac{\beta AR}{4 \left(\frac{s_m}{R} - 1 \right)^2} \left\{ \left(\frac{c_r}{\beta R} - 1 \right) \sqrt{\left(\frac{c_r}{\beta R} - 1 \right)^2 - c^2} - c^2 \cosh^{-1} \left[\frac{\left(\frac{c_r}{\beta R} - 1 \right)}{c} \right] \right\} \quad (D-16)$$

Case B

We now have the forward boundary of the region of influence intersecting the wing tip



The area S_1 is given in a form analogous to equation (D-14).

$$S_1 = \frac{R^2 \beta}{2} \left\{ \left(\frac{x^*}{\beta R} - 1 \right) \sqrt{\left(\frac{x^*}{\beta R} - 1 \right)^2 - c^2} - c^2 \cosh^{-1} \left[\frac{\frac{x^*}{\beta R} - 1}{c} \right] \right\} \quad (D-17)$$

With the value of x^* given by equation (D-6) we find

$$S_1 = \frac{R^2 \beta}{2} \left\{ \left(\frac{s_m}{R} - 1 \right) \sqrt{\left(\frac{s_m}{R} - 1 \right)^2 + c^2} - c^2 \sinh^{-1} \left[\frac{\left(\frac{s_m}{R} - 1 \right)}{c} \right] \right\} \quad (D-18)$$

The second area S_2 is

$$S_2 = (c_r - x^*) (s_m - R) \quad (D-19)$$

or

$$S_2 = R^2 \beta \left(\frac{s_m}{R} - 1 \right) \left[\left(\frac{c_r}{\beta R} - 1 \right) - \sqrt{\left(\frac{s_m}{R} - 1 \right)^2 + c^2} \right] \quad (D-20)$$

The value of λ_{12} in this case is given by

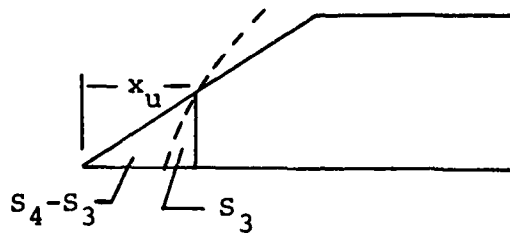
$$\lambda_{12} = \frac{S_1 + S_2}{S_F}$$

or

$$\lambda_{12} = \frac{\frac{\beta R}{2}}{\left(\frac{s_m}{R} - 1 \right)^2} \left\{ \frac{1}{2} \left[\left(\frac{s_m}{R} - 1 \right) \sqrt{\left(\frac{s_m}{R} - 1 \right)^2 + c^2} - c^2 \sinh^{-1} \left(\frac{\left(\frac{s_m}{R} - 1 \right)}{c} \right) \right] + \left(\frac{s_m}{R} - 1 \right) \left[\left(\frac{c_r}{\beta R} - 1 \right) - \sqrt{\left(\frac{s_m}{R} - 1 \right)^2 + c^2} \right] \right\} \quad (D-21)$$

Case C

The forward boundary of influence now intersects the fin leading edge.



The x coordinate of the intersection is found by simultaneous solution of the equation for the leading edge

$$\frac{y-R}{x} = \frac{s_m - R}{c_r(1-\lambda)} \quad (D-22)$$

and equation (D-5). The solution yields

$$x_u = \frac{\beta R \left\{ 1 + \sqrt{1 - (1-c^2) \left[1 - \frac{\beta^2 R^2 \left(\frac{s_m}{R} - 1 \right)}{c_r^2 (1-\lambda)^2} \right]} \right\}}{1 - \frac{\beta^2 R^2 \left(\frac{s_m}{R} - 1 \right)^2}{c_r^2 (1-\lambda)^2}} \quad (D-23)$$

Area S_3 is given by

$$S_3 = \frac{R^2 \beta}{2} \left[\xi_u \sqrt{\xi_u^2 - c^2} - c^2 \cosh^{-1} \left(\frac{\xi_u}{c} \right) \right] \quad (D-24)$$

where

$$\xi_u = \frac{x_u}{\beta R} - 1 \quad (D-25)$$

Area S_4 is given by

$$S_4 = \frac{1}{2} \frac{x_u^2 (s_m - R)}{c_r (1-\lambda)}$$

$$\lambda_{12} = \frac{s_i}{s_F} = \frac{s_F - s_4 + s_3}{s_F}$$

$$\lambda_{12} = 1 - \frac{s_4}{s_F} + \frac{s_3}{s_F} \quad (D-26)$$

Utilizing the foregoing results we obtain finally

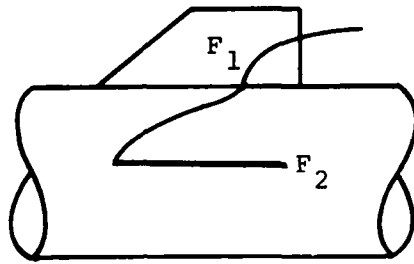
$$\lambda_{12} = 1 - \frac{x_u^2 AR}{4c_r(1-\lambda)(s_m - R)} + \frac{\beta AR}{4\left(\frac{s_m}{R} - 1\right)^2} \left[\xi_u \sqrt{\xi_u^2 - c^2} - c^2 \cosh^{-1}\left(\frac{\xi_u}{c}\right) \right] \quad (D-27)$$

D.4 RELATIONSHIP FOR NO INTERFERENCE BETWEEN OPPOSING FINS

Panel-panel interference between opposing fins is generally smaller than between adjacent fins and is often negligible. To obtain an expression for the panel-panel interference factor between opposing fins, we will use a simplifying approximation. At $M_\infty = 1$ opposing fins are fully within each others regions of influence, and λ_{24} is unity. At some Mach number, M_u , an opposing fin just pass out of the region of influence of the opposing fin and λ_{24} is zero. We will assume that λ_{24} varies linearly with M_∞ between these extremes.

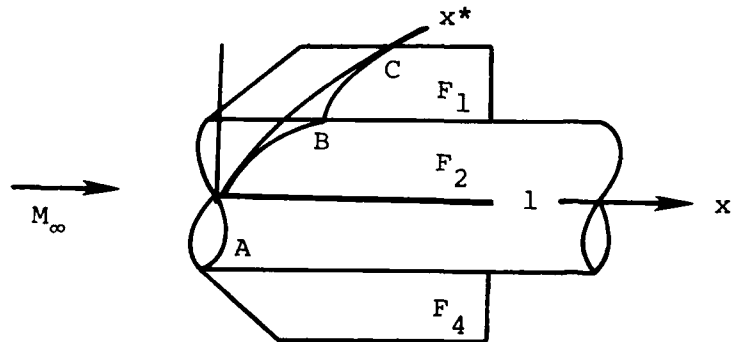
$$\lambda_{24} = \frac{M_u - M_\infty}{M_u - 1} ; \quad 1 \leq M_\infty \leq M_u \quad (D-28)$$

Let us now obtain M_u using considerations similar to those for interference between adjacent fins. Consider first the case where the forward boundary of the region of influence of fin F_2 on F_1 intersects the trailing edge of fin F_1 .

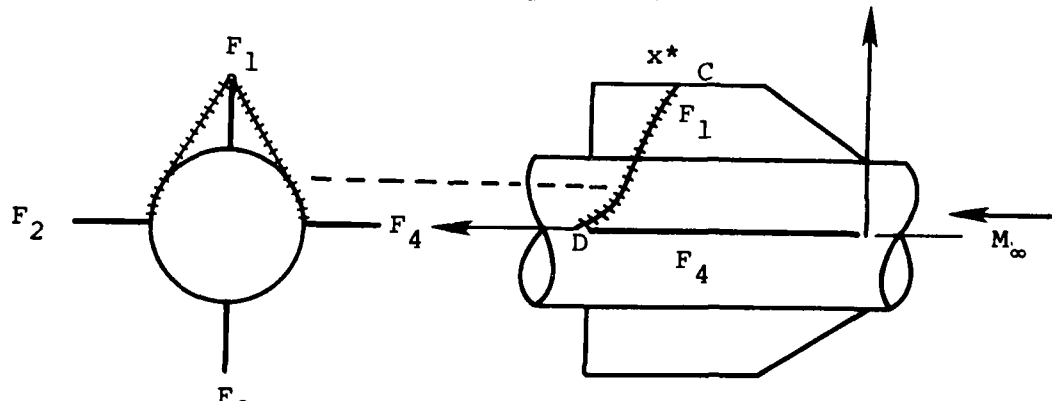


In this case (Case C) λ_{24} is necessarily zero.

Consider next the case where the forward boundary intersects fin F_2 on the tip.



and consider the picture between F_1 and F_4 at the same time.



From the point C on F_1 to the juncture of F_4 the shortest direct

path is the mirror image of the shortest path from the juncture point A of fin F_2 to the top of fin F_1 at point C. (It is not obvious that some indirect path is not shorter). Thus we assume the x coordinate of point D is $2x^*$. Only if $2x^* < c_r$ will there be influence of fin F_2 or F_4 , and this can occur only if $\lambda \geq 0.5$. Thus if $\lambda \geq 0.5$, the criterion for calculating M_u is

$$c_r = 2x^* \quad (D-29)$$

Using equation (D-6) we find that

$$\sqrt{M_u^2 - 1} = \frac{c_r/2R}{1 + \sqrt{\left(\frac{s_m}{R} - 1\right)^2 + \left(\frac{\pi}{2} - 1\right)^2}} ; \lambda \geq 0.5 \quad (D-30)$$

If $\lambda \leq 0.5$, the region of influence of F_2 must intersect the leading edge of F_1 if F_2 is to influence F_4 . The criteria for fin F_4 to lie just forward of the region of influence of F_2 is that

$$c_r = 2x_u$$

where x_u is given by equation (D-23). This results in the following expression of M_u .

$$\frac{c_r}{2\beta_u R} = \frac{1 + \sqrt{1 - (1-c^2)} \left[1 - \frac{\beta_u^2 R^2 (\frac{s_m}{R} - 1)^2}{c_r^2 (1-\lambda)^2} \right]}{1 - \frac{\beta_u^2 R^2 (\frac{s_m}{R} - 1)^2}{c_r^2 (1-\lambda)^2}} ; \lambda \leq 0.5 \quad (D-31)$$

This equation is solved by trial and error for β_u and hence for M_u .

Several points are worthy of mention in connection with these results. First at angle of attack the Mach number is variable and the analysis is no longer linear. However the Mach number changes in opposite directions on upper and lower surfaces and tends to have opposing effects with respect to the regions of influence on the two sides of the same surface. Secondly there is always the possibility of upstream influence through boundary layers or separated regions. These latter effects are obviously too difficult to consider within the scope of the present work.

APPENDIX E

MISSILE, A COMPUTER PROGRAM FOR CALCULATING
THE COMPONENT FORCES AND MOMENTS OF
ARBITRARILY BANKED CRUCIFORM MISSILES
WITH CONTROL DEFLECTIONS

APPENDIX E

MISSILE, A COMPUTER PROGRAM FOR CALCULATING
THE COMPONENT FORCES AND MOMENTS OF
ARBITRARILY BANKED CRUCIFORM MISSILES
WITH CONTROL DEFLECTIONS

E.1 INTRODUCTION

The purpose of this appendix is to describe the operation of the computer code MISSILE in sufficient detail to permit understanding and use of the program. The program computes forces and moments for each fin, for each section of the configuration, and for the complete configuration. Minimum drag is not computed. Intermediate output gives vortex strengths and positions along the body. The code, through the integer control variable, NFIN, is capable of handling the following missile configurations:

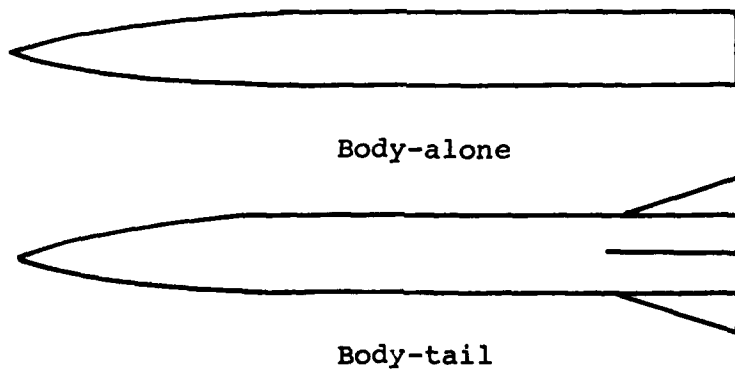
NFIN = 1: body-alone consisting of nose and cylindrical afterbody

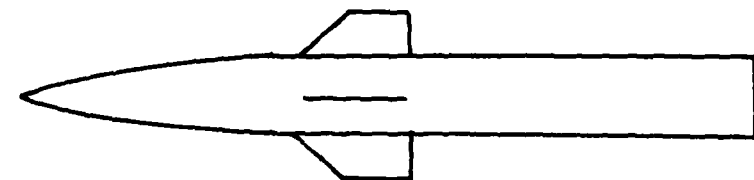
NFIN = 2: body-tail combinations (finner)

NFIN = 3: body-canard combination (body-wing)

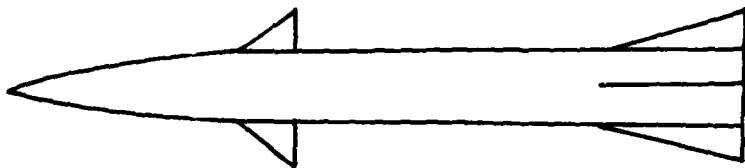
NFIN = 4: body-canard-tail combination (body-wing-tail)

Typical examples of the above configurations are given in the sketch below.





Body-canard



Body-canard-tail

Sketch E.1. Examples of missile configurations.

A description of the engineering method used is given in reference 6 and in the main text and Appendices A through D of this report.

The program is written in FORTRAN IV (029 punch) and has been run on the CDC 6600 and 7600 machines. No files other than INPUT and OUTPUT are required. The running time is roughly one CPU second per data point on the CDC 7600. Run times on the CDC 6600 are about six times those for the CDC 7600.

E.2 PROGRAM DESCRIPTION

For computational purposes, the missile to be studied is divided into four sections as shown in figure 1 of the main text. The nose section is defined to be from the nose tip to the leading edge of the root chord of the first finned section. The canard section (first finned section) is defined to be from the end of the nose section to the trailing edge of the first set of fins. The afterbody section is defined to be from the end of the canard section to the leading edge of the root chord of the second finned section. The tail section (second finned section) is defined to

be from the end of the afterbody section to the trailing edge of the second set of fins. The computations proceed as shown in figure E.1. The branching for the four possible configurations is shown in figure E.2. The main program MISSILE controls the flow of operations. It calls the routines which control the operations for each section of the missile. A more complete description of the program operation is given in figure E.1.

E.2.1 Calculation Procedure

After reading in the run identification information, the subprogram INPT reads in body geometry, run control parameters and flow conditions. All length quantities are then normalized by the body radius and all areas are normalized by the square of the body radius.

After all the input has been read in and all required interference factors have been computed, the main program MISSILE calls subroutine NOSE. This routine first computes the axial starting location of the nose vortices (if present). The locations and strengths of the nose vortices in the crossflow plane at the leading edge of the root chord of the first finned (canard) section are computed next. The subroutine then computes the forces and moments on the nose and returns control to MISSILE.

If NFIN = 1, the driver program prints a summary of the overall forces and moments and reads in a new data set. If NFIN \geq 2, subroutine CANARD is called. This routine computes the fin and body loadings for the first set of fins downstream of the nose.* The individual fin forces and moments in the absence of nose vortices are computed first. The user may choose to ignore the nose vortices over all or part of the missile if he believes

*Note that if the configuration is a body-tail combination, the tail section results are computed by subroutine CANARD and are output under the headings for "CANARD SECTION."

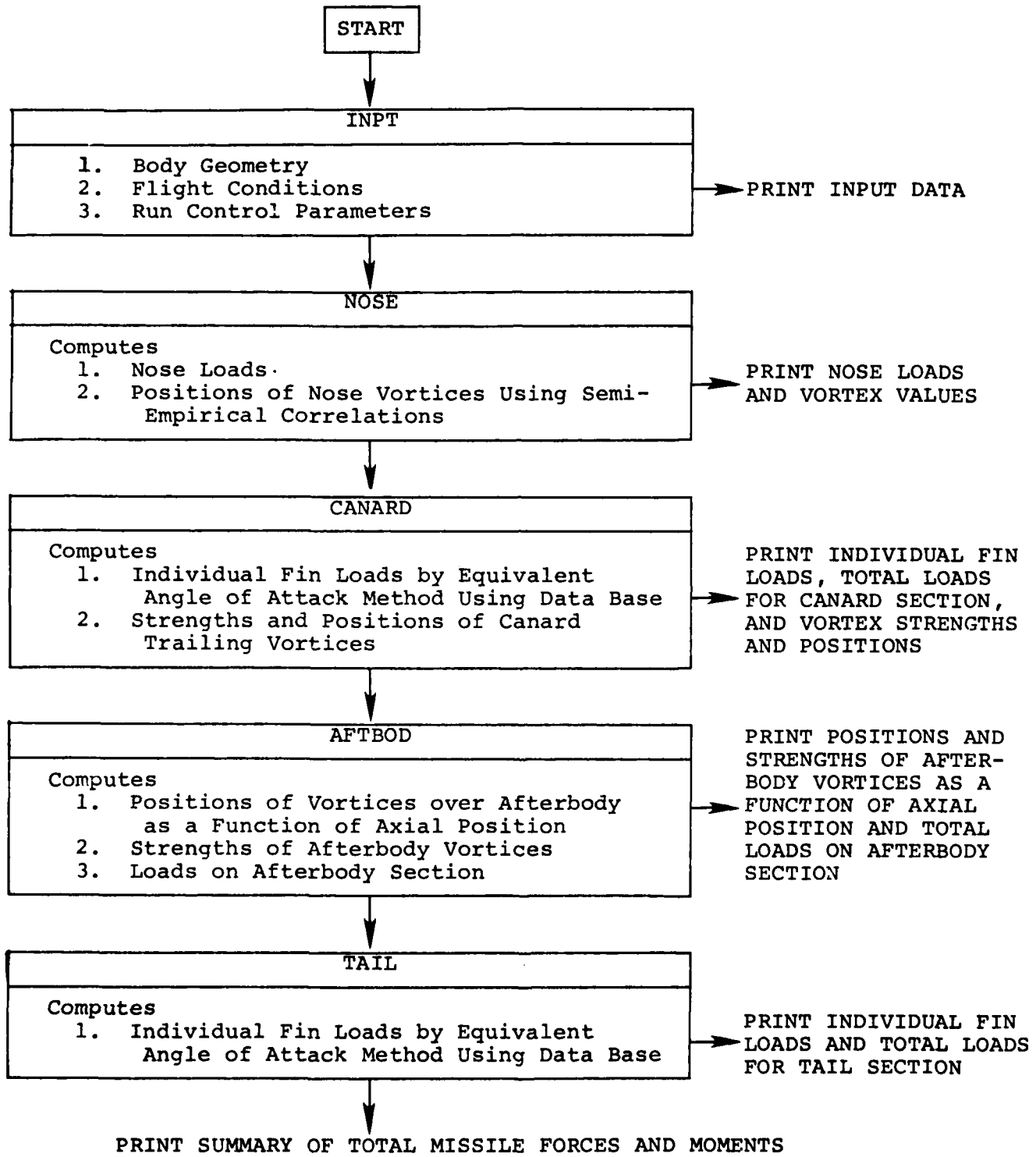


Figure E.1. Flow of program computations.

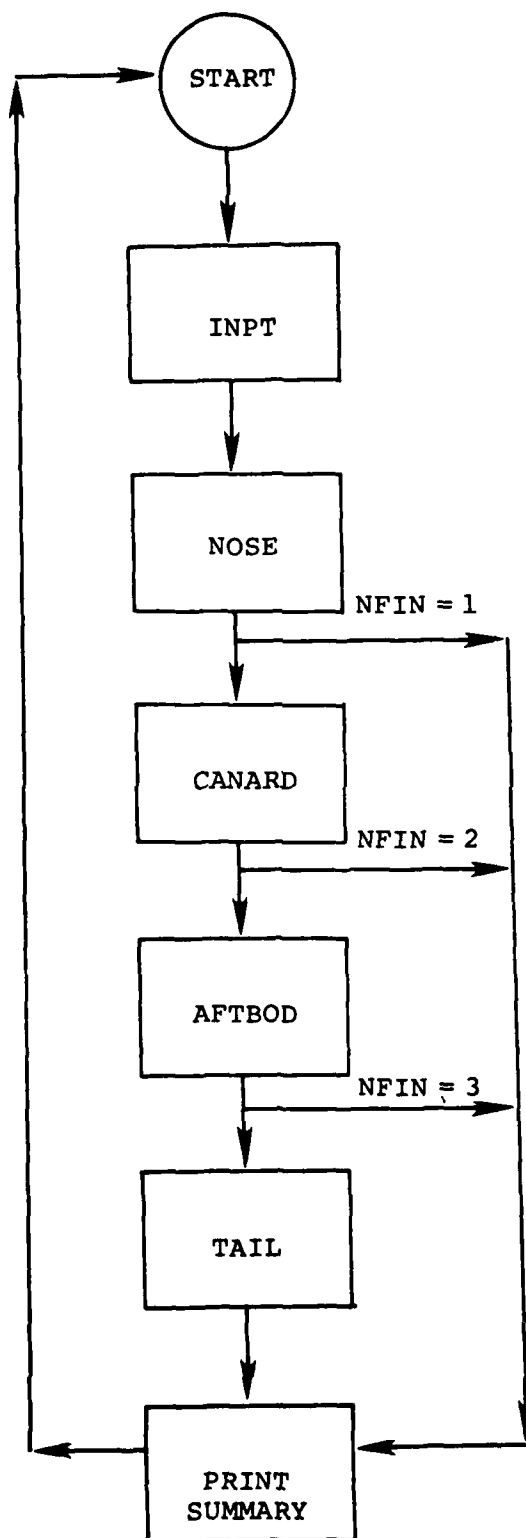


Figure E.2. Schematic description of control of
MISSILE operations by NFIN.

they have dispersed. This control is achieved through the parameter NVORT.

If nose vortices are present over the finned section, subroutine REVFL0 is called. REVFL0 computes the equivalent angle of attack and spanwise location of the center of pressure for the loading due to the nose vortices. Subroutine REVFL0 assumes the vortices to be infinite line vortices parallel to the body axis.

When REVFL0 returns control to CANARD, the total fin forces and moments and body forces and moments (for the canard section) are computed. The strengths and positions of the vortices shed from each fin are calculated next. After the above information has been printed out, control is returned to MISSILE.

If NFIN = 2, the driver program prints a summary of the overall forces and moments and reads in a new data set. If NFIN \geq 3, subroutine AFTBOD is called. This routine tracks the trailing vortices from the first set of fins and the nose vortices (if present) over the afterbody section. The routine also decides if afterbody vortices should be shed and computes their starting locations. If afterbody vortices are formed, they are tracked along with the other vortices present. The strengths of the afterbody vortices as functions of axial position are also computed. Once the vortex trajectories have been computed for the afterbody section, the forces and moments on the afterbody section are computed and control is returned to MISSILE.

If NFIN = 3, MISSILE prints a summary of the overall forces and moments and reads in a new data set. If NFIN = 4, subroutine TAIL is called. This routine proceeds in a manner similar to CANARD except that the trailing vortices of the tail fins are ignored. When TAIL has finished, it returns control to MISSILE. Subroutine MISSILE then computes and prints out the total forces and moments for the configuration and reads in a new data set.

E.2.2 Program Limitations and Precautions

The program makes a number of assumptions about the missile configuration and the flow field which are listed in section 2 of the main text.

E.2.3 Description of Subroutines

Subroutine INPT reads in all input and nondimensionalizes it.

Subroutine NOSE computes nose forces and moments.

Subroutine BVTEX computes nose vortex positions and strengths.

Subroutine CANARD controls the subroutines which compute vortex strengths and positions, individual fin forces and moments, body forces and moments and total forces and moments for the canard section.

Subroutine VORTEX computes the strengths and positions of the vortices shed from the trailing edges of the canard fins.

Subroutine DASCRU is the differential equation solver used by AFTBOD.

Subroutine CCL computes the influence coefficients used in the reverse flow-procedure.

Subroutine INFLU computes the effect of Mach number on panel-panel interference.

Subroutine FINTNR, FINTMR, FINTNL, FINTML compute integrands used in the reverse-flow procedure by CCL.

Subroutine SIMPL is a Simpson's rule integration package used by CCL.

Subroutine REVFLO computes the equivalent angles of attack and spanwise locations of the centers of pressure for a set of fins due to the presence of vortices.

Subroutine SIMSON is a Simpson's rule integration package used by REVFLO.

Subroutine VEL computes the velocities induced on a set of fins by the vortices present for use by REVFLO.

Subroutine LNTRP is a linear interpolation routine.

Subroutine CURVES is a BLOCK DATA routine for initializing a number of empirical tables used in the program.

Subroutine AFTBOD computes vortex positions and strengths and body loading for the afterbody section.

Subroutine DERIV computes derivatives needed by the differential equation solver of AFTBOD.

Subroutine TAIL controls the subroutines which compute vortex strengths and positions, individual fin forces and moments, body forces and moments and total forces and moments for the tail section.

Subroutines CHRT8, EQ24, EQ26, EQ30, EQ31, and CH1416 are used to compute K_B and \bar{x}_B based on the methods of reference E-1. These subroutines are described in reference E-2.

Subroutine INTFAC calculates some required interference parameters.

Subroutine XBAR computes the chordwise location of the fin center of pressure based on the methods presented in reference E-3.

Subroutine CNKW computes the fin K_W from the data base.

Subroutine YTAB computes the spanwise location of the fin center of pressure from the data base.

Subroutine WNGCNW computes the wing-alone normal force coefficient for a set of fins.

Subroutine WNGLKW computes k_w for a fin from the data base.

Subroutine WNGCNT computes the vortex-free, normal-force coefficient for a fin.

Subroutine CNT11, CNT14, CNT15, CNT23, CNT31 and CNT6 compute the vortex-free normal-force coefficient for fins in the data base.

Subroutine ICSICU, IBCIEU, and ICSEVU are routines used for cubic spline interpolation.

E.3 DESCRIPTION OF INPUT

This section describes the input for the program MISSILE. In the following discussion, the contents of all input cards are specified. All possible input variables are listed at the end of this section in the order of appearance in the input deck. The input format for all cards is shown in figure E.3 and the item numbers also refer to that figure. A sample input is described in section E.6 which discusses a sample case.

Item 1

These cards provide identification of the run. The information on them is printed on the first page of the output.

Item 2

This item provides run control information. It includes the variable NFIN which specifies the configuration. The following configurations may be studied:

NFIN = 1: body-alone configuration
NFIN = 2: body-tail configuration
NFIN = 3: body-canard configuration
NFIN = 4: body-canard-tail configuration

Also in this item is NI, the number of integration intervals plus one, used in the Simpson's rule integration routine called by REVFLO. The value of NI must be odd. A suitable value for NI depends on how close a vortex is to a fin. If a vortex is close to a fin, NI should be at least 51. Since REVFLO uses only

a small fraction of the total run time, it is recommended that NI be set equal to 99. If NFIN = 1, NI is ignored.

The integer variable NVORT is used to control the influence of the nose vortices. It has been observed (refs. 4 and 5) that nose vorticity for $\alpha_c \leq 20^\circ$ may disperse over the canard section. Since the present model for nose vorticity is incapable of representing such a situation, the user has the option of ignoring the influence of nose vorticity downstream. The options are:

NVORT = 0: nose vortices, if present, are tracked over entire configuration

NVORT = 1: nose vortices are ignored downstream of the leading edge of the canard root chord

NVORT = 2: nose vortices are ignored downstream of the trailing edge of the canard root chord

If NFIN = 1, NVORT is ignored.

For supersonic speeds, lift on the body due to the presence of the fins can be generated downstream of the fin trailing edges. If NAFTC = 1, the code will assume that there is sufficient body surface downstream of the canard fin trailing edges to fully develop that lift. If NAFTC = 2, it is assumed that there is no body after the canard fins. If $NFIN \geq 3$, always use NAFTC = 1. If NFIN = 2, the user should input NAFTC = 2 unless it is clear that significant lift carryover will be developed downstream of the canard fins. If NFIN = 1, NAFTC is ignored.

The quantity NXOUTB is equal to the number of integration intervals used in the calculations of afterbody loading. It is also the number of axial stations at which vortex positions and strengths are output. As a rule of thumb, use a value of NXOUTB greater than the length of the afterbody in body diameters. If the vortex positions change drastically between output stations, NXOUTB should be increased. If NFIN < 3, NXOUTB is ignored.

The integer NAFTT has the same function as NAFTC except that it is for the tail section. NAFTT should be set equal to 2 unless it is clear that significant lift carryover will be developed downstream of the tail fins.

The integer NNOSE is equal to the number of entries in the table of nose coordinates. The first value is the distance of the nose tip from missile station zero and the last value is the location of the shoulder. The integer variable, NCA, indicates whether the slope of the linear normal-force curve, $C_{N\alpha}$, is to be read in. If NCA equals zero, then $C_{N\alpha}$ is assigned the value 2.0 by the program. Otherwise, a value for $C_{N\alpha}$ is to be read in later.

The logical quantity TURB is used to determine which branch of the crossflow drag coefficient table is to be used in NOSE and AFTBOD. For crossflow Mach numbers below 0.6, the laminar and turbulent values of C_{d_C} differ. If there is doubt about which type of flow separation is present, use TURB = .TRUE.

The logical variable REFER is used to control the reference areas and lengths for the fin output. If REFER = .TRUE., the reference area for the fin loads is the fin planform area; the reference length for fin hinge moments is the fin root chord, and the reference length for fin rolling moments is the exposed span of the fin. If REFER = .FALSE., the input reference area and length are used for the fin output as well as the overall loads.

The logical quantity TOVORT is used to control the number of shed canard fin vortices. If TOVORT = .FALSE., only one vortex per canard fin is shed. If TOVORT = .TRUE., two vortices per canard fin are shed.

Item 3

This item provides geometric information and flight conditions. FMACH is the free-stream Mach number. LROUT and SROUT are the reference length and reference area, respectively. XMC is the moment center measured from MSO. The variable A is the radius

of the cylindrical section of the missile.

The variables TIPRAD and ETAN are entered. The variable TIPRAD is the radius of the spherical nose tip. For the case of a pointed nose, this value is zero. If the nose is pointed, then ETAN is the nose half-angle. If the nose is blunted, then ETAN is the angle between the body axis and the tangent to the nose at the juncture of the spherical cap and the rest of the nose.

The variable XCLE is the distance from missile station zero (MS0) to the leading edge of the root chord of the first set of fins unless NFIN = 1. If NFIN = 1, XCLE is the length of the body. Note that all length dimensions must have the same units. All areas must be given in the units of length squared.

Item 4 (optional)

The variable DCNDA is the slope of the nose normal-force coefficient due to attached flow. The reference area is the base of the nose.

Item 5

This item contains the nose coordinates.

Item 6

This item gives the list of angles of attack for which computations are to be performed.

Item 7 (optional)

This item gives the list of roll angles for which computations are to be performed.

This item also contains flight and geometric information required if at least one set of fins is present. The variables DELTAC and DELTAT are the fin deflection angles. The variable SPANC is the semispan of the fin in the first finned section. The variables XCHL, XCTIPL and XCTE are the axial positions of the hinge line, leading edge of the tip chord and trailing edge for the first finned section. All three variables are measured from the nose tip.

If a fin with a rectangular planform is to be specified, the user must set the leading-edge sweep to some small positive value. This should be accomplished by making $XCTIPL > XCLE$ by a small number, say 0.01.

Item 8 (optional)

If $TOVORT = .TRUE.$, this item is read. $T1$ and $T2$ are the spanwise locations measured from the body axis of the vortices shed from the fins.

Item 9 (optional)

This item contains information required for the afterbody computations. The variable, DXI , is the initial integration interval required by DASCRU for the trajectory calculations. It is nondimensionalized by the body radius. The initial interval can be automatically reduced by DASCRU by as much as a factor of 100 in an attempt to provide the desired accuracy. A value of DXI between 0.02 and 0.05 should work for most cases. When two vortices get very close together, or when a vortex gets very near the wing or body, a smaller value of DXI may be required.

The desired accuracy in the vortex trajectory calculations, referred to in the previous paragraph, is controlled through the variable EPS . This variable also controls the vortex strength calculations of the afterbody vortices. The value of EPS should be set equal to one half the desired accuracy. For instance, if EPS is set to 5×10^{-4} , this usually results in a solution accurate to three significant figures.

Experimental observations show that when two vortices of like sign come very close to one another they often combine or coalesce to form one vortex. This situation is included in the program through the variable $RVORT$. If vortices are not combined and they get too close, then computation time can increase dramatically. The variable $RVORT$ is entered as a separation distance in terms of body radii. When two vortices of like sign are within

this distance of each other, they are combined to form one vortex of strength equal to the two original strengths and at a position between the two inversely proportional to the original strengths. A value of 0.5 for RVORT has been found to be satisfactory.

The variable RVOA is the radial distance from the body centerline in body radii at which the afterbody vortices are to be placed initially. The suggested range of values for RVOA is 1.2 to 1.5. The results presented in this report were computed with RVOA = 1.2. If RVOA is too small, the afterbody vortices tend to be captured by their own images.

The variable OMEGA is an angle, measured from the z_0 axis within which the crossflow velocity vector must lie in order for afterbody vortices to be formed. This crossflow velocity vector is determined by first computing the upwash and sidewash at the body axis due to the external vortices. The quantity $\sin \alpha_c$ is then added to the upwash to account for the flow of the free stream around the cylindrical body. The resultant vector is the crossflow velocity vector. If OMEGA is set equal to zero, no afterbody vortices will form unless the flow is perfectly symmetrical about the plane containing the wind and body axes. If OMEGA is set equal to 180° , afterbody vortices may form regardless of the strength and direction of the crossflow velocity. A value of OMEGA = 45° is recommended.

The next to last variable on this card is XTLE which is the axial location of the end of the afterbody section.

The last variable on this card is RCOMB which controls the combination of vortices when they get too close to the windward side of the body. This sometimes happens when the vortices shed from the lower fins encounter the body as they rise in the cross-flow plane. If RCOMB > 1, vortices which get closer than RCOMB to the windward side of the body are combined with the appropriate afterbody vortex. If the user does not want to use this feature, he should set RCOMB = 0.

Item 1

(1) FORMAT (I5), 1 card

Column Number	5
Program Variable	NCARDS

(2) FORMAT (20A4), NCARDS cards

Column Number	1-80
Program Variable	HEAD

Item 2

(1) FORMAT (10I5, 3L5), 1 card

Column Number	5	10	15	20	25	30	35	
Program Variable	NFIN	NALFA	NI	NPHI	NVORT	NAFTC	NXOUTB	
	40	45	50	55	60	65		
	NAFTT	NNOSE	NCA	TURB	REFER	TOVORT		

Item 3

(1) FORMAT (8F10.5), 1 card

Column Number	10	20	30	40	50	60	
Program Variable	FMACH	LROUT	SROUT	XMC	A	TIPRAD	
	70	80					
	ETAN	XCLE					

Figure E.3(a). Input Formats for Computer Program MISSILE.

Item 4

(1) FORMAT (8F10.5), 1 card

Column Number

10	
DCNDA	

Program Variable

Item 5

(1) FORMAT (8F10.5), 8 values of XNOSE per card

Column Number

10	20	...	10xNNOSE	
XNOSE(1)	XNOSE(2)	...	XNOSE(NNOSE)	

Program Variable

(2) FORMAT (8F10.5), 8 values of RNOSE per card

Column Number

10	20	...	10xNNOSE	
RNOSE(1)	RNOSE(2)	...	RNOSE(NNOSE)	

Program Variable

Item 6

(1) FORMAT (8F10.5), 8 values of ALFAC per card

Column Number

10	20	...	10xNALFA	
ALFAC(1)	ALFAC(2)	...	ALFAC(NALFA)	

Program Variable

Item 7 (optional)

(1) FORMAT (8F10.5), 8 values of PHI per card

Column Number

10	20	...	10xNPHI	
PHI(1)	PHI(2)	...	PHI(NPHI)	

Program Variable

Figure E.3(b). Continued.

(2) FORMAT (8F10.5), 1 card

Column Number	10	20	30	40	50	
Program Variable	DELTAC(1)	DELTAC(2)	DELTAC(3)	DELTAC(4)	DELTAT(1)	

60	70	80
DELTAT(2)	DELTAT(3)	DELTAT(4)

(3) FORMAT (8F10.5), 1 card

Column Number	10	20	30	40	
Program Variable	SPANC	XCHL	XCTPL	XCTE	

Item 8 (optional)

(1) FORMAT (8F10.5), 1 card

10	20	
T1	T2	

Item 9 (optional)

(1) FORMAT (8F10.5), 1 card

Column Number	10	20	30	40	50	60	70	
Program Variable	DXI	EPS	RVORT	RVOA	OMEGA	XTLE	RCOMB	

Item 10 (optional)

(1) FORMAT (8F10.5), 1 card

Column Number	10	20	30	40	50	
Program Variable	SPANT	XTHL	XTTIPL	XTTE	PHIT	

Item 11

(1) FORMAT (I5), 1 card

5		
999		

Figure E.3(c). Concluded.

Item 10 (optional)

This item contains geometric information for the second set of fins. The variables have the same meaning as their counterparts for the first finned section. The variable PHIT is the tail section interdigititation angle. If PHIT = 0., the fins of both sections are aligned. If PHIT = 45°, the tail fins are interdigitated.

Item 11

This card ends the process of entering data. It should be the last card and follow all the data cards for the case(s) to be run. The computer program stops the search for more data and the run is finished.

E.4 SYMBOL LISTING

This section lists all input variables in the order in which they are entered, gives the algebraic symbol if one exists, and a brief definition. Refer to figure E.3 for the proper input format.

<u>Program Variable</u>	<u>Algebraic Symbol (If Applicable)</u>	<u>Comments</u>
<u>Item 1</u>		Alphanumeric information to identify the run.
NCARDS		Number of cards used to identify the run; NCARDS \geq 1.
HEAD(I)		(NCARDS) cards of alphanumeric information for identification of the run; $1 \leq I \leq \text{NCARDS}$.
<u>Item 2</u>		
NFIN		Integer specifying type of configuration. NFIN = 1 Body-alone. NFIN = 2 Body-tail. NFIN = 3 Body-canard. NFIN = 4 Body-canard-tail.

<u>Program Variable</u>	<u>Algebraic Symbol (If Applicable)</u>	<u>Comments</u>
NALFA		Number of angles of attack for which calculations are to be made; $1 \leq NALFA \leq 10$.
NI		One plus the number of intervals to be used in the Simpson's rule integration package in REVFL0; must be odd; $1 \leq NI \leq 99$.
NPHI		Number of roll angles for which calculations are to be made; $1 \leq NPHI \leq 10$. Ignored if NFIN = 1.
NVORT		Integer flag indicating how far along body influence of nose vortices is to be felt. NVORT = 0 Influence of nose vortices felt along entire body. NVORT = 1 Influence of nose vortices felt up to leading edge of canard root chord. NVORT = 2 Influence of nose vortices felt up to trailing edge of canard root chord. Ignored if NFIN = 1.
NAFTC		Integer flag indicating whether afterbody is present downstream of the first set of fins for computation of body carryover lift. NAFTC = 1 Afterbody present. NAFTC = 2 No afterbody present. Ignored if NFIN = 1.
NXOUTB		Number of axial stations along the afterbody at which vortex locations are to be output (see Item 2 of section E.3); ignored if NFIN < 3.
NAFTT		Integer flag indicating whether afterbody is present downstream of second set of fins for calculation of body carryover lift; ignored if NFIN < 4. NAFTT = 1 Afterbody present NAFTT = 2 No afterbody present.
NNOSE		Number of entries in the table of nose coordinates; $2 \leq NNOSE \leq 20$.

<u>Program Variable</u>	<u>Algebraic Symbol (If Applicable)</u>	<u>Comments</u>
NCA		Integer flag specifying whether $C_{N\alpha}$ of nose is to be entered. NCA = 0 $C_{N\alpha}$ not entered. NCA ≠ 0 $C_{N\alpha}$ entered.
TURB		Logical variable stating whether cross-flow on body is laminar or turbulent. TURB = .TRUE. Crossflow is turbulent. TURB = .FALSE. Crossflow is laminar.
REFER		Logical variable concerning output reference areas and lengths for fins. REFER = .TRUE. Use fin planform area, root chord and exposed semispan. REFER = .FALSE. Use input reference area and reference length.
TOVORT		Logical variable concerning number of shed vortices for each canard fin. TOVORT = .TRUE. Two vortices per fin. TOVORT = .FALSE. One vortex per fin.

Item 3

FMACH	M_∞	Free-stream Mach number.
LROUT	l_r	Reference length used in center of pressure calculations.
SROUT	S_R	Reference area used in force calculations.
XMC	x_{MC}	Moment center of missile, dimensional.
A	a	Radius of missile, dimensional.
TIPRAD		Nose tip radius, dimensional.
ETAN	n	Half angle of body nose for pointed body; or angle between tangent to nose at juncture of spherical cap and rest of nose and the body axis, degrees.
XCLE		If NFIN = 1, XCLE is the length of the body. If NFIN ≠ 1, XCLE is the distance from the nose tip to the leading edge of the root chord of the first finned section, dimensional.

<u>Program Variable</u>	<u>Algebraic Symbol</u>	<u>Comments</u>
		<u>(If Applicable)</u>
<u>Item 4</u> (optional)		Optional input to be read if NCA ≠ 0.
DCNDA	$C_{N\alpha}$	Slope of nose normal-force coefficient at $\alpha_c = 0$; entered if NCA ≠ 0.
<u>Item 5</u>		
XNOSE (M)		Axial location entries in nose coordinate table; $1 \leq M \leq NNOSE$; XNOSE(1) is axial location of nose tip from MS 0, dimensional.
RNOSE (M)		Corresponding radial location entries in nose coordinate table; $1 \leq M \leq NNOSE$, dimensional.
<u>Item 6</u>		
ALFAC (K)	$\alpha_c (K)$	Body angle of attack in degrees; $1 \leq K \leq NALFA$.
<u>Item 7</u> (optional)		Optional input to be read in if NFIN ≥ 2.
PHI (L)	$\phi (L)$	Bank angle in degrees; angle between z and z_ϕ axes; positive measured clockwise viewed from rear; $1 \leq L \leq NPHI$.
DELTAC (I)		Deflection angles in degrees of first set of fins (canards); $1 \leq I \leq 4$; I = number of canard fin.
DELTAT (I)		Deflection angles in degrees of second set of fins (tail); $1 \leq I \leq 4$; I = number of tail fin. Ignored if NFIN ≠ 4.
SPANC	s_m	Maximum semispan, measured from body centerline, of canard fins, dimensional.
XCHL	x_{HL}	Axial distance to canard hinge line, measured from MS 0, dimensional.

<u>Program Variable</u>	<u>Algebraic Symbol (If Applicable)</u>	<u>Comments</u>
XCTIPL		Axial distance to leading edge of canard tip chord, measured from MS 0, dimensional; XCTIPL > XCLE (see Item 7 of input section).
XCTE		Axial distance to canard trailing edge, measured from MS 0, dimensional.
<u>Item 8 (optional)</u>		Optional input to be read in if TOVORT = .TRUE. and NFIN > 2.
T1		Spanwise distance from the body axis to the location of the inboard shed vortex, dimensional.
T2		Spanwise distance from the body axis to the location of the outboard shed vortex, dimensional.
<u>Item 9 (optional)</u>		Optional input to be read if NFIN > 2.
DXI		Maximum value of integration interval in body radii for vortex tracking.
EPS		Accuracy criterion used in DASCRU.
RVORT		If the separation distance in body radii between vortices of like sign is less than RVORT, vortices are combined (afterbody section only).
RVOA	r_v/a	Distance from body centerline at which afterbody vortices are positioned initially, nondimensionalized by body radius.
OMEGA		Angle measured from z_∞ axis within which the crossflow velocity vector must lie in order for afterbody vortices to be formed, degrees.
XTLE		Location of end of afterbody section; position of leading edge of tail root chord if second set of fins are present and axial position of body base if only one set of fins present, dimensional.

<u>Program Variable</u>	<u>Algebraic Symbol (If Applicable)</u>	<u>Comments</u>
RCOMB		Radii measured from body axis within which windward vortices are combined with afterbody vortices; nondimensional
<u>Item 10</u> (optional)		Optional input to be read if NFIN = 4.
SPANT	s_m	Maximum semispan, measured from body centerline, of tail fins, dimensional.
XTHL		Axial distance to tail fin hinge line, measured from MS 0, dimensional.
XTTIPL		Axial distance to leading edge of tail tip chord, measured from MS 0, dimensional; XTTIPL > XTLE.
XTTE		Axial distance to tail fin trailing edge; measured from MS 0, dimensional.
PHIT	ϕ_T	Interdigitation angle between tail fins and canard fins, measured clockwise from canard fin no. 1 to tail fin no. 1, degrees.
<u>Item 11</u>		
999		This card causes the program to stop searching for more data and the run is stopped.

E.5 DESCRIPTION OF OUTPUT

This section describes the output of the computer program. The contents of each of the output items is specified and discussed. A sample output is included in the next section which discusses the sample case.

The output consists of a minimum of four items and a maximum of seven, depending upon the type of configuration. The first item consists of the input data and takes up the first two pages. The run identification and missile geometry appear on the first page.

The second page contains reference lengths, reference areas, and flight conditions. The program operation variables are also given on this page.

Page three marks the beginning of the force and moment results. Three items of information are given at the beginning of the output for each of the individual sections: (1) the name of the particular section (e.g., nose); (2) the value of α_c ; (3) the bank angle, ϕ . Following the output for the last section of the configuration is a summary giving total forces and moments. The overall forces and moments are all presented in coefficient form with SROUT as the reference area and LROUT as the reference length. In addition, the force and moment coefficients are listed as components along the appropriate Cartesian axes. The coefficients in unrolled coordinates are listed as CZO, normal force; CYO, side force, CXO, axial force; CMZO, yawing moment; CMYO, pitching moment; and CMXO, rolling moment. The same convention is used for the values in rolled coordinates. Note that $CZ_0 = C_N$, $CY_0 = C_y$, $CX_0 = C_A$, $CMX_0 = -C_l$, $CMY_0 = C_m$, and $CMZ_0 = -C_n$. Also printed is the contribution to the lift and drag coefficient from each section.

The loads on the nose section are reported on the third page of the output beginning with the axial starting position of the nose vortices, if any. If nose vortices have formed, their non-dimensional strength (normalized by $2\pi V_\infty a$) and their positions in the crossflow plane at the end of the nose section are presented next. Then the nose forces and moments are printed.

The results from the canard section (or first finned section) start on page three. Presented first are results for the individual fins in the absence of vortices. For each fin the following information is given: (1) the equivalent angle of attack; (2) the fin normal-force coefficient; and (3) the spanwise location of the fin center of pressure. CPY is nondimensionalized by LROUT and measured from the body centerline if REFER = .FALSE. It is nondimensionalized

by s_m/a and measured from the root chord if REFER = .TRUE.

The vortex induced equivalent angles of attack and corresponding spanwise locations of the centers of pressure for each fin are presented next. The spanwise locations of the centers of pressure are measured from the body centerline and are nondimensionalized by the body radius.

Total individual fin loads are presented next. For each fin the total equivalent angle of attack is used to determine the force normal to the fin (CN), the location of the normal-force center of pressure (CPX and CPY), the fin rolling moment (CRM), bending moment about the root chord (CBM), and hinge moment (CHM). These individual fin loads are then summed and added to the forces and moments acting on the body in the presence of the fins. The total are given in both rolled and unrolled coordinates. If a body-tail missile is being run, the results from the tail section, being the first set of fins, appear here.

Following the canard section results are the load contributions from the afterbody section. These results are presented in the form of vortex, flow field, and force information for each of the NXOUTB axial stations specified. From left to right the printout reads: X/A, the axial station, nondimensionalized by the body radius; I, the identification number of the vortices; GAMMA(I), the nondimensional strength of the vortices at X/A; Y(I)/A, the nondimensional y_o -coordinate of the vortices; Z(I)/A, the nondimensional z_o -coordinate of the vortices; FLOANG, the inverse sine in degrees of the magnitude of the crossflow velocity vector nondimensionalized by V_∞ ; THETA, the polar angle in degrees of the crossflow velocity vector measured from the positive y_o -axis counterclockwise; NORMAL FORCE, the increment of normal force acting on the afterbody over the preceding interval; and SIDE FORCE, the increment of side force acting on the afterbody over the preceding interval. If two vortices are combined (i.e., if two vortices of like sign come within a distance of RVORT of

each other), then their strengths are added and the indexing of the vortices is rearranged as described in the output. The contribution of the afterbody section to the total loads in the unrolled body coordinate system is presented after the trajectory information.

Results for the tail section appear next. The format is the same as for the canard section.

The final item of output is the summary of the total forces and moments on the configuration in both rolled and unrolled coordinates. Included in this section is the axial center of pressure due to the total normal force (CPX) and the axial center of pressure due to the total side force (CPY).

E.6 SAMPLE CASE

In this section we describe a sample case to illustrate the use of the computer program. The case consists of a body-canard-tail configuration at supersonic speed, unrolled, at an angle of attack, and with yaw control.

The configuration is shown in figure 7 and 8 of the main text and is the MICOM-NWC model of reference 4 with the N_3 nose, the C_6 canard fins, and the T_2 tail fins. The angle of attack is 30° , the model is at a bank angle of 30° . All fins are undeflected. Mach number is 1.3 and the crossflow is considered turbulent. The influence of nose vortices is calculated to the canard trailing edge (NVORT = 2). Afterbody vortices (if they form) are initially positioned at 1.2 radii from the body axis (RVOA = 1.2). Finally, vortices of like sign are combined along the afterbody if they come within a distance of 0.2 body radii of one another (RVORT = 0.2). The input deck for this case is shown in figure E.4. The output is presented in figure E.5.

2
 MICOM-NWC BODY-CANARD-TAIL CASE (BN₃C₆T₂)
 ONE VORTEX PER FIN

									T	F	P	
4	1	.99	1	2	1	20	1	19	0	.56	16.72	12.72
1.3		5.		19.634		26.		2.5			2.5	3.
1.274		1.524		1.424		1.524		1.673				
4.		5.		6.		7.		8.		9.	10.	11.
12.		13.		15.								
0.		.251		.481		.466		.537		.635	.779	.916
1.173		1.406		1.616		1.803		1.967		2.109	2.229	2.321
2.408		2.457		2.5								
30.												
30.												
0.		0.		0.		0.		0.		0.	0.	0.
6.25		15.		16.47		16.72						
.05		.001		.2		1.2		45.		45.	1.2	
6.		46.		46.5		50.		0.				
000												

Figure E.4 Input for sample case; MICOM-NWC body-canard-tail configuration (BN₃C₆T₂).

CALCULATION OF AERODYNAMIC LOADS ON A CHUCLIFORM MISSILE

MICOM-NXC BODY-CANARD-TAIL CASE (BN3.C6T2)

***** MISSILE BODY GEOMETRY *****
MISSILE IS A CANARD-TAIL COMBINATION

*** NOSE GEOMETRY ***

NOSE TIP DIAMETER .50000
NOSE HALF ANGLE 16.72000

*** NOSE COORDINATES ***

	1.000	1.024	1.024	1.075	2.000	2.500	3.000	4.000	5.000	6.000	7.000	8.000	9.000	10.000	11.000	12.000	13.000	14.000
ANGLE	.000	.231	.231	.337	.615	.779	.916	1.175	1.406	1.610	1.803	1.967	2.109	2.229	2.327	2.400	2.457	2.500

LINEAR NORMAL FINCH COEFFICIENT SLOPE IS 2.000

*** CANARD GEOMETRY ***

	ASPECT RATIO	SLASHSPAN	HINGE LINE	TIP LEADING EDGE	TIP TRAILING EDGE
1.000	6.25000	15.00000	12.72000	16.47000	16.72000

*** BODY GEOMETRY ***

BODY RADIUS 2.50000 CENTER OF MOMENTS 26.00000

*** TAIL GEOMETRY ***

	ASPECT RATIO	SLASHSPAN	HINGE LINE	RUNT LEADING EDGE	TIP LEADING EDGE	TRAILING EDGE	FHIT
1.00000	0.00000	0.00000	0.00000	43.00000	46.50000	50.00000	0.000

Figure E.5(a). Output for sample case; MICOM-NXC
body-canard-tail configuration (BN3.C6T2).

REFERENCE LENGTHS AND AREAS

REFERENCE LENGTHS

OUTPUT LENGTH =	5.00000
CPXRC =	4.00000
CPYRC =	3.75000
CPART =	7.00000
CPYRT =	3.50000

REFERENCE AREAS

OUTPUT AREA =	19.63500
CANARD WING-ALONE REF. AREA =	15.93750
TAIL WING-ALONE REF. AREA =	36.75000

FIN CN IS NORMALIZED BY OUTPUT AREA.

FIN COX IS NORMALIZED BY OUTPUT LENGTH.

FIN CPY IS NORMALIZED BY OUTPUT LENGTH AND IS MEASURED FROM R00Y AXIS.

FLIGHT CONDITIONS				PROGRAM OPERATION			
MACH NUMBER	TURBULENT FLOW	CANARD DEFLECTION ANGLES	TAIL DEFLECTION ANGLES	PANEL	PANEL	PANEL	PANEL
1.300		1 0.0	1 0.0				
		2 0.0	2 0.0				
		3 0.0	3 0.0				
		4 0.0	4 0.0				
ANGLES OF ATTACK	30.00						
ROLL ANGLES	30.00						
ACUMA	NXOUTS	NI	DXI	EPS	OMEGA	RVORT	ACUMB
1.200	20	99	.050	.00100	.05.000	.20	1.20

NOSE VORTICES ARE RUN TO CANARD TRAILING EDGE

Figure E.5(b). Continued.

THE FOLLOWING LOAD CALCULATIONS ARE FOR ALPHA = 30.000 AND PHI = 30.000
 CONTRIBUTION OF NOSE SECTION TO TOTAL LOADS
 NOSE VORTICES HAVE FORMED AT X/A = 2.38462

STRENGTHS AND POSITIONS OF VORTICES AT LEADING EDGE OF CANARD ROOT CHORD

	GAMMA/2PIVA	V0/A	Z0/A
1	.11277	.6272	1.3014
2	-.11277	-.6272	1.3014

NORMAL FORCE COEFFICIENT AND PITCHING MOMENT COEFFICIENT
 IN UNMILLED HULL COORDINATES

C20	C40
1.65613	5.62726
CL = 1.346	
CD = .777	

Figure E.5(c). Continued.

CANARD SECTION RESULTS FOR ALPHA = 30.000 AND PHI = 30.000							
VORTEX-FREE FIN LOADS							
PANEL	ALPHAEQ	CN	CPY	CNM	CPM	CNH	
1	8.74	.2309	.7938				
2	19.13	.4238	.7817				
3	21.00	.4741	.7742				
4	31.28	.6099	.7636				
VORTEX INDUCED EQUIVALENT ANGLE OF ATTACK, DEGREES	-2.84	-1.76	-1.12	-1.30			
CENTER OF PRESSURE FOR VORTEX INDUCED LOADS	1.17	1.08	1.58	1.57			
*** TOTAL CANARD FIN LOADS INCLUDING VORTEX EFFECTS ***							
PANEL	ALPHAEQ	CN	CPX	CPY	CNM	CPM	
1	5.95	1605	.4748	.6879	.1425	.0623	
2	16.53	.4957	.0825	.7548	.3106	.0127	
3	21.50	.4766	.4902	.7742	.3689	.0105	
4	33.07	.6081	.4974	.7635	.4643	.01307	
*** CONTRIBUTION OF CANARD SECTION TO TOTAL LOADS ***							
UNROLLED COORDINATES							
CX0 =	0.0000	CX10 =	.0377	CX =	0.0000	CXH =	.0727
CY0 =	-.0674	CY10 =	1.5361	CY =	-.9044	CYH =	2.9926
CZ0 =	1.6921	CZ10 =	.1431	CZ =	1.4317	CZH =	1.0930
CL =	1.4634						
CD =	.0461						
ROLLED COORDINATES							

Figure E.5(d). Continued.

AFTERBODY SECTION RESULTS FOR ALPHAS = 30.000 AND PHIS = 10.000						
		VORTEX TRACING RESULTS OVER AFTERBODY				
X/A	I	Gamma(1)	V(1)/A	Z(1)/A	FLOWANG	THETA
.0000E+01	1	1424E+01	1907E+01	3303E+01	20.43	92.19
	2	-1075E+00	1000SF+01	991E+00		
	3	-1364E+00	1351E+00	1611E+01		
	4	1941E+00	1566E+01	9040E+00		
<i>*** AFTERBODY VORTICES HAVE FURLED AT X/A = 4.69</i>						
THE LEFT VORTEX POSITION IS V(1)/A = 0.0000 AND Z(1)/A = .410						
THE RIGHT VORTEX POSITION IS V(1)/A = 0.122 AND Z(1)/A = .410						
.7214E+01	1	1424E+01	1894E+01	3545E+01	19.60	90.19
	2	-1073E+00	1013E+01	1251E+01		
	3	-1364E+00	1374E+00	1397E+01		
	4	1941E+00	1421E+01	6066E+00		
	5	-1593E+01	1416E+01	6744E+00		
	6	1751E+01	9667E+00	7462E+00		
.7739E+01	1	1424E+01	1862E+01	3976E+01	18.86	87.09
	2	-1073E+00	1543E+01	1554E+01		
	3	-1364E+00	1036E+01	1101E+01		
	4	1941E+00	1059E+01	2025E+00		
	5	-3090E+01	9944E+00	8843E+00		
	6	3213E+01	6222E+00	9839E+00		
.8265E+01	1	1424E+01	1842E+01	4104E+01	18.36	83.71
	2	-1073E+00	1046E+01	1810E+01		
	3	-1364E+00	1105E+01	9501E+00		
	4	1941E+00	1167E+01	3121E+01		
	5	-4460E+01	9546E+00	106MF+01		
	6	4467E+01	6676E+00	1157E+01		
.8780E+01	1	1424E+01	1826E+01	4426E+01	18.17	81.36
	2	-1073E+00	1046E+01	2708E+01		
	3	-1364E+00	1114E+01	7193E+00		
	4	1941E+00	1163E+01	353AE+00		
	5	-4669E+01	9266E+00	1242E+01		
	6	5003E+01	5641E+00	1295E+01		
.9310E+01	1	1424E+01	1806E+01	4704E+01	18.09	81.06
	2	-1073E+00	1037E+01	2546E+01		
	3	-1364E+00	1125E+01	4575E+00		
	4	1941E+00	1163E+01	6622E+00		
	5	-4664E+01	9103E+00	1414E+01		
	6	5119E+01	4840E+00	1408E+01		

Figure E.5(e). Continued.

0.9642E+01	1	-1.426E-01	-1.764E+01	-4.655E+01	18.76	62.96	.0592	.0252
	2	-1.675E+00	-1.527E+01	-2.607E+01				
	3	-1.384E+00	-1.350E+01	-1.145E+01				
	4	-1.881E+00	-1.593E+01	-9.591E+00				
	5	-1.959E+01	-9.820E+00	-1.955E+01				
	6	-7.913E+01	-4.212E+00	-1.500E+01				
0.1037E+02	1	-1.424E+01	-1.773E+01	-5.243E+01	19.84	66.04	.0720	.0171
	2	-1.075E+00	-1.774E+01	-2.633E+01				
	3	-1.384E+00	-1.326E+01	-1.166E+01				
	4	-1.091E+00	-1.551E+01	-1.554E+01				
	5	-1.094E+01	-6.651E+00	-1.752E+01				
	6	-9.220E+01	-3.727E+00	-1.573E+01				
0.1089E+02	1	-1.424E+01	-1.757E+01	-5.542E+01	20.86	69.02	.0639	.0160
	2	-1.075E+00	-1.231E+01	-3.115E+01				
	3	-1.384E+00	-1.519E+01	-3.946E+01				
	4	-1.081E+00	-1.514E+01	-1.562E+01				
	5	-1.031E+00	-6.915E+00	-1.912E+01				
	6	-1.094E+00	-3.660E+00	-1.630E+01				
0.1114E+02	1	-1.426E+01	-1.742E+01	-5.821E+01	22.27	91.10	.0615	.0217
	2	-1.075E+00	-1.297E+01	-3.362E+01				
	3	-1.384E+00	-1.694E+01	-6.647E+00				
	4	-1.081E+00	-1.605E+01	-1.627E+01				
	5	-1.163E+00	-6.954E+00	-2.055E+01				
	6	-1.264E+00	-3.181E+00	-1.675E+01				
0.1194E+02	1	-1.426E+01	-1.727E+01	-6.099E+01	23.58	92.24	.0626	.0226
	2	-1.075E+00	-1.142E+01	-5.646E+01				
	3	-1.384E+00	-1.275E+01	-9.119E+00				
	4	-1.081E+00	-1.915E+01	-2.111E+01				
	5	-1.174E+00	-6.929E+00	-2.210E+01				
	6	-1.304E+00	-5.123E+00	-1.715E+01				
0.1247E+02	1	-1.426E+01	-1.713E+01	-6.378E+01	24.71	92.70	.0656	.0354
	2	-1.075E+00	-1.111E+01	-5.346E+01				
	3	-1.384E+00	-1.262E+01	-1.144E+01				
	4	-1.081E+00	-1.541E+01	-2.391E+01				
	5	-1.157E+00	-8.616E+00	-2.347E+01				
	6	-1.167E+00	-5.177E+00	-1.737E+01				
0.1300E+02	1	-1.426E+01	-1.700E+01	-6.657E+01	25.62	92.75	.0633	.0362
	2	-1.075E+00	-1.062E+01	-4.055E+01				
	3	-1.384E+00	-1.264E+01	-1.567E+01				
	4	-1.081E+00	-1.245E+01	-2.682E+01				
	5	-1.116E+00	-6.944E+00	-2.476E+01				
	6	-1.203E+00	-3.292E+00	-1.807E+01				

Figure E.5(f). Continued.

.1152E+02	1	.142at=01	.1646E+01	.6936E+01	26.15	92.56	.0000	.0325
	2	-.1075E+00	.1025E+01	.4921E+01				
	3	-.1384E+00	.1205E+01	.1584E+01				
	4	-.1611E+00	.1201E+01	.1581E+01				
	5	-.1760E+00	.8635E+00	.2927E+01				
	6	-.2191E+00	.3419E+01	.2594E+01				
				.1666E+01				
.1409E+02	1	.142at=01	.1676E+01	.7214E+01				
	2	-.1075E+00	.4911E+01	.4554E+01				
	3	-.1384E+00	.1355E+01	.1605E+01				
	4	-.1611E+00	.1117E+01	.1616E+01				
	5	-.1949E+00	.6576E+00	.2697E+01				
	6	-.2597E+00	.5521E+00	.1934E+01				
.1457E+02	1	.142at=01	.1665E+01	.7494E+01				
	2	-.1075E+00	.4932E+01	.4766E+01				
	3	-.1384E+00	.1196E+01	.1454E+01				
	4	-.1611E+00	.1045E+01	.1394E+01				
	5	-.1949E+00	.6743E+00	.2780E+01				
	6	-.2597E+00	.5574E+00	.2111E+01				
.15110F+02	1	.142at=01	.1655F+01	.7774F+01				
	2	-.1075E+00	.3911E+00	.5016E+01				
	3	-.1384E+00	.1498E+01	.2311E+01				
	4	-.1611E+00	.9877E+00	.3635F+01				
	5	-.2306E+00	.6169E+00	.2452E+01				
	6	.3177E+00	.3560E+00	.2094E+01				
.1562E+02	1	.142at=01	.1645E+01	.6937E+01				
	2	-.1075E+00	.3212E+00	.5244E+01				
	3	-.1384E+00	.1540E+01	.2634E+01				
	4	-.1611E+00	.1044E+01	.3623E+01				
	5	-.2495E+00	.6177E+00	.2594E+01				
	6	.3465E+00	.3494E+00	.2178E+01				
.1615E+02	1	.142at=01	.1650E+01	.8349E+01				
	2	-.1075E+00	.4053E+00	.5711E+01				
	3	-.1384E+00	.1556E+01	.2974E+01				
	4	-.1611E+00	.1032E+01	.4027E+01				
	5	-.2693E+00	.8511E+00	.2942E+01				
	6	.3786E+00	.5393E+00	.2265E+01				
.1667E+02	1	.142at=01	.1624E+01	.8622E+01				
	2	-.1075E+00	.4957E+00	.5697E+01				
	3	-.1384E+00	.1510E+01	.3297E+01				
	4	-.1611E+00	.1043E+01	.4227E+01				
	5	-.2889E+00	.9195E+00	.2844E+01				
	6	.4012E+00	.6265E+00	.2341E+01				
.1720E+02	1	.142at=01	.1622E+01	.8905E+01				
	2	-.1075E+00	.6899E+00	.5925E+01				

Figure E.5(g). Continued.

*** CONTRIBUTION OF AFTERBODY SECTION TO TOTAL LOADS IN UNROLLED BODY COORDINATES **

3	*.1386E+00	*.1386E+00	*.3517E+01
4	*.1681E+00	*.1681E+00	*.4424E+01
5	*.3089E+00	*.1194E+01	*.2405E+01
6	*.4281E+00	*.3195E+00	*.2422E+01

*** CONTRIBUTION OF AFTERBODY SECTION TO TOTAL LOADS IN UNROLLED BODY COORDINATES **

CY0 =	.903	CH0 =	*2.074
CY1 =	1.947	CH1 =	.369
CL =	1.721		
CO =	.996		

Figure 8.5(h). Continued.

TAIL SECTION RESULTS FOR ALPHAS = 30,000 AND PHI = 30,000
W/ TAIL FIN LOADS

PANEL	ALPHAS	CX	CY	CPY
1	12.94	.5352	.8322	
2	22.04	.9450	.6037	
3	26.23	1.0963	.7935	
4	26.95	1.1775	.7882	

VORTEX INDUCED EQUIVALENT ANGLE OF ATTACK, DEGREES +15.51

CENTER OF PRESSURE FROM VORTEX INDUCED LOADS 1.57

*** TOTAL TAIL FIN LOADS INCLUDING VORTEX EFFECTS ***

PANEL	ALPHAS	CX	CY	CPY	CRM	CMR	CHM
1	+2.74	*.0957	.0671	.5122	*.0480	*.0162	*.0066
2	15.42	.6710	.7352	.6079	.5421	.2766	*.007
3	25.00	1.0751	.7725	.7937	.6534	.3158	*.1655
4	26.47	1.1637	.7755	.7884	.9175	.3356	*.2089

*** CONTRIBUTION OF TAIL SECTION TO TOTAL LOADS ***

UNROLLED COORDINATES

CX0 = 0.0000	CMX0 = +.5271	CX = 0.0000	CMX = -.5271
CY0 = .11C17	CMY0 = +13.5787	CY = -1.5146	CMY = +11.9666
CZ0 = 3.2057	CMZ0 = .414b	CZ = 2.8270	CMZ = +6.4503
CL = 2.7762			
CD = 1.0028			

*** SUMMARY OF TOTAL LOADS IN ROLLY COORDINATES ***

ALPHAS = 30,000 PHI = 30,000

ROLLED COORDINATES

CX0 = 0.00000	CMX0 = -.59976	CX = 0.00000	CMX = -.59976
CY0 = .43775	CMY0 = +6.08687	CY = +3.04448	CMY = +6.08621
CZ0 = 5.45916	CMZ0 = .92684	CZ = 7.52740	CMZ = +2.44076
CL = 7.10853	CPX = 5.96866		
CD = 4.21958	CPY = 7.31730		

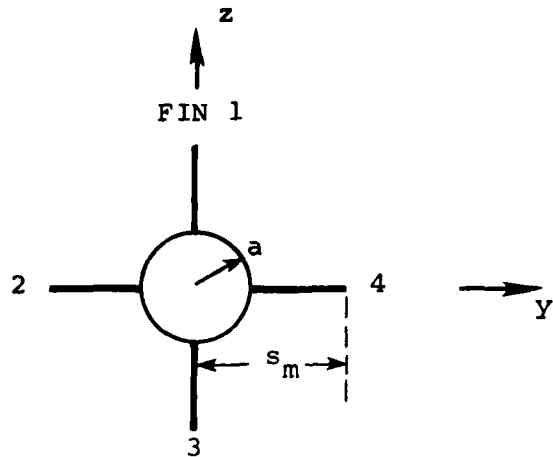
END OF CALCULATIONS FOR THIS CASE

Figure E.5(i). Concluded.

REFERENCES

- E-1 Nielsen, J. N.: *Missile Aerodynamics*. McGraw-Hill Book Co., 1960.
- E-2 Mendenhall, M. R., Goodwin, F. K., Dillenius, M. F. E., and Kline, D. M.: Computer Programs for Calculating the Static Longitudinal Aerodynamic Characteristics of Wing-Body-Tail Configurations. NASA CR-2474, January 1975.
- E-3 Aiello, G. F.: Aerodynamic Methodology. Bodies with Tails at Arbitrary Roll Angles. (Transonic and Supersonic.) Martin Marietta Corp., Orlando Div., Report OR 14,145, April 1976.

TABLE 1. FIN EQUIVALENT ANGLES OF ATTACK AND
LATERAL CENTER-OF-PRESSURE POSITIONS
FOR CONTROL DEFLECTION OF FIN 4 OF
CRUCIFORM WING-BODY COMBINATION;
SLENDER-BODY THEORY



δ_4 = deflection of Fin 4

(a) Equivalent angles of attack

a/s_m	$\frac{\Delta(\alpha_{eq})_1}{\delta_4}$	$\frac{\Delta(\alpha_{eq})_2}{\delta_4}$	$\frac{\Delta(\alpha_{eq})_3}{\delta_4}$	$\frac{\Delta(\alpha_{eq})_4}{\delta_4}$
0	-.275	.0789	.275	.921
.1	-.230	.0731	.230	.890
.2	-.188	.0658	.188	.878
.3	-.149	.0567	.149	.879
.4	-.112	.0460	.112	.889
.5	-.0784	.0343	.0784	.905
.6	-.0498	.0230	.0498	.925
.7	-.0272	.0130	.0272	.946
.8	-.0115	.00566	.0115	.966
.9	-.0027	.00134	.0027	.984
1.0	0	0	0	1.00

TABLE 1. CONCLUDED.

(b) Lateral center-of-pressure locations.

a/s_m	$ \bar{z}_1 - a$ $s_m - a$	$ \bar{y}_2 - a$ $s_m - a$	$ \bar{z}_3 - a$ $s_m - a$	$ \bar{y}_4 - a$ $s_m - a$
0	.358	.413	.358	.425
.1	.370	.410	.370	.431
.2	.381	.409	.381	.432
.3	.390	.409	.390	.432
.4	.398	.411	.398	.431
.5	.405	.413	.405	.429
.6	.411	.415	.411	.428
.7	.420	.422	.420	.427
.8	.426	.427	.426	.426
.9	.461	.462	.462	.425
1.0	.438	.456	.438	.424

 \bar{z}_1, \bar{z}_3 - center-of-pressure coordinates for fins F_1 and F_3 \bar{y}_2, \bar{y}_4 - center-of-pressure coordinates for fins F_2 and F_4

TABLE 2. WING-ALONE NORMAL-FORCE COEFFICIENTS FOR FINS
OF SYSTEMATIC DATA BASE

(a) $M_{\infty} = 0.8$

FIN	T36	T31	T32	T14	T15	T11	T23
Aspect ratio	0.5	0.5	0.5	1.0	1.0	1.0	2.0
Taper ratio	0	0.5	1.0	0	0.5	1.0	0.5
α , degs.							
0	.000	.000	.000	.000	.000	.000	.000
2	.022	.031	.025	.039	.050	.050	.062
4	.052	.071	.057	.088	.112	.107	.156
6	.088	.119	.097	.144	.184	.170	.269
8	.129	.175	.144	.207	.264	.240	.395
10	.176	.239	.198	.275	.351	.314	.503
...
12	.228	.310	.258	.348	.444	.394	.583
14	.284	.390	.326	.424	.541	.478	.649
16	.344	.474	.400	.503	.642	.564	.705
18	.408	.564	.482	.585	.746	.651	.755
20	.473	.658	.570	.670	.849	.734	.800
...
22	.538	.752	.664	.758	.942	.794	.842
24	.603	.846	.761	.849	1.012	.842	.881
26	.667	.938	.857	.943	1.068	.883	.917
28	.730	1.026	.950	1.036	1.115	.919	.951
30	.791	1.110	1.032	1.115	1.155	.952	.983
...
32	.850	1.186	1.094	1.179	1.191	.982	1.014
34	.906	1.252	1.145	1.229	1.222	1.010	1.043
36	.960	1.308	1.188	1.268	1.250	1.036	1.071
38	1.001	1.356	1.225	1.300	1.276	1.061	1.098
40	1.060	1.396	1.258	1.329	1.299	1.085	1.124
...
42	1.107	1.429	1.288	1.355	1.320	1.108	1.149
44	1.150	1.457	1.315	1.379	1.339	1.130	1.173
46	1.191	1.481	1.340	1.401	1.357	1.152	1.197
48	1.227	1.501	1.364	1.421	1.374	1.172	1.220
50	1.261	1.519	1.386	1.439	1.389	1.192	1.243
...
52	1.290	1.535	1.406	1.455	1.403	1.212	1.265
54	1.316	1.550	1.426	1.471	1.417	1.231	1.287
56	1.338	1.564	1.444	1.486	1.429	1.249	1.309
58	1.355	1.576	1.462	1.500	1.441	1.267	1.330
60	1.368	1.588	1.480	1.514	1.452	1.284	1.350

TABLE 2. WING-ALONE NORMAL-FORCE COEFFICIENTS FOR FINS
OF SYSTEMATIC DATA BASE

(b) $M_{\infty} = 1.2$

FIN	T36	T31	T32	T14	T15	T11	T23
Aspect ratio	0.5	0.5	0.5	1.0	1.0	1.0	2.0
Taper ratio	0	0.5	1.0	0	0.5	1.0	0.5
α , degs.							
0	.000	.000	.000	.000	.000	.000	.000
2	.025	.031	.029	.049	.057	.061	.109
4	.057	.071	.065	.104	.124	.131	.221
6	.094	.118	.109	.166	.200	.206	.335
8	.136	.174	.164	.231	.283	.289	.451
10	.183	.241	.230	.300	.374	.378	.567
...
12	.234	.313	.305	.373	.473	.471	.681
14	.289	.392	.386	.449	.575	.565	.793
16	.347	.474	.470	.526	.678	.659	.899
18	.408	.558	.555	.604	.781	.753	.997
20	.471	.642	.640	.682	.880	.844	1.088
...
22	.536	.726	.725	.759	.975	.933	1.169
24	.602	.808	.809	.834	1.063	1.018	1.240
26	.669	.887	.890	.906	1.145	1.099	1.299
28	.736	.964	.969	.975	1.218	1.174	1.348
30	.803	1.037	1.044	1.042	1.286	1.244	1.389
...
32	.860	1.106	1.116	1.103	1.343	1.306	1.424
34	.925	1.170	1.183	1.159	1.390	1.363	1.455
36	.989	1.229	1.243	1.208	1.426	1.413	1.483
38	1.051	1.281	1.297	1.253	1.456	1.454	1.506
40	1.111	1.325	1.341	1.294	1.481	1.488	1.527
...
42	1.167	1.364	1.373	1.330	1.501	1.517	1.545
44	1.220	1.398	1.398	1.363	1.519	1.541	1.557
46	1.277	1.428	1.421	1.394	1.534	1.563	1.574
48	1.320	1.451	1.441	1.423	1.547	1.582	1.589
50	1.359	1.472	1.459	1.450	1.559	1.599	1.601
...
52	1.395	1.491	1.475	1.475	1.569	1.615	1.612
54	1.428	1.508	1.491	1.498	1.577	1.629	1.623
56	1.456	1.523	1.505	1.519	1.585	1.641	1.633
58	1.482	1.537	1.519	1.539	1.592	1.652	1.642
60	1.505	1.550	1.531	1.557	1.600	1.662	1.650

TABLE 2. WING-ALONE NORMAL-FORCE COEFFICIENTS FOR FINS
OF SYSTEMATIC DATA BASE

(c) $M_{\infty} = 2.0$

FIN	T36	T31	T32	T14	T15	T11	T23
Aspect ratio	0.5	0.5	0.5	1.0	1.0	1.0	2.0
Taper ratio	0	0.5	1.0	0	0.5	1.0	0.5
α , degs.							
0	.000	.000	.000	.000	.000	.000	.000
2	.035	.046	.047	.050	.064	.064	.066
4	.070	.092	.093	.100	.124	.124	.130
6	.107	.142	.144	.151	.187	.185	.197
8	.146	.196	.199	.203	.250	.291	.265
10	.188	.250	.254	.260	.318	.321	.339
...
12	.235	.309	.314	.319	.387	.394	.416
14	.285	.369	.375	.381	.460	.472	.498
16	.337	.431	.438	.444	.532	.549	.582
18	.390	.493	.501	.510	.608	.629	.672
20	.443	.554	.563	.576	.683	.708	.763
...
22	.496	.615	.625	.642	.758	.786	.848
24	.549	.674	.685	.708	.831	.863	.927
26	.602	.733	.745	.773	.903	.938	1.004
28	.655	.792	.806	.836	.972	1.010	1.076
30	.708	.851	.867	.887	1.039	1.079	1.146
...
32	.762	.909	.926	.956	1.103	1.146	1.211
34	.817	.969	.988	1.013	1.164	1.209	1.272
36	.874	1.030	1.050	1.068	1.224	1.271	1.332
38	.933	1.093	1.115	1.120	1.280	1.329	1.387
40	.995	1.159	1.182	1.170	1.333	1.383	1.439
...
42	1.058	1.225	1.250	1.218	1.385	1.436	1.489
44	1.122	1.292	1.318	1.264	1.434	1.487	1.536
46	1.183	1.356	1.383	1.308	1.481	1.536	1.579
48	1.241	1.417	1.446	1.350	1.526	1.582	1.621
50	1.295	1.473	1.503	1.389	1.567	1.624	1.659
...
52	1.345	1.525	1.555	1.426	1.606	1.664	1.693
54	1.392	1.574	1.606	1.461	1.643	1.752	1.725
56	1.436	1.620	1.653	1.494	1.678	1.738	1.755
58	1.476	1.661	1.695	1.524	1.710	1.770	1.782
60	1.510	1.697	1.732	1.552	1.739	1.800	1.806

TABLE 2. WING-ALONE NORMAL-FORCE COEFFICIENTS FOR FINS
OF SYSTEMATIC DATA BASE

(d) $M_{\infty} = 3.0$

FIN	T36	T31	T32	T14	T15	T11	T23
Aspect ratio	0.5	0.5	0.5	1.0	1.0	1.0	2.0
Taper ratio	0	0.5	1.0	0	0.5	1.0	0.5
α , degs.							
0	.000	.000	.000	.000	.000	.000	.000
2	.025	.035	.035	.037	.043	.042	.045
4	.054	.072	.072	.075	.088	.087	.092
6	.086	.112	.112	.116	.136	.134	.141
8	.122	.157	.158	.162	.189	.186	.196
10	.160	.203	.206	.210	.243	.236	.253
...
12	.200	.251	.256	.260	.300	.293	.313
14	.241	.299	.306	.311	.358	.355	.374
16	.284	.350	.359	.364	.418	.418	.436
18	.327	.400	.411	.418	.479	.485	.500
20	.371	.451	.464	.473	.541	.553	.567
...
22	.415	.501	.515	.528	.603	.623	.637
24	.460	.551	.567	.584	.616	.697	.708
26	.505	.601	.612	.641	.730	.770	.776
28	.552	.653	.671	.697	.793	.835	.841
30	.600	.705	.725	.755	.858	.900	.906
...
32	.650	.757	.778	.814	.924	.963	.970
34	.702	.815	.827	.873	.990	1.026	1.036
36	.756	.865	.888	.936	1.060	1.091	1.105
38	.812	.925	.950	1.000	1.131	1.158	1.165
40	.870	.980	1.006	1.063	1.201	1.225	1.253
...
42	.930	1.045	1.071	1.123	1.268	1.293	1.308
44	.991	1.095	1.122	1.182	1.334	1.364	1.372
46	1.054	1.155	1.183	1.238	1.388	1.421	1.420
48	1.119	1.210	1.239	1.292	1.435	1.477	1.465
50	1.184	1.265	1.294	1.342	1.480	1.525	1.505
...
52	1.244	1.315	1.345	1.389	1.515	1.555	1.545
54	1.299	1.365	1.395	1.430	1.550	1.580	1.570
56	1.349	1.410	1.441	1.465	1.575	1.600	1.595
58	1.395	1.450	1.481	1.497	1.595	1.620	1.615
60	1.435	1.480	1.512	1.525	1.615	1.640	1.630

248
 TABLE 3. WING-ALONE NORMAL-FORCE COEFFICIENTS
 FOR FIN C6 OF ASPECT RATIO 3.53

Aspect ratio = 3.53 Taper ratio = .06 S_R = wing planform area

C_{N_W}

α , degs.	$M_\infty = 0.8$	$M_\infty = 1.30$
0	0	0
2	.144	.133
4	.284	.267
6	.417	.399
8	.536	.525
10	.632	.643
12	.707	.754
14	.760	.857
16	.790	.952
18	.807	1.039
20	.817	1.119
22	.824	1.193
24	.831	1.260
26	.840	1.322
28	.853	1.378
30	.871	1.429
32	.895	1.476
34	.923	1.518
35	.956	1.557
38	.995	1.592
40	1.038	1.623
42	1.088	1.651
44	1.143	1.677
46	1.204	1.701
48	1.274	1.723
50	1.352	1.744
52	1.433	1.765
54	1.508	1.785
56	1.567	1.805
58	1.612	1.825
60	1.646	1.844

TABLE 4. LATERAL CENTER-OF-PRESSURE POSITIONS
FOR FINS OF SYSTEMATIC DATA BASE;
NO VORTEX EFFECTS

(a) $M_{\infty} = \underline{0.8}$ $a/s_m = \underline{0.5}$

$$(\bar{y}_p - a) / (s_m - a)$$

FIN	T11	T14	T15	T23	T31
Aspect ratio	1.0	1.0	1.0	2.0	0.5
Taper ratio	1.0	0	0.5	0.5	0.5
CNT4					
0	.611	.446	.472	.545	.433
.2	.591	.418	.458	.503	.420
.4	.570	.389	.444	.469	.411
.6	.549	.359	.430	.439	.404
.8	.528	.330	.416	.411	.398
1.0	.507	.301	.403	.385	.393
1.2	.486	.271	.388	.359	.390
1.4	.465	.242	.375	.335	.387

TABLE 4. LATERAL CENTER-OF-PRESSURE POSITIONS
FOR FINS OF SYSTEMATIC DATA BASE;
NO VORTEX EFFECTS

$$(b) \quad M_{\infty} = \underline{1.2} \quad a/s_m = \underline{0.5}$$

$$(\bar{y}_p - a) / (s_m - a)$$

FIN	T11	T14	T15	T23	T31
Aspect ratio	1.0	1.0	1.0	2.0	0.5
Taper ratio	1.0	0	0.5	0.5	0.5
CNT4					
0	.592	.462	.538	.528	.440
.2	.576	.430	.519	.508	.439
.4	.563	.399	.501	.486	.436
.6	.549	.371	.482	.465	.432
.8	.534	.344	.463	.444	.425
1.0	.519	.321	.445	.424	.418
1.2	.505	.301	.426	.405	.410
1.4	.490	.287	.407	.387	.401
1.6	.476	.279	.389	.371	—

TABLE 4. LATERAL CENTER-OF-PRESSURE POSITIONS
FOR FINS OF SYSTEMATIC DATA BASE;
NO VORTEX EFFECTS

(c) $M_{\infty} = \underline{2.0}$ $a/s_m = \underline{0.5}$

$$(\bar{y}_p - a) / (s_m - a)$$

FIN	T11	T14	T15	T23	T31
Aspect ratio	1.0	1.0	1.0	2.0	0.5
Taper ratio	1.0	0	0.5	0.5	0.5
CNT4					
0	.5314	.4345	.5120	.583	.5076
.2	.5087	.3874	.4837	.511	.4795
.4	.4934	.3464	.4628	.462	.4594
.6	.4824	.3202	.4464	.429	.4442
.8	.4737	.3074	.4334	.406	.4330
1.0	.4664	.2996	.4216	.391	.4236
1.2	.4601	.2940	.4107	.381	.4156
1.4	.4546	.2902	.4019	.374	.4083
1.6	.4490	—	.3936	.368	—

TABLE 4. LATERAL CENTER-OF-PRESSURE POSITIONS
FOR FINS OF SYSTEMATIC DATA BASE;
NO VORTEX EFFECTS

(d) $M_{\infty} = \underline{3.0}$ $a/s_m = \underline{0.5}$

$$(\bar{y}_p - a) / (s_m - a)$$

FIN	T11	T14	T15	T23	T31
Aspect ratio	1.0	1.0	1.0	2.0	0.5
Taper ratio	1.0	0	0.5	0.5	0.5
CNT4					
0	.5302	.4224	.4905	.5022	.4625
.2	.5154	.3827	.4779	.4834	.4526
.4	.5026	.3565	.4674	.4679	.4454
.6	.4922	.3382	.4578	.4547	.4394
.8	.4830	.3243	.4494	.4425	.4343
1.0	.4744	.3137	.4416	.4317	.4302
1.2	.4665	.3046	.4338	.4216	.4274
1.4	.4593	—	.4264	.4116	—
1.6	.4522	—	.4196	.4020	—

TABLE 5. LATERAL CENTER-OF-PRESSURE POSITIONS
FOR FIN C6 OF ASPECT RATIO 3.53;
NO VORTEX EFFECTS

Aspect ratio = 3.53 Taper ratio = .06 $a/s_m = 0.4$

$M_\infty = 0.8$		$M_\infty = 1.3$	
CNC 4	$(\bar{y}_p - a) / (s_m - a)$	CNC4	$(\bar{y}_p - a) / (s_m - a)$
0	.434	0	.3995
.2	.429	.2	.3987
.4	.416	.4	.3970
.6	.337	.6	.3942
.8	.342	.8	.3883
1.0	.355	1.0	.3790
1.2	.355	1.2	.3636
1.4	.355	1.4	.3538
1.6	.354	1.6	.3487

Reference area = wing planform area

254
 TABLE 6. NORMAL-FORCE COEFFICIENTS OF FINS
 ON BODY B₁ INCLUDING VORTEX EFFECTS

(a) FIN: T11 a/s_m: 0.5 AR: 1.0 λ: 1.0 M_∞: .8

CNT4, FIN NORMAL-FORCE COEFFICIENT

$\phi_4 \backslash \alpha_c$	0°	4°	10°	15°	20°	25°	30°	35°	40°	45°	50°
-90°	0	0	0	0	0	0	0	0	0	0	0
-80°	0	.0167	.0125	.0310	.0764	.1114	.1174	.020	.016	.0920	
-70°	0	.0360	.0472	.0174	.0406	.044	.056	.0849	.0544	.0014	
-60°	0	.0568	.1176	.1305	.1448	.1696	.2098	.3052	.3144	.1984	
-50°	0	.0790	.1965	.269	.333	.4035	.4925	.5765	.415	.279	
-40°	0	.1012	.285	.421	.544	.653	.743	.785	.703	.538	
-30°	0	.1221	.362	.541	.700	.835	.928	.951	.930	.879	
-20°	0	.140	.388	.589	.782	.962	1.049	1.015	1.056	1.075	
-10°	0	.1544	.493	.719	.888	.986	.960	.998	1.072	1.168	
0°	0	.1631	.480	.692	.831	.833	.857	.958	1.048	1.180	
10°	0	.1656	.493	.686	.706	.726	.827	.943	1.064	1.171	
20°	0	.1630	.484	.697	.764	.757	.829	.948	1.049	1.142	
30°	0	.1538	.488	.683	.843	.838	.856	.969	1.055	1.118	
40°	0	.1350	.386	.617	.820	.949	1.011	1.048	1.094	1.146	
50°	0	.1120	.322	.520	.734	.970	1.05	1.107	1.189	1.228	
60°	0	.0868	.242	.406	.595	.801	.993	1.092	1.131	1.182	
70°	0	.0598	.155	.265	.395	.538	.675	.796	.898	.977	
80°	0	.0310	.074	.127	.186	.246	.304	.357	.404	.442	
90°	0	0	0	0	0	0	0	0	0	0	

S_R = fin planform area

TABLE 6. NORMAL-FORCE COEFFICIENTS OF FINS
ON BODY B, INCLUDING VORTEX EFFECTS

(b) FIN: T14 a/s_m: 0.5 AR: 1.0 λ: 0 M_∞: .8

CNT4, FIN NORMAL-FORCE COEFFICIENT

256

TABLE 6. NORMAL-FORCE COEFFICIENTS OF FINS
ON BODY E, INCLUDING VORTEX EFFECTS

(c) FIN: T15 a/s_m: 0.5 AR: 1.0 λ: 0.5 M_∞: .8

CNT⁴, FIN NORMAL-FORCE COEFFICIENT

257

TABLE 6. NORMAL-FORCE COEFFICIENTS OF FINS
ON BODY B, INCLUDING VORTEX EFFECTS

$$(d) \quad \text{FIN: } \underline{\underline{T_{23}}} \quad a/s_m : \underline{\underline{0.5}} \quad AR: \underline{\underline{2}} \quad \lambda: \underline{\underline{0.5}} \quad M_\infty: \underline{\underline{.8}}$$

CNT 4, FIN NORMAL-FORCE COEFFICIENT

TABLE 6. NORMAL-FORCE COEFFICIENTS OF FINS
ON BODY B₁, INCLUDING VORTEX EFFECTS

(e) FIN: T31 a/s_m: 0.5 AR: 0.5 λ: 0.5 M_∞: .8

CNT 4, FIN NORMAL-FORCE COEFFICIENT

TABLE 6. NORMAL-FORCE COEFFICIENTS OF FINS
ON BODY B₁, INCLUDING VORTEX EFFECTS

$$(f) \quad \text{FIN: } \underline{\text{T11}} \quad a/s_m : \underline{0.5} \quad AR: \underline{1.0} \quad \lambda: \underline{1.0} \quad M_\infty: \underline{1.2}$$

CNT4, FIN NORMAL-FORCE COEFFICIENT

**TABLE 6. NORMAL-FORCE COEFFICIENTS OF FINS
ON BODY B, INCLUDING VORTEX EFFECTS**

(g) FIN: T14 a/s_m: 0.5 AR: 1.0 λ: 0 M_∞: 1.2

261

TABLE 6. NORMAL-FORCE COEFFICIENTS OF FINS
ON BODY B₁, INCLUDING VORTEX EFFECTS

$$(h) \quad \text{FIN: } \underline{\text{T15}} \quad a/s_m: \underline{0.5} \quad AR: \underline{1.0} \quad \lambda: \underline{0.5} \quad M_\infty: \underline{1.2}$$

CNT4, FIN NORMAL-FORCE COEFFICIENT

TABLE 6. NORMAL-FORCE COEFFICIENTS OF FINS
ON BODY B₁ INCLUDING VORTEX EFFECTS

(i) FIN: T23 a/s_m: 0.5 AR: 2.0 λ: 0.5 M_∞: 1.2

CNT 4, FIN NORMAL-FORCE COEFFICIENT

263

TABLE 6. NORMAL-FORCE COEFFICIENTS ON FINS
ON BODY B₁, INCLUDING VORTEX EFFECTS

(j) FIN: T31 a/s_m: 0.5 AR: 0.5 λ: 0.5 M_∞: 1.2

²⁰⁴
TABLE 6. NORMAL-FORCE COEFFICIENTS OF FINS
ON BODY B, INCLUDING VORTEX EFFECTS

(k) FIN: T11 a/s_m: 0.5 AR: 1.0 λ: 1.0 M_∞: 2.0

265

TABLE 6. NORMAL-FORCE COEFFICIENTS OF FINS
ON BODY B, INCLUDING VORTEX EFFECTS

$$(1) \quad \text{FIN: } \underline{\text{T14}} \quad a/s_m : \underline{0.5} \quad AR: \underline{1.0} \quad \lambda: \underline{0} \quad M_\infty: \underline{2.0}$$

CNT4, FIN NORMAL-FORCE COEFFICIENT

TABLE 6. NORMAL-FORCE COEFFICIENTS OF FINS
ON BODY B₁ INCLUDING VORTEX EFFECTS

(m) FIN: T15 a/s_m: 0.5 AR: 1.0 λ: 0.5 M_∞: 2.0

CNT4, FIN NORMAL-FORCE COEFFICIENT

267

TABLE 6. NORMAL-FORCE COEFFICIENTS OF FINS
ON BODY B₁, INCLUDING VORTEX EFFECTS

(n) FIN: T23 a/s_m: 0.5 AR: 2.0 λ: 0.5 M_∞: 2.0

268

TABLE 6. NORMAL-FORCE COEFFICIENTS OF FINS
ON BODY B, INCLUDING VORTEX EFFECTS

$$(o) \quad \text{FIN: } \underline{\text{T31}} \quad a/s_m: \underline{0.5} \quad AR: \underline{0.5} \quad \lambda: \underline{0.5} \quad M_\infty: \underline{2.0}$$

CNT 4, FIN NORMAL-FORCE COEFFICIENT

269

TABLE 6. NORMAL-FORCE COEFFICIENTS OF FINS
ON BODY B₁, INCLUDING VORTEX EFFECTS

(p) FIN: T32 a/s_m: 0.5 AR:0.5 λ: 1.0 M_∞: 2.0

CNT 4, FIN NORMAL-FORCE COEFFICIENT

TABLE 6. NORMAL-FORCE COEFFICIENTS OF FINS
ON BODY B₁, INCLUDING VORTEX EFFECTS

(q) FIN: T36 a/s_m: 0.5 AR: 0.5 λ: 0 M_∞: 2.0

CNT4, FIN NORMAL-FORCE COEFFICIENT

TABLE 6. NORMAL-FORCE COEFFICIENTS OF FINS
ON BODY B, INCLUDING VORTEX EFFECTS

(r) FIN: T11 a/s_m: 0.5 AR: 1.0 λ: 1.0 M_∞: 3.0

TABLE 6. NORMAL-FORCE COEFFICIENTS OF FINS
ON BODY B₁ INCLUDING VORTEX EFFECTS

(s) FIN: T14 a/s_m: 0.5 AR: 1.0 λ: 0 M_∞: 3.0

CNT4, FIN NORMAL-FORCE COEFFICIENT

α_c ϕ_4	0°	4°	10°	15°	20°	25°	30°	35°	40°	45°	50°
-90°	0	0	0	0	0	0	0	0	0	0	0
-80°	0	.0117	-.038	-.060	-.048	-.0225	.0035	.007	.009	.0015	-.013
-70°	0	.0231	-.0665	-.069	-.0315	-.010	.0090	.024	.0350	.0425	.007
-60°	0	.035	-.018	-.025	.000	.029	.051	.073	.096	.110	.106
-50°	0	.0478	.020	.004	.038	.0855	.1285	.168	.200	.224	.236
-40°	0	.0608	.061	.063	.112	.161	.211	.264	.311	.353	.386
-30°	0	.0728	.107	.130	.177	.243	.317	.385	.441	.484	.515
-20°	0	.0821	.130	.175	.260	.347	.430	.510	.585	.650	.705
-10°	0	.0889	.165	.232	.303	.383	.479	.585	.701	.821	.958
0°	0	.0934	.195	.260	.351	.457	.577	.707	.846	.972	1.072
10°	0	.0949	.213	.288	.376	.487	.648	.827	.980	1.105	1.205
20°	0	.0928	.211	.317	.427	.552	.690	.857	1.057	1.227	1.345
30°	0	2.17	3.22	4.27	5.51	7.73	8.77	1.092	1.288	1.395	1.44
40°	0	2.17	3.22	4.27	5.51	7.73	8.77	1.092	1.288	1.395	1.44
50°	0	2.17	3.22	4.27	5.51	7.73	8.77	1.092	1.288	1.395	1.44

TABLE 6. NORMAL-FORCE COEFFICIENTS OF FINS
ON BODY B_1 INCLUDING VORTEX EFFECTS

(t) FIN: T15 $a/s_m: 0.5$ $AR: 1.0$ $\lambda: 0.5$ $M_\infty: 3.0$

CNT 4, FIN NORMAL-FORCE COEFFICIENT

$\phi_4 \backslash \alpha_c$	0°	4°	10°	15°	20°	25°	30°	35°	40°	45°	50°
-90°	0	0	0	0	0	0	0	0	0	0	0
-80°	0	.0187	-.030	-.070	.0515	.032	-.015	-.004	.0087	.009	.005
-70°	0	.0370	-.0265	-.0673	-.037	.0083	.0175	.0413	.0587	.0644	.06
-60°	0	.0542	-.001	-.0165	.020	.055	.0855	.1187	.143	.1413	.1245
-50°	0	.0702	.057	.052	.0975	.1435	.185	.2215	.2495	.247	.220
-40°	0	.085	.109	.125	.176	.227	.278	.329	.376	.378	.340
-30°	0	.0976	.158	.202	.259	.325	.399	.466	.521	.556	.565
-20°	0	.1083	.205	.260	.345	.420	.500	.587	.668	.744	.805
-10°	0	.1162	.218	.305	.397	.494	.600	.711	.840	.977	1.105
0°	0	.1208	.245	.340	.450	.570	.700	.850	1.017	1.195	1.379
10°	0	.1212	.261	.368	.483	.615	.761	.935	1.150	1.395	1.590
20°	0	.1171	.261	.368	.493	.650	.833	1.030	1.257	1.527	1.795
30°	0	.1090	.255	.358	.488	.643	.825	1.038	1.277	1.610	1.870
40°	0	.0955	.234	.341	.461	.610	.778	.978	1.204	1.557	1.765
50°	0	.0787	.196	.295	.407	.540	.700	.875	1.085	1.375	1.683
60°	0	.052	.12	.21	.328	.438	.570	.724	.895	1.094	1.305
70°	0	.026	.08	.17	.288	.398	.520	.674	.844	1.044	1.255
80°	0	.010	.04	.09	.198	.308	.420	.574	.744	.944	1.155
90°	0	.002	.01	.02	.048	.158	.260	.374	.544	.744	.944

TABLE 6. NORMAL-FORCE COEFFICIENTS OF FINS
ON BODY B₁, INCLUDING VORTEX EFFECTS

(u) FIN: T23 a/s_m: 0.5 AR: 2.0 λ: 0.5 M_∞: 3.0

CNT4, FIN NORMAL-FORCE COEFFICIENT

$\phi_4 \backslash \alpha_c$	0°	4°	10°	15°	20°	25°	30°	35°	40°	45°	50°
-90°	0	0	0	0	0	0	0	0	0	0	0
-80°	0	.0117	-.014	.0595	-.038	.0205	-.013	-.012	.004	.006	.015
-70°	0	.0225	-.043	-.082	-.043	-.009	.0175	.039	.0565	.069	.078
-60°	0	.036	-.031	-.032	.020	.049	.091	.127	.155	.176	.190
-50°	0	.051	.046	.022	.075	.144	.194	.236	.273	.308	.340
-40°	0	.065	.102	.110	.179	.249	.308	.362	.412	.460	.508
-30°	0	.0786	.150	.210	.275	.350	.433	.517	.608	.700	.792
-20°	0	.0902	.197	.275	.355	.466	.535	.632	.731	.835	.936
-10°	0	.1010	.230	.325	.430	.540	.658	.784	.913	1.045	1.175
0°	0	.1094	.255	.370	.485	.617	.763	.92	1.093	1.305	1.535
10°	0	.1128	.276	.400	.520	.667	.845	1.048	1.270	1.500	1.730
20°	0	.1094	.263	.400	.550	.710	.918	1.155	1.400	1.645	
30°	0	.1010	.251	.387	.537	.720	.924	1.163	1.433	1.725	2.250
40°	0	.090	.220	.355	.510	.690	.900	1.125	1.375	1.637	1.900
50°	0	.0756	.190	.305	.431	.600	.790	1.005	1.245	1.491	1.725
60°	0	.0586	.157	.238	.335	.470	.638	.834	1.033	1.205	1.335
70°	0	.044	.124	.221	.305	.424	.573	.735	.883	1.010	1.120

275
 TABLE 6. NORMAL-FORCE COEFFICIENTS OF FINS
 ON BODY B₁, INCLUDING VORTEX EFFECTS

(v) FIN: T31 a/s_m: 0.5 AR: 0.5 λ: 0.5 M_∞: 3.0

		CNT4, FIN NORMAL-FORCE COEFFICIENT										
α_c	ϕ_4	0°	4°	10°	15°	20°	25°	30°	35°	40°	45°	50°
-90°	0	0	0	0	0	0	0	0	0	0	0	0
-80°	0	.0108	-.015	.0714	.0435	.0205	.0057	.004	.0095	.0115	.0115	.0115
-70°	0	.022	-.021	.0505	-.022	.0041	.0248	.0398	.0512	.061	.0697	.0697
-60°	0	.0332	.004	.000	.0193	.0465	.0735	.0998	.1297	.152	.167	.167
-50°	0	.045	.047	.0525	.079	.120	.1603	.2002	.2375	.268	.290	.290
-40°	0	.057	.084	.112	.154	.199	.244	.293	.348	.407	.468	.468
-30°	0	.0692	.121	.170	.224	.282	.350	.420	.496	.577	.664	.664
-20°	0	.0808	.155	.215	.285	.363	.450	.542	.637	.736	.836	.836
-10°	0	.0905	.190	.260	.341	.445	.568	.700	.820	.926	1.011	1.011
0°	0	.0974	.213	.296	.390	.510	.645	.797	.945	1.075	1.185	1.185
10°	0	.1008	.227	.325	.427	.561	.714	.885	1.050	1.197	1.323	1.323
20°	0	.0996	.236	.340	.452	.593	.758	.938	1.115	1.281	1.432	1.432
30°	0	.0930	.234	.332	.445	.591	.761	.951	1.143	1.303	1.426	1.426
40°	0	.0834	.211	.311	.420	.565	.735	.920	1.115	1.278	1.377	1.377
50°	0	.0708	.177	.270	.375	.510	.663	.831	1.005	1.196	1.395	1.395
60°	0	.0555	.145	.215	.297	.411	.543	.691	.850	1.010	1.153	1.153
70°	0	.0377	.100	.151	.211	.290	.382	.483	.608	.757	.925	.925
80°	0	.0180	.049	.076	.110	.148	.191	.240	.304	.392	.502	.502

TABLE 6. NORMAL-FORCE COEFFICIENTS OF FINS
ON BODY B, INCLUDING VORTEX EFFECTS

(w) FIN: T32

$$a/s_m : \underline{0.5}$$

AR:0.5

λ : 1.0

$M_\infty : 3.0$

CNT4, FIN NORMAL-FORCE COEFFICIENT

TABLE 6. NORMAL-FORCE COEFFICIENTS OF FINS
ON BODY B, INCLUDING VORTEX EFFECTS

(x) FIN: T36 a/s_m: 0.5 AR:0.5 λ: 0 M_∞: 3.0

CNT 4, FIN NORMAL-FORCE COEFFICIENT

TABLE 7. NORMAL-FORCE COEFFICIENTS OF CANARD FIN C6
OF ASPECT RATIO 3.53 INCLUDING VORTEX EFFECTS

(a) FIN: C6 a/s_m: .400 AR: 3.53 λ: .06 M_∞: 0.8

CNC4, FIN NORMAL-FORCE COEFFICIENT

$\phi_4 \backslash \alpha_c$	0°	4°	10°	15°	20°	25°	30°	35°	40°	45°	50°
-90°	0	0	0	0	0	0	0	0	0	0	0
-80°	0	.084	.168	.254	.306	.338	.308	.269	.089	-.096	
-70°	0	.138	.320	.444	.537	.579	.542	.505	.239	-.113	
-60°	0	.192	.451	.579	.683	.729	.724	.702	.431	-.049	
-50°	0	.241	.554	.675	.769	.808	.853	.857	.663	.182	
-40°	0	.286	.626	.744	.779	.838	.936	.973	.899	.611	
-30°	0	.313	.665	.786	.744	.838	.961	1.050	1.087	.986	
-20°	0	.333	.690	.803	.754	.813	.946	1.106	1.232	1.249	
-10°	0	.350	.722	.813	.786	.855	.988	1.163	1.333	1.404	
0°	0	.362	.742	.818	.825	.949	1.096	1.232	1.390	1.488	
10°	0	.367	.744	.813	.853	.988	1.170	1.271	1.407	1.538	
20°	0	.362	.729	.811	.867	.981	1.178	1.286	1.404	1.515	
30°	0	.338	.692	.818	.869	.961	1.133	1.274	1.392	1.493	
40°	0	.288	.638	.798	.857	.926	1.020	1.227	1.299	1.404	
50°	0	.244	.562	.747	.828	.880	.973	1.148	1.222	1.333	
60°	0	.202	.461	.646	.764	.811	.853	1.003	1.035	1.126	
70°	0	.150	.335	.483	.599	.685	.700	.786	.803	.833	
80°	0	.081	.180	.269	.340	.416	.473	.471	.503	.505	
90°	0	0	0	0	0	0	0	0	0	0	

* S_R = fin planform area

TABLE 7. NORMAL-FCRCE COEFFICIENTS OF CANARD FIN C6
OF ASPECT RATIO 3.53 INCLUDING VORTEX EFFECTS

(b) FIN: C6 a/s_m: .400 AR: 3.53 λ: .06 M_∞: 1.3

CNC4, FIN NORMAL-FORCE COEFFICIENT

280
 TABLE 8. NORMAL-FORCE COEFFICIENTS OF FINS
 ON BODY B_1 WITHOUT VORTEX EFFECTS

(a) FIN: T11 a/s_m : 0.5 AR: 1.0 λ : 1.0 M_∞ : 0.8

CNT4 FIN NORMAL-FORCE COEFFICIENT												
α_c ϕ_4	0°	4°	10°	15°	20°	25°	30°	35°	40°	45°	50°	
-90°	0	0	0	0	0	0	0	0	0	0	0	
-80°	0	.025	.038	.072	.060	.110	.231	.613	.782	.683		
-70°	0	.050	.091	.197	.214	.424	.756	.938	.983	.987		
-60°	0	.073	.154	.355	.541	.781	.928	1.038	1.064	1.07?		
-50°	0	.095	.227	.489	.721	.884	.988	1.068	1.063	1.062		
-40°	0	.115	.309	.590	.795	.954	1.023	1.066	1.075	1.083		
-30°	0	.133	.379	.667	.847	1.002	1.048	1.107	1.112	1.132		
-20°	0	.146	.434	.716	.878	1.026	1.063	1.112	1.151	1.198		
-10°	0	.156	.473	.737	.886	1.019	1.033	1.087	1.159	1.248		
0°	0	.158	.494	.731	.863	.887	.931	1.036	1.122	1.238		
10°	0	.156	.495	.708	.749	.792	.882	.998	1.098	1.207		
20°	0	.150	.478	.704	.778	.790	.862	.980	1.084	1.160		
30°	0	.140	.443	.682	.851	.851	.879	.992	1.072	1.143		
40°	0	.126	.392	.617	.826	.957	1.017	1.062	1.116	1.177		
50°	0	.109	.325	.528	.746	.979	1.063	1.127	1.196	1.238		
60°	0	.086	.244	.414	.608	.821	1.009	1.099	1.152	1.194		
70°	0	.057	.159	.274	.421	.564	.704	.818	.914	.987		
80°	0	.024	.077	.130	.196	.259	.324	.387	.437	.484		
90°	0	0	0	0	0	0	0	0	0	0		

S_R = fin planform area

281

TABLE 8. NORMAL-FORCE COEFFICIENTS OF FINS
ON BODY B₁ WITHOUT VORTEX EFFECTS

(b) FIN: T14 a/s_m: 0.5 AR: 1.0 λ: 0 M_∞: 0.8

TABLE 8. NORMAL-FORCE COEFFICIENTS OF FINS
ON BODY B,₁ WITHOUT VORTEX EFFECTS

(c) FIN: T15 a/s_m: 0.5 AR: 1.0 λ: 0.5 M_∞: 0.8

283

TABLE 8. NORMAL-FORCE COEFFICIENTS OF FINS
ON BODY B, WITHOUT VORTEX EFFECTS

(d) FIN: T23 a/s_m: 0.5 AR: 2.0 λ: 0.5 M_∞: 0.8

284

TABLE 8. NORMAL-FORCE COEFFICIENTS OF FINS
ON BODY B, WITHOUT VORTEX EFFECTS

$$(e) \quad \text{FIN: } \underline{\text{T31}} \quad a/s_m: \underline{0.5} \quad AR: \underline{0.5} \quad \lambda: \underline{0.5} \quad M_\infty: \underline{0.8}$$

CNT 4 FIN NORMAL-FORCE COEFFICIENT

TABLE 8. NORMAL-FORCE COEFFICIENTS OF FINS
ON BODY B, WITHOUT VORTEX EFFECTS

(f) FIN: T11 a/s_m: 0.5 AR: 1.0 λ: 1.0 M_∞: 1.2

TABLE 8. NORMAL-FORCE COEFFICIENTS OF FINS
ON BODY B, WITHOUT VORTEX EFFECTS

(g) FIN: T14 a/s_m: 0.5 AR: 1.0 λ: 0 M_∞: 1.2

CNT4 FIN NORMAL-FORCE COEFFICIENT

287

TABLE 8. NORMAL-FORCE COEFFICIENTS OF FINS
ON BODY B, WITHOUT VORTEX EFFECTS

(h) FIN: T31 a/s_m: 0.5 AR: 0.5 λ: 0.5 M_∞: 1.2

CNT4 FIN NORMAL-FORCE COEFFICIENT

200

TABLE 8. NORMAL-FORCE COEFFICIENTS OF FINS
ON BODY B₁ WITHOUT VORTEX EFFECTS

$$(i) \quad \text{FIN: } \underline{\underline{T_{23}}} \quad a/s_m: \underline{\underline{0.5}} \quad AR: \underline{\underline{2.0}} \quad \lambda: \underline{\underline{0.5}} \quad M_\infty: \underline{\underline{1.2}}$$

CNT4 FIN NORMAL-FORCE COEFFICIENT

TABLE 8. NORMAL-FORCE COEFFICIENTS OF FINS
ON BODY B, WITHOUT VORTEX EFFECTS

(j) FIN: T15 a/s_m: 0.5 AR: 1.0 λ: 0.5 M_∞: 1.2

CNT4 FIN NORMAL-FORCE COEFFICIENT

290

TABLE 8. NORMAL-FORCE COEFFICIENTS OF FINS
ON BODY B, WITHOUT VORTEX EFFECTS

(k) FIN: T11 a/s_m: 0.5 AR: 1.0 λ: 1.0 M_∞: 2.0

TABLE 8. NORMAL-FORCE COEFFICIENTS OF FINS
ON BODY B, WITHOUT VORTEX EFFECTS

(1) FIN: T14 a/s_m: 0.5 AR: 1.0 λ: 0 M_∞: 2.0

TABLE 8. NORMAL-FORCE COEFFICIENTS OF FINS
ON BODY B, WITHOUT VORTEX EFFECTS

(m) FIN: T15 a/s_m: 0.5 AR: 1.0 λ: 0.5 M_∞: 2.0

293

TABLE 8. NORMAL-FORCE COEFFICIENTS OF FINS
ON BODY B₁ WITHOUT VORTEX EFFECTS

(n) FIN: T23 a/s_m: 0.5 AR: 2.0 λ: 0.5 M_∞: 2.0

TABLE 8. NORMAL-FORCE COEFFICIENTS OF FINS
ON BODY B₁ WITHOUT VORTEX EFFECTS

(o) FIN: T31 a/s_m: 0.5 AR: 0.5 λ: 0.5 M_∞: 2.0

295
 TABLE 8. NORMAL-FORCE COEFFICIENTS OF FINS
 ON BODY B₁ WITHOUT VORTEX EFFECTS

(p) FIN: T32 a/s_m: 0.5 AR: 0.5 λ: 1.0 M_∞: 2.0

CNT 4 FIN NORMAL-FORCE COEFFICIENT

$\alpha_c \backslash \phi_4$	0°	4°	10°	15°	20°	25°	30°	35°	40°	45°	50°
-90°				0	0	0	0	0			
-80°				.008	.010	.030	.110	.147			
-70°				.037	.057	.122	.237	.289			
-60°				.115	.198	.246	.361	.424			
-50°				.216	.332	.365	.481	.549			
-40°				.291	.419	.472	.589	.663			
-30°				.349	.486	.568	.689	.772			
-20°				.396	.538	.647	.774	.871			
-10°				.439	.584	.711	.844	.959			
0°				.474	.621	.759	.896	1.031			
10°				.497	.650	.792	.929	1.081			
20°				.506	.664	.801	.939	1.100			
30°				.504	.653	.790	.924	1.075			
40°				.472	.615	.747	.874	1.015			
50°				.411	.549	.667	.789	.929			
60°				.328	.446	.546	.671	.803			
70°				.229	.315	.396	.499	.614			
80°				.119	.165	.222	.260	.304			
90°				0	0	0	0	0			

296
 TABLE 8. NORMAL-FORCE COEFFICIENTS OF FINS
 ON BODY B_1 WITHOUT VORTEX EFFECTS

(q) FIN: T36 a/s_m : 0.5 AR: 0.5 λ : 0 M_∞ : 2.0

CNT4 FIN NORMAL-FORCE COEFFICIENT

α_c ϕ	0°	4°	10°	15°	20°	25°	30°	35°	40°	45°	50°
-90°						0	0	0			
-80°						.026	.043	.090			
-70°						.076	.114	.182			
-60°						.153	.205	.274			
-50°						.226	.298	.365			
-40°						.298	.387	.457			
-30°						.367	.473	.549			
-20°						.434	.554	.639			
-10°						.495	.630	.726			
0°						.554	.699	.804			
10°						.604	.752	.863			
20°						.640	.774	.897			
30°						.654	.790	.909			
40°						.645	.780	.904			
50°						.602	.731	.864			
60°						.509	.627	.756			
70°						.366	.454	.546			
80°						.182	.227	.224			
90°						0	0	0			

297

TABLE 8. NORMAL-FORCE COEFFICIENTS OF FINS
ON BODY B₁, WITHOUT VORTEX EFFECTS

(r) FIN: T11 a/s_m: 0.5 AR: 1.0 λ: 1.0 M_∞: 3.0

CNT 4 FIN NORMAL-FORCE COEFFICIENT

298

TABLE 8. NORMAL-FORCE COEFFICIENTS OF FINS
ON BODY S₁ WITHOUT VORTEX EFFECTS

(s) FIN: T14 a/s_m: 0.5 AR: 1.0 λ: 0 M_∞: 3.0

299
 TABLE 8. NORMAL-FORCE COEFFICIENTS OF FINS
 ON BODY B₁ WITHOUT VORTEX EFFECTS

(t) FIN: T15 a/s_m: 0.5 AR: 1.0 λ: 0.5 M_∞: 3.0

300

TABLE 8. NORMAL-FORCE COEFFICIENTS OF FINS
ON BODY B, WITHOUT VORTEX EFFECTS

(u) FIN: T23 a/s_m: 0.5 AR: 2.0 λ: 0.5 M_∞: 3.0

301

TABLE 8. NORMAL-FORCE COEFFICIENTS OF FINS
ON BODY B, WITHOUT VORTEX EFFECTS

$$(v) \quad \text{FIN: } \underline{\text{T31}} \quad a/s_m: \underline{0.5} \quad AR: \underline{0.5} \quad \lambda: \underline{0.5} \quad M_\infty: \underline{3.0}$$

**TABLE 8. NORMAL-FORCE COEFFICIENTS OF FINS
ON BODY B, WITHOUT VORTEX EFFECTS**

(w) FIN: T32 a/s_m: 0.5 AR: 0.5 λ: 1.0 M_∞: 3.0

CNT 4 FIN NORMAL-FORCE COEFFICIENT

TABLE 8. NORMAL-FORCE COEFFICIENTS OF FINS
ON BODY B_1 WITHOUT VORTEX EFFECTS

(x) FIN: T36 $a/s_m: 0.5$ AR: 0.5 $\lambda: 0$ $M_\infty: 3.0$

CNT 4 FIN NORMAL-FORCE COEFFICIENT

ϕ	α_c	0°	4°	10°	15°	20°	25°	30°	35°	40°	45°	50°
-90°						0	0	0	0	0	0	
-80°						.031	.058	.072	.071	.055		
-70°						.070	.117	.145	.150	.126		
-60°						.114	.174	.217	.234	.212		
-50°						.160	.233	.291	.323	.311		
-40°						.210	.292	.364	.416	.420		
-30°						.261	.351	.438	.511	.535		
-20°						.314	.410	.518	.609	.658		
-10°						.370	.471	.593	.709	.789		
0°						.420	.538	.675	.806	.915		
10°						.461	.598	.746	.890	1.023		
20°						.490	.641	.798	.948	1.085		
30°						.499	.664	.824	.973	1.108		
40°						.494	.654	.813	.961	1.101		
50°						.453	.603	.757	.900	1.046		
60°						.377	.502	.643	.778	.924		
70°						.267	.362	.466	.574	.702		
80°						.123	.195	.237	.298	.363		
90°						0	0	0	0	0		

TABLE 9. NORMAL-FORCE COEFFICIENTS OF CANARD FIN C6
OF ASPECT RATIO 3.53 WITHOUT VORTEX EFFECTS

(a) FIN: C6 a/s_m: 0.4 AR: 3.53 λ: .06 M_∞: 0.8

CNC4, FIN NORMAL-FORCE COEFFICIENT

$\phi_4 \backslash \alpha_c$	0°	4°	10°	15°	20°	25°	30°	35°	40°	45°	50°
-90°	0	0	0	0	0	0	0	0	0	0	
-80°	0	.068	.168	.262	.306	.338	.364	.312	.121	.010	
-70°	0	.133	.320	.452	.547	.592	.653	.554	.277	.040	
-60°	0	.191	.454	.582	.724	.758	.844	.736	.479	.115	
-50°	0	.241	.553	.678	.775	.814	.943	.872	.722	.387	
-40°	0	.282	.623	.749	.776	.837	.968	.982	.949	.733	
-30°	0	.313	.669	.788	.752	.840	.952	1.064	1.123	1.041	
-20°	0	.337	.703	.806	.754	.819	.993	1.123	1.256	1.272	
-10°	0	.354	.726	.814	.785	.859	1.100	1.187	1.346	1.426	
0°	0	.365	.740	.815	.825	.950	1.174	1.241	1.398	1.510	
10°	0	.367	.743	.814	.855	.985	1.188	1.278	1.420	1.540	
20°	0	.361	.733	.813	.866	.982	1.148	1.291	1.420	1.532	
30°	0	.335	.695	.818	.870	.961	1.072	1.278	1.394	1.497	
40°	0	.290	.640	.804	.859	.925	.971	1.234	1.326	1.432	
50°	0	.246	.562	.745	.828	.877	.848	1.146	1.208	1.318	
60°	0	.201	.461	.643	.763	.808	.689	1.000	1.037	1.117	
70°	0	.148	.333	.488	.596	.680	.487	.784	.806	.848	
80°	0	.081	.178	.275	.343	.413	.260	.474	.494	.484	
90°	0	0	0	0	0	0	0	0	0	0	

$S_R = \text{fin planform area}$

TABLE 9. NORMAL-FORCE COEFFICIENTS OF CANARD FIN C6
OF ASPECT RATIO 3.53 WITHOUT VORTEX EFFECTS

(b) FIN: C6 a/s_m: 0.4 AR: 3.53 λ: .06 M_∞: 1.3

CNC4, FIN NORMAL-FORCE COEFFICIENT

TABLE 10. ASYMMETRIC COMPONENTS OF NORMAL-FORCE COEFFICIENTS
OF FINS OF SYSTEMATIC DATA BASE

(a) FIN: T11 a/s_m : 0.5AR: 1.0 λ : 1.0 M_∞ : 0.82 (ΔC_N)

$\phi_4 \backslash \alpha_c$	0°	4°	10°	15°	20°	25°	30°	35°	40°	45°	50°
-90°		.025	.087			.078	.303	.12	.185	.07	
-80°		.020	.079			ε	.110	.05	ε	.035	
-70°		.022	.106			.255	.100	.10	.10	.16	
-60°		.024	.092			.290	.083	.20	.050	.18	
-50°		.022	.095			.22	.055	.19	ε	.22	
-40°		.024	.103			.090	ε	.11	.060	.20	
-30°		.018	.104			.020	.055	ε	.12	ε	
-20°		.023	.086			.109	.123	.06	ε		
-10°		.024	.083			.215	.080	.070	ε	.06	
0°		.018	.078			.213	.138	.050	ε	.04	
10°		.010	.027			.074	.075	.060	ε	.06	
20°		.009	ε			.084	.03	.070	ε		
30°		.010	ε			.047	.058	.085	ε		
40°		ε	ε			.069	.057	ε	.04		
50°		ε	ε			.050	.061	.04	ε	ε	
60°		ε	ε			ε	.070	.10	ε	ε	
70°		ε	ε			ε	ε	ε	.04		
80°		ε	ε			ε	ε	ε			
90°											

 S_R = fin planform area

ε ~ negligible quantity

TABLE 10. ASYMMETRIC COMPONENTS OF NORMAL-FORCE COEFFICIENTS
OF FINS OF SYSTEMATIC DATA BASE

(b) FIN: T14

$$a/s_m: \underline{0.5}$$

AR: 1.0

$$\lambda: \underline{0}$$

$$M_{\text{ca}} = 0.8$$

2 (Δ CNT)

308

³⁰⁸
TABLE 10. ASYMMETRIC COMPONENTS OF NORMAL-FORCE COEFFICIENTS
OF FINS OF SYSTEMATIC DATA BASE

(c) FIN: T15 a/s_m: 0.5 AR: 1.0 λ: 0.5 M_g: 0.8

2 (Δ CNT)

TABLE 10. ASYMMETRIC COMPONENTS OF NORMAL-FORCE COEFFICIENTS
OF FINS OF SYSTEMATIC DATA BASE

(d) FIN: T23 a/s_m: 0.5 AR: 2.0 λ: 0.5 M_∞: 0.8

2 (ΔCNT_‡)

310

TABLE 10. ASYMMETRIC COMPONENTS OF NORMAL-FORCE COEFFICIENTS
OF FINS OF SYSTEMATIC DATA BASE

$$(e) \quad \text{FIN: } \underline{\text{T31}} \quad a/s_m: \underline{0.5} \quad AR: \underline{0.5} \quad \lambda: \underline{0.5} \quad M_\infty: \underline{0.8}$$

2 (Δ CNT)

TABLE 10. ASYMMETRIC COMPONENTS OF NORMAL-FORCE COEFFICIENTS
OF FINS OF SYSTEMATIC DATA BASE

$$(f) \quad \text{FIN: } \underline{T_{11}} \quad a/s_m: \underline{0.5} \quad AR: \underline{1.0} \quad \lambda: \underline{1.0} \quad M_\infty: \underline{1.2}$$

a/s_m: 0.5

AR: 1.0

$$\lambda := 1.0$$

$$M_o: \underline{1.2}$$

2 (Δ CNT)

TABLE 10. ASYMMETRIC COMPONENTS OF NORMAL-FORCE COEFFICIENTS
OF FINS OF SYSTEMATIC DATA BASE

(g) FIN: T14 a/s_m: 0.5 AR: 1.0 λ: 0 M_ω: 1.2

2 (Δ CNT)

TABLE 10. ASYMMETRIC COMPONENTS OF NORMAL-FORCE COEFFICIENTS
OF FINS OF SYSTEMATIC DATA BASE

(h) FIN: T15 a/s_m: 0.5 AR: 1.0 λ: 0.5 M_g: 1.2

2 (ACNT)

314

**TABLE 10. ASYMMETRIC COMPONENTS OF NORMAL-FORCE COEFFICIENTS
OF FINS OF SYSTEMATIC DATA BASE**

(i) FIN: T23

a/s_m: 0.5

AR: 2.0

λ : 0.5

M₂: 1.2

2 (Δ CNT)

TABLE 10. ASSYMETRIC COMPONENTS OF NORMAL-FORCE COEFFICIENTS
OF FINS OF SYSTEMATIC DATA BASE

(j) FIN: T31

a/s_m : 0.5

AR: 0.5

λ : 0.5

$$M_{so} : \underline{1.2}$$

2 (Δ CNT)

TABLE 11. EXPERIMENTAL VALUES OF WING-BODY INTERFERENCE
 FACTOR K_w FOR FINS OF SYSTEMATIC DATA BASE
 TESTED ON BODY B_1 ; NO BODY VORTEX EFFECTS

(a) $M_\infty = \underline{0.8}$

FIN	T11	T14	T15	T23	T31	T32	T36
α_c , degs.							
4	1.407	1.511	1.321	1.409	1.314		
10	1.435	1.420	1.374	1.402	1.333		
15	1.378	1.402	1.393	1.461	1.317		
20	1.338	1.370	1.325	.779	1.322		
25	1.088	1.331	1.562	.789	1.311		
30	.953	1.230	.937	.892	1.248		
35	1.035	1.031	.831	1.024	1.102		
40	1.143	.903	.817	1.154	.898		
45	1.474	.944	.903	1.297	.807		
50							

TABLE 11. EXPERIMENTAL VALUES OF WING-BODY INTERFERENCE
 FACTOR K_W FOR FINS OF SYSTEMATIC DATA BASE
 TESTED ON BODY B₁; NO BODY VORTEX EFFECTS

(b) $M_\infty = \underline{1.2}$

FIN	T11	T14	T15	T23	T31	T32	T36
α_c , degs.							
4	1.254	1.405	1.470	1.366	1.417		
10	1.366	1.371	1.362	1.441	1.420		
15	1.426	1.354	1.390	1.465	1.309		
20	1.382	1.291	1.281	1.397	1.225		
25	1.419	1.204	1.274	1.349	1.282		
30	1.372	1.133	1.202	1.325	1.214		
35	1.249	1.072	1.151	1.279	1.128		
40	1.108	1.041	1.149	1.212	1.143		
45	.965	1.042	1.185	.972	1.115		
50							

TABLE 11. EXPERIMENTAL VALUES OF WING-BODY INTERFERENCE
 FACTOR K_w FOR FINS OF SYSTEMATIC DATA BASE
 TESTED ON BODY B₁; NO BODY VORTEX EFFECTS

(c) $M_\infty = 2.0$

FIN	T11	T14	T15	T23	T31	T32	T36
α_c , degs.							
4	1.297	1.394	1.343	1.413	1.231		
10	1.263	1.115	1.237	1.364	1.181		
15	1.264	1.057	1.172	1.302	1.131	1.160	
20	1.182	.930	.987	1.142	1.065	1.119	
25	1.067	.884	.964	.989	1.010	1.068	.950
30	.993	.880	.958	.934	.996	1.044	.975
35	.941	.856	.931	.930	.991	1.008	.946
40	.892	.810	.876	.897	.895		
45	.813	.740	.800	.807	.767		
50	.698	.647					

TABLE 11. EXPERIMENTAL VALUES OF WING-BODY INTERFERENCE
 FACTOR K_W FOR FINS OF SYSTEMATIC DATA BASE
 TESTED ON BODY B_1 ; NO BODY VORTEX EFFECTS

(d) $M_\infty = \underline{3.0}$

FIN	T11	T14	T15	T23	T31	T32	T36
α_c , degs.							
4	1.756	1.294	1.684	1.184	1.327	1.226	
10	1.226	.978	1.061	1.072	1.080	1.117	
15	1.064	.872	.986	1.038	1.002	1.080	
20	1.001	.855	.954	.991	.968	1.067	
25	.940	.818	.892	.919	.949	1.030	.878
30	.910	.807	.860	.883	.960	1.020	.926
35	.931	.810	.860	.883	.987	1.033	.945
40	.983	.811	.865	.871	.997	1.023	.922
45	.945	.786	.866	.880	.974	1.023	.881
50	.820	.731			.931	1.026	.810

320
 TABLE 12. ERRORS IN ESTIMATING FIN NORMAL-FORCE
 COEFFICIENTS USING LINEAR INTERPOLATION IN
 ASPECT RATIO AND TAPER RATIO
 (a) T36, $M_{\infty} = 2.0$

FIN: T36 $a/s_m: 0.5$ AR: 0.5 $\lambda: 0$ $M_{\infty}: 2.0$

$$E_{36} = T_{36} - [T_{31} - (T_{15} - T_{14})]$$

$\phi_4 \backslash \alpha_c$	0°	4°	10°	15°	20°	25°	30°	35°	40°	45°	50°
-90°					0	0	0				
-80°					.040	.014	.089				
-70°					.060	.013	.128				
-60°					.083	.013	.124				
-50°					.091	.012	.100				
-40°					.088	.010	.061				
-30°					.089	.026	.037				
-20°					.066	.043	.003				
-10°					.045	.058	.014				
0°					.026	.071	.040				
10°					.008	.071	.062				
20°					.009	.064	.070				
30°					.043	.064	.070				
40°					.071	.050	.090				
50°					.080	.020	.071				
60°					.067	.000	.033				
70°					.042	.035	.013				
80°					.009	.021	.044				
90°					0	0	0				

321
 TABLE 12. ERRORS IN ESTIMATING FIN NORMAL-FORCE
 COEFFICIENTS USING LINEAR INTERPOLATION IN
 ASPECT RATIO AND TAPER RATIO
 (b) T36, $M_\infty = 3.0$

FIN: T36 $a/s_m : 0.5$ AR: 0.5 $\lambda : 0$ $M_\infty : 3.0$

$$E_{36} = T_{36} - [T_{31} - (T_{15} - T_{14})]$$

$\phi_4 \backslash \alpha_c$	0°	4°	10°	15°	20°	25°	30°	35°	40°	45°	50°
-90°						0	0	0	0	0	
-80°						.016	.010	.000	.002	.018	
-70°						.027	.018	.002	.003	.034	
-60°						.033	.021	.006	.001	.050	
-50°						.037	.022	.013	.000	.067	
-40°						.037	.018	.016	.005	.076	
-30°						.031	.012	.014	.013	.072	
-20°						.023	.003	.013	.039	.050	
-10°						.008	.021	.005	.077	.001	
0°						.003	.030	.049	.122	.049	
10°						.001	.070	.031	.150	.183	
20°						.001	.016	.012	.160	.101	
30°						.006	.006	.010	.138	.110	
40°						.003	.020	.007	.119	.086	
50°						.002	.022	.005	.123	.040	
60°						.009	.008	.008	.136	.020	
70°						.016	.005	.013	.130	.050	
80°						.013	.011	.018	.079	.076	
90°						0	0	0	0	0	

322
 TABLE 12. ERRORS IN ESTIMATING FIN NORMAL-FORCE
 COEFFICIENTS USING LINEAR INTERPOLATION IN
 ASPECT RATIO AND TAPER RATIO

(c) T32, $M_{\infty} = 2.0$

FIN: T32 $a/s_m : 0.5$ AR: 0.5 $\lambda : 1.0$ $M_{\infty} : 2.0$

$$E_{32} = T_{32} - [T_{31} - (T_{15} - T_{14})]$$

$\phi_4 \backslash \alpha_c$	0°	4°	10°	15°	20°	25°	30°	35°	40°	45°	50°
-90°				0	0	0	0	0			
-80°				.010	.011	.029	.029	.058			
-70°				.027	.054	.043	.039	.084			
-60°				.043	.051	.035	.058	.080			
-50°				.044	.030	.029	.067	.069			
-40°				.027	.044	.031	.068	.045			
-30°				.025	.062	.037	.042	.026			
-20°				.040	.080	.047	.020	.005			
-10°				.046	.092	.054	.008	.009			
0°				.045	.104	.062	.005	.012			
10°				.043	.110	.071	.033	.006			
20°				.044	.104	.081	.030	.021			
30°				.037	.111	.077	.006	.021			
40°				.029	.107	.082	.010	.023			
50°				.022	.100	.096	.028	.015			
60°				.014	.074	.091	.019	.029			
70°				.010	.047	.049	.012	.010			
80°				.000	.000	.014	.025	.013			
90°				0	0	0	0	0			

TABLE 12. ERRORS IN ESTIMATING FIN NORMAL-FORCE COEFFICIENTS USING LINEAR INTERPOLATION IN ASPECT RATIO AND TAPER RATIO
 (d) T32, $M_{\infty} = 3.0$

FIN: T32 a/s_m: 0.5 AR: 0.5 λ: 1.0 M_∞: 3.0

$$E_{32} = T_{32} - [T_{31} - (T_{15} - T_{14})]$$

324
 TABLE 13. EXPERIMENTAL VALUES OF k_w FOR CANARD FIN C6
 TESTED ON ARMY GENERALIZED MISSILE

(a) $M_\infty = 0.8$

FIN: C6 a/s_m: 0.4 AR: 3.53 λ : .06 $\delta_{2,4} = 15^\circ$

Interference factor for control deflection, k_w

$\phi_4 \backslash \alpha_c$	0°	4°	10°	15°	20°	25°	30°	35°	40°	45°	50°
-90°		1.33	1.45	1.71	1.49	1.20	.87	.63	.50	.39	
-80°		1.27	1.39	1.58	1.39	1.13	.79	.52	.44	.32	
-70°		1.12	1.27	1.36	1.19	.98	.64	.39	.27	.16	
-60°		1.04	1.11	1.07	.94	.77	.45	.29	.14	.10	
-50°		1.02	1.03	.83	.76	.66	.40	.24	.11	.11	
-40°		1.03	1.00	.79	.70	.63	.41	.24	.12	.14	
-30°		1.07	1.01	.89	.77	.65	.45	.28	.15	.13	
-20°		1.11	1.04	.96	.84	.69	.48	.27	.16	.08	
-10°		1.09	1.07	.99	.88	.67	.47	.23	.14	.05	
0°		1.02	1.05	.99	.89	.55	.34	.21	.12	.07	
10°		1.05	1.02	.96	.83	.48	.24	.21	.14	.13	
20°		1.10	1.01	.93	.78	.44	.21	.21	.18	.16	
30°		1.12	1.00	.92	.78	.43	.20	.21	.19	.14	
40°		1.10	.99	.95	.82	.48	.20	.21	.17	.18	
50°		1.00	.89	.87	.88	.73	.25	.23	.17	.24	
60°		.79	.51	.55	1.20	1.22	.62	.60	.44	.42	
70°		.80	.64	.56	.55	.78	1.35	1.35	1.33	1.23	
80°		.96	.95	.79	.84	.62	.27	.29	.20	.13	
90°		1.04	1.02	.94	.93	.84	.62	.62	.52	.44	

TABLE 13. EXPERIMENTAL VALUES OF k_w FOR CANARD FIN C6
TESTED ON ARMY GENERALIZED MISSILE(b) $M_\infty = 1.3$ FIN: C6 a/s_m: 0.4 AR: 3.53 λ : .06 $\delta_{2,4} = 15^\circ$ Interference factor for control deflection, k_w

ϕ_4	0°	4°	10°	15°	20°	25°	30°	35°	40°	45°	50°
-90°	.856	.804	.763	.749	.737	.730	.714	.623	.491	.406	
-80°	.856	.834	.795	.758	.736	.667	.543	.431	.352	.294	
-70°	.857	.847	.806	.753	.711	.619	.398	.327	.278	.212	
-60°	.858	.838	.786	.725	.672	.580	.431	.319	.261	.166	
-50°	.859	.785	.740	.675	.622	.537	.435	.349	.262	.152	
-40°	.864	.760	.701	.633	.567	.489	.407	.324	.239	.131	
-30°	.870	.766	.684	.609	.526	.438	.349	.251	.160	.086	
-20°	.883	.791	.682	.599	.513	.391	.295	.196	.102	.038	
-10°	.912	.826	.691	.598	.510	.394	.348	.323	.262	.201	
0°	.941	.859	.711	.608	.496	.528	.488	.589	.671	.506	
10°	.955	.881	.741	.603	.453	.803	.943	.943	.783	.552	
20°	.942	.890	.770	.603	.421	.737	.863	.898	.722	.501	
30°	.893	.877	.796	.632	.423	.547	.638	.674	.633	.490	
40°	.847	.846	.817	.686	.453	.392	.440	.474	.439	.513	
50°	.824	.831	.835	.754	.505	.290	.285	.344	.437	.513	
60°	.812	.825	.852	.824	.587	.255	.173	.237	.316	.436	
70°	.808	.826	.866	.880	.706	.452	.160	.164	.200	.235	
80°	.808	.831	.874	.914	.852	.596	.338	.202	.227	.167	
90°	.811	.841	.873	.919	1.016	.690	.759	.650	.558	.480	

TABLE 14. EXPERIMENTAL VALUES OF WING-BODY INTERFERENCE
 FACTOR K_w FOR CANARD FIN C6 ON ARMY
 GENERALIZED MISSILE ; NO VORTEX EFFECTS

Aspect ratio = 3.53 Taper ratio = .06 $a/s_m = 0.4$

K_w

α	$M_\infty = 0.8$	$M_\infty = 1.3$
0	1.450	1.450
4	1.295	1.461
10	1.344	1.243
15	1.381	1.218
20	1.127	1.172
25	1.537	1.021
30	1.582	.943
35	1.536	.924
40	1.493	.941
45	1.381	.938
50		.912

LIST OF SYMBOLS

a	body radius
c_{d_c}	two-dimensional crossflow drag coefficient
c_r	length of fin root chord
c_t	length of fin tip chord
g_3	distance from beginning of body nose to starting position of third body vortex
k_B	wing-body interferences factor for body normal force for $\delta = 0, \alpha_c \neq 0$
k_w	wing-body interference factor for fin normal force for $\delta \neq 0, \alpha_c = 0$
k_w, SBT	value of k_w given by slender-body theory
l_{MRC}	distance from leading edge of tail fin to moment reference center, figure 6
l_r	reference length
n	number of vortices of like sign in distance $V_\infty \cos \alpha$ along body axis
q_∞	dynamic pressure of free stream
s_m	semispan of fin on body
t_1	spanwise distance of Γ_1 from body axis
t_2	spanwise distance of Γ_2 from body axis
\bar{t}	spanwise distance from axis of single vortex replacing Γ_1 and Γ_2
v	velocity component in y-direction
w	velocity component in z-direction
$(w_n)_{vor}$	average velocity induced normal to fin ($\delta = 0$) by collection of external vortices and their images
x_s	axial location of initial separation of body nose vorticity
x, y, z	missile body axes; x measured positive downstream along body rotational axis, y measured positive to right in the plane C4, and z measured upward in the plane of C1; origin is located at MS 0

LIST OF SYMBOLS (Continued)

x_o, y_o, z_o	special set of x, y, z axes for $\phi = 0$; also called unrolled body coordinates
x_{MC}	axial location of reference for moments acting on missile measured from MS 0
\bar{y}	lateral position of fin center of pressure with all effects present
\bar{y}_i	value of \bar{y} for i 'th fin
\bar{y}_p	lateral position of fin center of pressure with no vortex effects present
\bar{y}_v	lateral position of center of pressure for normal force induced by vortices
y_v, z_v	coordinates of vortex in the crossflow plane
AR	wing-alone aspect ratio
C_A	axial-force coefficient; axial force/ $q_\infty S_R$
$CBMi$	bending-moment coefficient of the i 'th fin about fin root
C_D	drag coefficient; lift/ $q_\infty S_R$
C_L	lift coefficient; lift/ $q_\infty S_R$
C_ℓ	rolling-moment coefficient; rolling moment/ $q_\infty S_R \ell_r$
C_m	pitching-moment coefficient; pitching moment/ $q_\infty S_R \ell_r$
C_N	normal-force coefficient; normal force/ $q_\infty S_R$
C_{Ni}	normal-force coefficient of i 'th fin
ΔC_N	increment in normal force of a pitched and yawed wing proportional to the product $\alpha\beta$
C_n	yawing-moment coefficient; yawing moment/ $q_\infty S_R \ell_r$
$C_{N_B(W)}$	normal-force coefficient for body in the presence of fins; normal force/ $q_\infty S_R$
C_Y	side-force coefficient; side force/ $q_\infty S_R$
$CNC1, CNC2, etc.$	normal-force coefficients associated with fins C1, C2, etc.

LIST OF SYMBOLS (Continued)

$(CNF)_v$	change in fin normal-force coefficient due to change in equivalent angle of attack by $(\Delta\alpha_{eq})_v$
CNT	normal-force coefficient for a general tail fin
\overline{CNT}	average of two different values of CNT associated with bistable vortex switching
$\Delta(CNT)$	one-half the positive difference between two values of CNT associated with bistable vortex switching
$(CNT)_p$	normal force of a general tail fin without vortex effects
$(CNT)_v$	component of tail fin normal force due to external vortices
CRMCl, CRMC2, etc.	rolling-moment coefficients associated with fins Cl, C2, etc.
CNT1, CNT2, etc.	normal-force coefficients associated with fins T1, T2, etc.
$(CNT4)_p$	value of CNT4 if no vortices present
C_{N_W}	normal-force coefficient of "wing alone" formed by joining two opposing fins; normal force/ $q_\infty S_R$
CRMi	rolling-moment coefficient of the i'th fin about body axis
CRMT	rolling-moment coefficient of general tail fin
CRMT0	value of CRMT when CNT is zero
CRMT1, CRMT2, etc.	rolling-moment coefficients associated with fins T1, T2, etc.
C1, C2, etc.	canard fins numbered counterclockwise from top at $\phi = 0$; also vortices associated with canard fins
D	cylinder diameter
E32	error made in estimating CNT for fin T32 by linear interpolation in aspect ratio or taper ratio
E36	error made in estimating CNT for fin T36 by linear interpolation in aspect ratio or taper ratio

LIST OF SYMBOLS (Continued)

H	height of body vortices above body centerline, figure 32
K_B	wing-body interference factor for body normal force for $\delta = 0$, $\alpha_c \neq 0$
K_W	wing-body interference factor for fin normal force for $\delta \neq 0$, $\alpha_c = 0$
$K_{W,0.5}$	value of K_W for $a/s_m = 0.5$
K_ϕ	wing-body interference factor for bank, $\delta = 0$ $\alpha_c \neq 0$
L	body length
L_n	length of body nose from tip to shoulder
M_c	crossflow Mach number, $M_\infty \sin \alpha_c$
$M_{critical}$	critical crossflow Mach number for a circular cylinder; 0.4
M_{cf}	local crossflow Mach number
M_{wake}	Mach number in the wake above an inclined body of revolution
M_1, M_2	two Mach numbers in the data base between which interpolation is to be performed
M_∞	free-stream Mach number
$MS\ 0$	missile station zero; origin of coordinate system
N	normal force
N_{FIN}	normal force acting on one fin
Q_M	value of a quantity at Mach number M greater than 3
$Q_{M_\infty=3}$	value of a quantity at $M_\infty=3$
Q_I	a quantity associated with an AR and λ in the ranges $1 < AR < 2 ; 0.5 \leq \lambda \leq 1.0$
Q_{II}	$1 \leq AR \leq 2 ; 0 \leq \lambda \leq 0.5$
Q_{III}	$0.5 \leq AR \leq 1 ; 0 \leq \lambda \leq 0.5$

LIST OF SYMBOLS (Continued)

Q_{IV}	$0.5 \leq AR \leq 1 ; 0.5 \leq \lambda \leq 1.0$
Q_1	any quantity depending on Mach number specified for an arbitrary Mach number M_1
Q_2	any quantity depending on Mach number specified for an arbitrary Mach number M_2
Q_∞	any quantity depending on Mach number evaluated at M_∞
ΔQ	difference in a quantity between $M_\infty = 3.0$ and $M_\infty = 2.0$
S	Strouhal number for flow over inclined cylinder, $\frac{nD}{V_\infty \sin \alpha_c}$
S_R	reference area; except where stated reference areas for isolated wings are wing planform areas and for wing-body combinations are maximum body cross-sectional areas.
$T_1, T_2, \text{etc.}$	tail fins number counterclockwise from top at $\phi = 0$
U_e	velocity at the side angle of a circular cylinder in crossflow
U_∞	free-stream velocity of a circular cylinder in crossflow
V_∞	free-stream velocity
X_{CTE}	axial position of the canard trailing edge
X_{TLE}	axial position of the leading edge of the tail root chord
Y	side force
α	body angle of attack
α_c	included angle of attack; angle between x axis and free-stream velocity
α_{eq}	equivalent angle of attack; that angle of attack of the wing alone for which its normal force is twice that of the fin; the wing alone is formed by joining two opposing fins together
$(\alpha_{eq})_i$	equivalent angle of attack of i 'th fin
$(\alpha_{eq})_{a/s_m}$	equivalent angle of attack for any a/s_m

LIST OF SYMBOLS (Continued)

$\alpha_{eq,exp}$	equivalent angle of attack including vortex effects
$\alpha_{eq,p}$	equivalent angle of attack when no vortices are present
$\alpha_{eq,0}$	fin equivalent angle of attack with no control deflection
$(\alpha_{eq})_{0.5}$	equivalent angle of attack for $a/s_m = 0.5$
$\alpha_{eq,\delta}$	equivalent angle of attack with control deflection
α_w	wing-alone angle of attack
$\Delta(\alpha_{eq})_1, \Delta(\alpha_{eq})_2,$ $\Delta(\alpha_{eq})_3, \Delta(\alpha_{eq})_4$	changes in the equivalent angle of attack of fin T1, T2, T3, and T4 due to control deflection δ_4 of T4; see Table 1
$(\Delta\alpha_{eq})_v$	change in α_{eq} due to a collection of external vortices and their images
β	fin angle of sideslip
Γ	vortex strength
Γ_1, Γ_2	strength of a pair of vortices representing one fin
γ	rate per unit time per unit length that vorticity is shed along a line of separation
$\gamma_{M=0}$	value of γ for $M=0$
$\gamma_{M \neq 0}$	value of γ for $M \neq 0$
$\delta_1, \delta_2, \text{etc.}$	incidence angles associated with fins C1, C2, etc., for $\phi = 0$, δ_1 and δ_3 are positive for trailing edges to the right viewed from the rear, and δ_2 and δ_4 are positive for trailing edges down
θ	semi-apex angle of Mach cone, $\sin^{-1} \frac{1}{M_\infty}$
θ_s	angular position of separation point on a body of revolution measured from the windward meridian
λ	ratio of fin tip chord to root chord
λ_{12}	fraction of the planform of fin T2 (or C2) which lies within the field of influence of T1 (or C1) for a cruciform wing-body combination

LIST OF SYMBOLS (Concluded)

λ_{24}	fraction of the planform of fin T2 which lies within the field of influence of fin T4 for a cruciform wing-body combination
ρ_∞	density of fluid in free stream
σ	ratio of $\gamma_{M=0}$ to $\gamma_{M \neq 0}$; equation (28)
ϕ	roll angle, angle between z axis and z_0 axis; positive measured clockwise viewed from rear
$\phi_1, \phi_2, \phi_3, \phi_4$	angular position of T1, T2, T3, and T4, respectively, measured clockwise from the values for $\phi = 0$
ϕ_T	interdigitation angle, angle between canard fin C1 and tail fin T1 measured clockwise from fin C1

Subscripts

l	lower fin surface
$l.e.$	leading edge
$t.e.$	trailing edge
u	upper fin surface
v	vortex

Special symbols used in the individual appendices are defined therein.